Title
Electrochemical Approaches to Renewable Energy

Author
Lobaccaro, Peter

Publication Date
2016

Peer reviewed|Thesis/dissertation

Electrochemical Approaches to Renewable Energy

By

Peter Lobaccaro

A dissertation submitted in partial satisfaction of the

requirements for the degree of

Doctor of Philosophy

In

Chemical Engineering

in the

Graduate Division

of the

University of California, Berkeley

Committee in charge:

Professor Joel Ager, Co-Chair
Professor Roya Maboudian, Co-Chair
Professor Alexis Bell
Professor Ali Javey

Fall 2016

Abstract

Electrochemical Approaches to Renewable Energy

by

Peter Lobaccaro

Doctor of Philosophy in Chemical Engineering

University of California, Berkeley

Professor Joel Ager, Co-Chair / Professor Roya Maboudian, Co-Chair

Renewable energy is becoming an increasingly important component of the world's energy supply as the threat of global warming continues to rise. There is a need to reduce the cost of this renewable energy and a future challenge to deal with the strain intermittent power sources like renewables place on the power grid. In this dissertation, electrochemistry is harnessed to address possible solutions to both of these issues. First, it is used to develop a low cost alternative photovoltaic material. Then, it is used to investigate the production of chemical fuel stocks which can be used for energy storage.

In chapter 2, advances are made in the electrochemical deposition of indium (In) on molybdenum foil which enables the deposition of electronic-grade purity, continuous films with thicknesses in the micron range. As an example application, the electrodeposited In films are phosphorized via the thin-film vapor-liquid-solid growth method. The resulting poly-crystalline InP films display excellent optoelectronic quality, comparable to films grown from more standard vacuum deposition techniques. This demonstrates the versatility of the developed electrochemical deposition procedure.

In the remaining chapters, renewable fuel production is investigated. First in chapter 3, molybdenum disulfide (MoS_2) is examined as a catalyst for the hydrogen evolution reaction (HER). Typically, high-cost synthesized MoS_2 is used as the catalyst because the pristine MoS_2 mineral is known to be a poor catalyst. The fundamental challenge with pristine MoS_2 is the inert HER activity of the predominant (0001) basal surface plane. Here, we report a general thermal process in which the basal plane is texturized to increase the density of HER-active edge sites. The process generates high HER catalytic performance in pristine MoS_2 across various morphologies such as the bulk mineral, films composed of micron-scale flakes, and even films of a commercially-available spray of nanoflake MoS_2.

In chapters 4-6, the electrochemical reduction of carbon dioxide (CO2R) is investigated as this reaction can produce hydrocarbons and alcohols as opposed to just hydrogen. First in chapter 4, the electrochemical cell, which is used to test the activity of CO2R catalysts, is scrutinized. The electrochemical cell is a mini-chemical reactor and it is important to monitor the reaction

conditions within the reactor to ensure that they are constant throughout the study. I show that operating cells with high catalyst surface area to electrolyte volume ratios (*S/V*) at high current densities can have subtle consequences during CO2R, particularly as they relate to the bulk electrolyte CO_2 concentration. By using the pH in the cell to measure the CO_2 concentration, significant undersaturation of CO_2 is observed in the bulk electrolyte, even at modest current densities of 10 mA cm^{-2}. Undersaturation of CO_2 produces large changes in the faradaic efficiency observed on copper electrodes, with hydrogen production becoming increasingly favored. I show that the size of the CO_2 bubbles being introduced into the cell is critical for maintaining the equilibrium CO_2 concentration in the electrolyte and I design an electrochemical cell that is able to maintain near-equilibrium CO_2 concentrations for catalyst testing.

Then in chapter 5, the use of selected-ion flow-tube mass spectrometry (SIFT-MS) as an analytical tool to detect the products of CO2R is investigated. The real-time analysis of the products of CO2R is especially of interest to enable the study of how and when the liquid products of the reaction are generated. This is currently only possible in some limited situations and an analytical tool that can do quantitative analysis of all the products of the CO2R reaction in real-time does not exist. I show that SIFT-MS is a promising technique which can uniquely detect the hydrocarbon, alcohols, and aldehydes produced during CO2R on copper. Furthermore, SIFT-MS should be able to provide quantitative results; however, further study is needed to rigorously prove this.

Finally in chapter 6, a CO2R catalyst platform is developed based on templated electrochemically deposited nanowires. This platform is used to investigate the role of high surface area in catalyst activity and selectivity. It is found that high surface area Cu nanowires can be made that still produce hydrocarbons, in contrast to several other reports in the literature. This platform is also used to investigate the sequential reduction of CO_2. Here silver nanowires are deposited on top of a planar Cu substrate. The Ag can convert the CO_2 to CO in close proximity to the Cu catalyst which can further upgrade the CO to hydrocarbons and alcohols. It is found that the sequential catalysis approach successfully selects for the production of hydrocarbons through the 2 electron CO intermediate and shuts down the production of the competing 2 electron product formic acid which is a dead-end reaction pathway.

To my family, who has always supported me…

whether I was wise enough to want it or not.

Table of Contents

Acknowledgements

It is has been my great honor to work with so many talented, knowledgeable, and patient colleagues and mentors during my time in graduate school. It has not always been the smoothest of journeys, so I appreciate your help along the way. I have not had a typical advising system during my time here, so it is difficult to now have to put my advisors name's down in any order. I would like to thank Prof. Roya Maboudian, Prof. Joel Ager, and Prof. Ali Javey all equally for the various roles they have played in my research advising over the years. Prof. Maboudian and Prof. Javey for their pivotal roles when I was just getting started and Prof. Ager particularly for taking my rather raw skill set and morphing it into those of an independent thinker. I would also like to thank Prof. Alex Bell for the close advising role he has played in the last few years, selflessly contributing his incredible depth of knowledge of catalysis and being an excellent teacher. All four of these excellent mentors has worked very closely with me and they comprise the committee for this dissertation as well. Few have been blessed to have so many excellent minds contributing so diligently to one dissertation. Finally, I would also like to thank Professors Nitash Balsara, Jeffrey Reimer, Susan Muller, and Daryl Chrzan for contributing their time as a member of my qualifying exam committee.

I must thank the many excellent students and post-docs who mentored me along my way. I'm particularly thankful to Dr. Albert Gutes, Dr. Rehan Kapadia, and Dr. Max Zheng for all of their guidance and help. I knew nothing about electrochemistry or device physics before I began talking with them and would have been lost without them. I would like to thank my co-authors for their contributions to the work presented here. These include Dr. Anahit Raygani, Andrea Oriani, Nicolas Miani, Alessandro Piotto, Dr. Rehan Kapadia, Dr. Maxwell Zheng, Dr. Zhibin Yu, Dr. Daisuke Kiriya, Hnin Yin Yin Nyein, Dr. Peyman Taheri, Mark Hettick, Hiroshi Shiraki, Dr, Carolin M. Sutter-Fella, Pieda Zhao, Dr. Wei Gao, Dr. Meenesh Singh, Ezra Clark, Dr. Youngkook Kwan, Prof. Luca Magagnin, and Prof. Daryl Chrzan.

I would also like to thank all of my collaborators for all of their support, training, feedback on talks and papers, willingness to exchange knowledge and ideas, and just making work somewhere I'm happy to come every day. Dr. Anna Harley-Trochimczyk, Dr. Lunet Luna, Dr. Shannon Klaus, Dr. Lena Trotochaud, Joe Zhao, Dr. Corsin Battaglia, Dr. Yongjin Lin, Dr. Ben Hsia, Dr. Latisha Paw U, Joy Wang, Kevin Chen, Dr. Lily Mandel, Dr. Mallikarjuna Rao Motapothula, Prof. Jens Martina, Prof. Thiru Venky, Dr. Youngkwan Kim, Dr. John Alper, Dr. Le Chen, Dr. Karl Walczak, and the many other members of the Maboudian Lab, Javey Lab, Ager Lab, Bell Lab, JCAP, and SinBeRISE. I'm particularly thankful as well to the staff engineers at JCAP, Alan Lyon and Jeff Beeman. As well to the Department of Chemical Engineering support staff, especially Carlet Altamirano, a true master of the bureaucratic system that comes with a public entity like UC Berkeley.

These research efforts have been supported by my funding sources, the Bay Area Photovoltaics Consortium (BAPVC), the Joint Center for Artificial Photosynthesis (JCAP), a DOE

Energy Innovation Hub, supported through the Office of Science of the U.S. Department of Energy under Award Number DE-SC0004993, and the Singapore-Berkeley Research Initiative in Sustainable Energy (SinBeRISE).

On a personal note, I would like to thank the members of my fellow class in the Dept. of Chemical Engineering and the many incredible people I've met during my time at Berkeley. Our department has a noble tradition of creating a supportive and cohesive environment and I'm sure that, despite all the struggles, that atmosphere will continue on. I'm especially thankful to my friends and roommates at the Channing Institute who have always made time for kicking back while not being afraid to dive deep into discussions about any topic on this planet. All of you have helped to keep me grounded when it can be easy to get lost or dejected in the bubble of grad school. For this I am eternally grateful. Finally, I would like to thank my family: my uncles for pushing me to go to grad school in the first place, my mom for supporting me even when I doubted myself, and my sister for always making me want to be the best version of myself.

1. Introduction

1.1. The Need for Renewable Energy

The future for our planet has become increasingly stark over the past decade. Global mean temperature and carbon dioxide concentration in the atmosphere continue to rise at alarming rates.[1] The Intergovernmental Panel on Climate Change (IPCC) has repeatedly increased their degree of certainty that human beings are contributing to or are the primary cause of these changes.[1,2] While the consequences of the already high concentrations of CO_2 in the atmosphere will not fully manifest themselves for decades,[2] some would argue that we are already observing the effects, with 15 of the warmest 16 years on record occurring in the last 15 years.[3] The last two years have each subsequently been the warmest year on record and 2016 is on pace to overtake the record again.[4] The threat of global warming is too great to not take immediate and substantial action.

Renewable energy is one of several resources that can be employed to reduce the CO_2 intensity of energy production around the world. Solar energy in particular is the most abundant of these resources (7,500 TW potential[5]), dwarfing the current annual world energy consumption (17 TW[6]). Solar has also proven to be a promising alternative to traditional fossil fuel power. In many locations, solar is becoming a cost competitive alternative to fossil fuel based generation[7,8] and installed solar capacity has been growing exponentially worldwide.[9]

Due to the large drop in solar module costs, the balance of systems cost, which is essentially everything else that is needed to have an installed solar system (mainly power inverter, installation, permitting, and financing costs), now represents the bulk of the cost of installed solar in the U.S.[10] This cost scales with the area of solar panels being installed; therefore one way to reduce its cost is to improve the efficiencies of the panels, thereby decreasing the required area to obtain a given power output. Thus, solar technologies that have a higher theoretical efficiency limit, while maintaining the low production costs of silicon, are still of interest to pursue.

III-V solar materials, such as gallium arsenide (GaAs) and indium phosphide (InP), have historically shown very high solar cell efficiencies. GaAs currently holds the world record for a single junction solar cell at ~28% efficiency.[11] However, typically high-cost synthesis methods are required to produce these materials,[12–16] precluding them from widespread terrestrial applications.[17] A low-cost synthesis technique, the thin-film vapor-liquid-solid (TF-VLS) growth method, was developed in our laboratory which proved capable of producing high quality InP from indium (In) thin films.[18] The method originally employed In films produced by traditional vacuum physical vapor deposition techniques, which can have a low utilization rate of the precursor In as well as high capital equipment costs.[19] To address this shortcoming, electrodeposition of In thin films was explored here as a low-cost, high materials utilization alternative to traditional vacuum deposition. In Chapter 2, I show that electrodeposition can be used to obtain In thin films of high purity that produce InP (via the TF-VLS process) of equal quality to that produced through vacuum deposition techniques.

1.2. The Need for Energy Storage

As renewable energy technologies become more prevalent in the electrical grid energy mix, it is expected that their intermittency may begin to pose a problem for grid stability.[20–22] In order to even out the intermittent supply of power, energy storage will be needed, especially at high renewable penetration rates.[21] There are many types of energy storage available and these can generally be judged by two metrics, the energy density (MJ/L) and specific energy (MJ/kg). Figure 1.1 plots a range of typical materials used for energy storage.[23] The ideal energy storage media would have both high energy density and high specific energy. In this regard, energy storage in chemical bonds is vastly superior to that available in electrical energy storage devices (gasoline vs. lithium ion batteries). Thus it is desirable to identify a technology for the production of chemical fuels (such as hydrocarbons or hydrogen) utilizing electricity. Electrochemical reduction is one such technology in which electricity can be used directly to convert precursor chemicals (carbon dioxide or water, respectively) into hydrocarbon or hydrogen fuels.

Hydrogen is one chemical which has been suggested as a renewable fuel.[24] As shown in Figure 1.1, it has the highest energy density of any chemical listed, which is appropriate for grid scale applications. The production of hydrogen has been shown to occur at lower overpotential on platinum (Pt);[25] however, the high materials cost of Pt as well as the low cost of the alternative natural gas steam reforming has limited the widespread use of this technology.[26] Here, I investigate a low cost catalyst material, molybdenum disulfide (MoS_2), which has been widely explored[27] for its high reported activity for the hydrogen evolution reaction (HER). In Chapter 3, I show that it is possible to convert the bulk mineral MoS_2, a material that is typically viewed as inactive to HER, into an effective catalyst through a simple thermal texturization process. In this way, expensive growth techniques, which have been needed to make active MoS_2 catalysts thus

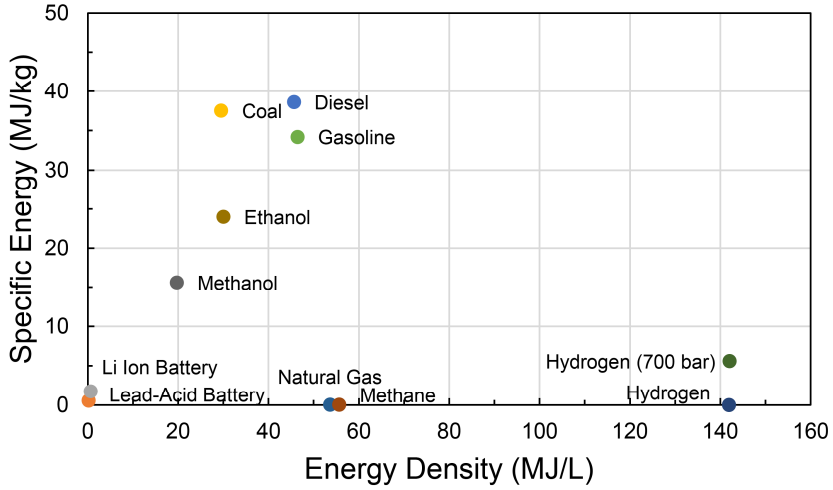

Figure 1.1 Energy Density vs Specific Energy of Typical Storage Media: The specific energy (MJ/kg) is plotted versus the energy density (MJ/L) of several different energy storage mediums. It can be seen that electrical storage in the form of batteries is fairly low in both metrics, whereas hydrogen has a high energy density and gasoline has both a high energy density and specific energy. An ideal energy storage medium has both a high energy density and specific energy. Data adapted from en.wikipedia.org/wiki/Energy_density

far, can be overcome. Thus a high activity, low cost catalytic pathway to electrochemical hydrogen production can be envisioned.

While hydrogen has a high energy density, its low specific energy makes it less than ideal for transportation applications, where the impact of weight is critical. For this application, hydrocarbon based fuels are the ideal storage medium for energy. There is a pathway to electrochemically produce hydrocarbons and liquid alcohols via the reduction of carbon dioxide (CO_2).[28] There is an additional advantage to this process, in that it could enable a closed loop system to halt further CO_2 emission into the atmosphere and avert future global warming. However, the field of electrochemical CO_2 reduction (CO2R) is comparatively young to that of HER. Thus efforts first need to be placed on developing rigorous, reproducible experimental methods for the evaluation of electrocatalysts for this reaction.

I initially targeted improvements in the electrochemical cell used to evaluate catalysts for CO2R. Here, it is highly desirable to have a high electrode surface area to electrolyte volume ratio (*S/V*), in order to maximize the ability to detect the liquid products of CO2R, which are often produced at low rates. It was found that the gas-liquid mass transfer from CO_2 flowing through the electrolyte, which supplies CO_2 to the catalyst surface, can greatly affect the evaluation of the catalyst. Because of this, depending on the design of the electrochemical cell, very different catalyst activity measurements are made for the same catalyst. In Chapter 4, I show that by performing standard temperature-corrected pH measurements on the bicarbonate electrolyte, the mass transfer issue can be elucidated and then eliminated by improved engineering of the electrochemical cell.

Next, improvements in the analytical equipment used to detect the many gaseous and liquid products of CO2R were investigated. There is currently limited instrumentation that can be used to detect all the products of CO2R in real-time (as many as 20 different liquid and gaseous chemicals are produced). Such real-time product analysis is desirable as it can provide additional insight into how the catalytic reaction proceeds, as well as allow for high throughput catalyst screening to accelerate the discovery of new catalysts. In Chapter 5, I investigate selected-ion flow-tube mass spectrometry (SIFT-MS) as an analytical tool which is capable of such real-time detection.

Finally, with the improved experimental procedures in place, a CO2R catalyst platform was designed which can be used to both elucidate fundamental questions about the role of high surface area in catalytic activity as well as be used to perform some of the first investigations into sequential catalysis. In Chapter 6, I show that with proper design of the high surface area nanowire copper catalyst, hydrocarbons can be produced. Furthermore, using a sequential catalysis platform of silver nanowires on copper, the CO2R reaction pathway can be tuned to select for the pathway that produces hydrocarbons and eliminate the competing path which produces only formic acid.

2. Electrodeposition of Indium Thin Films and its Application to Indium Phosphide Solar Cells[1]

2.1. Introduction

As the goal of this dissertation is to explore two preeminent problems with the implementation of renewable energy, being how to produce the energy cheaply and how to use that energy to make a renewable alternative to fossil fuels, this chapter explores the first of these issues. Specifically, this chapter explores if improvements in the way in which indium phosphide solar cells are fabricated can greatly reduce their cost while maintaining their high efficiency.

Indium (In) is widely used in the electronics industry, such as in high density bump bonds[29,30] and in low temperature soldering.[31,32] It is also an important component of many electronic and optoelectronic materials, such as indium phosphide (InP), indium selenide, copper indium selenide (CIS), copper indium gallium selenide (CIGS), indium arsenide (InAs), indium gallium phosphide, and indium tin oxide. Many different synthesis techniques exist for these materials, some of the most common being closed space sublimation,[33] metal organic chemical vapor deposition,[12–14] co-evaporation,[34] and molecular beam epitaxy.[15,16] An alternative deposition method is electrochemical deposition[35–44] (ECD), which has the advantages of[36,45] (a) low temperature, ambient pressure deposition, (b) high deposition rate which is easily controllable, (c) low cost equipment and precursors, and (d) high precursor utilization (as high as 98%). The high material utilization rate is especially important when considering the rarity and expense of indium.[46]

Direct ECD of semiconductors like CIGS,[35–37] CIS,[38] InAs,[39–41] and InP[42–44] have been shown in the literature. InP is particularly interesting due to its ideal energy band gap of 1.34 eV and similarity to gallium arsenide which recently resulted in the highest single junction solar cell efficiency to date (~28%).[47] The highest reported InP solar-cell efficiency to date is ~ 22%.[47] The direct ECD of InP has been claimed in the literature, though there is no report on the optoelectronic quality of the matrial.[42] However, the reported synthesis technique could not be reproduced by other groups[48] or by our group. This is in part because direct ECD of fully reduced phosphorus from aqueous solution is very difficult without a catalyst, such as nickel,[49,50] as suggested previously by Cattarin, *et al*.[48]

An alternative growth method to direct ECD for InP, as well as for CIS and CIGS, is a two-step method, where precursor indium thin films are deposited and then reacted at high temperatures with a phosphorus source. In this growth method, the material utilization of In is largely

[1] A modified version of this work was published as P. Lobaccaro, A. Raygani, A. Oriani, N. Miani, A. Piotto, R. Kapadia, M. Zheng, Z. Yu, L. Magagnin, D. C. Chrzan, R. Maboudian, and A. Javey, Electrodeposition of High-Purity Indium Thin Films and Its Application to Indium Phosphide Solar Cells. *J. Electrochem. Soc.* **2014**, 161 (14), D794–D800.

determined by the process used to deposit it, further motivating the use of ECD. The two-step growth approach has been explored for InP[48,51] and recently a new two-step growth method, named thin film vapor-liquid-solid (TF-VLS), has been developed and demonstrated for InP.[18,52] The TF-VLS growth method is unique due to the fact that thin films can be grown with grain sizes which are orders of magnitude greater than the film thickness on non-epitaxial substrates, breaking with the traditional constraints of vapor phase thin film growth.[14,33] Most importantly, it was demonstrated that indium evaporated on molybdenum foil and phosphorized by the TF-VLS process resulted in InP films of high optoelectronic quality, far surpassing that of previous two-step InP growth methods. Mo is an effective substrate for this process due to its chemical stability and high melting point.

For the two-step growth methods, the starting In thin films must be continuous, planar, and high purity. An optimal InP thin film should be 1-3 μm thick for solar cell applications. Since indium approximately doubles in thickness as it is converted to InP, there is an additional constraint of the In film thickness being 2 μm or less. The ECD of In has been explored in the past;[31,32] however, the previous applications do not meet the stringent quality requirements of optoelectronic thin film precursors outlined above. Due to the need for high purity In, organic additives, that are traditionally used to tailor deposition morphology in ECD, may not be used as they may get incorporated into the deposited matrix, creating potential defects, recombination sites, and acting as unintentional dopants in the final InP film. Furthermore, I explore In ECD on molybdenum (Mo) foil, a ubiquitously used substrate for high temperature growth due to its chemical stability and high melting point. Electrodeposition of a continuous In film of sub-1 μm thickness on Mo is difficult and has resulted in workarounds such as depositing In on Mo with a copper seed layer[53,54] or depositing In simultaneously with other metals.[35,54,55] This chapter reports on the electrodeposition of In thin films directly on Mo foil which meet the aforementioned requirements of thickness, roughness, and purity without the use of organic additives.

2.2. Experimental

2.2.1. Indium Electrochemical Deposition and Phosphorization

A schematic of the electrochemical deposition setup is shown in Figure 2.1. A CH Instruments Electrochemical Workstation potentiostat was used to carry out the electrochemical deposition. The potentiostat was operated in a 3-electrode cell using an Ag/AgCl reference electrode equilibrated in saturated potassium chloride. Indium metal ingots (99.99% Alfa) flattened into foils were used as the counter electrode. Mo foil, 0.1 mm thick, (99.95% Alfa) was cut into 2 x 1 cm^2 pieces and Kapton® tape was used to mask a 1 x 1 cm^2 active area to operate as the working electrode. The counter and working electrodes were clamped and suspended parallel to each other in the electrolyte solution by a Teflon® block that allowed controllable spacing of the electrodes (held at ~8 mm here). The reference electrode was also placed in the same position relative to the working and counter electrodes by this Teflon® block. The deposition bath was continuously

stirred using a magnetic stirrer at 200 RPM during deposition. The electrolyte solution was 1.0 M indium (III) chloride, $InCl_3$ (99.999%, Strem Chemicals). The electrolyte temperature was controlled by an external stirred bath of water (high temperature) or ethanol (low temperature) held at the desired temperature by a hot plate or a cooling unit (FTS FC55).

Cleaning and surface preparation were extremely important to obtain uniform deposits. The Mo foil was degreased by sonication in acetone and then isopropyl alcohol for 30 minutes each. Immediately before deposition, the foil was sonicated in concentrated HCl to remove surface oxide, rinsed with deionized water, and blown dry with nitrogen. The In electrode was prepared by a cleaning dip in aqua regia (HNO_3:HCl 1:3) and then rinsed with DI water and dried with nitrogen. This cleaning process was repeated if the indium surface was not uniformly reflective.

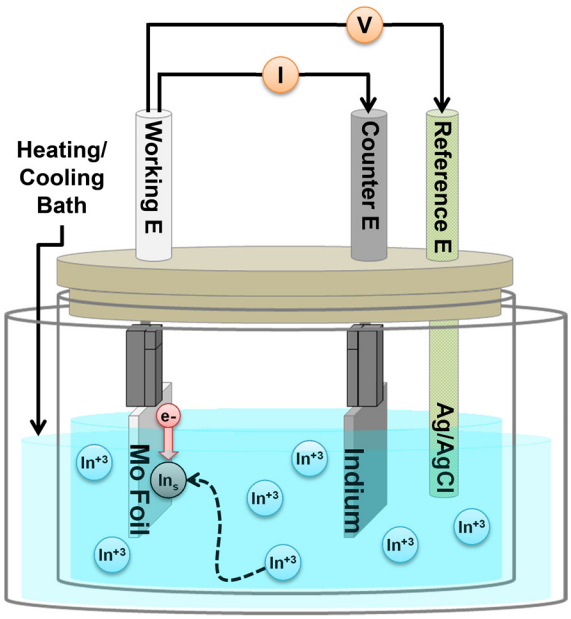

Figure 2.1. Schematic of electrodeposition bath apparatus with Mo foil as the working electrode, In metal as the counter electrode, and an Ag/AgCl reference electrode. The bath is contained inside a heating/cooling bath for temperature control.

Indium phosphide was grown from the ECD In films by the TF-VLS process reported in detail previously.[18] In short the ECD In was capped with 50 - 500 nm of electron-beam evaporated SiO_2. The stack was then phosphorized in a 1-zone furnace at 750 ºC and 100 Torr by flowing 10% phosphine in hydrogen (Voltaix 99.9995%). Samples were heated to 750 ºC under a pure hydrogen gas flow; phosphine gas was introduced once a stable temperature was achieved. Samples were held at the growth temperature for a given duration, ranging from 20 to 60 minutes depending on In film thickness and then rapidly cooled with continued phosphine flow.

2.2.2. Chemical, Structural, and Optoelectronic Characterization

The In and InP thin film morphologies were characterized by optical microscopy and scanning electron microscopy, SEM (JEOL 6340F SEM/EDS). Chemical composition was confirmed by X-ray diffraction, XRD (Bruker AXS D8 Discover GADDS XRD) and energy-dispersive X-ray spectroscopy, EDS (JEOL 6340F). Surface chemical composition analysis was performed via X-ray photoelectron spectroscopy, XPS (Kratos Axis Ultra DLD). Depth profiling was achieved by a sequence of sputtering (Kratos Minibeam 1) followed by XPS measurements. Trace chlorine and carbon contamination in the deposited In films were detected by secondary ion mass spectrometry (SIMS) performed by Evans Analytical Group. Film thickness was determined using a Dektak 150+ surface profiler and surface roughness was characterized using atomic force microscopy, AFM (Digital Instruments Nanoscope III) operated in tapping mode. Current

efficiency and average deposit thickness were determined using gravimetric analysis (Denver Instruments Company A-250).

The optoelectronic properties of the InP films were investigated with steady state photoluminescence (PL) and time-resolved PL (TRPL) apparatuses. The PL apparatus was made up of a helium-neon laser at 632.8 nm with ~5 μm spot size, and a silicon CCD detector (Andor iDus). The TRPL apparatus used a Mira 900-F Ti-sapphire tunable laser, which produced 200 fs pulses of 800 nm light at 75.3 MHz. The detector was a silicon avalanche photodiode (id Quantique id-100) connected to a TCSPC module (Becker & Hickl SPC-130).

2.3. Results and Discussion

2.3.1. Electrodeposition of Indium

The overall deposition reaction for In on the cathode (Mo foil here) can be described by Reaction 2.1:

$$In^{+3} + 3e^{-} \rightarrow In_{metal} \tag{2.1}$$

Initial testing found that it was important to use a soluble In metal counter electrode, instead of an insoluble one like platinum. When the anode is In metal, the reverse of Rxn. 2.1 occurs at its surface, thus avoiding In ion depletion from the deposition bath.

In the experiments reported here, I used constant DC current to drive the deposition so that the total charge passed per unit area, Q (C/cm^2), could be easily controlled by the time duration of the deposition. The main goal was to control the volume of In deposited, assuming the current efficiencies for the various conditions tested to be similar. The theoretical thickness of the In film deposited can be calculated using Faraday's law assuming the In is of uniform thickness and densely packed:

$$h = \eta_j * j * t * \frac{MW_{\mathrm{In}}}{F*n*\rho} = \eta_j * Q * \frac{MW_{\mathrm{In}}}{F*n*\rho} \tag{2.2}$$

where h is the thickness of the film in cm, η_j is the current efficiency for the process ($0 \leq \eta_j \leq 1$), j is the current density (A/cm^2), t is the deposition duration (s), MW is the molecular weight of In (114.8 g/mol), F is Faraday's constant (96485 C/mole), n is the number of electrons required for the deposition (3 here), and ρ is the density of In, assumed to be the same as bulk In (7.3 g/cm^3). Thus if η_j is assumed to be 1, to deposit a 1 μm thick film, the total charge passed per unit area is estimated to be 1.8 C/cm^2. The analysis assumes the film is completely continuous with characteristics of bulk In. From this analysis I focused primarily on depositing In thin films for Q = 1.8 C/cm^2.

The essential challenge to this approach is that when one attempts to deposit an indium film with μm thickness on Mo under standard conditions, it is not fully continuous (Fig. 2.2a). A continuous thin film is considered to be one where indium has no holes exposing the underlying

Mo. The nucleation mode observed here can be classically described as the Volmer-Weber growth mode on a foreign substrate,[56] as has been observed previously for In on Mo.[57] Therefore the most important variable to be examined in the films is whether they are continuous when a volume of In corresponding to $h = 1$ μm has been deposited (i.e. at $Q = 1.8$ C/cm^2). To quantify that, I define the variable fill factor (f) as:

$$f = \frac{Mo\ area\ covered\ by\ In}{unit\ area\ of\ Mo} \tag{2.3}$$

where a continuous film will have $f = 1$. A simple geometric model helps to motivate the experimental approach. I assume that the average nucleus is representative and spherical in shape. Nuclei are assumed to form with a number density N (measured per unit area). The fill factor is then given by:

$$f = \frac{(projected\ spherical\ area\ of\ single\ nuclei)(\#\ of\ neclei)}{unit\ area} = \pi r^2 N \tag{2.4}$$

with r, the average radius of the sphere, defining the nuclei. If I assume the nuclei grow isotropically, then the spacing of the nuclei will determine the minimum thickness at which a continuous film can be achieved. Therefore I must maximize the number density of nuclei, N, in order to minimize the height of a continuous film.

For thin film deposition from vapor phase, it is well known that increasing the flux of the precursor vapor to the substrate's surface increases the number density of nuclei.[56] It is reasonable to expect a similar behavior for ECD. Here the flux of In^{+3} ions is directly controlled by the magnitude of the current density as long as Rxn 2.1 is the only reaction occurring at the cathode. Accordingly, the effects of varying current density were explored.

2.3.2. Effect of Current Density

Constant current deposition at room temperature was explored for current densities in the range of 50 to 250 mA/cm^2. As described in the experimental section, the time duration of a given deposition current was chosen such that the same value of Q (1.8 C/cm^2) resulted. Thus, the same volume of In should be deposited at each current density tested, assuming the cathodic efficiency is the same for each condition. This assumption was confirmed by gravimetric analysis of the deposited In showing 90% ± 10% current efficiency for all conditions examined.

The fill factor was calculated from representative SEM/EDS images of the In deposit at each current density. Figure 2.2a shows a side-by-side image of the In deposit at 50 mA/cm^2 with an EDS elemental mapping depicting In and Mo regions. Characteristic SEM images in Figures 2.2a-c show that at higher deposition currents, the fill factor of In on Mo is higher, indicating the nucleation density is higher, as is expected from the analogy to vapor phase deposition. This is consistent with electrochemical theory as well, whereby higher current density requires a higher surface overpotential to drive the reaction, thus reducing the critical nucleus size and allowing higher nucleation density. While the fill factor continued to increase with increasing current density (Fig. 2.2d), it never reached 100% with a room temperature deposition bath, and 250

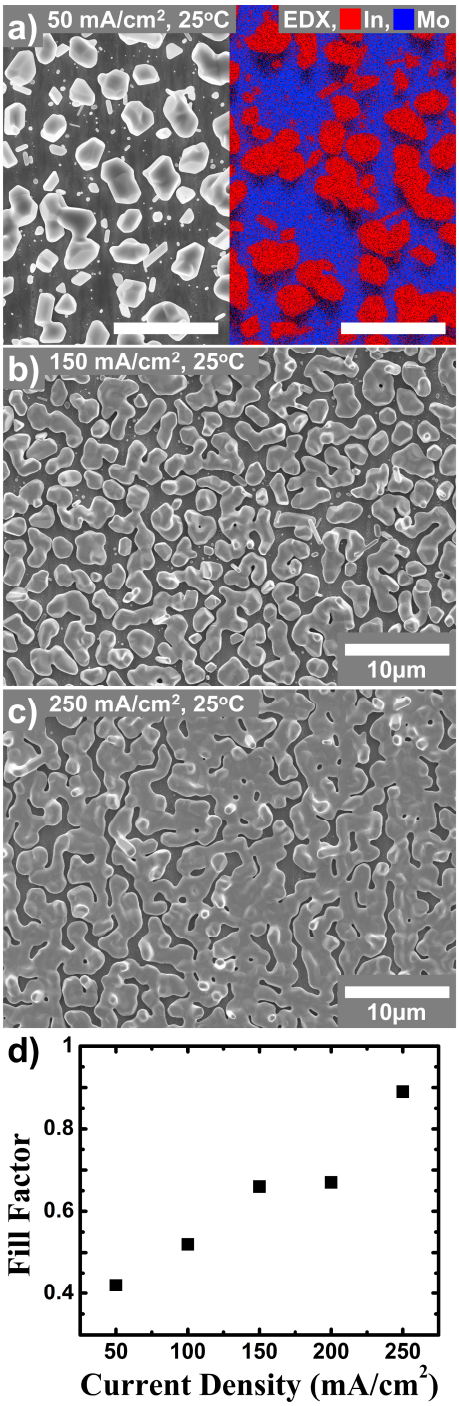

Figure 2.2. Characteristic SEM images of the In films deposited at room temperature and constant current values of 50 (a), 150 (b), and 250 mA/cm^2(c), with deposition times adjusted to yield Q = 1.8 C/cm^2. Panel (a) also shows an overlay with an EDS elemental mapping indicating which portions of the image are In and which are Mo. The scale bar represents 10 μm. The fill factor was calculated from these SEM images and is plotted versus applied current density (d).

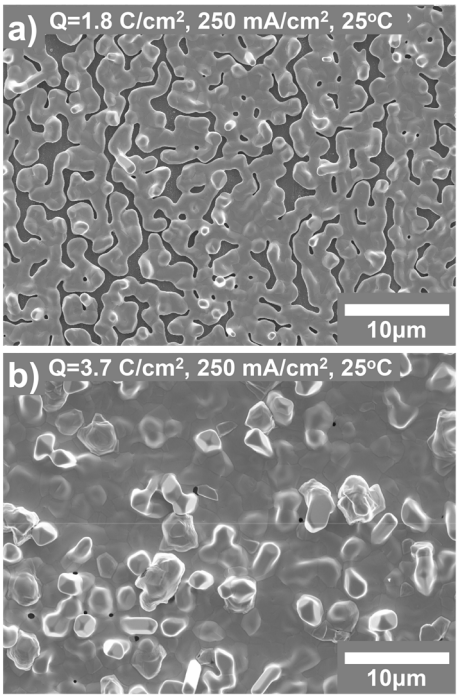

Figure 2.3. Constant current deposition at room temperature at 250 mA/cm^2 for two total charge conditions: (a) Q = 1.8 C/cm^2, (b) Q = 3.7 C/cm^2. In (b) large indium boulders can be seen dotting the surface.

mA/cm^2 represents the maximum current the potentiostat could apply while maintaining a reasonable size electrode.

It was found that by doubling Q, corresponding to film thickness, h, of 2 μm, a continuous film could be obtained. However, the resulting film was marked with micron tall boulders of In due to the 3-D growth mechanism described previously (Fig. 2.3b). This type of film thickness non-uniformity is highly undesirable for photovoltaic device fabrication. Attempts to control the size of these boulders using pulsed reverse current are described below, but none of the parameters examined were successful in fully removing the In boulders. Thus in order to obtain a continuous film with a Q = 1.8 C/cm^2, I explored alternatives to DC current deposition.

2.3.3. *Pulsed Current Deposition*

Pulsed current electrodeposition (PCE) is an electrochemical technique that provides a much greater control of nucleation through short current bursts followed by off times where zero current is passed.[58] The use of this technique for the electrodeposition of indium has not been widely explored in the literature[30] and this represents the first investigation on its use towards depositing indium thin films. The technique can be used to apply both cathodic (deposition, I_D) current and anodic (stripping, I_S) current. A characteristic waveform of the applied current can be seen in Figure 2.4. For controlling the nucleation density, only cathodic pulses were of interest, thus τ_S and I_S are considered to be zero. It is also important to note that the period (τ) was kept constant at 1 s for all trials and the duty cycle (γ) is defined as the time the current was on (τ_D) divided by the period (1 s).

There are two mechanisms whereby PCE can increase nucleation density. The first is by allowing the application of instantaneous currents (I_D) that are much higher than the deposition bath could support in DC deposition.[58] Higher I_D results in a higher nucleation density, which was shown earlier as being the key to getting a continuous film. In addition, mass transport limitations does not hinder the nucleation because of the rest time which lets the deposition bath equilibrate. The second mechanism is termed re-nucleation, which is a result of the solution equilibration that occurs during the rest time. In this case, keeping I_D the same as with DC, increased nucleation is expected.[58] This can be explained by the concentration gradients which form during deposition. When an indium nucleus forms, indium ions and indium adatoms from the surrounding solution and surface, respectively, are depleted as they deposit on the growing indium grain. This prevents additional nucleation in the depletion region around each nucleus. However, during the off time ($\tau_{off} = \tau - \tau_D - \tau_S$) the indium ions can re-equilibrate on the surface and in the solution. If the depletion width of adatoms on the surface is less than the depletion width of ions in solution after equilibration, then a new opportunity for nucleation occurs. Of the two mechanisms described here, only the second was available to explore due to potentiostat instrument limitations on the maximum sustainable current.

For the PCE experiments, 250 mA/cm^2 was used as the current during all pulses. The total charge deposited on the Mo foil was conserved at 1.8 C/cm^2 corresponding to a 1μm average film

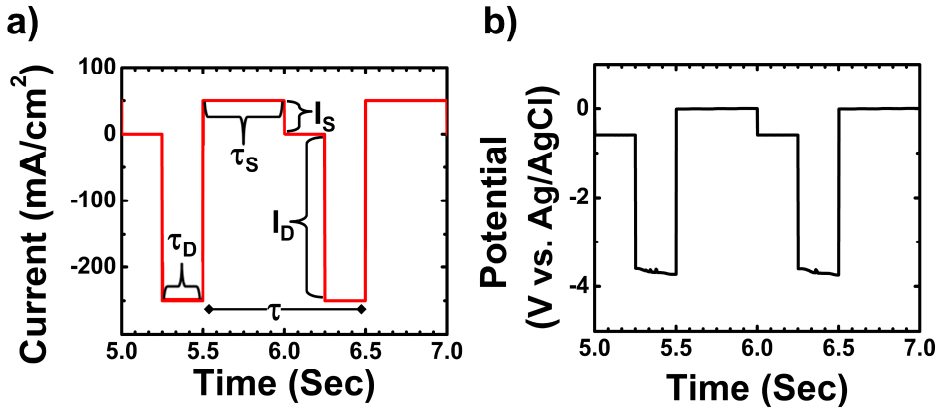

Figure 2.4. (a) A typical current profile applied to the Mo foil is shown with labels indicating the regions of deposition current (I_D) and stripping current (I_S). (b) Next to it a typical voltage response profile which is measured is shown.

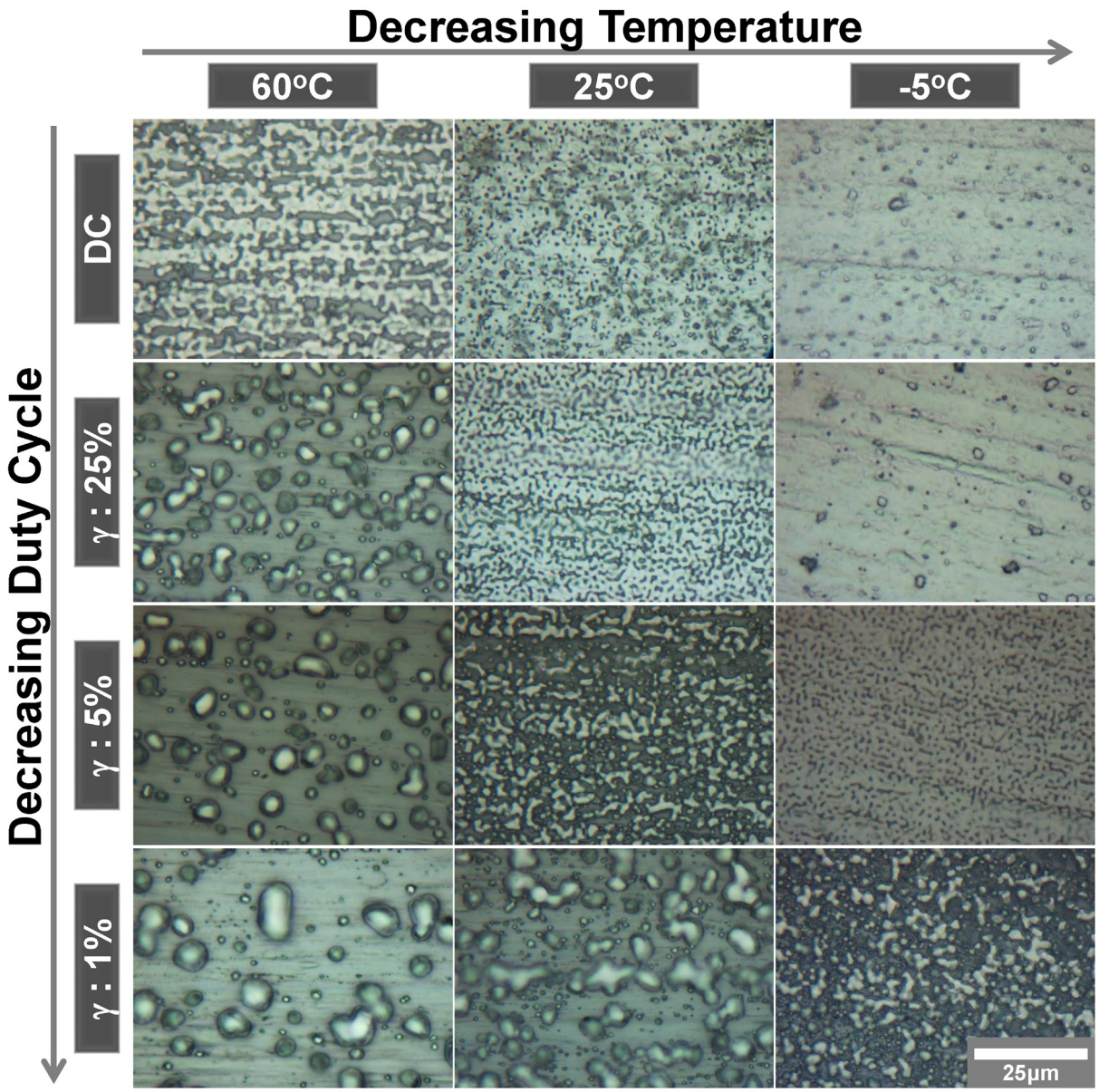

Figure 2.5. Morphological effects of changing deposition bath temperature and duty cycle are shown via optical microscopy. Duty cycles from 1% to DC deposition and temperatures from 60 ºC to -5 ºC are displayed. Current applied was 250 mA/cm^2 in all cases and total charge was conserved at Q = 1.8 C/cm^2 across the different conditions. It can be observed that regardless of temperature, a decrease in the duty cycle resulted in the deposits larger in grain size and less continuous.

thickness. Duty cycles ranging from 1% to 25% were explored and it was observed that γ_D greater than 50% produced films similar to those produced at the equivalent DC current density. The center column of Figure 2.5 shows that as γ_D is decreased, the deposits become less continuous and the grain size increases. This is in disagreement with my prediction. Given this result, it can be concluded that some other processes are dominating the growth mechanism. Two possible mechanisms may be dominating: (1.) the depletion width of adatoms on the surface is larger than that of ions in the solution, thus re-equilibrated ions still get sucked to existing nuclei when they

hit the surface, (2.) Oswald ripening occurs during the off time which dissolves newly formed small nuclei and coarsens larger nuclei. Thus pulsed current was unable to increase the fill factor beyond that which was obtained using DC deposition.

2.3.4. Pulsed Reverse Current

As was stated above, a continuous film of In could be obtained by increasing the amount of In deposited (doubling Q from 1.8 to 3.7 C/cm^2); however, the increase in film roughness that resulted made a film that was undesirable for photovoltaics applications. PCE was utilized to explore the possibility of using reverse current as a leveling agent, with the addition of τ_S and I_S as mentioned earlier and shown in Figure 2.4.

The occurrence of 3D growth in electrochemical deposition is a well-known phenomenon.[59] Three-dimensional growth is intensified over time because the peaks in the deposited films cause a concentration of current lines, resulting in accelerated deposition rates at these positions relative to the surrounding areas. This same mechanism which drives non-uniformity can be exploited to drive uniformity under the correct conditions. For the same reasons these peaks are preferential deposition sites, they are also preferential sites for stripping or removing of material. Stripping pulsed current electrodeposition (SPCE) was explored for currents up to half the magnitude of the I_D currents used previously and for stripping duty cycle (γ_S) ranging from 1% to 75% at room temperature only. In this case γ_S could at maximum be 100% minus γ_D. SPCE was successful in minimizing the size and number of the 3D indium boulders as was expected. Some characteristic optical microscopy images are shown in Figure 2.6 where γ_D = 25% and I_D = 250 mA/cm^2 were held constant and the stripping duty cycle was changed at a constant I_S = 5 mA/cm^2. Despite the range of conditions explored, none were successful in fully removing the islands observed without also

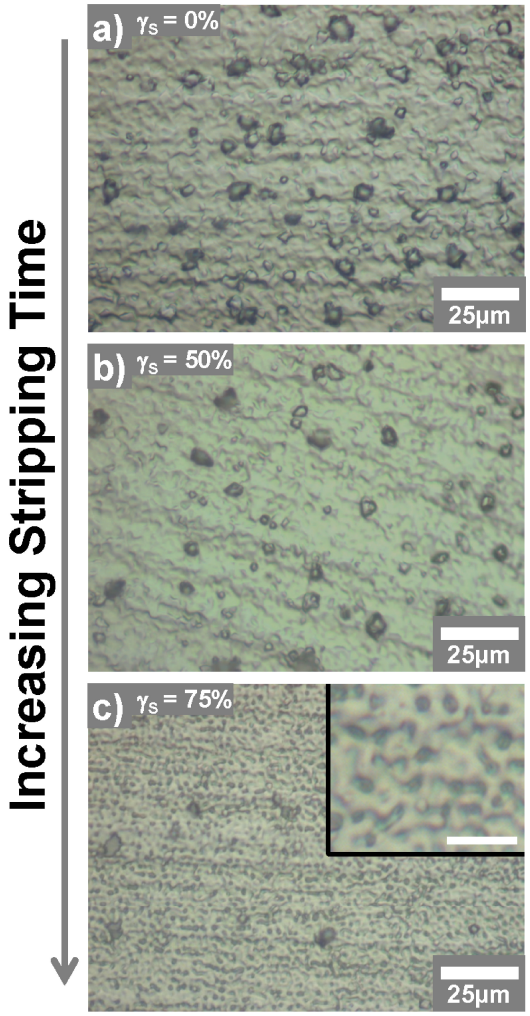

Figure 2.6. Optical Microscope images of In thin films as the stripping duty cycle was increased from (A) γ_S=0% to (B) γ_S=50% to (C) γ_S=75%. The deposition duty cycle was held constant at 25% at 250 mA/cm^2 and the stripping current used here was 5 mA/cm^2. It can be seen that the density of the In bumps begins to decrease (B); however, before they completely disappear, pitting begins to occur in the indium film (C). The inset if (C) is a higher magnification image of the In film where the dark area seen are holes in the In film. C insert scale bar = 10 microns

causing pitting in the indium layer beneath the islands. The experiments presented here exhausted my capabilities to obtain the desired In thin film by solely controlling the current density and time

2.3.5. Effect of Deposition Bath Temperature

There are many parameters, other than current and current profile, which can be controlled in electrochemical deposition, one of which is bath temperature. Bath temperature can affect many of the activated processes during deposition including interfacial binding energy and adatom surface diffusion rate. Consequently, I explored the effect of bath temperature, in the range of 60 ºC to -5 ºC, on the In film morphology. The total charge used for deposition was set at 1.8 C/cm^2 for all conditions. To achieve maximum fill factor, DC current was applied at 250 mA/cm^2 based on the results discussed in the previous sections. Characteristic SEM images of the films deposited at different temperatures are shown in Figures 2.7a-c. The higher bath temperature results in a lower fill factor and a larger grain film, while the lower bath temperature results in a fully continuous film composed of finer In grains. Though temperature affects several governing processes for ECD, I hypothesize the dominating effect is on the adatom diffusion rate, which is known to affect nucleation density in vapor phase deposition.[60,61]

The effect of deposition bath temperature was also explored using the same PCE experimental conditions used above to see if any further improvements could be made. Characteristic optical microscope images of the deposited In morphology can be seen in Figure 2.5. The results were in agreement with those obtained from the DC deposition runs. The

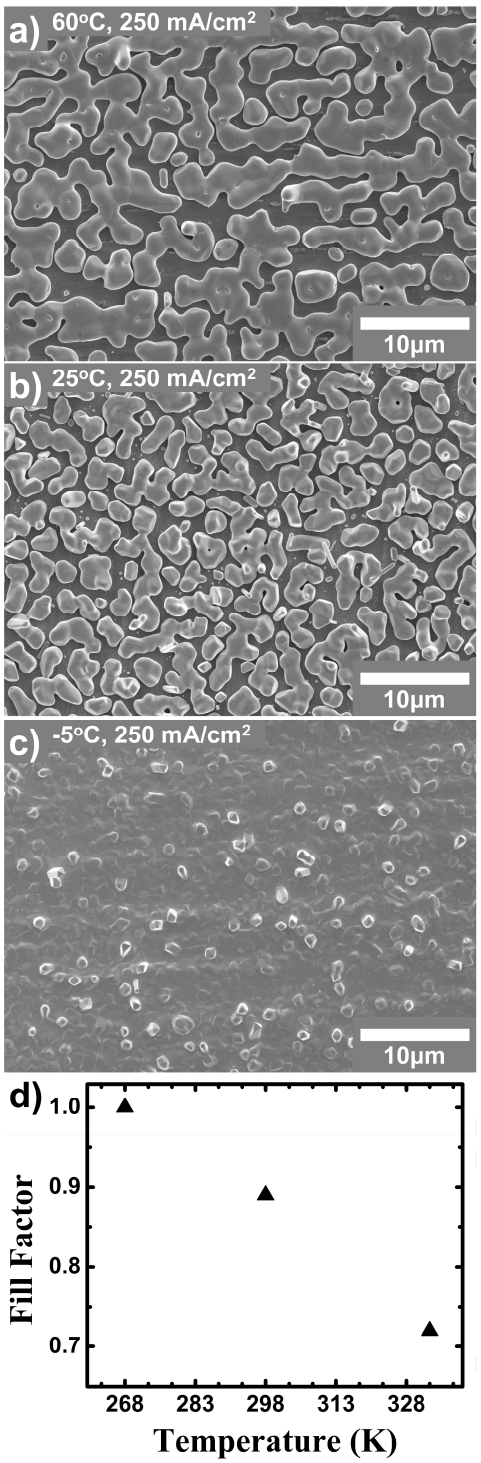

Figure 2.7. Characteristic SEM images for constant current deposition at 250 mA/cm^2 and Q = 1.8 C/cm^2 for the bath temperatures of 60 ºC (a), 25 ºC (b), and -5 ºC (c). The fill factor was calculated from these SEM images and is plotted versus temperature (d).

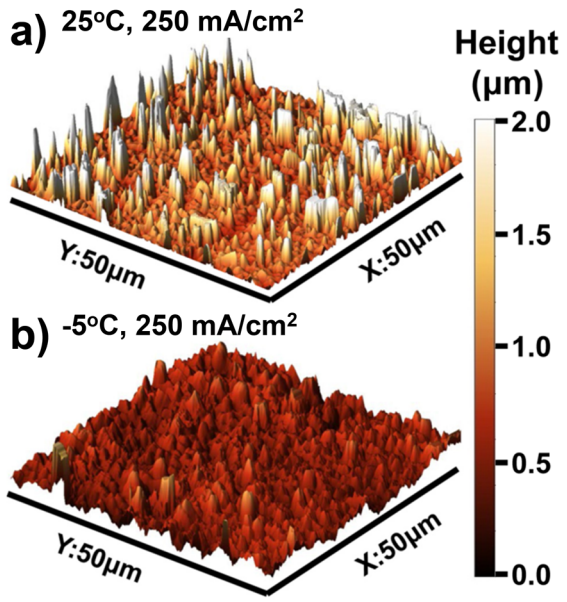

Figure 2.8. AFM images of the In thin film deposited at 250 mA/cm^2 and Q = 1.8 C at 25 °C (a), and -5 °C (b). The 3-D growth causing high surface roughness is clearly inhibited at -5 °C.

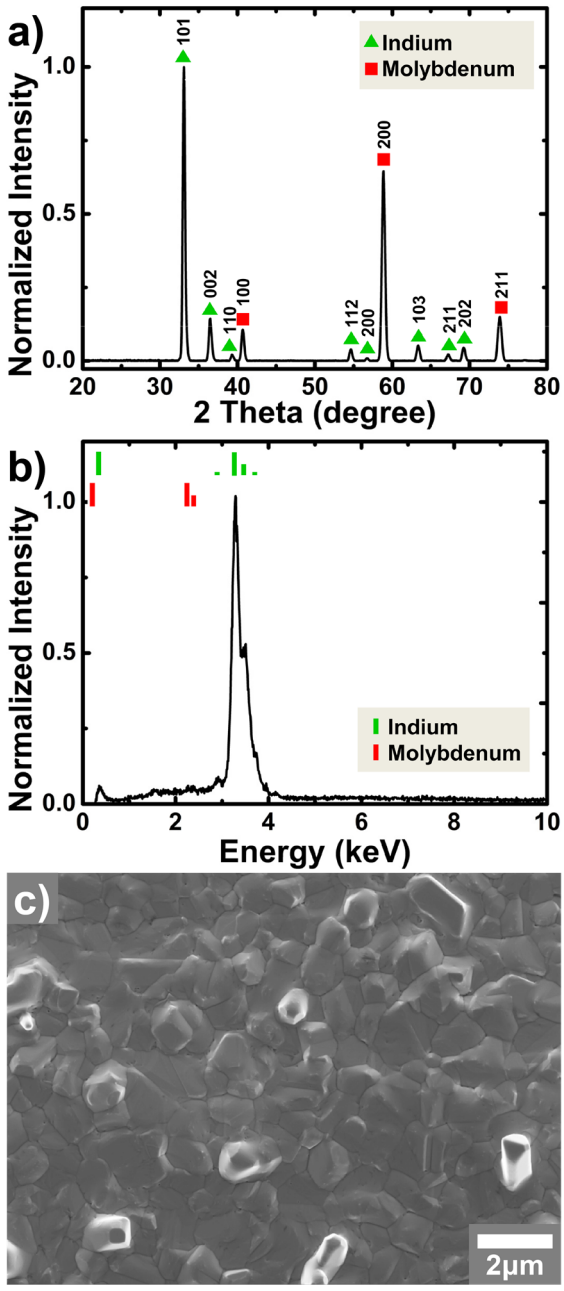

Figure 2.9. (a) XRD spectrum of the In ECD thin film on Mo deposited at -5 °C, normalized to the maximum peak intensity. (b) EDS spectrum of the same In thin film showing no other elemental impurities, normalized to the maximum peak intensity. (c) SEM image of the optimal In thin film displaying a grain size of ~1 μm.

higher deposition temperature resulted in a less continuous, larger grain film, while the -5°C deposition temperature resulted in more continuous, smooth thin film. However, as was observed previously, the addition of a pulsed current profile did not provide any further improvements in fill factor over DC deposition.

Atomic force microscopy was performed on the continuous films deposited at -5°C and 250 mA/cm^2 which showed a root-mean-square roughness of about 100 nm over 50 x 50 μm^2 area. This root-mean-square (RMS) roughness is ~3 times lower than the films produced under the same conditions in a room temperature bath (Fig. 2.8). The In thin films were further characterized by XRD to obtain crystallographic information (Fig. 2.9a). The films showed preferential orientation for the (101) plane. Elemental analysis was performed by EDS (Fig. 2.9b) which showed that only In was present. Finally, high resolution SEM (Fig. 2.9c) showed the characteristic surface morphology of the In films. The In thin film produced with these optimal conditions meets all the morphological requirements initially identified.

Further elemental analysis was performed to assess the purity of the deposited In films. Initial XPS analysis showed, in addition to In, the presence of carbon, oxygen, and chlorine but no other elements. As the surface of the film was sputtered away, the signals due to these impurity elements decreased and dropped below the XPS detection limit, (being ~1 atomic percent of the few nm layer probed) leaving behind only the characteristic In signal. The depth profiling analysis signifies that the impurity elements are only present in a thin (a few nm) surface layer. The carbon surface contamination is expected from environmental interactions with the sample. The oxygen signal is most likely due to the native oxide which forms on the metal surface. Finally the chlorine contamination (Fig. 2.10a) is hypothesized to be the result of indium chloride crystallites left behind on the surface from the deposition bath. In corroboration of this hypothesis, it was observed that the thickness of the surface chloride layer was dependent on the post deposition rinsing procedure which would affect the amount of salt left behind.

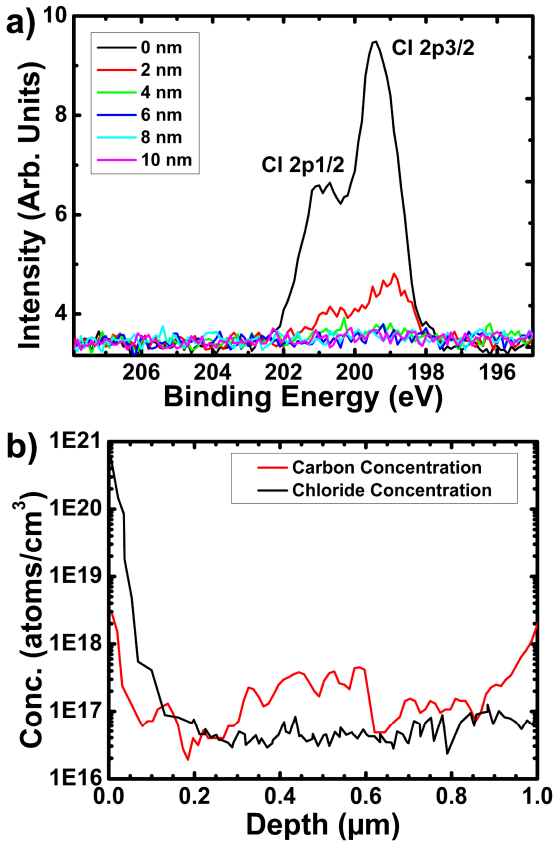

Figure 2.10. (a) Sputtering XPS was performed on a characteristic sample deposited at -5 ºC and 250 mA/cm^2 to monitor the chloride contamination. It showed that after a small surface impurity layer, the chloride signal disappeared. (b) Further C^- and Cl^- analysis was done via SIMS which found the chloride impurity in the bulk of the sample to be at most ~5x10^{16} /cm^3.

To quantify the bulk purity of the indium, secondary ion mass spectroscopy (SIMS) was performed to track the two major impurities which were observed in XPS, namely, carbon and chlorine. Any bulk chlorine contamination is significant as it is the only elementary species in the bath which cannot be purified out. The SIMS analysis (Fig. 2.10b) showed that both carbon and chlorine concentrations dropped from high concentrations at the surface to values in the bulk of at most 5x10^{17} cm^{-3} for carbon and at most 5x10^{16} cm^{-3} for chlorine. The carbon concentration seen here is not considered a major impurity as it is roughly equal to the background concentration of carbon seen in SIMS resulting from residual carbon in the ambient system. It is known that the first several nanometers of analysis in SIMS can have some errors that result in artificially high elemental concentrations.[62] The region can be broadened to the order of magnitude of the surface roughness, ~100nm in the sample examined here. This corresponds well with the depth of the Cl impurity observed in the SIMS results (Fig. 2.10b). Therefore in this case, the XPS depth profiling data yields a more accurate view of the thickness of the surface contamination which appears to be in the few nm range. This

analysis confirms that the In film has a thin surface contamination layer but is otherwise composed of high purity indium.

2.3.6. *TF-VLS of Electrodeposited Indium to Obtain InP*

Next I explored the use of ECD In for thin film vapor-liquid-solid growth of InP. Indium films of 1 to 3 μm in thickness were deposited using the optimal deposition parameters described above, namely 250 mA/cm^2 at -5°C. Thicker In thin films were obtained by simply increasing *Q*. The In film was then phosphorized via the TF-VLS technique,[18] for which a process flow schematic is shown in Figure 2.11a. In Figure 2.11b, the SEM image shows the surface morphology after phosphorization remains unchanged, which is due to the SiO_x capping layer. The capping layer plays the critical role of confining the In film structurally during the phosphorization process. The cross sectional SEM (Fig. 2.11c) shows the Mo substrate beneath a continuous grain of InP greater than 8 μm laterally, despite being only 2 μm tall, a defining characteristic of TF-VLS as described earlier. Figure 2.11d shows the XRD pattern obtained from the phosphorized ECD In thin film. No In metal peaks can be seen in this spectrum, suggesting that all of the In has been converted to InP. The remaining peaks in the spectrum can be assigned to Mo and MoP. MoP is seen in this spectrum because Mo at the interface with InP reacts with the phosphine gas during the growth process, resulting in a thin MoP layer.

The optoelectronic properties of the InP films were investigated using steady state photoluminescence and time resolved photoluminescence. For reference, the data were compared to evaporated In of the same

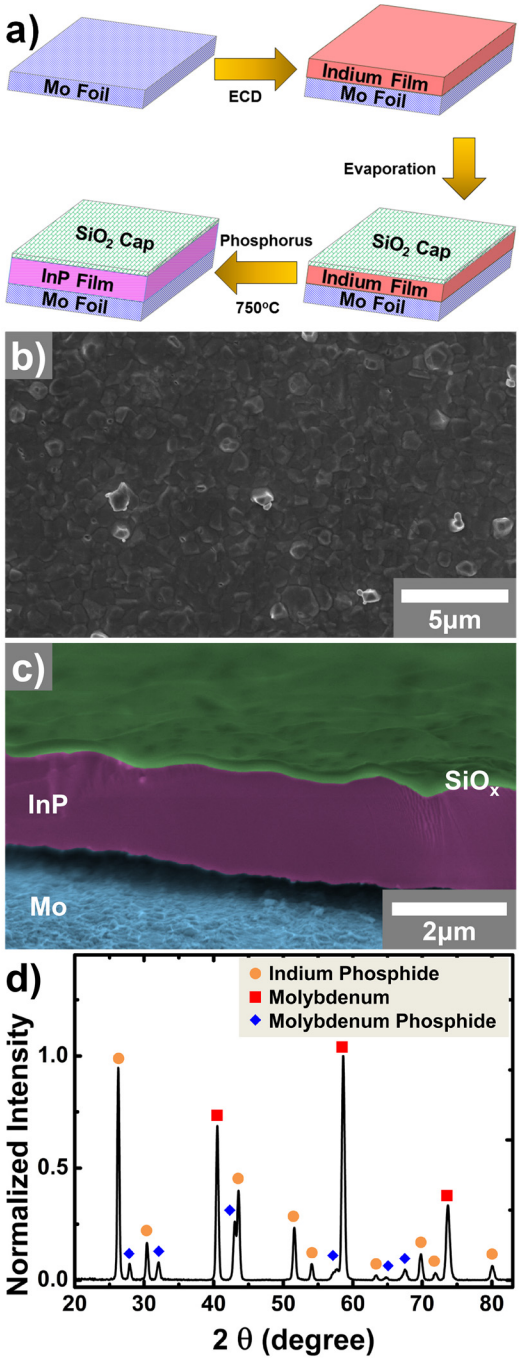

Figure 2.11. (a) Schematic of the TF-VLS phosphorization of ECD In thin films. (b) Top down SEM of ECD In deposited at optimal conditions after phosphorization. (c) False color cross sectional SEM of the same sample. The SiO_2 cap can be observed as a thin green line at the top of the sample and the Mo foil can be seen as the rough blue surface beneath the InP thin film (purple). (d) XRD of the phosphorized In thin film showing InP, Mo, and MoP signatures, normalized to the maximum peak intensity.

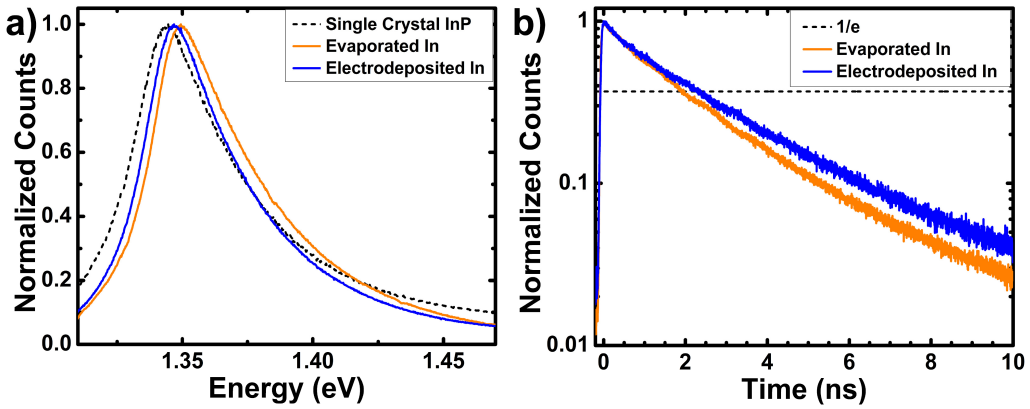

Figure 2.12. (a) Steady state photoluminescence of an ECD In thin film deposited at optimal conditions after phosphorization at 750°C (blue) compared against an evaporated In thin film phosphorized at the same temperature (orange). Both are compared to a single crystal n-type InP wafer (dashed black) and normalized to the maximum peak intensity. (b) Time resolved photoluminescence of a similar ECD In thin film phosphorized at 750°C (blue) compared to evaporated In phosphorized at the same temperature (orange), normalized to the maximum peak intensity. The dashed line represents the 1/e decay of the maximum peak intensity.

thickness, phosphorized at the same temperature, and to single crystal InP (100) (Wafertech) where appropriate (Fig. 2.12). The PL data show that the ECD In produces InP with similar peak positions and full width half maximum (~1.347 eV and 43 meV, respectively) in comparison to InP resulting from TF-VLS growth from evaporated indium (~1.349 eV and 46 meV) and single crystal InP wafer (~1.345 eV and 46 meV). This confirms that optoelectronic-quality InP is grown from the ECD In film. The TRPL data show that the ECD In produces an InP film that performs as well as, if not better than, the InP film obtained from evaporated In with an average 1/e effective carrier lifetime of 2.3 ns. The data further confirms that the In being deposited here is of electronic grade purity.

2.4. Conclusion

A simple electrochemical deposition bath was developed to produce continuous, smooth, high purity In thin films of ~1 μm on Mo foil. Two key developments have been shown here that allowed us to maintain the film morphology as well as its high purity. The first was the ability to control nucleation density of In on Mo with current density and bath temperature. By increasing current density and decreasing bath temperature, a fill factor of 100% could be achieved at ~1 μm In film thickness. The second development was the ability to improve the surface roughness of the deposited In by decreasing bath temperature. Using the example system of TF-VLS grown InP, I were able to show that the ECD In films can yield high quality InP thin films, comparable to those obtained from evaporated In films. That no special environment was used to keep the deposition bath pure, outside of those taken in a normal wet lab, suggests even higher quality results can be obtained in industrial-level controlled processes. The ability to produce electronic grade In from ECD may be enabling for many In-based technologies, as ECD increases the material utilization rate of In over traditional vacuum deposition techniques. In the example

system of TF-VLS InP, a scalable and low cost growth system can be envisioned for wide-scale PV implementation.

2.5. Acknowledgements

This work was funded by the Bay Area Photovoltaics Consortium (BAPVC). The modeling of In ECD process and optoelectronic characterization of InP were supported by the Director, Office of Science, Office of Basic Energy Sciences, Materials Sciences and Engineering Division of the U.S. Department of Energy under Contract No. DE-AC02-05CH11231. The XPS measurements were performed at JCAP, Joint Center for Artificial Photosynthesis, a DOE Energy Innovation Hub, supported through the Office of Science of the U.S. Department of Energy under Award Number DE-SC0004993. The SIMS analysis was performed by the Evans Analytical Group.

3. General Thermal Texturization Process of MoS_2 for Efficient Electrocatalytic Hydrogen Evolution Reaction[2]

3.1. Introduction

Having explored how electrodeposition can be used in combination with the TF-VLS growth technique to produce high quality, potentially low cost solar material, the second main theme of this dissertation is taken up; how renewable energy, such as electricity produced by solar, can be used to make a renewable alternative to fossil fuels. First the production of hydrogen using a molybdenum disulfide catalyst is discussed and in following chapters the production of fuels via electrochemical reduction of carbon dioxide will be explored.

Renewable energy sources such as wind and solar have shown great promise in the last decade; however, the issue of their intermittency, and thus the need for energy storage, remains unsolved.[63] Energy storage via chemical fuels is highly desirable due to their high energy densities and while hydrocarbon-based liquid fuels remain the most desirable, hydrogen presents an attractive alternative. Hydrogen production via electrochemical water splitting, specifically the hydrogen evolution reaction (HER), has been widely studied[64–67] and has inspired a vision of a hydrogen powered economy.[24,68] This goal has stimulated a large portfolio of research in catalysts to reduce the overpotential required by the hydrogen evolution reaction. MoS_2 has emerged as a promising catalyst for HER because it is earth abundant, cheap, and chemically-stable.[69–71] Although bulk MoS_2 (i.e. the pristine mineral) is not an active HER catalyst, it is known that exposed MoS_2 edge sites act as highly-active catalytic sites.[72–74] For this reason various MoS_2 HER catalysts have been synthesized *via* solution-based or vapor-based methods, which effectively maximize the density of edge sites through synthesizing nano-sized flakes,[75,76] porous structures,[77,78] or vertically aligned structures.[79–81] However, if the pristine MoS_2 mineral, which is the basic structure of all MoS_2 morphologies, could be converted into an efficient catalyst, a wide array of MoS_2 starting materials could also be converted into HER catalysts. In order to achieve this, pristine MoS_2 needs to overcome several fundamental issues to increase its catalytic activity. First, the (0001) plane is dominant in the pristine MoS_2 mineral which is an inactive plane for HER.[74,77] Second, pristine MoS_2 is predominately of the 2H crystal phase which exhibits poor conductivity.[82–84] These issues generally eliminate pristine bulk MoS_2 as an electrochemical HER catalyst.

Here, I demonstrate a general thermal texturization procedure which can convert bulk MoS_2 of many morphologies into a HER catalyst. Bulk mineral MoS_2, micron-scale commercial

---

[2] A modified version of this work was published as P. Lobaccaro, D. Kiriya, H. Y. Y. Nyein, P. Taheri, M. Hettick, H. Shiraki, C. M. Sutter-Fella, P. Zhao, W. Gao, R. Maboudian, J. W. Ager, and A. Javey, General Thermal Texturization Process of MoS_2 for Efficient Electrocatalytic Hydrogen Evolution Reaction. *Nano Lett.*, **16**, 4047–4053 (2016).

MoS_2 powders, and even a commercially-available, nanoflake MoS_2 based lubricant spray, all of which showed poor HER activity before treatment, show high HER performance after thermal texturization. I find that annealing in a hydrogen environment increases the surface area and reduces the resistivity of the MoS_2 starting material by decomposing the MoS_2 into edge sites and forming Mo clusters on the surface. The work presents a general platform for using MoS_2 mineral as an efficient HER catalyst.

3.2. Experimental

3.2.1. Sample Preparation

Bulk mineral MoS_2 was purchased from SPI Supplies. Micron-scale (microflake) MoS_2 was purchased from Graphene Supermarket. Some microflake MoS_2 was further prepared by grinding it with a mortar and pestle in an attempt to make smaller flakes. This material is called ground microflake. The as-received microflakes were in powder form, thus it was necessary to cast the powder into a film in order to test its HER activity. Microflake and ground microflake films were prepared by the following processes, consisting of dispersing the flakes in dimethylformamide (DMF) at a concentration of 30 mg/ml via sonication, and then casting the suspension (~100 μL) on a 1 cm × 1.5 cm Mo foil on a hotplate at 120 °C. After drying off the DMF solvent (about 5 min), the suspension casting was repeated again. The microflake film consists of flakes of ~2-5 μm in width. All samples termed as-received MoS_2 (bulk and microflake film) or as-ground (ground microflake film) underwent a 250 ºC forming gas anneal for 3 hrs to clean the surface and remove any remaining DMF solvent. This temperature has essentially no effect on MoS_2. High temperature annealed samples were annealed at 700 °C, 800 ºC, or 900 °C in forming gas for 3 hrs. The samples were allowed to cool below 50 ºC before being taken out of the annealing chamber.

3.2.2. Hydrogen Evolution Activity Measurements

Bulk mineral MoS_2 samples needed to be mounted before they could be used as electrodes. Silver paste (Circuit Works) was used to mount the flakes to a glass slide. The stack was then annealed at 70 °C in air to cure the Ag paste. Then Cu tape was placed on the edge of the Ag paste to make an electrical lead connection. Finally, insulating, acid-resistant, polymer resin was painted over the entire area except for the desired MoS_2 area identified for measurement. For the microflake and ground microflake film samples, the same resin was used to cover the whole area of the film except for the identified measurement area. These samples were placed as working electrode in the 3-electrode cell as shown in Figure 3.9a.

The HER measurements were done in 0.5 M H_2SO_4 (Sigma-Aldrich) with a calibrated Ag/AgCl reference electrode and a platinum counter electrode. The electrolyte was initially sparged with N_2 bubbling for more than 10 mins to remove oxygen. High purity N_2 gas was then flown over the headspace of the electrolyte during the measurements. The electrolyte was

constantly stirred at 750 RPM with a magnetic, Teflon-coated stir bar. A Biologic SP-300 potentiostat was used to make all electrochemical measurement. IR drop was corrected for during the cyclic voltammetry measurements by first running electrochemical impedance spectroscopy from 10^6 to 1000 Hz to identify the uncompensated resistance.[85,86] This resistance was found to typically be less than 10 Ω. Cyclic voltammetry was used at two different scan rates to obtain the data for the Tafel plots (5 mV/sec) and polarization curves (50 mV s^{-1}) shown below. The Tafel plot is a plot of the applied overpotential versus logarithm of the current density. From this plot, kinetic parameters like the exchange current density and Tafel slope can be extracted (further details are given in section 3.3.3). Polarization curves are simply a plot of current density versus applied potential. From this plot, improvements in the overall activity of the catalyst over a range of potentials can be observed.

3.2.3. Electrochemical Active Surface Area (ECSA) Measurement

To identify the electrochemically active surface areas to normalize the obtained polarization curves above, ECSA measurements were used.[77] Bulk MoS_2 (as-received and annealed samples) were mounted as stated to be used as the working electrode in the three electrode setup shown in Figure 3.9a. I employed electrochemical impedance spectroscopy, using a Biologic SP-300 potentiostat, at open circuit potential scanning frequencies from 10 Hz to ~0.05 Hz. Then a R-C equivalent circuit was used to fit the data to determine the double-layer capacitance of each sample. The measured double layer capacitances values were as follows: As-received, ~ 4.14 μF cm^{-2}; 700 °C annealed sample, ~ 0.47 μF cm^{-2}; 800 °C annealed sample, ~ 2.95 μF cm^{-2}; 900 °C annealed sample, ~ 2.83 μF cm^{-2}. The relative active surface areas are obtained from the relative values of the above double layer capacitances. Using these values, the currents (mA) were normalized.

3.2.4. Chemical and Structural Characterizations

Scanning electron microscope (SEM) images were obtained with either a FEI Quanta 200 FEG SEM with an operating voltage of 15 kV or with a FEI Nova NanoSEM650 with an operating voltage of 5 kV. XPS characterization was performed using a Kratos Axis Ultra DLD system using a monochromatic Al Kα source ($h\nu$ = 1486.6 eV). The XRD patterns were taken on a Rigaku SmartLab system which is capable of measuring both grazing incidence and normal XRD patterns. TEM images were taken with a FEI Titan microscope with an operating voltage at 200 kV.

3.3. Results and Discussion

3.3.1. Texturization of MoS_2

To generate the catalytic activity of the pristine bulk mineral MoS_2, the surface was intentionally dissociated as shown schematically in Figure 3.1a. Thermal annealing in a hydrogen environment is a straightforward dissociation process; sulfur atoms in MoS_2 would be removed as H_2S gas leading to the formation of vacancies and edges in the (0001) plane of the MoS_2. Simultaneously, the excess Mo forms metal clusters on the flake. It was hypothesized that this

process could improve the HER activity of the bulk mineral MoS_2 by increasing the edge site density on the surface and by making the flake conductive through the generation of Mo clusters. Figure 3.1b shows schematically the expected results of increased HER performance for the annealed bulk MoS_2 as compared to the pristine bulk MoS_2. This thermal texturization strategy would be simple and effective, having universal applicability to not only bulk mineral MoS_2, but also to other MoS_2 morphologies with higher starting edge-to-surface ratios, such as micron-size MoS_2 flakes, to further improve HER activity (Figure 3.1b).

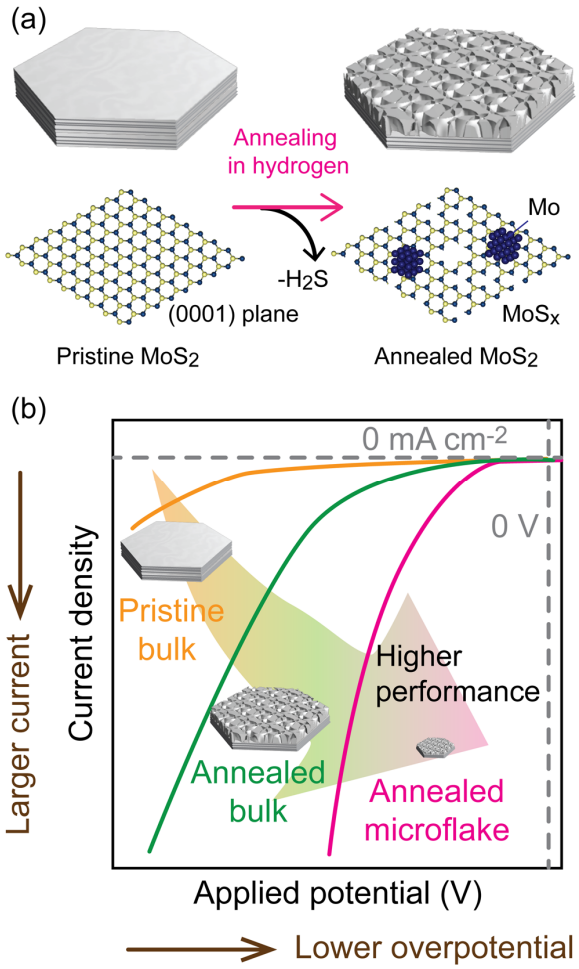

Figure 3.1. (a) Schematic illustration of the thermal texturization process of the (0001) plane of MoS_2. Annealing under a hydrogen environment generates H_2S through dissociation of the MoS_2 surface which increases the edge site density and generates Mo clusters. (b) Schematic illustration of the polarization (current density vs. applied potential) curves for pristine bulk MoS_2, annealed bulk MoS_2 and annealed microflake MoS_2. The annealing process is expected to improve the HER performance (higher current density), more dramatically so for the microflake MoS_2.

Figure 3.2 shows representative SEM images for bulk mineral MoS_2, micron-scale flakes (microflake), and mechanically ground micron-scale flakes of MoS_2 (ground microflake). As-received (i.e. no thermal damage) bulk MoS_2 shows smooth (0001) crystal planes (Figure 3.2a). Upon annealing at 700 °C in a forming gas (H_2/N_2 = 5%/95%) atmosphere for 3 hrs, the surface shows signs of dissociation thereby increasing the defect density, including edge sites, with the effect further increasing at 900 °C (Figure 3.2a). The microflake films, annealed under the same conditions as the bulk mineral MoS_2, show a reduction in flake sizes, especially for the 900 °C annealing condition, again indicating an increase in the number of exposed edges (Figure 3.2b). The as-prepared ground microflake film (as-ground), shows similar changes to the microflake films under the same annealing condition (Figure 3.2c).

In order to investigate how deep the apparent surface texturization extended into the MoS_2 flakes, cross-sectional SEM images of the 900 °C annealed bulk MoS_2 were obtained (Figure 3.3a). It can be observed that the thermal texturization penetrated about 1 μm into the flake after which the flake resembles the as-received bulk MoS_2 (smooth) (Figure 3.3b). This indicates that the

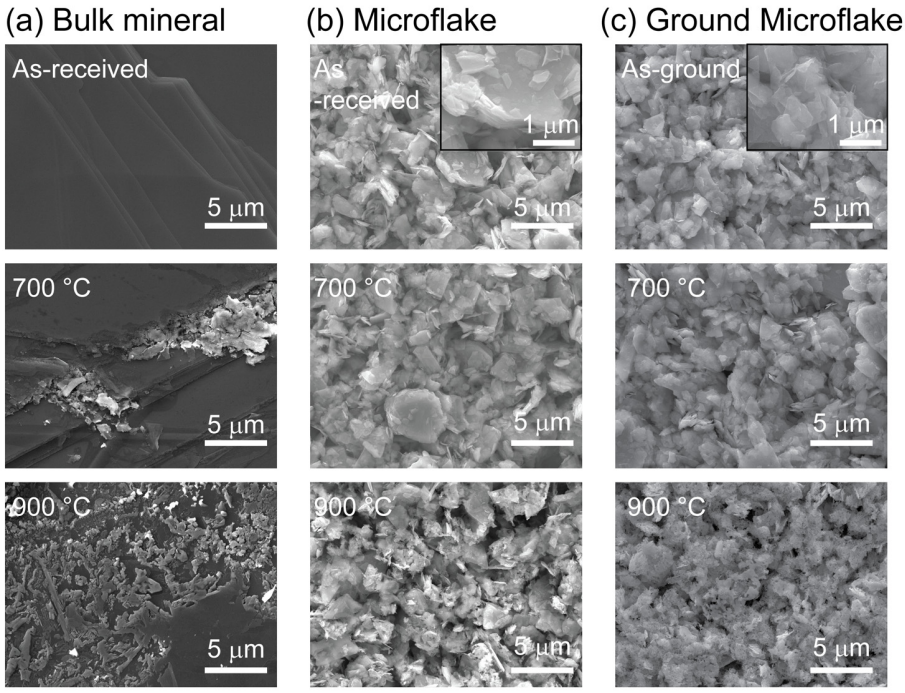

Figure 3.2. SEM images for (a) bulk mineral MoS_2, (b) microflake MoS_2, and (c) ground microflake MoS_2 after annealing at 250 °C (as-received or as-ground), 700 °C, and 900 °C for 3 hrs. The latter two microflake MoS_2 samples are both deposited as films on Mo foil.

dissociation occurs mainly at the surface exposed to hydrogen gas. X-ray diffraction (XRD) analysis shows the sample bulk remains as MoS_2 (Figure 3.3c). Surface sensitive grazing angle XRD patterns indicate the presence of Mo on the surface (assumed to be clusters), with increasing Mo peak intensity as the annealing temperature is increased (Figure 3.3d). X-ray photoelectron spectroscopy (XPS) elucidates the surface elemental composition (Figures 3.3e and f). As-received bulk MoS_2 shows a doublet corresponding to Mo^{4+} $3d_{3/2}$ and $3d_{5/2}$ around 233 eV and 230 eV, respectively. The annealed samples show another doublet, which would correspond to Mo^0 $3d_{3/2}$ and $3d_{5/2}$ around 232 eV and 229 eV, respectively. The presence of Mo^0 indicates the generation of Mo on the surface. Moreover, the relative size of this Mo^0 doublet increases in comparison to the Mo^{4+} doublet with increasing annealing temperature, showing that the surface becomes increasingly Mo rich, in agreement with grazing angle XRD data. A peak due to Mo^{6+} is also observed in the annealed samples, which corresponds to the presence of MoO_3 in the near surface region. The presence of the oxide is thought to be due to thermally generated Mo^0 atoms which can be oxidized in air. Since MoO_3 dissolves in aqueous solutions, the MoO_3 would not affect the HER activity of the sample. Furthermore, sulfur 2p signals were observed around 163 eV in all annealed samples, indicating that the annealed samples maintain some MoS_2 at the surface even after annealing at 900 °C for 3 hrs. The valence band edges for the annealed MoS_2 flakes were also examined as shown in Figure 3.4. The flakes, after annealing at higher than 700 °C, show detectable density of states (DOS) around the Fermi level (at 0 eV). The DOS could potentially be from MoS_2 converted to the 1T metallic phase by hydrogen doping but it is probable

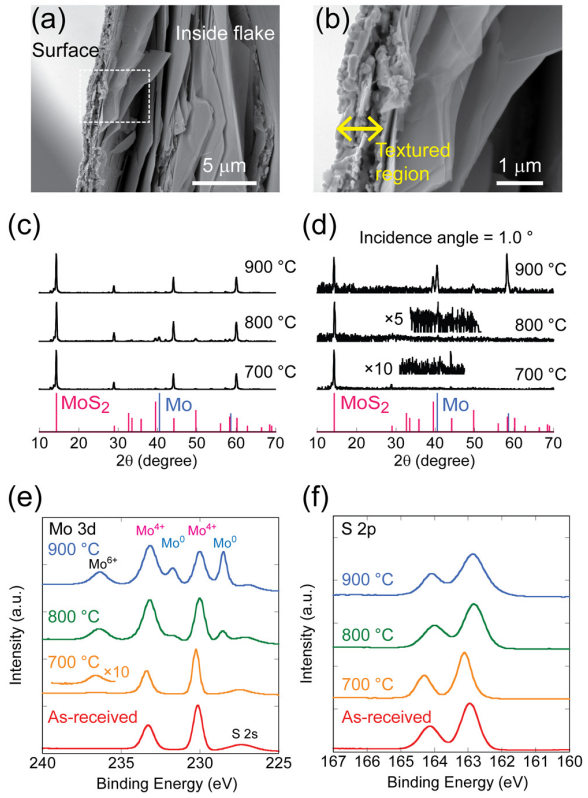

Figure 3.3. (a and b) Cross-sectional SEM images of annealed bulk MoS_2 at 900 °C for 3 hrs under a forming gas environment. (c) Powder XRD patterns for annealed bulk MoS_2 at 700 °C, 800 °C, and 900 °C with reference patterns for MoS_2 and Mo. (d) Grazing incident XRD (incident angle of X-Rays to surface = 1 °) for the same samples as in Figure 3.3c. Increasing the annealing temperature induces stronger Mo signal at the surface. (e and f) XPS spectra for as-received and annealed bulk MoS_2 samples focused on the Mo 3d (e) and S 2p (f) regions. Increasing the annealing temperature induces an increase in the Mo^0 doublet signal but all annealing conditions still show sulfur signal.

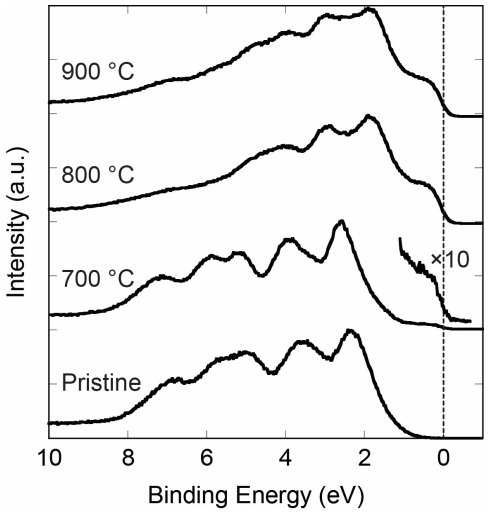

Figure 3.4. XPS spectra around the valence band region of the bulk mineral MoS_2 of pristine (annealed at 250 °C for 3hrs) and annealed at 700 °C to 900 °C for 3 hrs.

that the main contribution is from Mo nanoparticles on the surface, especially for the flakes annealed at 800 °C and 900 °C, where the reduced states are also clearly visible in the core level spectra.

To further investigate the crystalline structure of the catalyst surface, cross-sectional transmission electron microscopy (TEM) was performed on a texturized sample (700 °C). It was observed that the crystalline structure of the sample near the surface was similar to that observed several hundred nm deep in the same sample (Fig. 3.5). Fast Fourier transform (FFT) analysis of the images show both regions to be highly crystalline and all diffraction peaks obtained could be assigned to MoS_2, confirming that the MoS_2 structure remains near the surface after the hydrogen annealing treatment. Therefore, the MoS_2 crystalline structure has survived even at the surface after annealing at 700 °C for 3 hrs. At this temperature, there should be a small amount of texturization and, based on the grazing angle XRD and XPS, there should be a small amount of Mo metal near the surface. However, it is a well-known issue with cross-sectional TEM that imaging very near the sample surface is difficult due to platinum redeposition during the focused ion beam milling process. Thus, it is possible that these regions did exist on this sample but it was not possible to observe them with the TEM done here.

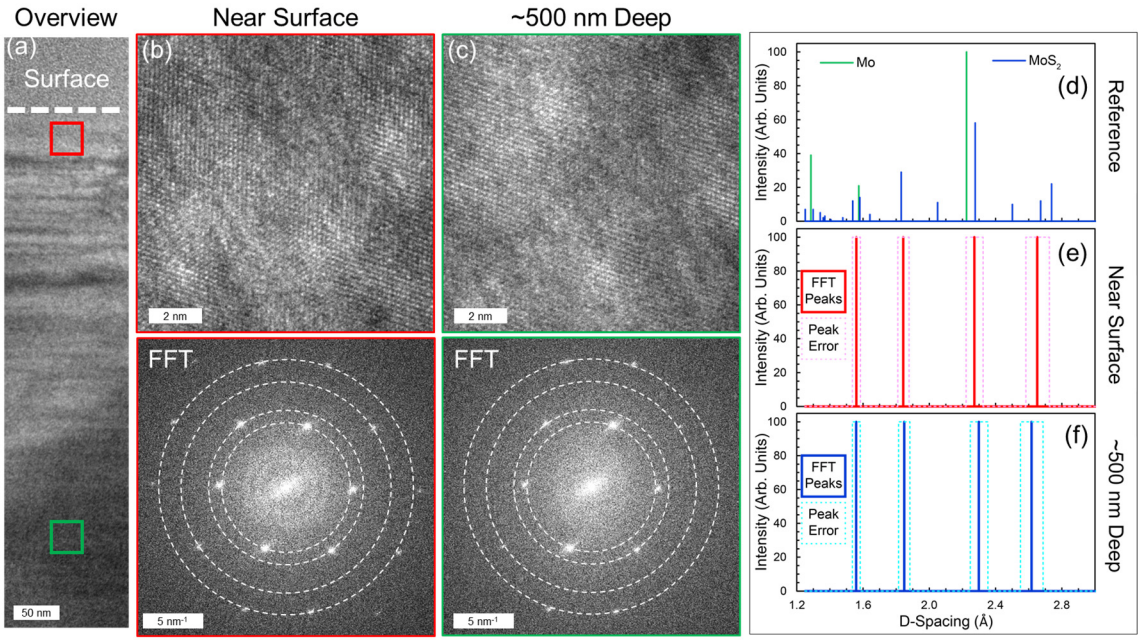

Figure 3.5. The structure of a thermally texturized sample at 700 °C (3 hrs annealing) was investigated using cross-sectional TEM. (a) Low resolution TEM image of the sample. High-resolution TEM images near the surface approximately ~25 nm (b) and deeper inside the sample, approximately 500 nm from the surface (c). Fast Fourier transform (FFT) of these images are shown below. (d-f) D-spacings were obtained from the FFT patterns in Figure 3.5b and c and other images not shown here. (d) Reference powder XRD patterns of MoS_2 and Mo, compared to D-spacing patterns obtained from the FFT analysis for the near surface region (e) and for the deeper region (f). FFT peaks (solid line) and errors (dot line) are shown in the plot.

To investigate the thermal texturization mechanism, SEM images of the bulk mineral MoS_2 were analyzed for three different annealing times (1, 3, and 5 hrs). As shown in Figure 3.6, the MoS_2 dissociation, which is observable as texturization of the surface, can be seen starting after 3 hrs of annealing. After 5 hrs of annealing, the dissociation on the surface is more obvious (Fig. 3.6b). It can further be observed that the texturized areas have grown from defects and edges on the (0001) plane (Fig. 3.6c). The texturization is arranged in a radial fashion, which indicates that the structure has grown from a defect. The surface texturization is only displayed when annealing in a hydrogen atmosphere and was not observed in a nitrogen atmosphere (Fig. 3.7). After annealing in nitrogen at 800 °C, the surface is still macroscopically smooth, not rough like the samples annealed in forming gas. This difference would be explained because of the reaction between hydrogen and sulfur on the MoS_2 surface which is necessary to generate H_2S and dissociatively texturize the surface. In the nitrogen atmosphere, this reaction cannot occur and thus sulfur atoms are not removed effectively from the surface and the texturization does not occur.[87]

The effect of thermal texturization can be monitored in metal-oxide semiconductor field-effect transistors (MOSFETs) as well. MOSFETs were fabricated with a standard photolithography process for mechanically exfoliated MoS_2 flakes (~100 nm in thickness) which were placed on a p^+-Si substrate with 260 nm SiO_2. The flakes were annealed under different

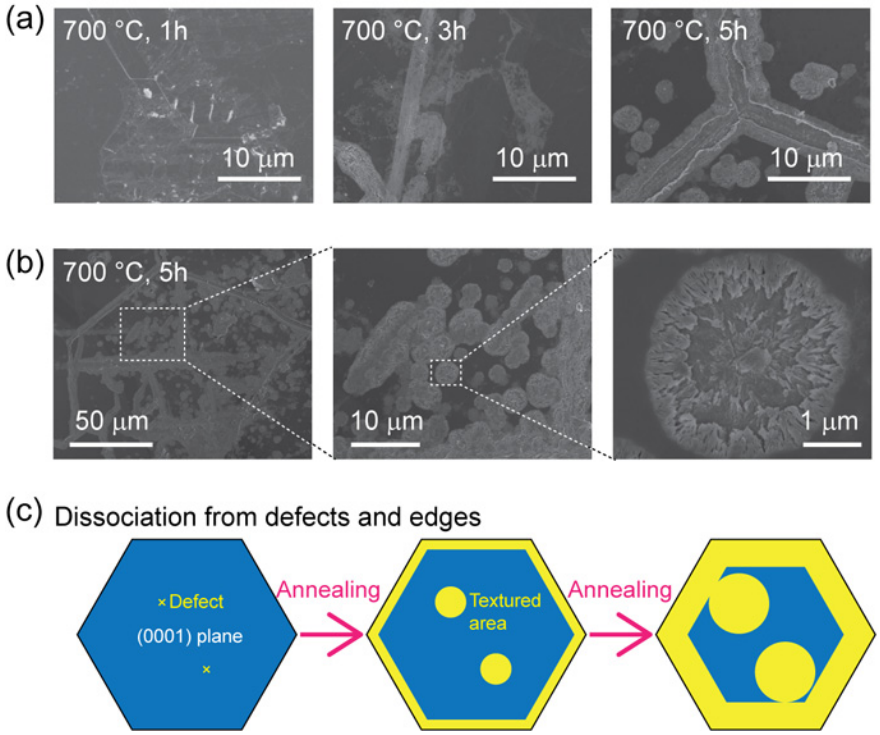

Figure 3.6. Mechanism of the thermal texturization process which occurs on the MoS_2 surface under a forming gas environment ($H_2/N_2$5/95 =5%/95%). (a) SEM images of the bulk mineral MoS_2 annealed at 700 °C for different annealing times (1h to 5 hrs). The light gray areas are dissociatively textured by the thermal annealing processes. Annealing longer than 3 hrs shows clear dissociation under SEM. (b) The detailed surface morphology for the bulk MoS_2 annealed at 700 °C for 5 hrs. The surface texturization is observed as either lines or circles. The circles are radially grown, indicating the dissociation occurs from a defect at the center. (c) A plausible mechanism for the thermal texturization process is shown. The texture would emanate from defects and edges on the surface.

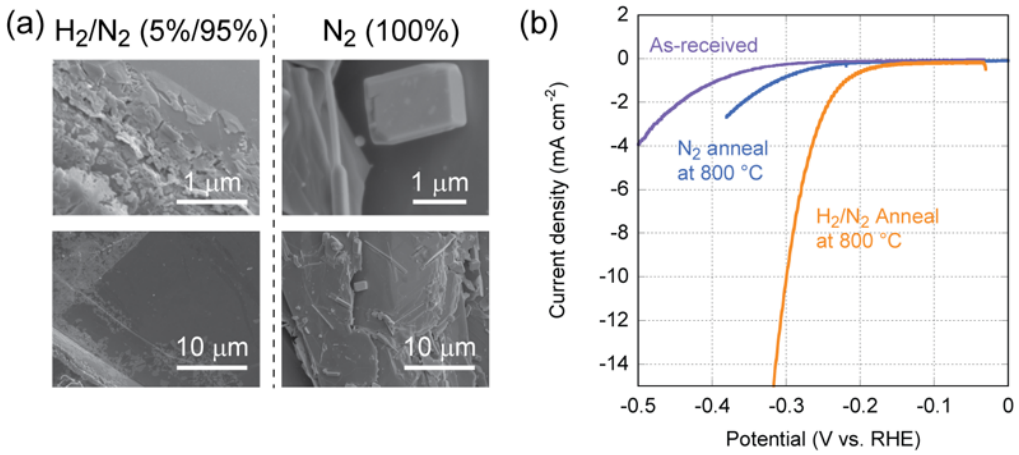

Figure 3.7. Environmental effect of the annealing process on bulk mineral MoS_2. (a) SEM images of the annealed bulk MoS_2 in forming gas (left) and nitrogen (right) at 800 °C for 3 hrs. In the case of annealing under forming gas, the dissociation causes texturization of the surface. On the other hand, in the nitrogen anneal case, the surface is still smooth even after annealing at 800 °C and large cubic structures are observed. (b) Polarization curves for the HER activity of as-received bulk MoS_2, 800 °C annealed bulk MoS_2 under nitrogen, and 800 °C annealed bulk MoS_2 under forming gas are shown. The nitrogen-annealed sample shows much lower HER performance than the sample annealed in forming gas.

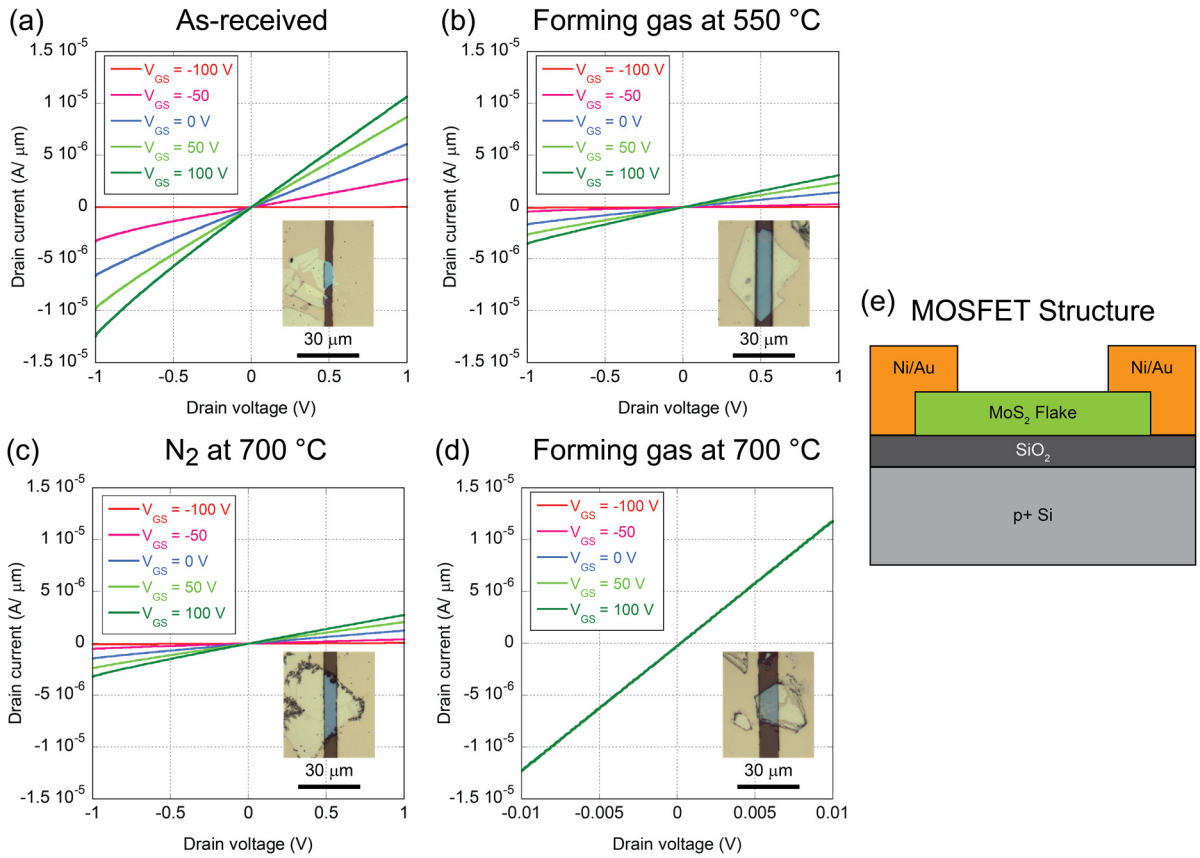

Figure 3.8. Output characteristic curves for the MOSFETs of (a) as-received bulk MoS_2, (b) annealed bulk MoS_2 at 550 °C in forming gas, (c) annealed bulk MoS_2 at 700 °C in nitrogen, and (d) annealed bulk MoS_2 at 700 °C in forming gas. The MOSFET device structure is shown in (e). These samples were annealed at their respective temperatures for 3 hrs. MoS_2 flakes (thickness of ~100 nm) were prepared by a mechanical exfoliation technique, then annealed at the aforementioned temperatures followed by a typical lithography process to make the devices. The channel length was fixed at 10 μm in all cases. Back gate potential was applied from -100 V to 100 V. Except for the forming gas 700 ºC annealed sample, all samples showed gate dependency, indicating semiconducting n-type MoS_2. The characteristics curve in Figure 3.8d shows a sample with no gate dependency, indicating metallic behavior of the MoS_2 flake after the thermal texturization process. Top down optical images of the device structure are shown in the insets of each of plot.

conditions and then fabricated into the same device structure with a 10 μm channel length. As-received MoS_2 showed gate-dependency of the drain current, as did low temperature annealed MoS_2 (forming gas at 550 °C) (Fig. 3.8a,b). This behavior indicates that the carrier concentration of these samples can be modulated electrostatically. On the other hand, the sample annealed at 700 °C in forming gas showed no gate dependency (Fig. 3.8d), indicating the metallic state of the material, due most likely to the generation of Mo clusters. The sample annealed in nitrogen at 700 °C still shows a gate dependency (Fig. 3.8c). These findings again support the importance of hydrogen to the effective dissociative texturization of the MoS_2.

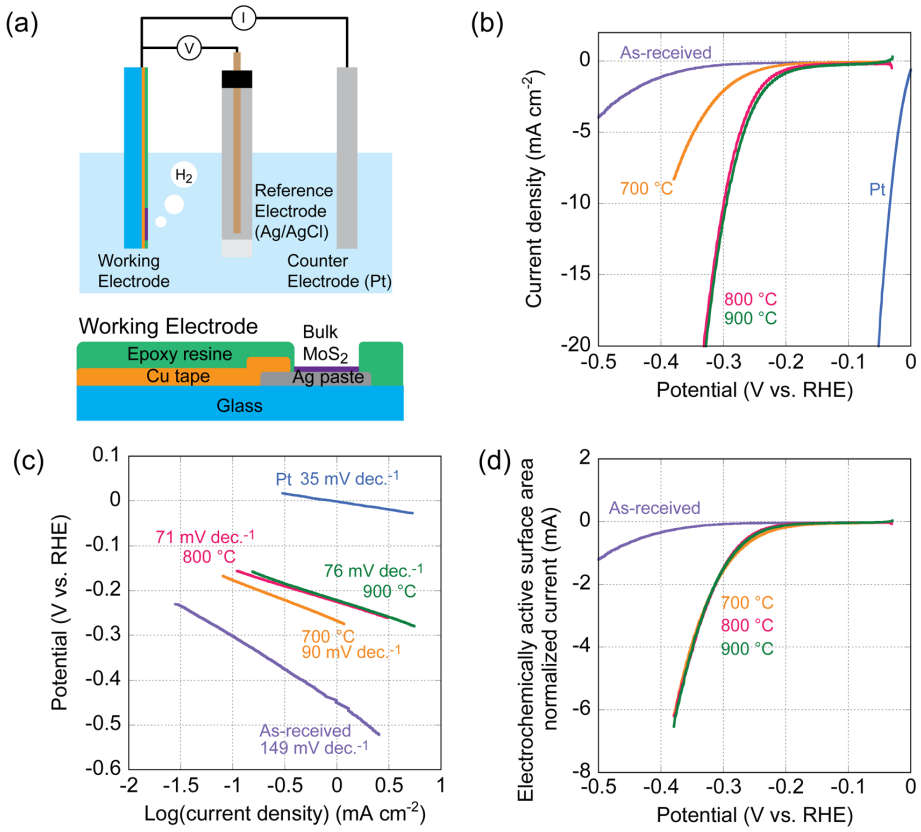

Figure 3.9. HER performance of the annealed bulk mineral MoS_2. (a) Illustration of the three electrode setup with a working electrode of bulk mineral MoS_2. (b and c) The polarization curves for as-received and annealed bulk samples (3 hrs under forming gas) and their corresponding Tafel plots. (d) Electrochemically active surface area normalized polarization curves from (b). The three curves representing annealed samples from 700 °C to 900 °C fall onto the same curve, indicating the active sites for all three samples are similar. The similar Tafel slopes from (c) corroborate this conclusion.

3.3.2. Hydrogen Evolution Reaction Activity of Texturized MoS_2

The HER activity of the samples was analyzed with a standard three-electrode setup using a 0.5 M H_2SO_4 electrolyte, as shown in Figure 3.9a. All curves presented here were corrected for the voltage drop due to solution resistivity (IR drop), measured before each run via electrochemical impedance spectroscopy (EIS). Figure 3.9b shows the polarization curves for the bulk mineral MoS_2. The as-received bulk MoS_2 shows current density $j < 5$ mA cm^{-2} even up to -0.5 V vs. the reversible hydrogen electrode (RHE) due to the dominant (0001) surface plane and the low density of active edge sites. In contrast, the forming gas annealed bulk MoS_2 shows fair HER performance with higher current densities at lower overpotentials. The Tafel plots for the bulk MoS_2 samples are shown in Figure 3.9c. The annealed samples show similar Tafel slope values of 70 to 90 mV decade^{-1}, which indicates the hydrogen evolution mechanism is similar for these samples.

I further analyzed the HER performance of each sample by considering the electrochemically active surface area normalization of each sample. EIS measurements were applied to evaluate the relative active surface area for each bulk MoS_2 sample as shown

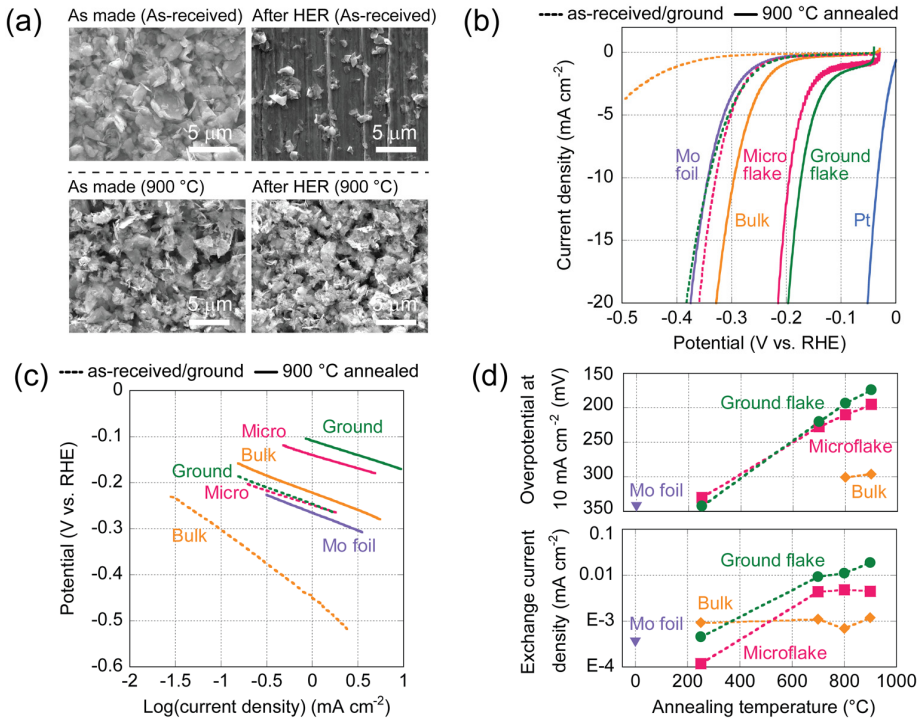

Figure 3.10. Improvement of HER performance for the microflake/ground microflake MoS_2 films by the thermal texturization process. (a) SEM images of the as-received and 900 °C annealed microflake MoS_2 films on Mo foil before (as made) and after hydrogen generation. The as-received film shows delamination. (b) The polarization curves for the bulk, microflake and ground microflake films of MoS_2 as-received or as-ground (dot line) and annealed at 900 °C (solid line). As-received and as-ground microflake films were evaluated after delamination. The scan rate was 50 mV s^{-1}. Curves for bulk mineral MoS_2 are identical to Figure 3.9b. (c) Tafel plots for the bulk, microflake, and ground microflake films as-received/as-ground and annealed at 900 °C. Curves for the bulk mineral MoS_2 are identical to Figure 3.9c. (d) (Top) Overpotential required to obtain a current density of 10 mA cm^{-2} for each sample. All MoS_2 samples (bulk, microflake, and ground microflake) show a corresponding decrease in the required overpotential with increasing annealing temperature. Samples annealed at 250 °C correspond to the as-received or as-ground sample. Both as-received and 700 ºC annealed bulk MoS_2 did not show 10 mA cm^{-2} within the range measured. The values for the as-received and as-ground microflake films are after delamination. (Bottom) Plot of exchange current density vs. annealing temperature. Decreasing the flake size from bulk to ground microflake, the exchange current density increases.

previously.[77] Figure 3.9d shows the polarization curves normalized to electrochemically active surface area. All the curves for the annealed samples fall onto a similar line, meaning the forming gas dissociation process generates similar active sites on the surface with the main difference between samples annealed at different temperatures being the density of edge sites generated, thus explaining the changes in *j-V* behavior in Figure 3.9b.

To demonstrate the effectiveness of this thermal texturization approach to generate catalytic HER performance with other MoS_2 materials, the texturization process is applied to microflake and ground microflake films. Microflakes and ground microflakes have larger edge-to-body ratios than bulk mineral MoS_2 (Fig. 3.2), therefore, they have a higher realizable catalytic performance. I found that the as-received microflake and as-ground microflake MoS_2 films (annealed at 250 °C in forming gas) are difficult to operate in HER experiments; once hydrogen

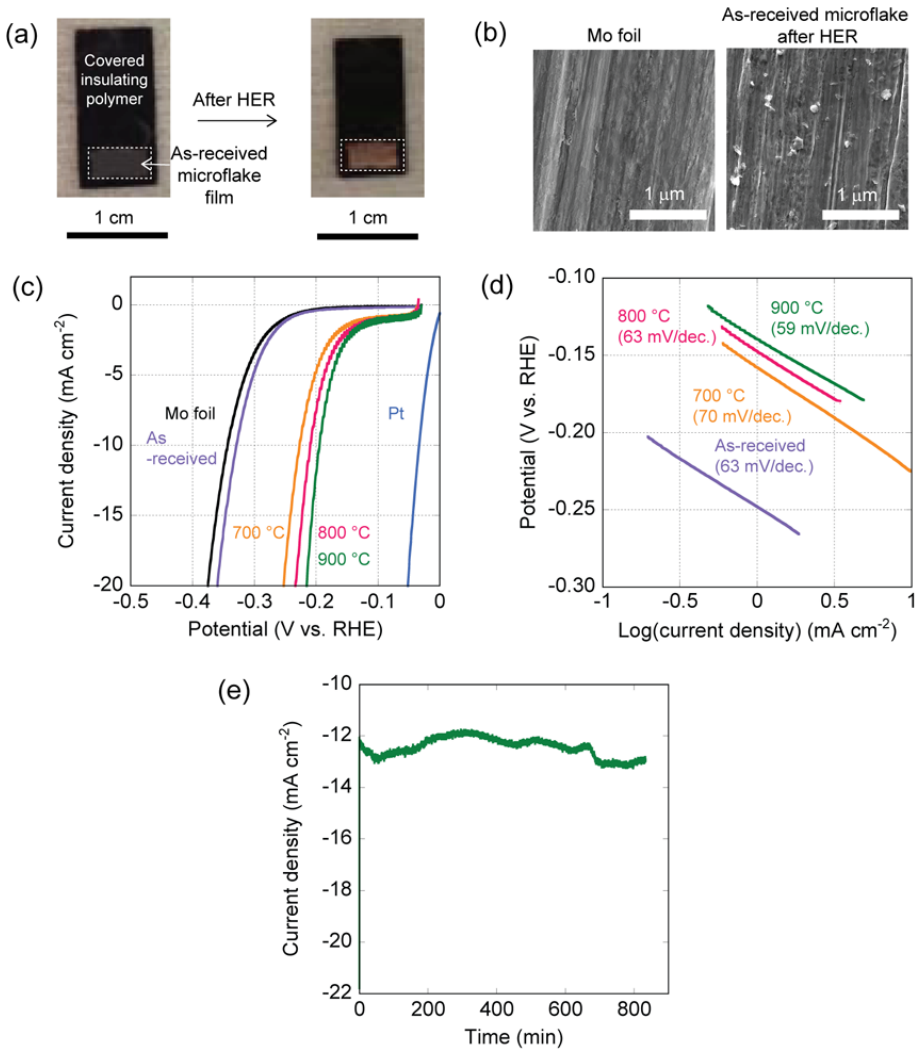

Figure 3.11. (a) Macroscopic images for the as-received microflake MoS_2 films (annealed at 250 °C for 3hrs) on Mo foil as the working electrode before (left) and after (right) HER in 0.5 M H_2SO_4. The area exposed during electrolysis was completely delaminated by the generation of hydrogen bubbles. (b) SEM images of Mo foil (left) and the surface of the as-received microflake MoS_2 film after delamination (right). Small amounts of MoS_2 flakes remained on the Mo foil after the delamination. (c) Polarization curves (50 mV s^{-1}) in 0.5 M H_2SO_4 for the microflake MoS_2 samples annealed at different temperatures, including Mo and Pt foils for reference. (d) Tafel plot of the samples shown in Figure 3.11c taken at 5mV s^{-1}. (e) Chronoamperometric curve (*j-t*) measured for a microflake MoS_2 film annealed at 900 °C for 13hrs.

bubbles are generated, the films easily delaminate from the substrate (Fig. 3.10a and 3.11a,b). It is difficult to keep the films on the substrate, making it difficult to use as a catalyst in a film configuration on a conductive substrate. On the other hand, after the texturization process, the samples did not delaminate from the surface (Fig. 3.10a), although some partial flaking off could occur. Therefore, for microflake and ground microflake MoS_2 samples, the annealing process is useful towards making an effective HER catalyst.

Figure 3.10b shows polarization curves for bulk, microflake, and ground microflake films of MoS_2 annealed at 250 °C (as-received/as-ground, dotted) and 900 °C (solid). As-received and

as-ground microflake films produce similar curves to Mo foil because of the large amount of delamination that occurred with these films. The annealed samples however, show a clear trend; a monotonic increase in current density with decreasing flake size. This trend can be explained as an increasing density of edge sites due to the shrinking size of the flakes. The Tafel slopes of the annealed micro and ground microflakes samples are ~60-70 mV decade^{-1} (Figs. 3.10c, 3.11d, 3.12b and Table 3.1). The mechanism of hydrogen adsorption/desorption is similar in these cases and the Tafel slope value is close to the Heyrovsky reaction regime (40 mV decade^{-1}), indicating that the rate-limiting step here is the electrochemical desorption step (further details given below).

Two important parameters used to evaluate the HER activity of a sample are the magnitude of the required overpotential and the exchange current density (j_0).[27,88] A common way of evaluating the required overpotential is to report the overpotential (η) needed to obtain 10 mA cm^{-2} (Fig. 3.10d).[27] For all samples, η monotonically decreases from as high as 342 mV to as low as 174 mV as the annealing temperature increases (Fig. 3.10d and Table 3.1), showing that the thermal texturization is effective for all sample morphologies. The exchange current density was also evaluated and is shown in Figure 3.10d. It can be seen that decreasing the flake size, from bulk to microflake to ground microflake, increased j_0 from ~10^{-3} mA cm^{-2} (bulk) to ~0.019 mA cm^{-3} (ground microflake) in the 900 °C annealing case. It is important to note here that the as-received/as-ground microflake films were evaluated after delamination had completely stopped (surface similar to that shown in Figure 3.10a after HER), thus, it is not surprising that the overpotential to reach 10 mA cm^{-2} and the j_0 for these samples are similar to Mo foil which is the underlying substrate. Finally, the long-term stability of the MoS_2 microflake film annealed at 900 °C was examined by a chronoamperometry measurement (*j-t*). The electrolysis measurement was performed for more than 12 hrs at a constant potential and a current density of about 12 mA cm^{-2} was maintained (Fig. 3.11).

I further demonstrate the wide-range of applicability of this thermal texturization process by applying it to a commercially-available spray of MoS_2 (CRC company), for which the intended

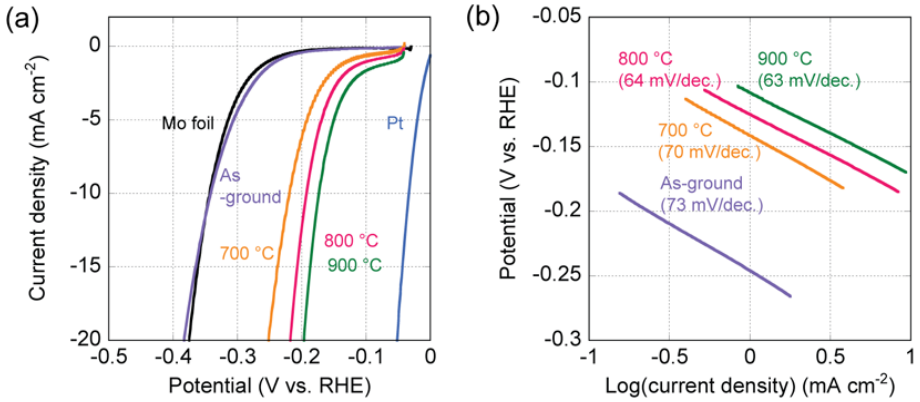

Figure 3.12. (a) Polarization curves (50 mV s^{-1}) in 0.5 M H_2SO_4 for the ground microflake MoS_2 samples annealed at different temperatures, including Mo and Pt foils for reference. The as-ground MoS_2 film delaminated after evolving hydrogen similar to what is shown in Figure 3.11a, resulting in the observed activity matching closely to Mo foil. (b) Tafel plot of the samples shown in Figure 3.12a taken at 5mV s^{-1}.

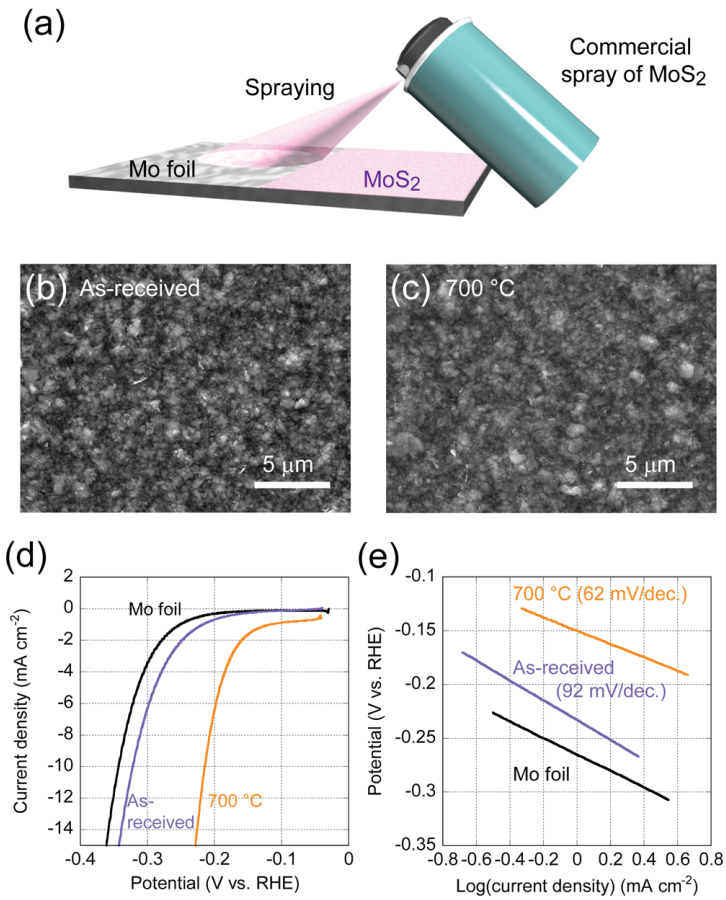

Figure 3.13. (a) Schematic illustration of the preparation process for a film made from a commercially-available spray lubricant containing MoS_2. (b, c) SEM images of the as-received (b) and 700 °C annealed (c) sprayed films. Nanoflakes (~200 nm width) were observed. Polarization curves (d) and Tafel plots (e) for the as-received sprayed nanoflake film, 700 °C annealed sprayed MoS_2 films, and Mo foil (which is the underlying substrate).

application is lubrication. The MoS_2 spray was applied to a Mo foil, as shown in Figure 3.13a, and was found to be composed of nano-sized flakes of MoS_2 with ~200 nm size under SEM (Figs. 3.13b, c). After annealing in forming gas at 700 °C, the overpotential at 10 mA cm^{-2} decreased from 322 mV to 215 mV, a ~100 mV drop (Fig. 3.13d and Table 1). Furthermore, the makeup of the spray helped adhere the film to the Mo foil substrate even for the as-received case (250 °C heated). Thus unlike the previous cases, the relative comparison between as-received and 700 °C annealed is reasonable. The Tafel slopes for the as-received sprayed MoS_2 and the annealed sample are 92 and 62 mV $decade^{-1}$, respectively (Fig. 3.13e). The decrease in the Tafel slope is substantial and brings it close to the value observed for the microflake films above. From all the results presented here, I believe my thermal texturization method could be applied to all MoS_2 materials and could be effective to further improve already high performance synthesized MoS_2 catalysts.

3.3.3. Tafel Slope Analysis

To attempt to understand the HER mechanism for the samples, the Tafel plots were examined. The Tafel plots importance is derived from the Butler-Volmer equation (Eq. 3.1), the classic defining relationship between overpotential (driving force for the reaction) and current density (the rate of reaction).[86]

$$j = j_0 \left[\exp\left(\frac{\alpha_a F}{RT}\eta_s\right) - \exp\left(-\frac{\alpha_c F}{RT}\eta_s\right)\right] \tag{3.1}$$

where j is the current density, j_0 is the exchange current density, α_a and α_c are the apparent transfer coefficients for the anodic and cathodic reaction respectfully, F is Faraday's constant, R is the ideal gas constant, T is temperature, and η_s is the surface overpotential. This equation shows that the net rate of reaction (j) is the difference between the rate of reaction in the anodic direction (the first term in Eq. 3.1) and the rate of reaction in the cathodic direction (the second term in Eq. 3.1). At large overpotentials, one of these terms will dominate and the equation can be simplified to,

$$j = j_0 \exp\left(\frac{\alpha F}{RT}\eta_s\right) \tag{3.2}$$

From this equation, the Tafel equation is derived:

$$\eta = b * \log(j) + a, \tag{3.3}$$

$$b = \frac{2.303RT}{\alpha F} \tag{3.4}$$

$$a = -\frac{2.303RT}{\alpha F}\log(j_0) \tag{3.5}$$

where b is the Tafel slope and a is the Tafel constant. To obtain the experimental Tafel plots, the data was plotted this way and the Tafel slope, b, was extracted. All the measurements for this analysis were carried out with 5 mV sec^{-1} scan rates. The obtained Tafel slopes for the samples are shown in Table 3.1.

The three possible reaction mechanisms for HER in acidic media are known as the Volmer, the Heyrovsky, and the Tafel reactions:[75,89]

Volmer step: $H_3O^+ + e^- \rightarrow H_{ads} + H_2O$

Heyrovsky step: $H_{ads} + H_3O^+ + e^- \rightarrow H_2 + H_2O$

Tafel step: $H_{ads} + H_{ads} \rightarrow H_2$

If the rate determining step in HER is one of the above reactions, the Tafel slope should be close to either ~120 mV $decade^{-1}$, ~40 mV $decade^{-1}$, or ~30 mV $decade^{-1}$ for the Volmer, the Heyrovsky, or the Tafel reaction respectively.[25,86] According to the above considerations, the rate determining step for the as-received bulk MoS_2 is suggested to be the Volmer reaction (Tafel slope ~150 mV $decade^{-1}$) and the annealed bulk MoS_2 samples could possibly be the Heyrovsky reaction (Tafel slope ~60 mV $decade^{-1}$).

The exchange current density (j_0) is also an important parameter which indicates the inherent catalytic activity of the material. The exchange current density was calculated from the

Tafel plot by applying a linear fit to the data and extracting the value at the x-intercept (where $\eta = 0$). The inverse logarithm of this x-intercept is the exchange current density. These values are tabulated in Table 3.1.

Table 3.1. Electrochemical parameters for bulk mineral, microflake, ground microflake and sprayed nanoflake films of MoS_2.

Morphology	Annealing Temp. (°C)	Overpotential (mV) at j = 10 mA cm^{-2}	j_0 (mA cm^{-2})	Tafel slope (mV decade^{-1})
Bulk mineral	250*	–**	0.00093	149
Bulk mineral	700	–**	0.0011	90
Bulk mineral	800	300	0.00069	71
Bulk mineral	900	296	0.0012	76
Microflake	250*	330	0.00012	63
Microflake	700	227	0.0044	67
Microflake	800	210	0.0048	63
Microflake	900	195	0.0045	59
Ground microflake	250*	342	0.00046	73
Ground microflake	700	220	0.0093	70
Ground microflake	800	193	0.011	64
Ground microflake	900	174	0.019	63
Sprayed nanoflake	250*	322	0.0030	92
Sprayed nanoflake	700	215	0.0038	62

* The samples are referred to as as-received or as-ground in the manuscript. Annealing at 250 °C does not damage MoS_2 flakes.

** Not observed in the measurement range.

3.4. Conclusion

In summary, I have demonstrated a simple method to generate or improve the catalytic HER performance of MoS_2 by thermal texturization. The process involves a simple thermal annealing in a hydrogen environment and is applicable to a wide range of MoS_2 morphologies, such as bulk and microflakes. The overpotential required to obtain 10 mA cm^{-2} can be decreased as low as 174 mV for the case of ground microflake film. The method is further applicable to a commercially-available MoS_2 lubricant spray, which shows more than a 100 mV decrease in required overpotential as compared to the as-received MoS_2 spray. This indicates the universality of this method to improve MoS_2 HER performance as well as its potential to be a scalable production method with a cheap material. Moreover, this method relies on removing the atoms from the chalcogen sites to generate edges on MoS_2, and it could be still more widely applicable to other 2D materials, such as WS_2, as a means to activate/improve their catalytic properties.[90,91]

3.5. Acknowledgements

XPS, SEM, XRD, and the final electrochemical characterization work was performed in collaboration with the Joint Center for Artificial Photosynthesis (JCAP), a DOE Energy Innovation Hub, supported through the Office of Science of the U.S. Department of Energy under Award Number DE-SC0004993. Processing and initial electrochemical characterization were performed in the Electronic Materials Program, which is supported by Director, Office of Science, Office of Basic Energy Sciences, Materials Sciences and Engineering Division, of the U.S. Department of Energy under Contract No. DE-AC02-05CH11231. TEM work was performed in collaboration with Mary Scott at the Molecular Foundry, which is supported by the Office of Science, Office of Basic Energy Sciences, of the U.S. Department of Energy under Contract No. DE-AC02-05CH11231.

4. Effects of Temperature and Gas-Liquid Mass Transfer on the Operation of Small Electrochemical Cells for the Quantitative Evaluation of CO_2 Reduction Electrocatalysts[3]

4.1. Introduction

Conversion of atmospheric CO_2 to fuels and value-added chemicals is a potential approach to combat the emission of greenhouse gases and, eventually, allow for a closed-loop global carbon cycle.[92–94] Electrochemical reduction of CO_2 (CO2R) has been proposed as one possible technology for the production of fuels from CO_2 using electricity obtained from renewable sources.[95–98] Studies of CO2R in aqueous solution date back to the 1950s,[99] and an extensive and thorough body of work was published by Hori and co-workers starting in the 1980s.[28,100–104] This work identified the key challenges in implementing electrochemical CO2R for fuel or chemical synthesis. While there are metal catalysts that show high degrees of selectivity to carbon monoxide (e.g. Ag and Au) or formic acid (e.g. Pb, In, and Sn), copper is the only known metal that shows activity to producing more reduced hydrocarbons and alcohols at appreciable current densities (~10 mA cm^{-2}). Recently, there has been a renewal of interest in electrochemical CO2R, with reports of both reductions in overpotentials for 2 electron products such as CO[105] and formate[106] and improved selectivity for higher order products such as ethylene[107] and ethanol.[108] However, there are still no known catalysts which show high selectivity to a CO2R product requiring more than 2 electron transfers. Clearly, improvements in both CO2R catalyst activity and selectivity will be required if there is to be widespread implementation of this technology.[109–112]

In order to drive progress in the CO2R electrocatalysis community, commonly accepted, easily reproducible testing conditions need to be established,[113] similar to those suggested for photoelectrochemical water splitting.[114] Hori and co-workers have already identified many good practices for experimentation in this area[101,104,115,116] and some further insight into polarization losses was provided by Singh *et al*.[117] However, examining the recent literature, one can observe that several different methods of analyzing CO2R electrocatalysts have been used which employ different cell designs and testing conditions.

In particular, the cell designs vary widely (see Table 4.1 for a detailed comparison). In many designs, CO_2[104,108,118–124] or the electrolyte[85] (or both[125,126]) is flowed through the cell; in others, the cell is charged initially and then sealed.[105] Reactor vessels range from classic Pyrex H-cells[101,118,122,124] to compact sandwich compression cells.[119–121,125,126] The electrochemical cells used for the analysis of CO2R catalysts are, in fact, miniature chemical reactors in which known

[3] A modified version of this work was published as P. Lobaccaro, M. Singh, E. L. Clark, Y. Kwan, A. T. Bell, and J. W. Ager, Effects of Temperature and Gas-Liquid Mass Transfer on the Operation of Small Electrochemical Cells for the Quantitative Evaluation of CO_2 Reduction Electrocatalysts. *Phys. Chem. Chem. Phys.* (2016).

Table 4.1 Discussion of CO2R Reaction Cells Used in Literature Reports: The design parameters of CO2R reaction cells used in a number of literature reports are tabulated. Shading is used to indicate designs with electrode surface area to electrolyte volume (*S/V*) ratios of greater than 0.5. In those cells, based on the results of this study, depletion of CO_2 could conceivably be a concern depending on the current and CO_2 sparging method used.

Report	Design	Cathode *S/V* Ratio (cm^{-1})	Comments
Hori *et al.*, 1989.[104]	H-Cell, 3 compartment cell, gas flow	8/60 = 0.133	Used temperature control bath. In 3-compartment design, 2 counter electrodes faced both sides of the working electrode foil so that epoxy was not necessary.
Azuma *et al.*, 1990.[174]	H-Cell, gas flow	Not given	Typical of early work.
Köleli *et al.*, 2003.[268]	Fixed-Bed reactor, gas flow	148-345/100 = 1.48-3.45	Mili-bead catalysts used. Possibly first attempt to do electrochemical CO2R in this type of cell. No bulk electrolyte pH reported.
Li *et al.*, 2005.[126]	Sandwich style, gas & liquid flow	Not Applicable	Early version of flow cell. Gaseous CO_2 flown concurrently with saturated carbonate electrolyte.
Kuhl *et al.*, 2012[121]	Sandwich style, gas flow	4.5/8 = 0.56	High ratio of catalyst area to electrolyte volume enabled detection of C_2^+ products by NMR. No bulk electrolyte pH reported.
Li *et al.*, 2012.[118]	H-Cell, gas flow	2/20 = 0.1	Larger volume cell, similar to Azuma *et al.* Relaxes constraints on bubble size and mass transfer limitations. No bulk electrolyte pH reported.
Lu *et al.*, 2014.[105]	H-Cell, no gas flow	(0.25-1)/80 = 0.003-0.01	Reactor is initially charged with CO_2 and sealed. Nass transfer enhanced with magnetic stirring. No bulk electrolyte pH reported.
Kim *et al.*, 2014.[120]	Sandwich style, gas flow	1.1/33 = 0.033	No bulk electrolyte pH reported.
Manthiram *et al.*,2014.[119]	Sandwich style, gas flow	5.2/5 = 1.04	Single bubble sparger used. No bulk electrolyte pH reported.
Li *et al.*, 2014.[108]	Same as Li *et al.*, 2012.	2/20 = 0.1	
Sen *et al.*, 2014.[122]	H-Cell, gas flow	Not Given	Modest current densities observed. No bulk electrolyte pH reported.
Kas *et al.*, 2015.[123]	Pressure Cell, similar to H-Cell, gas flow	Not reported	No bulk electrolyte pH reported.
Ma *et al.*, 2015.[233]	Sandwich style, gas flow	Not Given	No bulk electrolyte pH reported.
Clark *et al.*, 2015.[85]	Sandwich style, liquid flow	1/0.025 = 40	External saturation of CO_2 is used. No bulk electrolyte pH reported for electrolyte exiting cell.
Kortlever *et al.*, 2015[124]	H-Cell, gas flow	Not reported	No bulk electrolyte pH reported.
This work	Sandwich style, gas flow	1/0.5-1.5 = 2-0.67	In-situ probing of pH and temperature to identify CO_2 depletion issues

reaction conditions must be maintained.[127] This concept has been emphasized in the electrochemical engineering literature,[128–130] with a number of studies focused on gas sparged systems[131–134] similar in design to the cells described above. Notably, the dilute electrolyte conditions and corresponding mass transfer limitations typical of CO2R make the cell design implications even more important.

The compact sandwich compression cells are of particular interest. This design can reduce the electrolyte volume (*V*) compared to the electrode surface area (*S*), allowing liquid products to accumulate in the uncirculated electrolyte to a detectable level more quickly. Notably, the use of this type of high *S/V* (> 0.5 cm^{-1}) cell led to insights into the CO2R mechanism on copper through the detection of five previously unreported trace liquid products.[121] However, when using high *S/V* cells there could be an increased potential for heating to occur in the cell due to the lower thermal mass of electrolyte and for dissolved CO_2 in the electrolyte to be depleted.[86,128] It is known that the cell temperature can change catalyst activity, in part due to the change in CO_2 solubility.[101] Furthermore, maintaining CO_2 saturation in general may be difficult due to the slow dissolution kinetics of CO_2 in water, as has been recently experimentally quantified for a system similar to that used in CO2R.[135] In either case the concern arises that deviations from expected standard testing conditions could occur which would cause the catalytic activity measurement to incorrectly reflect the true catalytic activity of a material.

Here I critically examine the near-equilibrium steady-state operation of high *S/V*, sandwich type, electrochemical cells for CO2R catalyst characterization. I illustrate how changes in the electrolyte temperature and in the dissolved CO_2 concentration can affect the electrolyte composition and electrolyte pH. Importantly, I show that changes in gas-liquid mass transfer within the cell can cause CO_2 depletion in the bulk electrolyte and that this has a pronounced effect on the observed product distribution for Cu electrodes. Finally, I outline the design parameters required to operate high *S/V* electrochemical cells under near equilibrium, steady-state conditions, providing guidance towards standardizing electrochemical CO2R catalyst characterization conditions.

4.2. Experimental

4.2.1. Electrochemical Cell Design

Two compression-sealed electrochemical cells with the same overall architecture were constructed for the study. Both cells have a cathode surface area of 1 cm^2. The primary difference between the cells is the volume of electrolyte in the cathode and anode chambers: 0.5 cm^3 for Cell A (Fig. 4.1a) versus 1.5 cm^3 for Cell B (Fig. 4.1b), yielding *S/V* ratios of 2 cm^{-1} and 0.67 cm^{-1}, respectively. I emphasize that a larger *S/V* ratio should lead to faster liquid product accumulation and thus shorter run times and more sensitive product detection (see below for detailed discussion). Cell A was designed to create the maximum *S/V* ratio possible with a typical 1 cm^2 cathode while still incorporating replaceable CO_2 bubblers and gas tight fittings. Cell B was the highest *S/V*

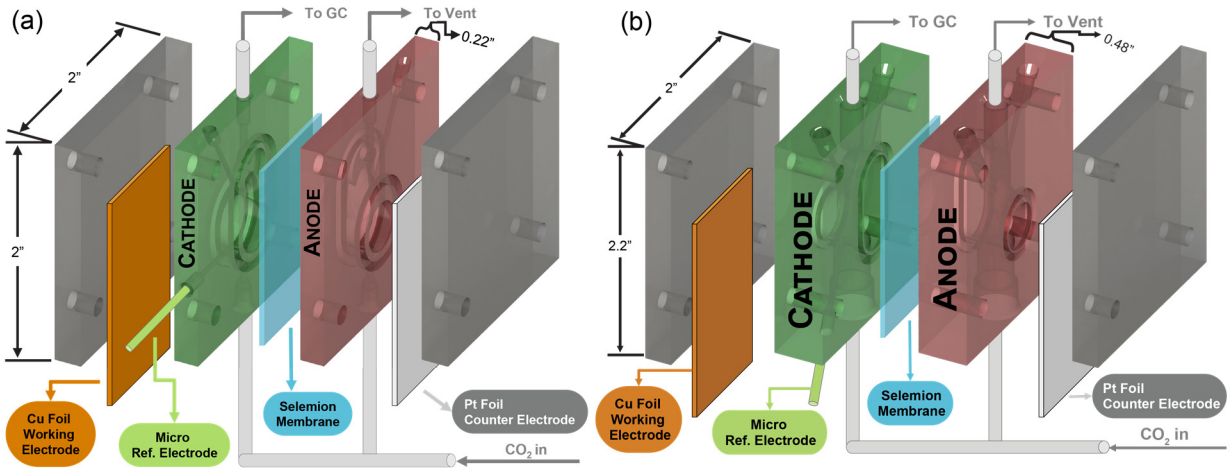

Figure 4.1 CO2R Electrochemical Cell Design: (a) Cell A with the smaller electrolyte volume is pictured (b) Cell B with the larger electrolyte volume is pictured. The cell is made up of two polycarbonate compartments with identical volumes separated by a membrane. Both sides are sparged with CO_2 and the gaseous products produced at the cathode are swept away to be analyzed by GC. The liquid products in the cathode chamber accumulate over the course of the reaction and are analyzed by HPLC

design possible in which a removable glass frit bubbler could be installed to reduce the size of the sparging CO_2 bubbles, an effect I will later show is important.

The cells are composed of an anode and cathode chamber, separated by an anion-conducting membrane, Selemion AMV (AGC Engineering Co.). The two chambers were fabricated from polycarbonate, and all components were designed to be removable for cleaning purposes. It is advantageous to have a cell with replaceable parts since small contamination sources can have a disproportionally large effect on the results of CO2R studies.[115,136] The cell was also designed to maintain parallel plate electrode geometry to ensure a uniform voltage field over the catalyst surface. A 1 mm OD Ag/AgCl reference electrode (Innovative Instruments) was inserted into the cathode chamber to monitor the working electrode potential. This reference electrode was calibrated against an ideal reversible hydrogen electrode. The cell was sealed by compressing the stack of counter electrode, anode chamber, membrane, cathode chamber, and working electrode between two outer plates secured with bolts. The seals were made with Buna-N O-rings (Apple Rubber). During measurements, both sides of the cell were sparged with CO_2 at 1 atmosphere and the gas exiting the cathode compartment was directed to a gas chromatograph (GC) for gaseous product analysis.

4.2.2. Electrochemical Cell Operation

99.9999% base metal pure sodium carbonate (Na_2CO_3) (Sigma-Aldrich) was used as the precursor salt for making the 0.1 M sodium bicarbonate ($NaHCO_3$) electrolyte used in this study. The conversion of carbonate to bicarbonate electrolyte is achieved by sparging the carbonate electrolyte with 1 atmosphere of CO_2. 99.9999% 0.1 mm thick copper (Cu) foil (Alfa-Aesar) was used for the working electrode. The foil was cut into 2x2 cm pieces and degreased by sonication in acetone and iso-propyl alcohol for 60 minutes each. Before use, each foil was electrochemically

polished. ACS grade phosphoric acid (Sigma-Aldrich) was used as the bath (~300 ml) and the bath was stirred with a Teflon stir bar at ~400 rpm. A 99.9999% pure 0.1 mm thick Cu foil was used as the counter electrode. The electrodes were set 20 mm apart and then polished at +2 V vs. the counter electrode for 5 minutes with a biologic VSP-200 potentiostat.

The cell was assembled with a new electropolished Cu foil working electrode, a platinum foil counter electrode, and a piece of Selemion membrane. Before each experiment 0.5 ml or 1.5 ml of electrolyte was injected into each compartment of Cell A and Cell B, respectively, and CO_2 was bubbled through the cell. A Biologic VSP-300 potentiostat with electrochemical impedance package was used throughout the remaining experiments and was first used to measure the electrochemical impedance of the cell in order to enable *in-situ* ohmic resistance correction. 75% compensation was used to correct for the cell resistance (the uncompensated resistance was ~40 ohms for Cell A and ~80 ohms for Cell B). A constant voltage was applied versus the Ag/AgCl reference electrode for 2 hours and the product distribution measured by the GC was converted back into Faradaic efficiencies for each product.

4.2.3. Gaseous Product Detection

The methods for detecting the products of CO2R are well established.[104,137] Here, the CO_2 flow through the cell sweeps away the gaseous products evolving at the cathode. The CO_2 stream exiting the cell was passed through the sampling loop of a GC which can identify the expected gaseous reaction products, namely hydrogen (H_2), carbon monoxide (CO), methane (CH_4), and ethylene (C_2H_4).

The CO_2 flow rate was set with some care. It must be high enough to provide good mixing in the chamber as well as to maintain the saturation of CO_2 in the electrolyte. On the other hand, higher flow rates can dilute the concentration of gaseous products below the quantitative detection range of the analytical equipment. Based on these considerations, the flow rate of CO_2 through both the cathode and anode chambers was set to 5 sccm throughout all experiments. 4.5 LS grade CO_2 (Praxair) was used as the reactant gas. This gas was further purified using a CO_2 gas purifier

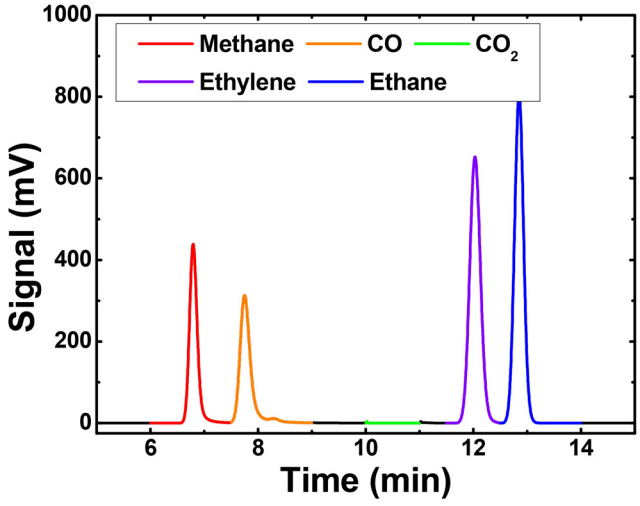

Figure 4.2 GC FID Product Detection: 1000 ppm standards of expected gaseous products of CO_2 were injected together to produce the chromatogram. The area where the CO_2 purge gas would elute is highlighted in green; a bypass valve was used to isolate this gas from the detector. Good separation is achieved between all the 4 major gaseous products

(Vici) to bring the gas purity above 6.0. The gas flow rate into the cell was controlled with an Alicat Scientific mass flow controller which has a control range of 0.5-100 sccm. The gas flow rate out of the cell was monitored with an Alicat Scientific mass flow meter to ensure there were no gas leaks. Gas was continuously sparged through the electrochemical cell at 5 sccm and then through 2 sampling loops of a SRI multigas #3 EPC gas chromatogram.

The GC has two separate channels. Channel 1 contains a 6' Heysep-D and a 6' Molsieve 13x column, a 1 ml sampling loop, and uses He carrier gas. It is equipped with a thermal conductivity detector (TCD) and a flame ionization detector (FID) with a methanizer attachment for the conversion of CO to CH_4. The quantitative detection limits for this channel are 2 ppm for CH_4, CO, and C_2H_4. Channel 2 contains a 6' Heysep-D column, a 2 ml sampling loop, and N_2 carrier gas. It is equipped with a TCD detector and has a quantitative detection limit of 100 ppm for H_2. N_2, He, and H_2 gases supplied to the GC were 5.0 ultra-high purity grade (Praxair) and each passed through its respective gas purifier (Vici) to bring the gas purity up to 6.0. At the chosen flow rate and a cathode area of 1 cm^2, the minimum detectable partial current densities are 1.5 $\mu A/cm^2$ (CO), 5 $\mu A/cm^2$ (CH_4), 8 $\mu A/cm^2$ (C_2H_4), and 70 $\mu A/cm^2$ (H_2). Ethane (C_2H_6) can also be detected with my GC method but was not observed in any experiments performed in this study.

The GC method developed here eluted the relevant gases in ~ 13 minutes (Fig. 4.2). The next step in the cycle was a bake, performed after every injection, to insure all water vapor was removed from the columns before the next injection. The CO_2 gas is not observed due to the use of a bypass valve which was activated to divert the CO_2 to around the FID detector. Gas flowing from the electrochemical cell was sampled every 20 minutes. Actual GC chromatograms are shown in Figure 4.3 for the FID and TCD detectors which show the detection of hydrogen, methane, carbon monoxide, and ethylene for a Cu catalysts CO2R run. I note that the CO_2 flow through the cell could potentially entrain volatile liquid products; however, this can generally be mitigated by hydrating the CO_2 before it enters the cell.

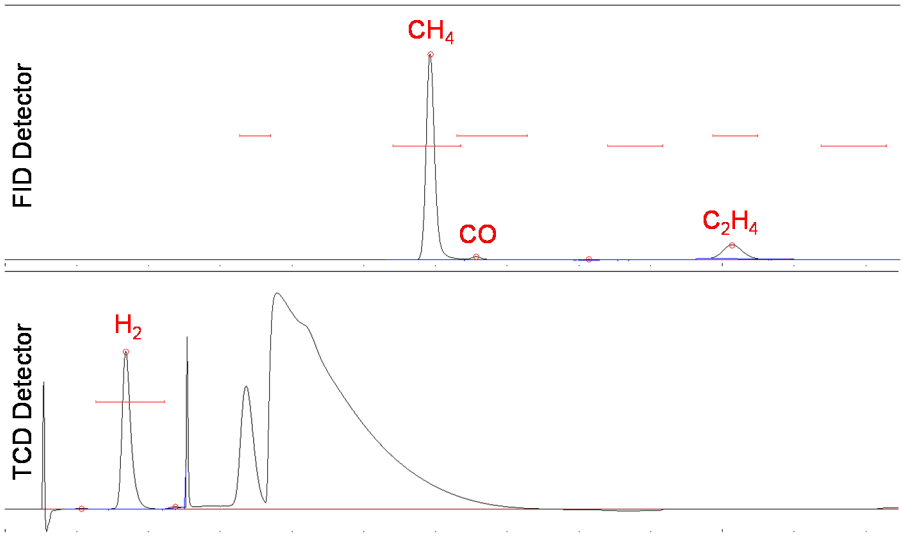

Figure 4.3 FID & TCD GC Chromatograms: The raw data chromatograms produced by the GC are shown for the TCD detector, which is used to detect hydrogen, and the FID detector, which is used to detect methane, carbon monoxide, and ethylene. All of these products were detected for this Cu catalyst run under CO2R conditions.

4.2.4. Liquid Product Detection

Liquid products evolved at the cathode mix with the electrolyte in the cell and must accumulate for a sufficient period of time in order to reach the detection limits of typical analytical tools, such as nuclear magnetic resonance (NMR) or high pressure liquid chromatography (HPLC). Here, liquid products were detected by HPLC (UltiMate 3000, Thermo Scientific) at the end of the run (2 hours) by extracting the electrolyte from both the anode and cathode chamber. Analysis of both chambers is required as negatively charged species evolved at the cathode, such as formate and acetate, can cross the anion conducting membrane and accumulate in the anode chamber.

The column used was an Aminex HPX 87-H (Bio-Rad) with a dilute sulfuric acid (1 mM) eluent. The column was maintained at 60°C in a column oven, and the effluent from the column was passed through a refractive index detector (RID) to identify compounds of interest. Vials with the collected samples were placed in a chilled autosampler holder and 10 µL of sample was injected onto the column. In order to quantitatively identify the constituents in the sample, a standard calibration curve was generated for the expected products of CO2R (e.g. formate, acetate, acetaldehyde, ethanol, propionaldehyde, 1-propanol) as shown in Figure 4.4. As discussed below, for a run with similar electrochemical parameters, the concentration of liquid products in Cell A, with a larger *S/V* ratio, was larger than that produced by Cell B, as expected.

4.2.5. Electrolyte Temperature Measurements

To evaluate cell heating during operation, the cell was assembled exactly as it was for the product analysis experiments, except the cell was not connected to the GC. A 0.5 mm OD stainless steel thermocouple (Omega) was inserted to monitor the electrolyte temperature in each chamber of the electrochemical cell every 5 minutes. The small size of the thermocouple ensured a very small thermal load on the system so as not to influence the temperature in the small amount of electrolyte. The thermocouple was also not left in the solution for more than the 10 seconds required to get an accurate reading. The temperature was recorded at each current density over a 1 hour period to ensure a steady-state temperature was reached.

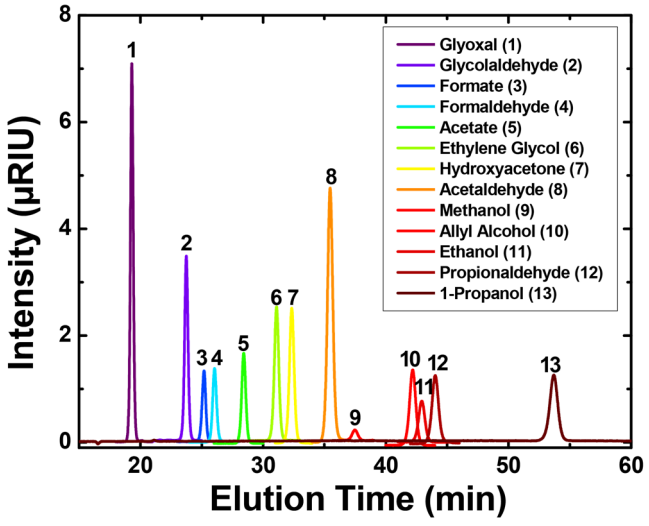

Figure 4.4 HPLC Liquid Product Detection: A chromatograph shows the ability to separate all 13 liquid products of interest for CO2R. 10 mM standards of each compound were injected sequentially and their traces overlaid to produce this plot.

4.2.6. Electrolyte pH Measurements

The cell was assembled exactly as it was for the product analysis experiments, except the cell was not connected to the GC. Two different pH probes were used to acquire *in-situ* measurements in the two cells. A 1 mm OD pH probe (Innovative Instruments) was used to measure the pH in Cell A, the small diameter being required for a cell of that size. A Hannah Instruments pH probe, ~3 mm in diameter, was used to measure the pH in Cell B. Both probes were calibrated with 7.01 and 4.01 buffer standards (Hanna Instruments) before each measurement. The measurement uncertainty of the small probe was larger than that of the larger Hannah probe; this is reflected in the error bars in the figures.

In order to get a pH measurement that accurately reflected the pH of the electrolyte during experimentation, the experiment was precisely halted by stopping the bubbling and potential applied to the cell at the same time. The respective pH probes where then carefully inserted into both chambers of the cell to obtain a reading. The anode chamber, which was being constantly sparged with CO_2 but did not consume CO_2, provided an internal reference point to ensure that the pH probes were taking accurate measurements. The pH of each chamber was measured before and after 1 hour of electrocatalysis over a range of current densities.

4.3. Results and Discussion

4.3.1. Liquid Product Detection Limits as a Function of S/V

The use of high S/V electrochemical cells will facilitate detection of liquid products. As an example, I consider a hypothetical catalyst which has a 5% partial faradaic efficiency for producing ethanol (12 e^-/mol) at 5 mA/cm^2. The amount of time required for ethanol to accumulate to 1 mM (a typical detection limit for HPLC or NMR) in the solution can be related to the *S/V* ratio of the cell as follows:

$$\text{Time [min]} = \frac{C_x\, n_x\, F}{S/_V\; FE_x\, J\; 60{,}000} \tag{4.1}$$

where C_x is the concentration of the target analyte x in mM, n_x is the number of electrons required per reaction to produce compound x, F is Faraday's constant (96485.3 C/mol), *S/V* is the surface area to volume ratio of the electrochemical cell in cm^{-1}, FE_x is the partial faradaic efficiency to produce product x, and J is the current density in mA cm^{-2}. Figure 4.5 graphs the required time to reach the detection limit vs. *S/V*. For this example, a *S/V* ratio of >1 cm^{-1} will be required to detect ethanol within one hour of cell operation.

A control experiment was performed to experimentally verify the improved detection limit for liquid products in the cell with the larger *S/V* ratio, Cell A. Cu foil was used as the cathode and in order to reduce any possible mass transfer effects on this experiment the cells were operated at ~ -0.95V vs. RHE where the current densities are lower, ~ 4.45 mA cm^{-2}. At this potential, only small amounts of liquid products are expected to be generated. Also, to show the speed with which

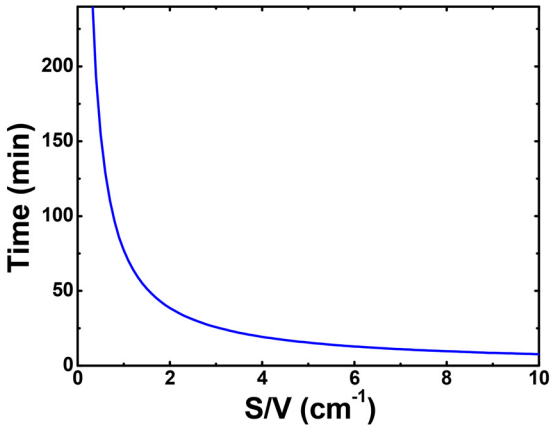

Figure 4.5 S/V Ratio Effect on Detection Speed: Time required to detect ethanol at a detection limit of 1 mM for a hypothetical CO2R catalyst producing ethanol at 5% faradaic efficiency at 5 mA cm^{-2} graphed as a function of the electrode surface to electrolyte volume ratio *S/V*.

Table 4.2: Summary of results of formate detection in the electrolyte of Cell A and Cell B after performing commensurate CO2R experiments. Cu foil was used as the cathode in 0.1M $NaHCO_3$ with CO_2 sparging at 5 sccm at 1 atmosphere

Conditions (units)	*Cell A*	*Cell B*
Applied Voltage (V vs. RHE)	-0.933	-0.963
Current Density (mA/cm^2)	4.59	4.32
Run Time (min)	30	30
Charge Passed (C)	8.35	7.76
$FE_{Formate}$ (%)	2.8	4.3
Peak Area [Formate] (Arb.)	0.094	0.041
Concentration (mM)	1.985	0.869
Concentration/Charge Passed (mM/C)	0.24	0.11

liquid products can be accumulated in these cells, the run time was reduced to only 30 minutes after which time the liquid was extracted from the anode and cathode chambers of each cell. I re-emphasize that the liquid needed to be extracted from both chambers because negatively charged liquid CO2R products, like acetate and formate, can cross over the selemion membrane from the cathode chamber to the anode chamber. The concentrations of liquid products of the two chambers were then added together for the final analysis.

During the experiments, similar amounts of charge were passed and the faradaic efficiencies for formate, the only detected liquid product, were comparable (Table 4.2). As expected, Cell A, which has a higher *S/V* ratio, showed a higher total signal than Cell B and both were comfortably within the detection limit of the HPLC (~ 0.1 mM). The approximate doubling in the concentration of formate detected per charge passed from Cell A to Cell B was expected based off the increase in *S/V* between the two cells.

4.3.2. CO_2/Carbonate Family Thermodynamic Relations

The relevant chemical equilibria for the CO_2, bicarbonate, carbonate family in aqueous solution are:

$$CO_{2(g)} \rightleftharpoons CO_{2(aq)} \tag{4.2}$$

$$CO_{2(aq)} + H_2O \rightleftharpoons H^+ + HCO_3^- \tag{4.3}$$

$$HCO_3^- \rightleftharpoons H^+ + CO_3^{-2} \tag{4.4}$$

$$H_2O \rightleftharpoons H^+ + OH^- \tag{4.5}$$

with corresponding equilibrium constants: K_0 (Henry's law constant), K_1, K_2, and K_w. The term for $CO_{2(aq)}$ includes both dissolved CO_2 and the very small amount of carbonic acid which would be expected under these conditions.[138] Additionally, charge neutrality within the electrolyte must be maintained, shown here for a $NaHCO_3$ solution:

$$[HCO_3^-] + 2[CO_3^{-2}] + [OH^-] = [Na^+] + [H^+] \quad (4.6)$$

The thermodynamics of CO_2 in water[139–142] and salt solutions[143–149] has been widely studied since the 19th century. The value of K_0 depends on the electrolyte and generally decreases with increasing ionic strength, leading to the "salting-out" effect.[149–151] However, at the ionic strength used here, 0.1 M, the CO_2 solubility would be expected to be reduced by less than 5% (see Appendix 4.6 for details).[151] Salt concentration is also known to affect the acid dissociation constants.[146–148] However, again, these changes are predicted to be small for the conditions employed here. Thus, for this study the equilibrium thermodynamic relations for the carbonate system were taken from those recommended for pure water.[142,152]

From Eqs. (4.2)-(4.6), it is clear that if the salt concentration, solution temperature, and CO_2 pressure in the headspace are known, then the solution pH can be calculated. For a 0.1 M $NaHCO_3$ solution at 25°C, this calculation yields that the solution pH should be 6.82 with a dissolved CO_2 concentration of 34.2 mM.[149] I were able to confirm this calculation by measuring a pH of 6.82 ± 0.01 for a 0.1 M $NaHCO_3$ solution which was allowed to equilibrate with 1 atm of CO_2 at 25°C. Experimentally, it is convenient to make a temperature corrected pH measurement, whereas measuring the dissolved CO_2 concentration is not as readily accessible.[138,140,149] Using the thermodynamic relationships established above, pH and temperature can be readily used to calculate the CO_2 concentration in an electrolyte of known concentration, as shown in Figure 4.6 for three temperatures. Interestingly, under the driving conditions of CO_2 bubbling typically used in the experiments, a lower pH of ~6.7 was typically observed. This lower pH is due to a supersaturated concentration of dissolved CO_2 concentration in the electrolyte; this is a frequently observed phenomena.[153,154]

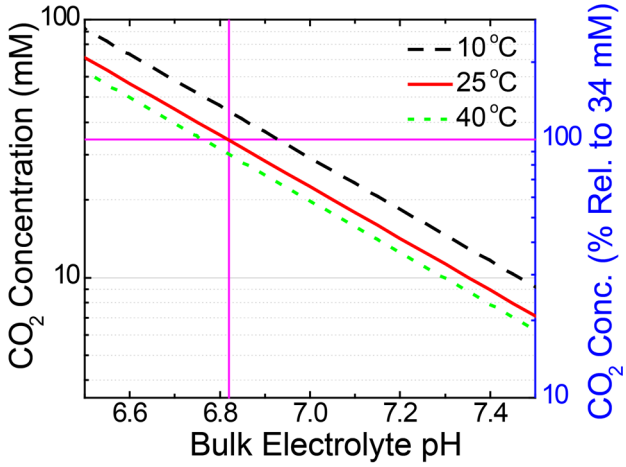

Figure 4.6 CO_2 Concentration vs. pH: By solving Eqs. (4.2)-(4.6), the equilibrium relationship between dissolved CO_2 concentration and pH was obtained for a 0.1 M $NaHCO_3$ electrolyte by varying the gas phase pressure of CO_2. The pink lines indicate the equilibrium CO_2 concentration (34.2 mM) at 25°C and 1 atmosphere of CO_2; the right hand axis is normalized to this value

4.3.3. *Effect of In-Situ Heating*

In-situ heating of the cell is an expected phenomenon due to the overpotentials required to drive the reaction at both the cathode and anode and to the ohmic and polarization losses caused by the finite conductivity of the electrolyte and the transport limitations of the ionic species. As most CO2R catalysts require very large overpotentials (greater than 1V) to drive appreciable CO2R currents,[111] the heating of the cell could be appreciable. As the temperature in the cell rises, the CO_2 solubility in the electrolyte will drop, which could affect the observed kinetics and selectivity of the reaction. Figure 4.7, which was obtained by solving Eqs. (4.2)-(4.6) for a 0.1 M $NaHCO_3$ buffer solution at 1 atm of CO_2, illustrates the effect of temperature on solution pH and dissolved CO_2 concentration. It can be seen that the temperature slightly changes the bulk electrolyte pH and for only a 5°C shift in electrolyte temperature the concentration of dissolved CO_2 changes by more than 10%.

To assess the importance of cell heating, the temperature in Cell A and Cell B was measured as a function of current density from 7.5 to 20 mA cm^{-2} (Fig. 4.8). In both cells the change in electrolyte temperature was small, less than 2°C up to 15 mA cm^{-2}, and less than 4°C for a current densities of 20 mA cm^{-2}. It was initially surprising that Cell B, which has a larger thermal mass due to the larger electrolyte volume, showed a larger temperature change at high current densities. However, I note that the distance between the anode and cathode is larger for Cell B: 25.5 mm vs. 11.5 mm for Cell A. I infer that at higher current densities, the greater distance

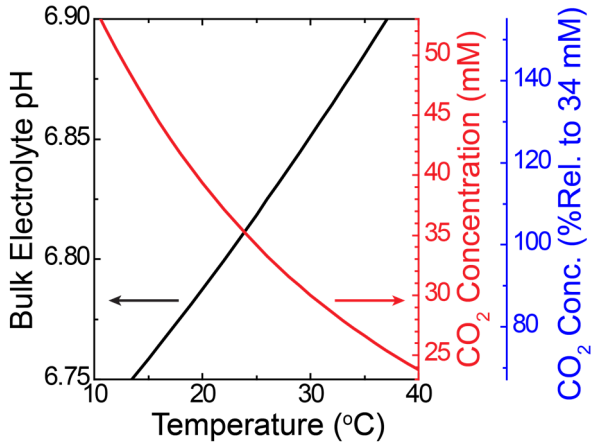

Figure 4.7 Temperature Effect on Electrolyte: By solving Eqs. (4.2)-(4.6), the effect of temperature on the equilibrium pH (black) and equilibrium dissolved CO_2 concentration (red) was obtained for a 0.1 M $NaHCO_3$ electrolyte in equilibrium with 1 atm of CO_2. The far right hand axis (blue) shows the dissolved CO_2 concentration normalized to the value for 25°C (34.2 mM).

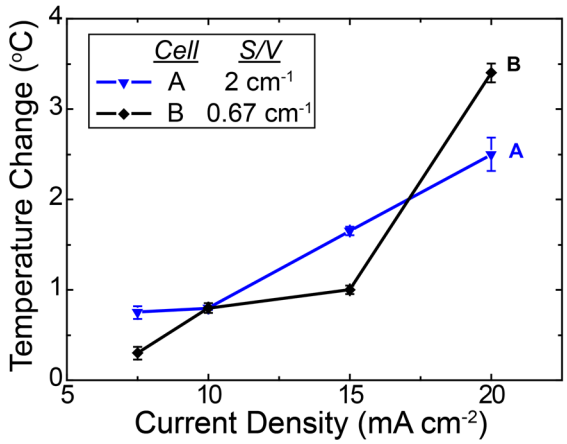

Figure 4.8 In-Situ Electrolyte Heating Experiments: The two electrochemical cells, A and B, with the same electrode surface areas and different electrolyte volumes (giving different *S/V* ratios), were operated under CO2R conditions with a Cu foil cathode in 0.1 M $NaHCO_3$ buffer. The temperature rise in the cell was monitored until a steady-state value was obtained. At current densities up to 15 mA cm^{-2} both cells maintain temperature changes less than 2°C and even at the maximum current density of 20 mA cm^{-2} the temperature change was less than 4°C. From the equilibrium calculations discussed in the text, the dissolved CO_2 concentration will change by less than 10% in both cells.

between the two working electrodes, and the increased resistive heating, leads to the larger temperature rise in this cell.

Hori and co-workers have studied the effects of temperature on the product distribution of CO2R on Cu foil, finding that increasing the electrolyte temperature caused an increase in selectivity towards hydrogen and ethylene and a decrease in selectivity towards methane in 0.5 M $KHCO_3$.[101] However, for the cells evaluated here, the change in electrolyte temperature is not large enough to have a considerable impact on product distribution according to those results. For instance, in Hori's work on Cu foil, a change from 10°C to 20°C changed the methane production by less than 10% faradaic efficiency. Moreover the concerns of temperature increase could be mitigated with improved external temperature controls, like air circulation or a water bath, as has been applied in previous CO2R studies[28,101] and other areas of electrochemical research.[128]

4.3.4. Effect of CO_2 Supply to the Electrochemical Cell

The CO_2 concentration in the electrolyte can be experimentally measured by a measurement of the pH and temperature, as shown in Fig. 4.6. For example, a 0.1 change in pH corresponds to a ~25% change in the dissolved CO_2 concentration. A typical pH probe is capable of measuring with an accuracy of 0.01 pH units. Near the equilibrium pH of 6.83, this results in an uncertainty of only ~2% in the measurement of the dissolved CO_2 concentration using this method.

To assess CO_2 depletion in the electrochemical cells, the electrolyte pH was monitored before and after 1 hour of electrolysis as a function of current density as shown in Figure 4.9. The shading denotes the border between the super-saturated regime (pH < 6.82) and under-saturated regimes, relative to the equilibrium value at 25°C and 1 atm of CO_2. For all the experimental conditions tested in both cells, the electrolyte pH increased from the initial super-saturated value of ~6.7. In Cell A, the electrolyte became under-saturated for current densities greater than 7.5 mA cm^{-2}, with a pH increase as large as 0.35 pH units at 20 mA/cm^2. In contrast, in Cell B the increases in pH were smaller, less than 0.1 pH units, except at the highest current density where the electrolyte became slightly unsaturated.

The pH changes are much larger than any which would be expected due to temperature rise in the cell. Even at the maximum

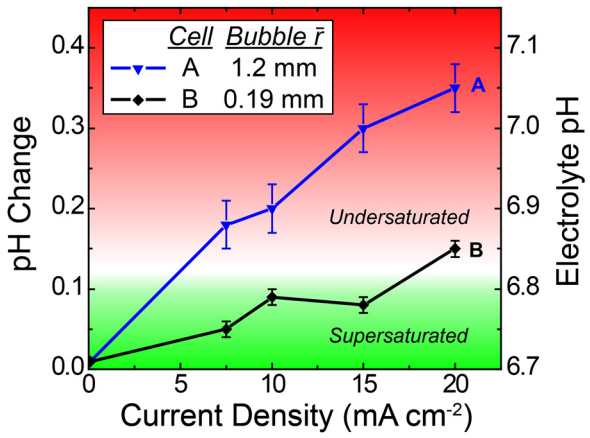

Figure 4.9 In-Situ Dissolved CO2 Depletion Experiments: The two electrochemical cells, A and B, with different size CO_2 sparging bubbles were operated under CO2R conditions with a Cu foil cathode in 0.1 M $NaHCO_3$ buffer. The electrolyte pH change was measured after 1 hour of operation. It was found that the small bubbles (Cell B, $\bar{r}$ = 0.19 mm) enabled the electrolyte to maintain CO_2 saturation up to 15 mA cm^{-2} whereas the larger CO_2 bubbles were unable to do so (Cell A, $\bar{r}$ = 1.2 mm) at any current density.

temperature rise observed above (4°C), the change in pH would be less than 0.03 pH units. Thus, the increase in pH is due to a decrease in CO_2 concentration, which can be quantified as shown in Figure 4.6. For example at 10 mA cm^{-2}, the steady state CO_2 concentration in Cell A was ~63% of the initial value, while in Cell B the CO_2 concentration was higher at ~82% of the initial concentration.

Cells A and B are identical in design except for their *S/V* and bubble introduction method. In Cell A (S/V 2 cm^{-1}) a capillary tube was used to introduce CO_2 into the cell. In Cell B (S/V 0.67 cm^{-1}) a glass P4 frit was used to introduce CO_2 into the cell (see experimental for how bubbler was chosen). It is expected that smaller bubbles will improve gas to liquid CO_2 mass transfer and thus prevent CO_2 depletion. Still frame imaging was used to capture pictures of the bubbles in the cells and statistical analysis was performed to obtain an average spherical bubble size (Figs. 4.10). The capillary bubbler produced 1.2 ± 0.07 mm radius bubbles and the glass frit produced 0.19 ± 0.05 mm radius bubbles. Clearly the smaller bubble size aided in maintaining the concentration of CO_2 in the electrolyte, although it had no effect on the starting point.

The effect of CO_2 depletion in the electrolyte was further explored by examining the product distribution. Experiments were performed at -1.05 V vs. RHE (current density ~10-12 mA/cm^2 for all experiments) and the ratio of methane to hydrogen faradaic efficiency was used as a figure of merit, as shown in Figure 4.10. In Cell B, which had small bubbles produced by the frit and a steady-state CO_2 concentration which was ~80% of the initial concentration, a CH_4/H_2 ratio of 2 was observed. In Cell A, which had a steady state CO_2 concentration only ~60% of the initial value, the CH_4/H_2 was less than 1, which is significantly smaller than in Cell B with the smaller bubbles.

To verify the crucial role of the bubble size, and hence the CO_2 mass transfer, the P4 frit

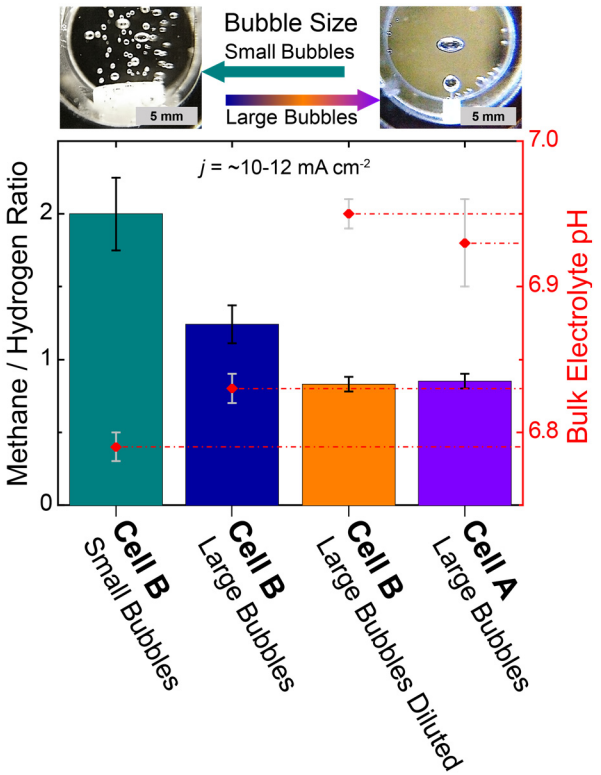

Figure 4.10 The Effect of CO2 Depletion on CO2R Product Distribution: CO2R experiments were performed in 0.1M $NaHCO_3$ with Cu foil held at -1.05 V vs. RHE with various CO_2 feed conditions. The methane to hydrogen Faradaic efficiency ratio is reported as well as the bulk electrolyte pH observed after 1 hour of operation. (B: Small Bubbles) Cell B with a P4 frit bubbler, (B: Large Bubbles) Cell B with a capillary tube bubbler, (B: Large Bubbles Diluted) Cell B with a capillary tube bubbler, bubbled with 75% CO_2 25% Ar, (A: Large Bubbles) Cell A with a capillary tube bubbler. Methane is the dominant and expected product from Cu foil at this potential; however, if the CO_2 concentration decreases due to poor gas liquid mass transfer, hydrogen becomes the dominant product. The observed current was ~10-12 mA cm^{-2} for all conditions tested.

bubbler in Cell B was replaced with a capillary tube bubbler, which produces larger bubbles. Under the same Cu CO2R conditions, a shift in bulk electrolyte pH from 6.79 to 6.83 was observed, corresponding to a further 10% decrease in CO_2 concentration. Additionally, the methane to hydrogen ratio decreased (Fig. 4.10, Cell B: Large Bubbles). While I would expect larger bubbles to lead to an increase in pH in both cells, it is not expected for this change to be exactly the same because of differences in the hydrodynamics in the two cells. Thus it was observed that the large bubbles lead to a smaller degree of CO_2 depletion in Cell B than was observed in Cell A. To further increase the CO_2 depletion in Cell B, the CO_2 flow was diluted to 75% by volume with argon gas. Under this reaction condition the same (low) methane to hydrogen ratio was produced as seen in Cell A (Fig. 4.10, Cell B: Large Bubbles Diluted). Moreover, the pH shift in Cell B observed under this bubbling condition was almost identical to the pH shift seen in Cell A, indicating that similar degrees of CO_2 depletion were produced. Based on these experiments, I conclude that the CO_2 depletion in the electrolyte causes the decrease in the methane to hydrogen ratio. Consistent with this conclusion, previous studies with copper electrodes have shown that reducing the CO_2 concentration by decreasing its partial pressure causes the methane to hydrogen ratio to decrease.[155]

It is expected that as the CO_2 concentration in the bulk electrolyte decreases, the corresponding concentration of CO_2 at the surface of the catalyst decreases.[123,156,157] I evaluated this effect by adapting the simple 1D diffusion model of Gupta *et al.*[158] to calculate the surface concentration of CO_2 and the pH (see Appendix 4.6.2 for details). The boundary layer thickness was assumed to be 100 μm here. The model predicts a ~20% lower CO_2 concentration at the surface of the Cu catalyst in Cell A compared to Cell B and also a slight decrease in pH (Fig. 4.11 and Tables 4.3 and 4.4). The decrease in CO_2 concentration at the electrode would favor hydrogen evolution over CO_2 reduction, which is what is experimentally observed. I note that this change in product distribution could have been incorrectly attributed to catalyst deactivation, a common concern with CO2R catalysts,[115] instead of being the result of inadequate gas-liquid mass-transfer

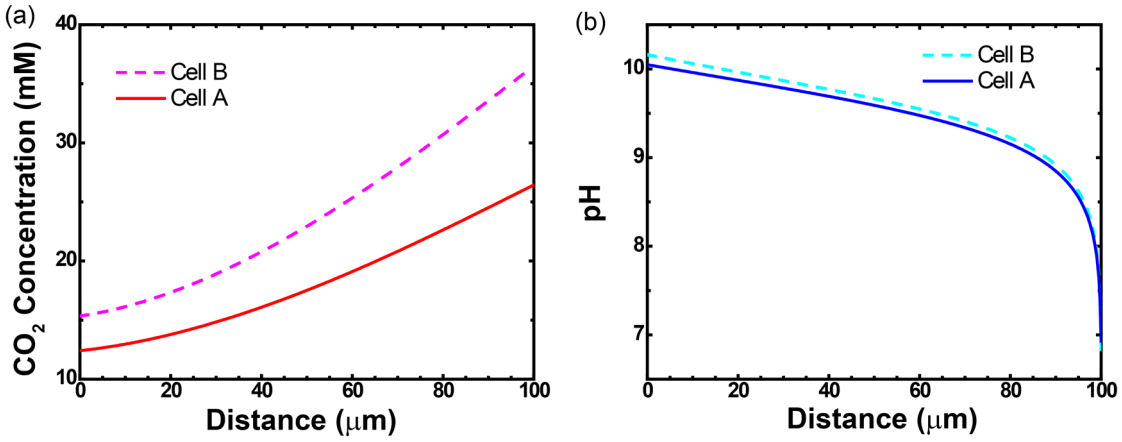

Figure 4.11 Boundary Layer Depletion: The concentration profile of CO_2 (a) and pH profile (b) in the boundary layer are shown for the two extreme cases of Cell A and Cell B. The inadequate gas-liquid transfer in Cell A leads to a lower surface concentration of CO_2 and a slightly lower surface pH.

in the cell. Additional details, including faradaic efficiency data for all observed products, in appendix 4.6.3.

Table 4.3: Tabulated bulk and surface conditions obtained by 1D modeling for the CO2R experiment in Cell A at ~ -1.05 V vs. RHE on Cu foil in 0.1M $NaHCO_3$.

Component	Bulk Condition	Surface Condition
CO_2	26.44 mM	12.41 mM
HCO_3^{-1}	99.92 mM	82.51 mM
CO_3^{-2}	0.04 mM	43.09 mM
OH^-	8.98 x10^{-5} mM	0.12 mM
pH	6.93	10.05

Table 4.4: Tabulated bulk and surface conditions obtained by 1D modeling for the CO2R experiment in Cell B at ~ -1.05 V vs. RHE on Cu foil in 0.1M $NaHCO_3$.

Component	Bulk Conditions	Surface Conditions
CO_2	36.51 mM	15.34 mM
HCO_3^{-1}	99.94 mM	81.99 mM
CO_3^{-2}	0.03 mM	55.46 mM
OH^-	6.44x10^{-5} mM	0.15 mM
pH	6.79	10.16

4.3.5. Implications of Mass Transfer for CO2R reactor design

Gas-liquid mass transfer and its effect on the properties of electrochemical cells have been widely studied.[131,134] The extensive literature on gas-liquid mass transfer for bubble column reactors[159–168] can be used to develop insights into how CO_2 mass transfer from the electrolyte to the cathode can be improved in high *S/V* cells.

The steady state mass balance for CO_2 dissolution into the electrolyte and its consumption at the cathode is given by:

$$N_{CO_2} S_c V^{-1} = K_L a\,(c^* - c^b), \tag{4.7}$$

where N_{CO_2} is the flux of CO_2 consumed at the electrode surface, S_c is the surface area of the catalyst, V is the electrolyte volume, K_L is the liquid mass transfer coefficient in the two-phase system, a is the interfacial surface area of the bubbles per volume of liquid, c^* is the solubility limit of carbon dioxide in water, and c^b is the concentration of carbon dioxide in the electrolyte. As demonstrated by the experiments presented above, it is desirable to keep c^b as close to c^* as

possible. Thus, for a given total consumption rate of CO_2 (the product of N_{CO2} and S_c), large values of K_La are required.

Since it is difficult to decouple K_L and a, they are frequently treated as a single variable.[160,164–167] K_La has been shown to be a function of the gas and liquid composition used, the characteristic size of the reactor, and the gaseous volume fraction (also known as the gas hold up).[160,164,165,167] The gaseous volume fraction is directly related to the superficial velocity of the gas.[160,162,169] Of the above mentioned parameters, the superficial gas velocity has the strongest effect on K_La.[162,164,169] Thus for the following discussion, ways to modulate the superficial velocity will be the focus. To maintain a 0.1 mM decrease of c^b from c^*, a K_La of greater than ~10^{-2} sec^{-1} is necessary in my cell, for typical CO_2 surface fluxes. This should be accessible within a reasonable range of superficial gas velocities, based on previous measurements for bubble column reactors.[169]

The superficial velocity is defined as

$$U_s = Q/A_x, \tag{4.8}$$

where U_s is the superficial velocity, Q is the volumetric gaseous flow rate, and A_x is the cross sectional area for gas flow. Thus U_s can be increased by increasing Q or decreasing A_x. From an experimental perspective, Q is the easiest variable to control; however, the value of Q must be kept below a level at which entrainment of electrolyte will occur, resulting in electrolyte loss from the cell. While A_x can be designed to be smaller, for a fixed value of S/V, a decrease in A_x requires an increase in the height of the electrolyte column. Increasing the cell height might be expected to lead to bubble coalescence and a corresponding decrease in K_La;[170] however, this effect is unlikely to be significant due to the short height of typical electrochemical cells.

It is also possible to increase the gas hold up by decreasing the bubble size, the effect that was exploited here. The gas hold up increases with decreasing bubble size for a given superficial velocity, because smaller bubbles rise more slowly than larger bubbles.[170,171] The lower rise time of smaller bubbles reduces the value of K_L; however, the larger increase in a overcomes this effect, leading to an overall increase in K_La for small bubbles.[170] Changing the bubble size in the cell can be accomplished by changing the gas inlet into the cell, but precise control over the bubble size requires further investigation, as it depends on the flow rate of gas, interfacial surface tension, and hydrophobicity of the gas inlet material.[160] Here, the optimal engineering solutions available to us were implemented to create a high S/V cell with a small bubble size. However, further increases in S/V would be possible if smaller frit bubblers or some other small bubble sparging device could be implemented.

As the rate of CO_2 consumption at the cathode increases, the magnitude of K_La needed to maintain electrolyte saturation increases. For example, an electrode would consume ~10 nMol of CO_2 cm^{-2} sec^{-1} if it produces 100% CO operating at 2 mA/cm^2 or 100% CH_4 operating at 8 mA/cm^2. Thus it is clear that if a CO_2R experiment is conducted at high current density, the conditions for mass transfer and thus K_La are more stringent. An alternative way to conduct these

experiments is in a liquid flow cell where the liquid is saturated with CO_2 externally and the pH of the effluent from the cell is actively monitored to ensure CO_2 saturation conditions are maintained. The disadvantage of using electrolyte recirculation is that it would most likely require a larger volume of electrolyte, thereby lengthening the time required to accumulate a sufficient concentration of liquid-phase products to be detectable. This issue has been considered recently in more detail by Clark *et al.*[85]

4.4. Conclusion

Electrochemical CO_2 reduction on Cu foil, performed in two small cells with similar design, illustrates the importance of maintaining cell electrolyte temperature and dissolved CO_2 saturation in order to perform rigorous CO2R catalyst characterization. While in this study, heating was not found to be a major concern at typically employed current densities, it is nevertheless recommended to measure electrolyte temperature in all cell designs.

In contrast, depletion of CO_2 in the bulk was found to be a larger effect, particularly in the cell with small electrolyte volume and thus a high *S/V* ratio (Cell A). In the larger cell (Cell B), CO_2 depletion was mitigated by using a glass frit bubbler which produces small bubbles, less than 0.2 mm in radius. The improved mass transfer of these smaller bubbles maintained the CO_2 concentration at a steady-state near equilibrium condition throughout the reduction experiments, as monitored by pH. In contrast, use of a capillary tube in the same cell, producing larger bubbles, caused depletion of CO_2. Most importantly, the CO_2 depletion caused large changes in the relative Faradaic efficiencies of CO2R experiments on Cu foil: a decrease from 65% to 45% FE to CH_4 and an increase of 33% to 54% FE for H_2. I note that these changes could have been incorrectly interpreted as a decrease in catalyst selectivity or as catalysts deactivation. Thus I recommend that pH be actively monitored to ensure near-equilibrium conditions are maintained over the course of the reaction, particularly in small volume cells. I note that it would be interesting to explore the effects of CO_2 pressure on mass transfer in a future study as my present cell design does not allow these types of studies.

Guidance from existing gas-liquid mas transfer models is used to understand how to meet the mass transfer requirements of the CO2R reaction. Finally, I provide the design parameters for a small volume, high *S/V* ratio, electrochemical cell for CO_2 reduction over Cu that can be operated at current densities of up to 15 mA/cm^2 with a minimal temperature change of 2°C while maintaining the electrolyte at near equilibrium saturation.

4.5. Acknowledgments

Initial fabrication and cell design testing were supported by the California Energy Commission under agreement 500-11-023. Detailed CO2R testing and modelling of the electrochemical cell were performed within the Joint Center for Artificial Photosynthesis, a DOE

Energy Innovation Hub, supported through the Office of Science of the U.S. Department of Energy under Award Number DE-SC0004993. I thank Eric Granlund, the manager of the Berkeley College of Chemistry Machine Shop, for his expertise in machining and cell fabrication and Yanwei Lum for helpful discussions. I thank Adams and Chittenden Scientific Glass for their assistance in designing the frit unit.

4.6. Appendix

4.6.1. Equilibrium Equations for CO_2/Carbonate/Bicarbonate Family

For this detailed discussion of the CO_2/carbonate/bicarbonate equilibria, Eqs. (4.2)-(4.5) of the main text, are reproduced here as (A4.1)-(A4.4).

$$CO_{2(g)} \rightleftharpoons CO_{2(aq)} \tag{A4.1}$$

$$CO_{2(aq)} + H_2O \rightleftharpoons H^+ + HCO_3^- \tag{A4.2}$$

$$HCO_3^- \rightleftharpoons H^+ + CO_3^{-2} \tag{A4.3}$$

$$H_2O \rightleftharpoons H^+ + OH^- \tag{A4.4}$$

Equilibrium constants for reactions (A4.1)-(A4.4) are as follows:

$$K_0 = \frac{[CO_{2(aq)}]}{[CO_{2(g)}]} = \frac{[CO_{2(aq)}]}{[f_{CO_2}]} \tag{A4.5}$$

$$K_1 = \frac{[H^+][HCO_3^-]}{[CO_{2(aq)}]} \tag{A4.6}$$

$$K_2 = \frac{[H^+][CO_3^{-2}]}{[HCO_3^-]} \tag{A4.7}$$

$$K_w = [H^+][OH^-] \tag{A4.8}$$

K_0, the Henry's Law coefficient, and the equilibrium constants K_1, K_2, and K_w all depend on temperature and, to some extent, on the composition of the electrolyte. The solubility of a gas in a salt solution (C_G) relative to that in pure water ($C_{G,0}$) is expressed by the Sechenov equation:[150,151,172]

$$\log\left(\frac{C_{G,0}}{C_G}\right) = K_s\, C_s\,, \tag{A4.9}$$

where K_s is the Sechenov constant and C_s is the concentration of the salt solution. Using data from 22 gases with 24 cations and 26 anions, Weisenberger and Schumpe found that the Sechenov constant could be fit with the following equation:[151]

$$K_s = \Sigma(h_i + h_G) \tag{A4.10}$$

where h_i is an ion dependent model fitting parameter and h_G is the gas dependent model fitting parameter. h_G is further dependent on temperature:

$$h_G = h_{G,0} + h_T(T - 298.15\ \text{K}) \tag{A4.11}$$

where T is the temperature of the solution of interest in Kelvin, h_T is the temperature dependent model fitting parameter, and $h_{G,0}$ is the fitting parameter for the reference state at 298.15 K. There is extensive literature on the solubility of gases (O_2, CO_2, N_2O, etc.) in aqueous salt solutions and

this general approach has been shown to effectively replicate experimental data for a wide range of gases and salt solutions. Although a direct measurement of the CO_2 solubility in bicarbonate buffer could not be found, the Schumpe parameters for Na^+ and HCO_3^- can be used to estimate the "salting out" effect expected here for 0.1 M solution at 25°C. A sample calculation is shown below (Table A4.1, A4.2, Eq A4.12, A4.13)

Table A4.1: Ion Dependent Schumpe Model Parameters

Ion	h_i [M]
Na^+	0.1143
HCO_3^-	0.0967

Table A4.2: Gas Dependent Schumpe Model Parameters

Gas	$h_{G,0}$ [M]	h_T [M k^{-1}]
CO_2	-1.72E-02	-3.38E-04

$$h_G = -0.0172 - 3.38 * 10^{-4} * (298 - 298.15) = -0.01715 \quad \text{(A4.12)}$$

$$\begin{aligned} \log\left(\frac{C_{G,0}}{C_G}\right) &= 0.1 * (0.1143 - 0.01715) \qquad [Na^+] \\ &+ 0.1 * (0.0967 - 0.01715) \qquad [HCO_3^-] \\ &= 0.1767 \end{aligned} \quad \text{(A4.13)}$$

At 25°C C_G is 96.5% of $C_{G,0}$ and over the entire temperature range of 10°C to 40°C C_G is 96.3% to 96.7% of $G_{G,0}$.

It is furthermore known that K_1 and K_2 depend on the salt concentration in aqueous solution from marine chemistry.[147] The following equations, derived from field measurements, describe the changes found for the range of salinity S (5-40, in parts per thousand by mass) and temperature (0-40°C) found in sea water:

$$\log(K_1) = -\frac{3633.86}{T} + 60.88998 - 9.6777 * \ln(T) + 0.011555 * S - 0.0001152 * S^2 \quad \text{(A4.14)}$$

$$\log(K_2) = -\frac{471.78}{T} - 26.94623 + 3.16937 * \ln(T) + 0.01781 * S - 0.0001122 * S^2 \quad \text{(A4.15)}$$

where T is the temperature in Kelvin. It should be noted that these equations do not apply to arbitrary salt solutions, as do the Schumpe relationships for Henry's constant. Nevertheless, it is possible to estimate the effect of salt concentration on K_1 and K_2 using this empirical data. A comparison was made between the values given by Eq. A4.14-A4.15 when the salinity of the solution (being the weight of the sodium ions in solution) was used as compared to when the salinity was set to zero. It was found that for K_1 and K_2 the difference was less than 10%.

The results of this analysis led us to use data for pure water for K_0, K_1, K_2, and K_w The Henry's constant (Mol L^{-1}) and equilibrium constants K_1 (Mol L^{-1}) and K_2 (Mol L^{-1}) were taken from the comprehensive review of Plummer *et al.*[152]

$$\log(K_0) = 108.3865 + 0.01985076 * T - \frac{6919.53}{T} - 40.4515 * \log(T) + \frac{669365}{T^2} \quad \text{(A4.16)}$$

$$\log(K_1) = -356.3094 - 0.06091964 * T + \frac{21834.37}{T} + 126.8339 * \log(T) - \frac{1684915}{T^2} \quad \text{(A4.17)}$$

$$\log(K_2) = -107.8871 - 0.03252849 * T + \frac{5151.79}{T} + 38.9256 * \log(T) - \frac{563713.9}{T^2} \quad \text{(A4.18)}$$

The water dissociation constant (K_w) was taken from Bandura *et al.*[142]

$$\log(K_w) = 12 * \left(\log(1+Z) - \frac{Z}{Z+1} * D_{H_2O} * \left(0.642044 - \frac{56.8534}{T} - 0.375754 * D_{H_2O} \right) \right) \quad \text{(A4.19)}$$
$$+ pK_w^G + 2 * \text{Log}\left(\frac{M_w}{1000}\right)$$

$$Z = D_{H_2O} * \exp\left(-0.864671 + \frac{8659.19}{T} - \frac{22786.2}{T^2} * \left(D_{H_2O}\right)^{\frac{2}{3}} \right) \quad \text{(A4.20)}$$

$$pK_w^G = 0.61425 + \frac{48251.33}{T} - \frac{67707.93}{T^2} + \frac{10102100}{T^3} \quad \text{(A4.21)}$$

T is in the units of Kelvin throughout Eq. A4.16-A4.21. Furthermore, for the water dissociation constant, which is dependent on the density of water (D_{H_2O}), a constant density of 1 g/cm^3 was used. Figure A4.1 shows the results of solving equations A4.5-A4.8 and A4.16-A4.21 as a function of temperature for a 0.1 M $NaHCO_3$ buffer solution in equilibrium with 1 atm of CO_2. As discussed in the main text, using the pure water formulas here, the pH of 0.1M $NaHCO_3$ in equilibrium with 1 atm of CO_2 was found to be 6.82. This was then experimentally confirmed, supporting the decision to use the pure water thermodynamic equations.

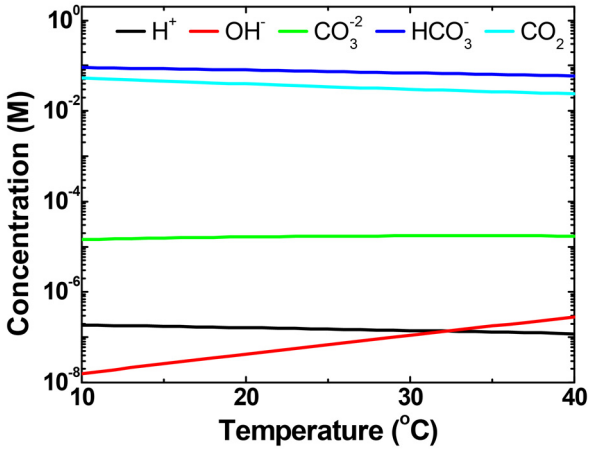

Figure A4.1 Equilibrium Electrolyte Species Conc. Vs. Temp: By solving Eqs. A5-A8, the equilibrium concentrations of the ionic species and the dissolved CO_2 was obtained for a 0.1 M $NaCO_3$ buffer solution in equilibrium with 1 atm of CO_2.

4.6.2. Modeling of Electrode Boundary Layer

The effect of changes in the bulk CO_2 concentration on the concentration of CO_2 and the pH at the surface of the electrode was modeled by solving the reaction-diffusion equations for CO_2, HCO_3^-, CO_3^{-2}, and OH^- in the boundary layer (H^+ and OH^- were assumed in equilibrium). Although more sophisticated models have been developed,[117] I used the simple 1D model developed by Gupta *et al.*[158] as it captures the essential phenomena and has been used recently in the literature for similar analyses.[123] The equilibrium constants for reactions (A4.1)-(A4.4) used were the same as those discussed above and the forward and reverse reaction rate constants for (A4.2) and (A4.3), as well as the diffusion coefficients for CO_2, HCO_3^-, CO_3^{-2}, and OH^- were taken from the recent modeling study of Singh *et al*.[117] It was assumed that electro-neutrality applies and a boundary layer thickness of 100 μm was also assumed. The experimentally measured pH was used to calculate the concentrations of CO_2, HCO_3^-, and CO_3^{-2} in the bulk electrolyte, which was used as the boundary condition at the border between the bulk electrolyte and the boundary layer. The two extreme cases were modelled; Cell A with a bulk pH of 6.92, the value being elevated as compared to the initial saturated value of 6.7 due to inadequate gas-liquid mass transfer, and Cell B with a bulk pH of 6.78. The experimentally measured current density and product distribution were applied as the boundary conditions at the electrode surface (see Fig 4.11). The results of this calculation are shown in Figure 4.11 and Table 4.3 and 4.4. While there is only a small decrease in pH for Cell A compared to Cell B, the effect on the predicted surface concentration of CO_2 is substantial, with a 20% lower concentration for Cell A. I note that an even lower concentration would have been predicted if CO_2 reduction current density were higher; clearly, the reduction in bulk pH translates into reductions in the surface CO_2 concentration, which in turn affects the product distribution. Further details on solving this numerical problem will now be given along with the full Matlab code used to solve the problem.

When solving this problem, only the layer of solution near the electrode surface is considered and the problem is simplified to one dimension. It is only in this layer of electrolyte near the electrode surface that concentration gradients develop. The left boundary condition is the condition at the electrode surface and the right boundary condition is the bulk electrolyte. The distance between the surface and bulk electrolyte is called the boundary layer thickness (δ). The boundary conditions at the electrode surface are the flux conditions due to the consumption or production of molecular species based off the reactions taking place there. The bulk electrolyte is assumed to be well mixed and thus the boundary condition there is that the concentrations of the molecular species of interest are constant.

The four variables of interest in solving this problem are CO_2, HCO_3^-, CO_3^{-2}, and OH^-. It is assumed that electro-neutrality applies in this region and that water is in equilibrium with OH^- and H^+. For the purpose of this simple calculation, only the diffusional driving forces and not the electrostatic driving forces are considered on the charged molecules. This results in four mass balance equations.

$$\frac{\partial CO_2}{\partial t} = \mathcal{D}_{CO_2}\frac{\partial^2 CO_2}{\partial x^2} - k_{1R}CO_2OH^- + k_{1F}HCO_3^- \quad \text{(A4.22)}$$

$$\frac{\partial HCO_3^-}{\partial t} = \mathcal{D}_{HCO_3^-}\frac{\partial^2 HCO_3^-}{\partial x^2} + k_{1R}CO_2OH^- - k_{1F}HCO_3^- - k_{2R}HCO_3^-OH^- + k_{2F}CO_3^{-2} \quad \text{(A4.23)}$$

$$\frac{\partial CO_3^{-2}}{\partial t} = \mathcal{D}_{CO_3^{-2}}\frac{\partial^2 CO_3^{-2}}{\partial x^2} + k_{2R}HCO_3^-OH^- - k_{2F}CO_3^{-2} \quad \text{(A4.24)}$$

$$\frac{\partial OH^-}{\partial t} = \mathcal{D}_{OH^-}\frac{\partial^2 OH^-}{\partial x^2} - k_{1R}CO_2OH^- + k_{1F}HCO_3^- - k_{2R}HCO_3^-OH^- + k_{2F}CO_3^{-2} \quad \text{(A4.25)}$$

With these differential equations 8 boundary conditions are also required. The boundary conditions at $x = \delta$ is that the concentrations of all the species are equal to the bulk electrolyte concentrations as calculated by the thermodynamic relationships described in section 4.6.1. The boundary at $x = 0$ (the electrode surface) are,

$$\mathcal{D}_{CO_2}\frac{\partial^2 CO_2}{\partial x^2} = J_{CO_2} \qquad \mathcal{D}_{HCO_3^-}\frac{\partial^2 HCO_3^-}{\partial x^2} = 0 \quad \text{(A4.26, A4.27)}$$

$$\mathcal{D}_{CO_3^{-2}}\frac{\partial^2 CO_3^{-2}}{\partial x^2} = 0 \qquad \mathcal{D}_{OH^-}\frac{\partial^2 OH^-}{\partial x^2} = J_{OH^-} \quad \text{(A4.28, A4.29)}$$

$$J_{CO_2} = \left(\frac{j}{F}\right)\left(\sum_i \frac{\text{mol of } CO_2 \text{ consumed per rxn}_i}{\#\text{ of } e^- \text{ per rxn}_i} * FE_i\right) \quad \text{(A4.30)}$$

$$J_{OH^-} = \left(\frac{j}{F}\right)\left(\sum_i \frac{\text{mol of } OH^- \text{ produced per rxn}_i}{\#\text{ of } e^- \text{ per rxn}_i} * FE_i\right) \quad \text{(A4.31)}$$

Because the goal of this calculation is to solve for the steady state concentration gradients of these species, the time dependencies of equations A4.22 - A4.25 can be removed. The resulting second order ordinary differential equations can be converted into a set of first order differential equations in order to solve for the steady state solution. For this conversion, CO_2 is set equal to y_1 and $\partial CO_2/\partial x$ is set equal to y_2. An example is worked below for CO_2 and then the remaining equations are simply listed

$$CO_2 = y_1 \qquad \frac{\partial CO_2}{\partial x} = y_2 \qquad \frac{\partial^2 CO_2}{\partial x^2} = \frac{\partial y_2}{\partial x}$$

$$HCO_3^- = y_3 \qquad \frac{\partial HCO_3^-}{\partial x} = y_4 \qquad \frac{\partial^2 HCO_3^-}{\partial x^2} = \frac{\partial y_4}{\partial x}$$

$$CO_3^{-2} = y_5 \qquad \frac{\partial CO_3^{-2}}{\partial x} = y_6 \qquad \frac{\partial^2 CO_3^{-2}}{\partial x^2} = \frac{\partial y_6}{\partial x}$$

$$OH^- = y_7 \qquad \frac{\partial OH^-}{\partial x} = y_8 \qquad \frac{\partial^2 OH^-}{\partial x^2} = \frac{\partial y_8}{\partial x}$$

$$0 = \mathcal{D}_{CO_2}\frac{\partial^2 CO_2}{\partial x^2} - k_{1R}CO_2OH^- + k_{1F}HCO_3^- \quad \text{(A4.32)}$$

$$0 = \mathcal{D}_{CO_2}\frac{\partial y_2}{\partial x} - k_{1R}y_1y_7 + k_{1F}y_3 \quad \text{(A4.33)}$$

$$\frac{\partial y_2}{\partial x} = -\left(\frac{1}{\mathcal{D}_{CO_2}}\right)(k_{1F}y_3 - k_{1R}y_1y_7) \tag{A4.34}$$

Note that because there is no first derivative with respect to CO_2 in this differential equation (A4.32), the expression for y_1 is simply,

$$\frac{\partial y_1}{\partial x} = y_2 \tag{A4.35}$$

The remaining equations A4.23 - A4.25 can be separated in a similar manner as A4.32

$$\frac{\partial y_3}{\partial x} = y_4 \tag{A4.36}$$

$$\frac{\partial y_4}{\partial x} = -\left(\frac{1}{\mathcal{D}_{HCO_3^-}}\right)(k_{1R}y_1y_7 - k_{1F}y_3 - k_{2R}y_3y_7 + k_{2F}y_5) \tag{A4.37}$$

$$\frac{\partial y_5}{\partial x} = y_6 \tag{A4.38}$$

$$\frac{\partial y_6}{\partial x} = -\left(\frac{1}{\mathcal{D}_{CO_3^{-2}}}\right)(k_{2R}y_3y_7 - k_{2F}y_5) \tag{A4.39}$$

$$\frac{\partial y_7}{\partial x} = y_8 \tag{A4.40}$$

$$\frac{\partial y_8}{\partial x} = -\left(\frac{1}{\mathcal{D}_{OH^-}}\right)(-k_{1R}y_1y_7 + k_{1F}y_3 - k_{2R}y_3y_7 + k_{2F}y_5) \tag{A4.41}$$

Equations A4.34 – A4.41 can now be solved using a coupled ordinary differential equation solver like “bvp5c” in Matlab. The code for solving this set of equations will now be provided.

Main Code:

```
%% CO2 reaction/diffusion in boundary layer
%  Use the Matlab ODE solve to solve for steady state

%% Housekeeping
clear all;   % do not need "clear all" just "clear" in general
close all;   % Close all the plot windows - or not

%% Globals and units for equation
global k1f k1r k2f k2r;
global DCO2 DHCO3  DCO3  DOH;
global MCO2 MHCO3 MCO3 MOH;
global CO2bulk OHbulk HCO3bulk CO3bulk; %units of mol/m^3
global g0CO2 g0OH g0HCO3 g0CO3;
global zHCO3 zCO3 zOH;
global F R T;
global Efield;

%% Initialize rate constants and equilibrium constants
Temp = 25; %oC
T = 273 + Temp; %K
buffer = 0.1; % molar, using the concentration of salt for experiments here

pHm = 6.82;  % pH measured in bulk electrolyte for a real experiment

% Solve for the bulk electrolyte species concentrations based off measured
% temperature and pH of electrolyte
[CO2bulk, OHbulk, HCO3bulk, CO3bulk]= CO2equilibriaSolver(Temp,buffer,pHm);

CO2parametersUpdate;  % Feeds in relevant constants

Hbulk = Kw./OHbulk;

%Make bulk concentrations from M to mM (aka Mol/m^3)
CO2bulk   = CO2bulk*1000;
OHbulk    = OHbulk*1000;
HCO3bulk  = HCO3bulk*1000;
CO3bulk   = CO3bulk*1000;
Hbulk     = Hbulk*1000;

%% Flux at the electrode surface
% Take the actual experimental measurements and input here.

jTotal = 5;     % mA cm^-2;      % need to convert to A/m^2 (10*mA/cm^2)
jTotal = jTotal*10; % A m^-2

g0CO2 = DCO2^-1*(jTotal/F)*(FEmethane/zMethane + FEformate/zFormate + ...
                                FECO/zCO       + 2*FEethylene/zEthylene ) ;
g0OH  = -DOH^-1*(jTotal/F)*(8*FEmethane/zMethane + FEformate/zFormate+ ...
                           2*(FECO/zCO)  +     12*FEethylene/zEthylene ) ;
g0HCO3  = 0;   % no reaction
g0CO3   = 0;   % no reaction

%% Boundary Conditions on Voltage
% Not currently used as electrostatics aren't considered
dphidx = jTotal*(-F^2*((zHCO3^2*(DHCO3/(R*T))*HCO3bulk) + ...
                       (zCO3^2*(DCO3/(R*T))*CO3bulk) + ...
                       (zOH^2*(DOH/(R*T))*OHbulk) + ...
                       (zH^2*(DH/(R*T))*Hbulk) + ...
                       (zK^2*(DK/(R*T))*buffer)));  %Units of V/m
%This is done assuming there is no diffusion gradients supporting current
%at the edge of the BL.  Therefore migration must support all of it and
```

```
%that determines the potential gradient through the bulk solution.
Vsurface = 0;  %Setting the voltage at the surface = 0

%% Geometry
global boundaryLayer;
boundaryLayer = 100*10^-6; % m
L = boundaryLayer;

%% Finite difference parameters
meshPoints = 5000;
solutionPoints = 400;

%% Solving BVP with bvp5c
%  3 steps: bvpinit, bvpset, and bvp5c.

disp('bvp5c')      % writes a string to the command line
tic                % times length of solver

% These are initial guesses for the concentration and the gradient in
% the concentration.
solinit = bvpinit(linspace(0,L,meshPoints),...
                                  [CO2bulk CO2bulk/L ...
                                   HCO3bulk HCO3bulk/L ...
                                   CO3bulk -CO3bulk/L ...
                                   OHbulk -OHbulk/L]);

options = bvpset('Stats','on');

sol = bvp5c(@CO2RRODEs3,@CO2RRBCs,solinit,options);  % calling the solver

xsol = linspace(0,L,solutionPoints);
   % x values for the solution, defaults to 100 points
   % deval = Evaluate differential equation solution structure
solution=deval(sol,xsol);
   % maps solution onto x mesh
   % odds will be solution, evens derivatives
xint = linspace(0,L,solutionPoints);
   % x values for the solution, defaults to 100 points
Sxint = deval(sol,xint);
   % maps solution onto x mesh

x   = xint*10^6; % distance into boundary layer micron
CO2 =  solution(1,:);   % Extracting the solutions all in mol/m^3 (mM)
HCO3= solution(3,:);
CO3 =  solution(5,:);
OH  =  solution(7,:);
H   =  Kw./(OH/1000);  % H in Molar
pH  = -log10(H);       % pH
spaceCharge = buffer*1000 + H +...
              -OH -HCO3 -2*CO3;
dCO2dz  =  solution(2,:);   % gradients
dHCO3dz =  solution(4,:);
dCO3dz  =  solution(6,:);
dOHdz   =  solution(8,:);

NCO2  = -DCO2*dCO2dz;      % molar fluxes
NHCO3 = -DHCO3*dHCO3dz - zHCO3*((F*DHCO3)/(R*T))*Efield*HCO3;
NCO3  = -DCO3*dCO3dz - zCO3*((F*DCO3)/(R*T))*Efield*CO3;
NOH   =   -DOH*dOHdz - zOH*((F*DOH)/(R*T))*Efield*OH;

toc
```

```
%% Plotting -
figure(1)
subplot(2,2,1);
plot(x,CO2)
title({'CO2'})
grid on
xlabel('x (microns)')
ylabel('Concentration (mM)')

subplot(2,2,2);
plot(x,HCO3)
title({'HCO3-'})
grid on
xlabel('x (microns)')
ylabel('Concentration (mM)')

subplot(2,2,3);
plot(x,CO3)
title({'CO3--'})
grid on
xlabel('x (microns)')
ylabel('Concentration (mM)')

subplot(2,2,4);
plot(x,OH)
title({'OH-'})
grid on
xlabel('x (microns)')
ylabel('Concentration (mM)')

figure(2)
plot(x,pH,'-go')  % -ro means lines, red, circles
title({'pH at electrode'})
grid on
xlabel('x (microns)')
ylabel('pH')

fprintf('%f is the CO2 concentration at the surface in mM \n', CO2(1));
fprintf('%f is the pH\n', pH(1));
fprintf('%d is the H+ concentration in M\n', H(1));
fprintf('%d is the OH concentration in mM\n', OH(1));
fprintf('%d is the bicarbonate in mM \n', HCO3(1));
fprintf('%d is the carbonate in mM\n', CO3(1));
```

CO_2 Equilibrium Solver:

```
function [CO2, OH, HCO3, CO3]  = CO2equilibriaSolver(Temp,buffer,pH)

% Takes in salt concentration (Molar), temp (oC), and pH to give out all
% the rest.  This can be used to test experimental results where the pH of
% the bulk electrolyte is known.

%% Initialize
T = 273+Temp; %Pass temp to K
ConcNa = buffer;

%% Initialize the equilibrium parameters
% The below equilibrium constants are for the following reactions.
% Ko -> CO2(g) -> CO2(aq)          Ko = [CO2(aq)]
% K1 -> CO2(aq) -> H+ + HCO3-      K1 = [H+][HCO3-]/[CO2]
% K2 -> HCO3- -> H+ + CO3-2        K2 = [H+][CO3-2]/[HCO3-]
```

```
%Note that these equations are for freshwater
A = [108.3865,-356.3094,-107.8871];
B = [0.01985076, -0.06091964 , -0.03252849 ];
C = [-6919.53, 21834.37 , 5151.79 ];
D = [-40.4515 , 126.8339 , 38.9256 ];
E = [669365, -1684915, -563713.9];

Ko = 10.^(A(1) + B(1).*T + C(1)./T + D(1).*log10(T) + E(1)./T.^2); %Molar
K1 = 10.^(A(2) + B(2).*T + C(2)./T + D(2).*log10(T) + E(2)./T.^2); %Molar
K2 = 10.^(A(3) + B(3).*T + C(3)./T + D(3).*log10(T) + E(3)./T.^2); %Molar

DH2O = 1; %g/cm^3
Mw = 18.02; %g Water/mol Water
pKwg = 0.61425 + 48251.33.*T.^(-1) - 67707.93.*T.^(-2) + 10102100.*T.^(-3);
A = [-0.864671, 8659.19, -22786.2];
B = [0.642044, -56.8534, -0.375754];
Z = DH2O.*exp(A(1) + A(2).*T.^(-1) + A(3).*T.^(-2).*DH2O.^(2/3));
pKw = -2.*6.*(log10(1+Z) - Z./(Z+1).*DH2O.*(B(1) + B(2).*T.^(-1) + B(3)*DH2O))+ pKwg
+2*log10(Mw/10^3);
Kw = 10.^(-pKw); %Molar^2

%% Solve for Concentrations
H    = 10.^(-pH); %Molar
OH   = Kw/H; %Molar
HCO3 = (ConcNa+H-OH)/(1+2*K2/H); %Molar
CO3  = (K2*HCO3)/H; %Molar
CO2  = H/K1*HCO3; %Molar

fprintf('%f is the CO2 concentration in mM \n', CO2*1000);
fprintf('%f is the pH\n', pH);
fprintf('%d is the H+ concentration in M\n', H);
fprintf('%d is the OH concentration in mM\n', OH*1000);
fprintf('%d is the bicarbonate in mM \n', HCO3*1000);
fprintf('%d is the carbonate in mM\n', CO3*1000);
```

CO_2 Parameters:

```
% Constants for the CO2 reduction problem

%% Equilibrium parameters
% The below equilibrium constants are for the following reactions.
% Ko -> CO2(g) -> CO2(aq)        Ko = [CO2(aq)]
% K1 -> CO2(aq) -> H+ + HCO3-    K1 = [H+][HCO3-]/[CO2]
% K2 -> HCO3- -> H+ + CO3-2      K2 = [H+][CO3-2]/[HCO3-]
%Note that these equations for freshwater will now no longer consider salinity
A = [108.3865,-356.3094,-107.8871];
B = [0.01985076, -0.06091964 , -0.03252849 ];
C = [-6919.53, 21834.37 , 5151.79 ];
D = [-40.4515 , 126.8339 , 38.9256 ];
E = [669365, -1684915, -563713.9];

Ko = 10.^(A(1) + B(1).*T + C(1)./T + D(1).*log10(T) + E(1)./T.^2); %Molar
K1a = 10.^(A(2) + B(2).*T + C(2)./T + D(2).*log10(T) + E(2)./T.^2); %Molar
K2a = 10.^(A(3) + B(3).*T + C(3)./T + D(3).*log10(T) + E(3)./T.^2); %Molar

DH2O = 1; %g/cm^3
Mw = 18.02; %g Water/mol Water
pKwg = 0.61425 + 48251.33.*T.^(-1) - 67707.93.*T.^(-2) + 10102100.*T.^(-3);
A = [-0.864671, 8659.19, -22786.2];
B = [0.642044, -56.8534, -0.375754];
Z = DH2O.*exp(A(1) + A(2).*T.^(-1) + A(3).*T.^(-2).*DH2O.^(2/3));
```

```
pKw = -2.*6.*(log10(1+Z) - Z./(Z+1).*DH2O.*(B(1) + B(2).*T.^(-1) + B(3)*DH2O))+ pKwg
+2*log10(Mw/10^3);
Kw = 10.^(-pKw); %Molar^2

% Want the equilibrium for the following reactions
% Ko -> CO2(g) -> CO2(aq)          Ko = [CO2(aq)]
% K1 -> HCO3- -> CO2(aq) + OH-     K1 = [OH-][CO2]/[HCO3-]
% K2 -> CO3-2 -> HCO3- + OH-       K2 = [OH-][HCO3-]/[CO3-2]
% Kw -> H2O -> H+ + OH-
Ko  = Ko;       %Molar
K1  = Kw/K1a;   %Molar
K2  = Kw/K2a;   %Molar
Kw  = Kw;       %Molar^2

%% Kinetics
% For the 2nd set of reactions above.  Note different sources give
% different values.

factor1 = 10^-0; %Use to slow the reactions to improve solver convergence

k1f    = 9.71*10^-5; %sec^-1
k1ra    = factor1*k1f/K1; %molar^-1 * sec^-1

k2f    = 3.06*10^5; %sec^-1
k2ra    = factor1*k2f/K2; %molar^-1 * sec^-1

% Put in units of m^3 mol^-1 sec^-1
k1r = k1ra/1000;
k2r = k2ra/1000;

%% Diffusion (meter^2 * sec^-1)
DCO2     = 1.91 * 10^-9;
DHCO3    = 1.185 * 10^-9;  %From Singh, Gupta switched the two and is wrong
DCO3     = 9.23 * 10^-10;  %From Singh, Gupta switched the two and is wrong
DOH      = 5.273 * 10^-9;
DH       = 9.311 * 10^-9;
DK       = 1.957 * 10^-9;

%% Mobility (not used here)
MCO2     = 0;
MHCO3    = 0.462 * 10^-7;  %* meter^2 * volt^-1 * sec^-1;
MCO3     = 0.359 * 10^-7;  %* meter^2 * volt^-1 * sec^-1;
MOH      = 2.054 * 10^-7; %* meter^2 * volt^-1 * sec^-1;
MH       = 3.626 * 10^-7; %* meter^2 * volt^-1 * sec^-1;
MK       = 0.762 * 10^-7;  %* meter^2 * volt^-1 * sec^-1;

% Note that this is really mobility (m^2 mol J^-1 sec^-1) multiplied by
% Faraday's constant to get this value.  So when using this value and the
% equation for mobility, you need to drop Faraday's constant.

%% Faradaic efficiencies
%Real State
FEmethane      = 0.00;
FEethylene     = 0.00;
FECO           = 1.00;
FEformate      = 0.00;
FEH2           = 0.00;

%% Electrons exchanged
zMethane       =  8;
zEthylene      = 12;
zCO            =  2;
zFormate       =  2;
```

```
zH2             =  2;

%% charges (not used here)
zHCO3           = -1;
zCO3            = -2;
zOH             = -1;
zH              = 1;
zK              = 1;

%% Physical constants
F       = 96485.3;        % Faraday constant
R       = 8.3144598;       % in SI units, J mol-1 K-1
```

ODEs:

```
function [dydx]=CO2RRODEs3(x,y)

% System of 8 first-order ODEs
% returns derivatives

global DCO2 DHCO3 DCO3 DOH;
global k1f k1r k2f k2r;
global zHCO3 zCO3 zOH;
global T;

dydx(1) = y(2);                          % dCO2/dx
dydx(2) = -DCO2^-1.*(k1f.*y(3) - k1r.*y(1).*y(7));  % 2nd deriv dCO2/dx

dydx(3) = y(4);                          % dHCO3/dx
dydx(4) = -DHCO3^-1*( ...                % 2nd deriv dHCO3/dx
                  k1r.*y(1)*y(7) - k1f.*y(3) - k2r.*y(3).*y(7) + k2f.*y(5));

dydx(5) = y(6);                          % dCO3/dx
dydx(6) = -DCO3^-1*(...                  % 2nd deriv dCO3/dx
                    k2r.*y(3).*y(7) - k2f.*y(5));

dydx(7) = y(8);                         % dOH/dx
dydx(8) = -DOH^-1*(...                  % 2nd deriv dOH/dx
                -k1r.*y(1).*y(7) + k1f.*y(3) - k2r.*y(3).*y(7) + k2f.*y(5));

dydx=dydx';   % transpose

end
```

ODE BCs:

```
function [res]=CO2RRBCs(y0,yL)
% Boundary conditions for 8 first-order ODEs
% order does not matter

global CO2bulk OHbulk HCO3bulk CO3bulk;
global g0CO2 g0OH g0HCO3 g0CO3;

% Note y0 is a left hand boundary condition aka one at the electrode surface.
% YL is a right hand boundary condition aka at the bulk electrolyte
% interface.
res(1)=y0(2)-g0CO2;      % CO2 gradient
res(2)=yL(1)-CO2bulk;    % CO2 fixed
```

```
res(3)=y0(4)-g0HCO3;       % bicarbonate gradient = 0
res(4)=yL(3)-HCO3bulk;     % bicarbonate fixed

res(5)=y0(6)-g0CO3;
res(6)=yL(5)-CO3bulk;

res(7)=y0(8)-g0OH;
res(8)=yL(7)-OHbulk;

res=res';

end
```

When this code is run successfully for the sample case listed of 5 mA cm^{-2} producing 100% CO with a pH 6.82 starting electrolyte, the following output should be obtained

Command Window:

>> CO2DiffusionReactionMatlabODEv01
34.072344 is the CO2 concentration in mM
6.820000 is the pH
1.513561e-07 is the H+ concentration in M
6.970551e-05 is the OH concentration in mM
9.993834e+01 is the bicarbonate in mM
3.087003e-02 is the carbonate in mM
bvp5c
The solution was obtained on a mesh of 5000 points.
The maximum error is 4.501e-01.
There were 266897 calls to the ODE function.
There were 73 calls to the BC function.
Elapsed time is 14.234115 seconds.
11.543622 is the CO2 concentration at the surface in mM
9.969914 is the pH
1.071731e-10 is the H+ concentration in M
9.844223e-02 is the OH concentration in mM
8.553809e+01 is the bicarbonate in mM
3.706605e+01 is the carbonate in mM

Plots:

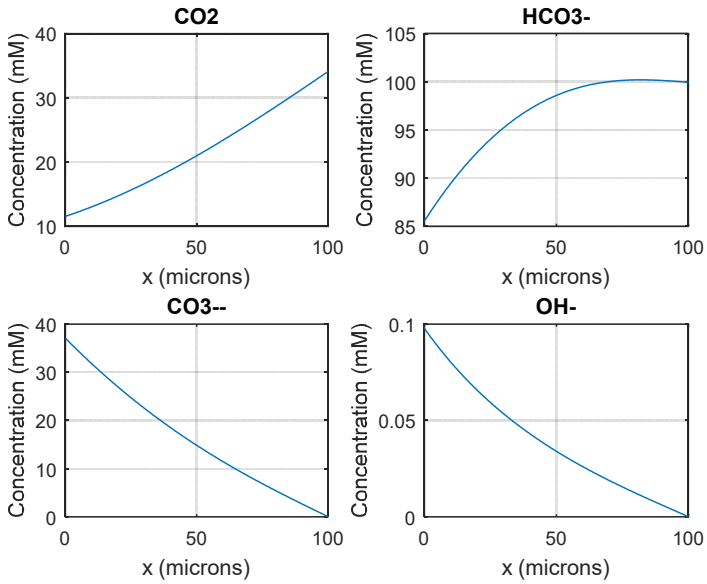
CO2
HCO3-
CO3--
OH-
Concentration (mM)
x (microns)

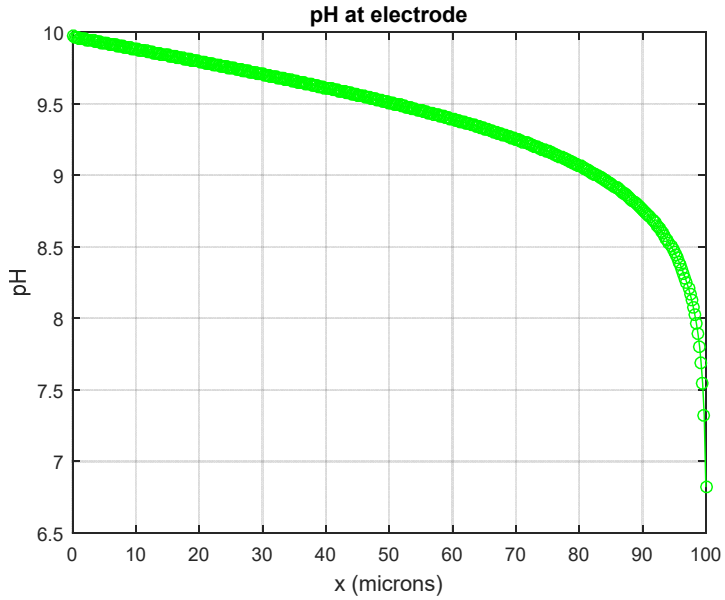
pH at electrode
pH
x (microns)

4.6.3. Gaseous Products of CO2R on Cu Foil

Figure A4.2 and Tables A4.3 and A4.4 summarize the faradaic efficiencies for gaseous products (CH_4, CO, H_2, C_2H_4) produced by electropolished copper foil at -1.05 V vs. RHE in 0.1 M $NaHCO_3$. Data from Cell A and Cell B are compared. Clearly, H_2 generation dominates in the smaller Cell A (*S/V* = 2) compared to the larger cell, where CH_4 is the dominant product. This effect is due to depletion of CO_2 in the small cell, as discussed earlier in the chapter. It can also be seen that both product distributions are quite stable over time except for the ethylene production in Cell B. It is still unclear at this time what is causing the decrease in faradaic efficiency for this product; however, it is commonly observed in my experiments. It could possibly be due to *in-situ* surface rearrangement of the polycrystalline Cu surface which is known to happen over time.[173]

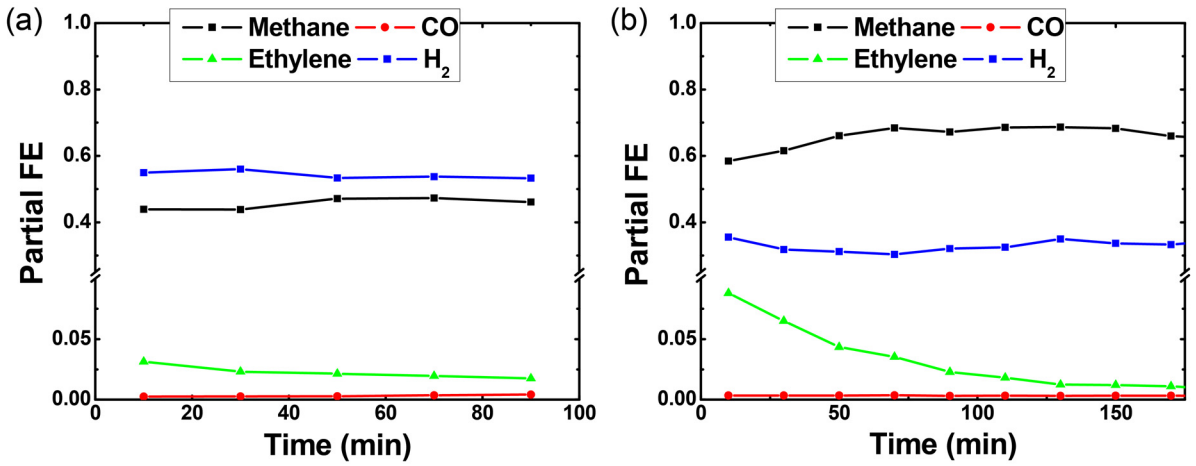

Figure A4.2 Gaseous Products of CO2R vs. Time: Characteristic data of the gaseous products of CO2R at -1.05 V vs. RHE on Cu foil in 0.1M $NaHCO_3$ is plotted here over the course of a 1.5 hr run in Cell A (a) and a 3hr run in Cell B (b)

Table A4.3: Tabulated current and faradaic efficiency data for CO2R experiment in Cell A at ~ -1.05 V vs. RHE on Cu foil in 0.1M $NaHCO_3$

Time (min)	Current Density (mA/cm^2)	Methane	Carbon Monoxide	Ethylene	Hydrogen	Sum
10	12.40	43.88	0.25	3.13	54.90	102.16
30	12.25	43.82	0.26	2.31	56.02	102.41
50	11.86	47.10	0.28	2.15	53.32	102.85
70	11.66	47.29	0.35	1.96	53.75	103.35
90	11.35	46.10	0.41	1.75	53.30	101.56
Average	11.90	45.64	0.31	2.26	54.26	102.46
Standard Dev	0.43	1.69	0.07	0.53	1.18	0.68

Table A4.4: Tabulated current and Faradaic efficiency data for CO2R experiment in Cell B at ~ -1.05 V vs. RHE on Cu foil in 0.1M $NaHCO_3$

Time (min)	Current Density (mA/cm^2)	Methane	Carbon Monoxide	Ethylene	Hydrogen	Sum
10	11.86	58.40	0.34	8.80	35.54	103.07
30	11.94	61.56	0.34	6.50	31.76	100.16
50	11.45	66.08	0.34	4.34	31.15	101.91
70	11.04	68.37	0.35	3.53	30.34	102.59
90	10.94	67.20	0.31	2.29	32.09	101.89
110	10.75	68.56	0.33	1.81	32.49	103.18
130	10.52	68.65	0.31	1.25	34.94	105.14
150	10.41	68.24	0.33	1.22	33.65	103.44
170	10.23	65.96	0.33	1.10	33.25	100.63
190	9.88	65.02	0.28	0.80	34.69	100.79
Average	10.90	65.80	0.33	3.16	32.99	102.28
Standard Dev	0.68	3.39	0.02	2.67	1.72	1.52

5. Feasibility Analysis of Real-Time Product Detection for Electrochemical Reduction of CO_2 via Selected-Ion Flow-Tube Mass Spectrometry

5.1. Introduction

In the previous chapter the potential impact of electrochemical CO_2 reduction (CO2R) on the production of renewable hydrocarbon based fuels was motivated. The importance of the electrochemical cell used to characterized catalysts in a research environment was outlined. Here the analytical equipment which is coupled to that electrochemical cell is considered. The quantification of multicomponent liquid and gaseous mixtures has been well established for decades and is especially important when studying CO2R catalysts.[137] Metals like copper (Cu) have been shown to simultaneously produce up to 16 different chemicals.[121] For the gaseous products, gas chromatography (GC) is typically used and for the liquid products, nuclear magnetic resonance (NMR) or high performance liquid chromatography (HPLC) are typical. All three of these techniques are well established to give quantitative, reproducible results.

Online GC analysis is often utilized to detect the gaseous products of CO2R.[104,108,119,121,136,174–176] In this set up, gas flowing through the electrochemical cell is sampled by the GC (akin to the set up in Ch 4). Due to the GC's reliance on product separation before detection, most literature reports obtain data points only every 10 to 20 minutes. Liquid products are typically only analyzed once per run, at the conclusion. It is conceivable to take liquid aliquots every 10 to 20 minutes to be analyzed like with the GC, although this is rarely done.[177,178] Liquids tend to be generated at very low rates and thus more time is needed for them to accumulate in the electrolyte before they can be detected. Thus, the traditional analytical equipment, while reliable, has some limitations if real-time analysis of CO2R products is desired.

The time dependent behavior of CO2R electrocatalysts has been shown to be a subject of great importance, especially related to catalyst deactivation.[115] In particular the dynamics of liquid product formation are almost entirely unexplored. The working assumption of most reports is that liquid products are being generated at a constant partial current density throughout the run. Using the information a GC provides, the faradaic efficiency loop can be closed assuming that liquids account for all the missing current. Although this is not a rigorous approach, it can be used to estimate if the magnitude of all liquid products being produced is constant (or not) throughout a run. However, the assumption that every liquid product (of which there can be as many as 14) is generated at a constant rate has limited experimental validation. To confirm this an experimental technique needs to be developed which can detect simultaneously all the gaseous and liquid products of CO2R.

In addition, the real-time sensitivity of such a technique would allow for catalyst exploration to greatly accelerate by reducing the time needed to evaluate a catalyst from days to potentially a few hours. This could also enable the use of high throughput approaches to catalyst

discovery.[179] This high through-put catalyst screening has already been successfully implemented to catalyst discovery for the oxygen evolution reaction[180–184] and the hydrogen evolution reaction (HER).[184–186] However, the task of identifying a more active catalyst is simplified for these reactions because only one product is being made (namely oxygen or hydrogen). Thus only current or the production of that one product needs to be monitored to identify a "hit" (i.e. a catalyst for further investigation). Screening CO2R catalysts is more complicated due to the production of multiple products and the competing HER reaction. Thus monitoring current alone will not provide the necessary information to identify a hit and product detection is necessary. As of yet, there has only been one implementation of high through-put screening in CO2R due to the general lack of a suitable analytical tool.[187,188]

For all the aforementioned reasons, considerable effort has been put into developing systems which can acquire real-time data. Historically, in electrochemistry, this effort has been focused on differential electrochemical mass spectrometry (DEMS),[189,190] which has more recently seen specific adaptation to CO2R systems.[85,188,191,192] In these systems, electron ionization mass spectrometry (EI-MS) is typically coupled to a specialized electrochemical cell or sample collection tip. Of particular note are the systems developed by Koper and co-workers[191] and Bell and co-workers[85] for CO2R. Koper's online electrochemical mass spectrometer (OLEMS) places a porous tip very close to the electrochemical surface, where it collects both gaseous and liquid products. While this approach is not quantitative, it has shown the ability to detect hydrogen, methane, ethylene, ethane, methanol, acetaldehyde, and ethanol in specific situations. Bell's DEMS system relies on an innovative electrochemical flow cell, which enables quantitative product analysis. This system extracts liquid and gaseous products through a membrane and can quantify hydrogen, methane, ethylene, and ethane, as well as 1-propanol and ethanol with some assistance from ex-situ HPLC analysis. While these systems show promise, they have insufficient sensitivity or are unable to decouple, and thus detect, all of the products of CO2R, especially the liquid products.

Detection and quantification of the products of a reaction can be broken down into three levels of detail. At the first level, the analytical system can simply identify whether or not a group of chemicals is present. For example, a detection system could identify if alcohols are being produced, but not which ones or how much of each. At the second level, the system can identify each chemical individually. Thus, which specific alcohol is being produced is known. At the third and most detailed level, the detection system can identify each chemical individually as well as how much of that chemical is being produced, allowing for full quantifiable analysis of each product. An ideal real-time production detection system for CO2R would be able to detect and quantify (level 3) all the products that have been observed. In addition, the system would be able to do this on a relevant time scale, where sub-second resolution would be ideal. Here I explore the first application of selective-ion flow-tube mass spectrometry (SIFT-MS) to the *in-situ* detection of the volatile products of CO2R. SIFT-MS uses a gentle chemical ionization process to detect

analytes and in this way is more adept at analyzing complex multi-component mixtures like that of the 20 potential liquid and gaseous products of CO2R.

5.1.1. Complication of Electron Ionization Mass Spectrometry

The main reason current DEMS systems have trouble delineating all the products of CO2R (level 1 analytical system) is that they depend on electron ionization mass spectrometry (EI-MS). Electron ionization is a harsh process in which sample molecules are not only ionized but often broken down into many constituent fragments. The reason so much fragmentation occurs is due to the high energy (~10 eV) required to ionize a molecule in comparison to the typical energy required to cleave bonds (~3 eV).[193,194] This so called fragmentation pattern is a fingerprint for the molecule; however, the high degree of fragmentation complicates the analysis of multi-component mixtures, if the components produce many of the same fragments. This is the case with the products of CO2R which are all small molecule hydrocarbons, alcohols, or aldehydes. This is further complicated because the primary constituent of gaseous samples, making up 99% of the sample, is CO_2 while the remaining gases and entrained liquid vapors, to be detected, represent only a very small fraction of the sample. Thus when the sample is injected onto an electron ionization source, the CO_2 ionization fragments produce a large background signal at masses that would be monitored to detect the other chemicals. This issue can be easily avoided by the separation that is achieved with gas chromatography mass spectrometry, but then the real-time aspect of the analysis is lost.

Table 5.1 shows a list of all the products that have been reported for CO2R on copper.[121] Formaldehyde, methanol, ethane, and propene have also been included as these have been reported as CO2R products on other catalysts and would be of particular interest as fuels.[122,156,195–201] The table shows a heat map of what ionization fragments (*m/z*) are produced for each molecule, from green being abundantly produced to gray being scarcely produced.[202] Furthermore the *m/z* patterns for water and CO_2 are shown, as these components will make up the bulk of a sample being injected.[202] *m/z* values highlighted in red indicate masses where water or CO_2 will make major contributions and thus no other component will be detectable at these masses. These masses have been crossed out across the table as a result.

Examining the remaining map, it is possible to identify which compounds can be detected and quantified if an unknown mixture were sampled. For this analysis it was assumed that any secondary fragment less than 25% in intensity of the primary *m/z* could be ignored. This resulted in identifying unique *m/z* values for hydrogen, ethylene, propylene, formic acid, methanol, acetic acid, ethylene glycol, and allyl alcohol. A unique *m/z* means that this compound could be directly quantified by calibrating just one mass fragment. Further analysis showed methane, ethane, and ethanol could be quantified by subtraction. All other compounds which contributed significantly to the identified *m/z* could be subtracted away leaving only the contribution of the one remaining compound. Thus as long as the contributions to a specific *m/z* are a linear sum of the parts, which it should be for electron ionization MS, compounds can be reliably identified by subtraction.

Table 5.1 CO2R EI-MS m/z Response: The electron ionization mass fragmentation fingerprint for all the relevant products of CO2R are presented in a heat chart. For the products of CO2R, bright green is the most likely *m/z* to be produced while gray is the least likely. For water and CO_2, bright red is the most likely *m/z* to be produced while gray is the least likely. The #### indicate masses which can be used to uniquely identify their corresponding analyte.

However, this analysis shows that the remaining products (carbon monoxide, formaldehyde, glyoxal, glycolaldehyde, acetaldehyde, hydroxyacetone, acetone, propionaldehyde, and 1-propanol) cannot be deconvoluted from each other and thus are unquantifiable, preventing level 3 analytical detection.

EI-MS is an extremely sensitive analytical technique, which has been regularly shown to be capable of quantifiably detecting picogram amounts of analyte.[194] However, this high level of sensitivity does not resolve the above mentioned issues with mass overlap when analyzing a complex mixture of similar compounds. If a gentler ionization technique could be coupled to the extremely sensitive detection method of MS, then it may be possible to overcome some of the detection issues EI-MS faces, as outlined above. Here, SIFT ionization, as an alternative to EI, is explored as one possibility. The advantage of SIFT-MS is that it uses a gentler chemical ionization technique, which, in principle, produces a far simpler fragmentation pattern where molecules only produce several characteristic ions instead of dozens.[203] In addition the technique does not ionize CO_2, as will be explained in more detail below, thus avoiding the large background issue. In this way, level 3 analytical detection of a more complex multi-component system should be possible.

5.1.2. Brief History and Applications of SIFT-MS

The selected ion flow tube (SIFT) technique was developed in 1976[203] where it was used for further study in the well-established ion-molecule reaction kinetics field.[204,205] It was then adapted in 1996 to use the well-established ion-molecule reaction data to quantify unknown samples injected into the flow tube.[206] Combining the two yields a technique for doing spectrometry and was thus renamed selected ion flow tub mass spectrometry (SIFT-MS). The technique has been well reviewed,[207–209] and essentially consists of an unknown gas mixture being fed into the reaction flow tube where it undergoes "soft" chemical ionization by reaction with injected reagent ions. These reagent ions are typically H_3O^+, NO^+, and O_2^+ and the flow tube contains fast flowing carrier gas (typically He) at ~1 Torr such that the residence time of analyte molecules in the tube is short, keeping the reaction chemistry simple. The combined mixture of now ionized unknown molecules in the carrier gas is sampled at a downstream quadrupole mass spectrometer. Utilizing the known reaction product library, the unknown samples can be identified

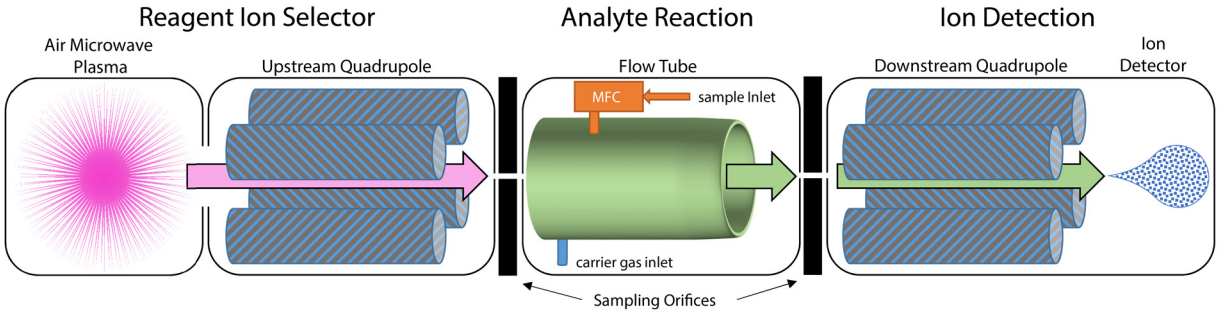

Figure 5.1 Schematic of SIFT-MS: A schematic of the different sections of a SIFT-MS are shown. In the first section, the reagent ions H_3O^+, NO^+, and O_2^+ are generated from air and then selected by the upstream quadrupole. The reagent ions are injected into the flow tube where they can react with the sample. The product ions of this reaction are then detected by a downstream mass spectrometer.

in a way similar to electron-ionization mass spectrometry. A schematic of the system is shown in Figure 5.1.

The true power in SIFT-MS is the use of multiple reagent ions, as compared to proton transfer reaction mass spectrometry (PTR-MS) in which only H_3O^+ is used as the reagent ion.[210] The reagent ions in SIFT-MS are selected by an upstream quadrupole such that only one is injected at a time into the flow tube. Each reagent ion has unique reactions with an analyte molecule, thus allowing for multiple avenues to confirm the identity of an unknown species. This is particularly useful when trying to analyze complicated mixtures of similar molecules like that produced by CO2R. Furthermore, because the chemical ionization is not strong enough to ionize O_2, N_2, Ar, or CO_2 but is very reactive with most volatile organics, SIFT-MS has routinely shown ppb level detection of analytes without separation from their makeup gas.[208,211] Additionally, because the reaction rates of many molecules with these reagent ions have been well studied,[212–216] it is claimed that SIFT-MS does not require external calibration. The makeup of the analyte can simply be back calculated using the known reagent ion concentration, the known reaction rate, and the measured products of the reaction. Thus obtaining quantitative information should be much simpler than the rigorous calibration process typically required of a GC or EI-MS analytical system.

SIFT-MS has been utilized mainly for environmental impact studies, analyzing trace gases in atmospheric air, and for biological studies, analyzing the metabolites in exhaled breath. In these applications, hydrocarbon and volatile organic compounds (VOCs), respectively, are the main target analytes.[207,217,218] Real-time detection is important due to VOCs' tendency to adsorb onto storage container walls, preventing accurate quantification. With SIFT-MS the samples are taken directly from the atmosphere, without the need for storage, eliminating this issue. The real-time detection is also important for environmental applications, where improper release of chemicals in the air can be detected immediately and addressed.

Three potentially important attributes of SIFT-MS can be observed from these previous applications which may make it well-suited for CO2R.

1. SIFT-MS has already been used to detect the types of chemicals that are relevant to CO2R.
2. SIFT-MS can readily detect products in real-time with sub-second time resolution.
3. SIFT-MS can detect VOCs simply from the vapor released by these liquids. Thus it may be possible to eliminate direct sampling of the liquid to identify the liquid products of CO2R.

5.2. Prospective Outlook on the use of SIFT-MS with CO2R

In order to understand if SIFT-MS can provide any advantages over traditional analytical techniques, the first step is to use the literature to determine if all the CO2R products can be uniquely identified if injected together. The CO2R products are the analytes to be detected by reaction with the SIFT-MS reagent ions. These reactions will create product ions that are detected

by the MS. First, it is important to have a brief understanding of the molecular chemistry involved, especially to highlight why such a low number of product ions are expected per injected analyte. The three reagent ions used in SIFT-MS – H_3O^+, NO^+, and O_2^+ – will be examined one by one. This information has been reviewed in much greater detail by Smith and Španěl.[208]

5.2.1. The H_3O^+ Reagent

H_3O^+ generally reacts with analytes via an exothermic proton transfer as exemplified by reaction 5.1.

$$H_3O^+ + M \rightarrow MH^+ + H_2O \quad (5.1)$$

This will occur when the proton affinity (PA) of an analyte (M) is greater than that of H_2O. It is possible that the resulting ion (MH^+) can undergo dissociation, such as the loss of a H_2O by the combination of H^+ with an available OH group. This is most common with alcohols and aldehydes and is a way in which two product ions can be made per analyte instead of just one.

5.2.2. The NO^+ Reagent

NO^+ can undergo a wide range of reactions with an analyte molecule, often resulting in the formation of multiple product ions. The possible reactions include charge transfer (5.2), hydride (5.3) or hydroxide ion transfer (5.4), and ion-molecule association (5.5).

$$NO^+ + M \rightarrow M^+ + NO \quad (5.2)$$

$$NO^+ + MH \rightarrow M^+ + HNO \quad (5.3)$$

$$NO^+ + MOH \rightarrow M^+ + HNO_2 \quad (5.4)$$

$$NO^+ + M + X \rightarrow NO^+M + X \quad (5.5)$$

The charge transfer reactions can only proceed if the electron ionization (EI) energy of the analyte is less than that of NO (9.26 eV). The molecular association reactions often proceed at a low rate due to the need for a third body (X, usually a carrier gas molecule).

5.2.3. The O_2^+ Reagent

O_2^+ generally reacts with analytes via a simple charge transfer reaction. This charge transfer reaction can proceed if the EI energy of the analyte is less than that of O_2 (12.07 eV). Thus O_2^+ will react with a much wider range of molecules than NO^+. It is also common for the generated product ion to dissociate into two or more ion fragments. In this way several product ions can be produced per analyte molecule. An example of this decomposition is shown for acetone in reactions 5.7a and 5.7b.

$$O_2^+ + M \rightarrow M^+ + O_2 \quad (5.6)$$

$$O_2^+ + CH_3COCH_3 \rightarrow CH_3COCH_3^+ + O_2 \quad (5.7a)$$

$$O_2^+ + CH_3COCH_3 \rightarrow CH_3CO^+ + CH_3 + O_2 \quad (5.7b)$$

5.2.4. The Role of Water

It is important to understand the role of water in this reaction chemistry, as it plays a major role when sampling humidified gas. As was stated earlier, SIFT-MS has been routinely used for breath analysis. One of the key advantages of SIFT-MS that lead to this is its relative insensitivity to the humidity of the incoming gaseous sample.

H_2O molecules interact differently with each reagent ion so they need to be addressed individually. With H_3O^+ reagent ions, H_2O readily reacts to create a cluster ion according to the following reaction,

$$H_3O^+ + n{\cdot}H_2O + X \rightarrow H_3O^+(H_2O)_n + X \quad (5.8)$$

where X is a third body (typically a carrier gas molecule) that allows the change in momentum of the molecules to occur. These new cluster ions can act as reagent ions and can be present in very high concentration depending on the humidity of the inlet gas. Thus the reaction chemistry in the H_3O^+ reagent ion channel must account for the reaction of the analyte with mass 19 (H_3O^+), 37 ($H_3O^+(H_2O)$), 55 ($H_3O^+(H_2O)_2$), and possibly even 73 ($H_3O^+(H_2O)_3$).

With NO^+, the ionization energy of water (12.62 eV) is too high for charge transfer to occur; however a slow molecular association reaction does occur to make NO^+H_2O. While this reaction is slow, the additional reaction of the analyte with a mass 48 needs to be taken into account. With O_2^+, the same situation occurs. Only slow molecular association of O_2^+ with water is possible to make $O_2^+H_2O$, requiring that the analyte reaction with a mass 50 be taken into account. In both cases the quantity of NO^+H_2O and $O_2^+H_2O$ should be low in comparison to their parent reagent ion.

5.2.5. Evaluation of SIFT-MS

With this understanding of the reaction chemistry now in hand, the literature was surveyed to build a library of expected product ions for the same products of CO2R listed in Table 5.1.[212–216] This information is summarized in Table 5.2. For several CO2R products, no data was available (glycolaldehyde, hydroxyacetone, allyl alcohol). For these chemicals the IE[219] and PA[220] were obtained from the literature, if available, and then the appropriate reaction was applied from those listed above and an expected *m/z* hypothesized. For example, the IE of both hydroxyacetone and ally alcohol were found to be less than that of O_2, thus it is expected that these molecules will undergo a charge transfer reaction with O_2^+ producing *m/z* 74 and 58 respectively. Because this data only represents an educated guess, it was not included in the further analysis below. Data was available for formic acid and acetic acid; however, these compounds were neglected from further analysis because at the pH of a typical CO2R experiment (~7) they are mostly deprotonated and ions have no vapor pressure.

It can be observed from Table 5.2 that many of the target analytes would produce the same *m/z* fragments (highlighted cells). However, due to the multiple reagent ions and the limited fragmentation patterns it is possible to deconvolute these overlaps and hypothesize a scheme in

Table 5.2 Prospective Outlook on SIFT-MS: The expected product ion mass numbers are tabulated for each compound to be detected using SIFT-MS. The duplicate masses for each reagent ion are highlighted indicating where overlap and deconvolution may be necessary

	Reagent Ions		
	H_3O^+	NO^+	O_2^+
Mass of Reactant Ions	***19 (37, 55)***	***30 (48)***	***32 (50)***
Analyte	*m/z* Products	*m/z* Products	*m/z* Products
Hydrogen	NR	NR	NR
Carbon Monoxide	NR	NR	NR
Methane	NR	NR	47
Ethylene	29 47	58	28
Ethane	NR	NR	29 30 28
Propylene	43	72	42
Formic Acid	ND	ND	ND
Formaldehyde	31 49 61	NR	29 30 31
Methanol	33 51 65	62	31 32
Glyoxal	59	88	29 30 58
Acetic Acid	ND	ND	ND
Glycolaldehyde	UNK	UNK	UNK
Acetaldehyde	45 63 81	43 61	43 44
Ethylene Glycol	45 63 81	61 92	31 33 62
Ethanol	47 65 83	45 63	45 46 63
Hydroxyacetone	UNK	UNK	74*
Acetone	59 77 117	88	43 58
Allyl Alcohol	UNK	UNK	58*
Propionaldehyde	59	57	57 58
1-Propanol	43 61 79	59	31 42

Duplicate *m/z* | Duplicate *m/z* | Duplicate *m/z*

NR = No Reaction ND = Not Detectable UNK = Unknown Reaction

* = estimated *m/z* product based off hypothesized reaction

which all the target analytes can be identified. Table 5.3 summarizes which *m/z* values can be used to identify which analytes for each reagent ion. Highlighted in green are masses which are unique identifiers for their specific analyte; no other analyte produces this *m/z* value. Highlighted in orange are the masses which can be used to identify the target analyte but require deconvolution first. Multiple analytes contribute at this *m/z* but the contributions of all the other analytes, other than the target molecule, can be subtracted away. Finally there are several reagent ion/analyte combinations which produced a highly convoluted *m/z* value which could not be used to identify any individual analyte. These such combinations were labelled as “no usable reaction” and highlighted in red. Despite the presence of several of these combinations, it is still possible to find at least one reagent ion *m/z* which can be used to identify each product of CO2R. In this way, it is hypothesized that SIFT-MS can be used to identify and quantify methane, ethylene, ethane, propylene, formaldehyde, methanol, glyoxal, acetaldehyde, ethylene glycol, ethanol, acetone,

propionaldehyde, and 1-propanol; a substantial improvement over previous real-time analytical techniques.

Tables 5.2 and 5.3 also shows that SIFT-MS cannot be used to detect hydrogen or carbon monoxide.[208] Thus it would not be possible to completely close the faradaic efficiency loop without additional analytical equipment. It would be possible to add a real-time hydrogen detector to the system in the form of an in-line thermal conductivity detector; however, the accuracy of such a system has not yet been proven. There is no clear solution for detecting CO in real-time. While this is a drawback of SIFT-MS, coupling the system to a GC would provide periodic information to help close this information gap.

With this strong framework supporting the investigation of SIFT-MS as an analytical tool for detecting the products of CO2R, the remainder of this chapter is dedicated to exploring the practical implementation of this technique for CO2R experiments. The analytical framework suggests that almost all the expected products can be quantified; however, this hypothesis needs to be experimentally validated.

Table 5.3 Prospective Outlook on SIFT-MS: The mass library was analyzed to identify which masses can be used to specifically identify each compound. Those masses listed in green are unique to that chemical and require no deconvolution to use. The masses listed in orange would require deconvolution with other compounds that produce that mass, but those contributions can be subtracted away.

	Reagent Ions		
Analyte	H_3O^+	NO^+	O_2^+
Hydrogen	NR	NR	NR
Carbon Monoxide	NR	NR	NR
Methane	NR	NR	47
Ethylene	29	58	NUR
Ethane	NR	NR	28
Propylene	43	72	NUR
Formic Acid	ND	ND	ND
Formaldehyde	31/49	NR	30/29
Methanol	33	62	NUR
Glyoxal	NUR	NUR	58
Acetic Acid	ND	ND	ND
Glycolaldehyde	UNK	UNK	UNK
Acetaldehyde	NUR	43	44
Ethylene Glycol	NUR	92	33/62
Ethanol	47	45	45/46
Hydroxyacetone	UNK	UNK	UNK
Acetone	77	NUR	43
Allyl Alcohol	UNK	UNK	UNK
Propionaldehyde	NUR	57	57
1-Propanol	61	59	NUR

Green = Unique Mass *Orange* = Deconvolution Required
Red / NUR = No Usable Reaction, Deconvolution Not Possible
NR = No Reaction ND = Not Detectable UNK = Unknown Reaction

5.3. Experimental

The SIFT-MS used in this study was a Voice 200, a commercial tool manufactured by SYFT Technologies. 99.999% pure nitrogen gas was used as the flow tube carrier gas and 99.99% CO_2 was used in some of the experiments (Air Products). The tool used lab air to create the air plasma that supplied the reagent ions. To control the inlet flow of gas into the flow tube, a mass flow controller (MFC, Alicat Scientific) with a 0.5 – 100 sccm range was used. For all the experiments presented here, an inlet flow rate of 1 sccm was used. The low pressure in the flow

tube drove the flow of gas through the MFC, allowing the gas coming from the CO2R reaction cell to remain at atmospheric pressure. The flow of gas from the cell in excess of the 1 sccm inlet to the SYFT was vented (Fig. 5.2).

In order to confirm and quantify the ionization patterns of the product ion library described above for the various products of CO2R, these chemicals were injected into the SIFT-MS one by one. For the gaseous products (methane, ethylene, ethane, propylene), gas cylinders with 100-3000 ppm of a single gas were used (Air Products). The cylinders were balanced with carbon dioxide. The concentrations of the gases were selected according to the expected range of concentrations that each gas would reach in the outlet flow of an actual CO2R electrochemical reactor. It was important to purchase these calibration cylinders as single component mixtures, unlike those which are typically used to calibrate a GC, which contain all the gaseous species of interest. The single component mixtures allowed an unconvoluted examination of what masses were produced by each gas in SIFT-MS.

To measure the SIFT-MS response to these gaseous products, the gas first needed to be hydrated. The gas needed to be hydrated as the presence of water vapor in the analyte gas had a large effect on which product ions were observed. To accomplish this, one half of the electrochemical cell developed in chapter 4 (pictured in Figure 5.2) was used, filled with water. However, this cell was made from polyether ether ketone (PEEK) to enable easier cleaning. Teflon plates were used in place of the electrode and membrane for the half-cell being used. Gas flow into the electrochemical cell was controlled by an MFC. The outlet flow of the half-cell was connected to a mass flow meter (MFM, Alicat Scientific), to ensure there were no leaks in the cell,

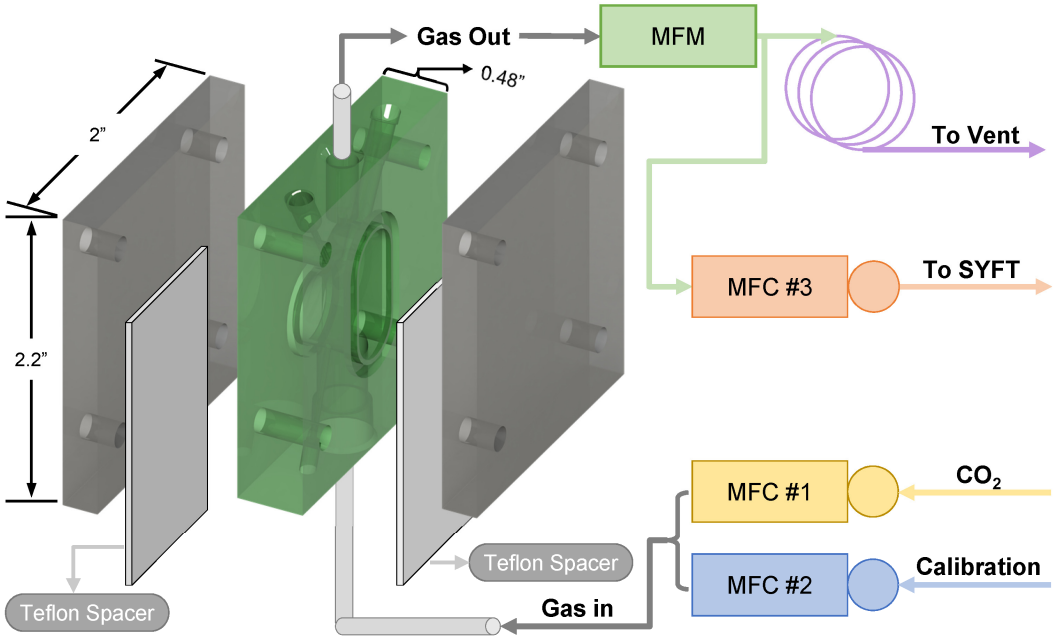

Figure 5.2 SIFT-MS Product Library Testing Schematic: A schematic representation of the experimental setup is shown. The electrochemical cell used is one half of the cell design in Ch 4. The mass flow controllers (MFC) selected the flow of either calibration gas or CO_2 or both into the cell. The mass flow meter (MFM) monitored the flow of gas out of the cell and a portion of this flow was sampled by the SIFT-MS and the rest went to atmosphere.

and then to a T-union. One connection of the T went to the MFC that controlled the inlet flow of gas into the SIFT-MS and the other connection went to some tubing that was open to the atmosphere. It is important to insure that the flow of gas from the cell remains greater than the gas sampling rate of the SIFT-MS, so that the SIFT-MS would not sample the ambient atmosphere. This was confirmed by the observance of methane (which is present in the atmosphere at ~3 ppm) when the inlet was open to atmosphere and the disappearance of this signal when only pure CO_2 was flown past the inlet in the configuration just described. Furthermore, all metal tubing after the electrochemical cell was wrapped in heating tape to prevent the adsorption of water or other chemicals to the walls. In order to calibrate the SIFT-MS at multiple concentration points per gas, the calibration gas was diluted by co-flowing CO_2 into the electrochemical half-cell using a second MFC.

In order to calibrate the SIFT-MS response to the liquid products of CO2R, formic acid, formaldehyde, methanol, acetaldehyde, ethanol, propionaldehyde, and 1-propanol of the highest available purity were acquired (Sigma-Aldrich). 1 mM standard solutions of these chemicals were made in water, except for formic acid which was made in 0.1 M potassium bicarbonate. These solutions were then placed in the half-cell and CO_2 was bubbled through at 5 sccm, the same flow rate which would be used in a real CO2R experiment. The SIFT-MS sampled the effluent gas from the cell in the same way as described above for the gaseous product measurements. In between measurements, the electrochemical cell was cleaned in 1 M nitric acid to ensure there was no cross contamination.

To build the library of product ions, a SIMS program was used on the SIFT-MS to monitor all masses from 19 to 150 for each of the three reagent ions. With this program it took ~90 seconds to complete one cycle of all the masses, thus each experiment was run for 15 minutes to allow the acquisition of 10 data points per *m/z*. This was enough data to confirm that the effluent being sampled was at steady state. In between sample runs, the inlet of the SIFT-MS was connected to a pure CO_2 flow and the baseline was monitored to ensure it returned to the expected state before continuing.

5.4. Results and Discussion

5.4.1. Complications Arising from the Presence of Water Vapor

Initially, the literature built product ion library was used to attempt to calibrate the SIFT-MS. A quick investigation revealed however that the SIFT reactions were not proceeding as suggested in the literature. Table 5.4 shows the results of individually injecting the three most commonly detected hydrocarbon gases: methane, ethylene, and ethane. Highlighted in blue are the expected product ion masses per reagent to monitor when these 3 gases are injected. Highlighted in green are the expected reagent ion counts and highlighted in red are the unexpected reagent ion counts seen in initial experimentation. For example, when the tool was flowing O_2^+ reagent ion (henceforth referred to as the O_2^+ channel), it would be expected that the counts for the

Table 5.4 Interference of Water Vapor with SIFT-MS Performance: A summary of the data collected for the injection of methane, ethylene, and ethane. The data shows that several masses are responding for ethylene and ethane, in particular in the O_2^+ channel, which were not expected to be produced. The high concentration of H_3O^+ reagent ion in the O_2^+ channel is most likely the cause of these additional masses in the O_2^+ channel. The H_3O^+ presence in this channel is due to water vapor in the sample gas be injected into the SIFT-MS

Raw Counts	**Reagent Ions**														
	H_3O^+				**NO^+**				**O_2^+**						
	19	37	29	47	19	30	37	58	19	32	37	28	29	30	47
Background	2.9 E+6	4.1 E+6	2.2 E+2	4.3 E+3	5.8 E+4	8.8 E+6	9.7 E+4	2.6 E+2	1.0 E+5	8.9 E+6	4.6 E+5	4.5 E+2	7.9 E+1	3.0 E+4	4.7 E+2
Methane 1000 ppm	3.5 E+6	3.9 E+6	3.1 E+2	3.7 E+3	6.6 E+4	8.5 E+6	8.4 E+4	2.3 E+2	1.1 E+5	9.6 E+6	3.9 E+5	4.9 E+2	2.7 E+2	3.2 E+4	2.7 E+4
Ethylene 1600 ppm	2.2 E+6	4.6 E+6	4.3 E+3	7.8 E+4		6.1 E+6		1.9 E+2		4.0 E+6		2.0 E+6	7.4 E+4	3.6 E+4	8.2 E+3
Ethane 1000 ppm	3.6 E+6	3.3 E+6	5.0 E+2	3.5 E+3	7.4 E+4	8.4 E+6	7.5 E+4	1.5 E+2	1.6 E+6	7.4 E+6	9.4 E+5	2.4 E+5	1.2 E+5	4.0 E+4	1.7 E+4

Response Factor = (PIC-BC)/BC	**Reagent Ions**														
	H_3O^+				**NO^+**				**O_2^+**						
	19	37	29	47	19	30	37	58	19	32	37	28	29	30	47
Background	2.9 E+6	4.1 E+6	2.2 E+2	4.3 E+3	5.8 E+4	8.8 E+6	9.7 E+4	2.6 E+2	1.0 E+5	8.9 E+6	4.6 E+5	4.5 E+2	7.9 E+1	3.0 E+4	4.7 E+2
Methane 1000 ppm	1.21	0.94	1.36	0.86	1.14	0.97	0.87	0.89	1.07	1.08	0.85	1.08	3.47	1.07	57.5
Ethylene 1600 ppm	0.75	1.13	19.2	18.0		0.70		0.72		0.45		4464	947	1.23	17.5
Ethane 1000 ppm	1.26	0.81	2.23	0.82	1.28	0.96	0.78	0.58	15.62	0.84	2.07	538	1563	1.35	35.7

Expected Reagent Ion Mass | Unexpected Reagent Ion Mass | Product Ion Mass

Green = Expected Product Ion Mass *Red* = Unexpected Product Ion Mass

other reagent ions will be negligible. It is possible for a small amount of NO^+ and H_3O^+ to leak past the upstream quadrupole and into the reaction chamber, but this rate is expected to be low. It is also possible for O_2^+ to react with water vapor in the incoming sample to generate H_3O^+ and H_3O^+ clusters; however, it was explained previously that this reaction should be slow. Despite this, it was found that H_3O^+ (*m*/z = 19) and $H_3O^+(H_2O)$ (*m*/z = 37) were present in the NO^+ and O_2^+ channels in significant concentrations.

As a result of this channel contamination, the product ions being produced for each gas were not always what were expected. The product ion counts in green text represent positive responses at masses that are expected for each analyte. For example, from Table 5.2, it is expected that only ethylene will produce counts at 29 and 47 when reacting with H_3O^+, and indeed in Table 5.4 those two masses did increase when ethylene was injected but not when methane or ethane was injected. However, the product ion counts in red text represent positive mass responses that were unexpected. In this case, it was observed that 28, 29, and 47 all responded to the injection of ethylene in the O_2^+ channel, when only 28 was expected. The presence of these 29 and 47 masses for ethylene can be explained by the high counts of the unexpected reagent ion H_3O^+ in the O_2^+ channel. Clearly the H_3O^+ must be reacting with ethylene to create these masses in the O_2^+ channel where they otherwise wouldn't be expected to be made. The additional unexpected masses, due to the presence of water vapor in the sample gas, seriously undermines the analytical framework that was established earlier to quantify the different products of CO2R. As one example, the observed production of $O_2^+(47)$ by ethylene and ethane directly conflicts with the ability to detect methane which only produces $O_2^+(47)$. The results of this initial investigation clarified the need for a more complete investigation of the product ions produced by SIFT-MS for humidified samples like those found in CO2R experiments.

To be sure that entrained water vapor in the sampled gas was the cause of the high H_3O^+ counts in the O_2^+ channel, attempts were made to dry the gas before entering the SIFT-MS. In this way the water vapor which is converted into the reactive H_3O^+ ion is eliminated. Several different methods were investigated to dry the gas, including chemical drying agents like magnesium sulfate and a low temperature moisture trap. These were found to be capable of removing the water vapor from gas taken directly from the cylinder; however, none of these were capable of removing the amount of water vapor that was picked up when bubbling the gas through water, as would be done in a CO2R experiment. Thus it was determined that it would be impractical to calibrate the tool for a condition that was incompatible with the final experimental procedure and no further attempts were made to precondition the gas for the SIFT-MS.

5.4.2. Building a New Product Ion Library

To build a new product ion library, a full mass SIMS scan was made to monitor all the masses from 19 to 150 for all three reagent ion channels. The four hydrocarbon gases, formic acid, and the C_1-C_3 aldehydes and alcohols were reviewed in this initial study. The other minor liquid products, like glyoxal and hydroxyacetone, have not yet been investigated and will be the subject of future study. The resulting mass spectra were then reviewed to determine which masses were

Table 5.5 New Mass Library for SIFT-MS: Using the full mass survey, all the masses which responded to each injected compound were recorded. Several more product ion masses were identified in this survey then were initially proposed by the literature review. Despite this, it is possible to identify masses that allow for the unique identification of each compound tested here.

	Reagent Ions		
	H_3O^+	NO^+	O_2^+
Mass of Reactant Ions	***19 (37, 55)***	***30 (48)***	***32 (50)***
Analyte	*m/z* Products	*m/z* Products	*m/z* Products
Methane	NR	NR	**47**
Ethylene	**29** 47 65 67 69	41 **56**	**28** **29** 42 46 47 57 58
Ethane	28	28	20 **21** 26 27 **28** **29** 47 51
Propylene	41 43 43 44 85	41 43 72	40 **41** 42 69
Formic Acid	ND	ND	ND
Formaldehyde	65	45 75	**75**
Methanol	33 51 52 53 69	33 51 52 **62**	31 49 51
Acetaldehyde	**45** 46 63 64 89	43 45 63 74	43 44 45 61 62 63
Ethanol	47 48 65 66	45 47 63 **65** 76	31 45 47 49 63 64 65
Propionaldehyde	41 58 59 60 77 78 117 118	29 **57** 58 59 60 75 76 77 133	29 40 48 57 58 59 75 76 77 116 117 118 133
1-Propanol	43 **79** **80**	**59** 60 77	31 42 49 59 77
	Duplicate *m/z*	Duplicate *m/z*	Duplicate *m/z*

NR = No Reaction ND = Not Detectable *Green* = Usable Unique Mass *Orange* = Usable Mass but Deconvolution Required

Table 5.6 Response Factor of CO2R Products in SIFT-MS: Selecting only the masses that will be used to identify the various products of CO2R, the response factors of every chemical is calculated. From these response factors it can be seen how sensitively the SIFT-MS can detect these various products. Masses that will require deconvolution in order to identify just one product of CO2R also become apparent.

	RESPONSE FACTOR												
	Methane	Ethylene*	Ethane	Propylene	Formic Acid	Form-aldehyde	Methanol	Acet-aldehyde	Ethanol	Propion-aldehyde	1-Propanol		
M/Z	1000 ppm	1600 ppm	1000 ppm	100 ppm	1 mM	1 mM	1 mM	1 mM	1 mM	1 mM	1 mM	***m/z* Assignment**	**Comments**
29+ (19+)	0.05	**18.4**	1.26	1.02	-0.27	-0.22	-0.26	-0.12	1.13	-0.26	-0.21	*Ethylene*	Not very sensitive
45+ (19+)	-0.07	-0.54	-0.11	-0.11	0.04	2.21	-0.04	**177**	-0.14	-0.35	-0.11	*Acetaldehyde*	Unique, negligible contribution from other components
79+ (19+)	-0.08	-0.42	-0.34	1.39	0.11	-0.44	-0.24	-0.28	-0.09	0.41	**12.9**	*1-Propanol*	Not very sensitive
80+ (19+)	0.17		0.08	0.83	0.21	-0.38	-0.25	-0.30	-0.36	0.77	**12.4**	*1-Propanol*	Not very sensitive
56+ (30+)	-0.33	**14.8**	0.36	3.60	0.36	0.04	-0.19	-0.40	0.18	-0.10	0.38	*Ethylene*	More unique than 29+ (19+) but lower sensitivity
57+ (30+)	-0.41	-0.77	-0.51	-0.40	-0.34	-0.14	-0.60	-0.57	-0.56	**621**	-0.55	*Propionaldeyde*	Unique
59+ (30+)	-0.71	-0.87	-0.75	-0.47	0.48	-0.76	-0.26	-0.78	-0.76	11.7	**58.1**	*1-Propanol*	More sensitive but requires propionaldehyde subtraction
62+ (30+)	-0.59	0.40	-0.76	-0.44	-0.50	1.50	**64.5**	0.17	-0.22	-0.40	-0.18	*Methanol*	Unique, negligible contribution from other components
65+ (30+)	-0.08		-0.31	-0.92	0.11	1.25	0.14	-0.01	**13.8**	-0.33	-0.17	*Ethanol*	Unique but not very sensative
21+ (32+)	0.28		**18.1**	0.20	-0.01	-0.42	-0.06	0.66	-0.07	0.09	-0.25	*Ethane*	Unique but not as sensitive 28+ (32+) or 29+ (32+)
28+ (32+)	-0.36	**2676**	**322**	0.00	-0.48	-0.43	-0.65	-0.61	-0.51	6.70	-0.43	*Ethane/Ethylene*	Requires subtraction
29+ (32+)	0.20	**327**	**541**	2.08	-0.81	-0.77	-0.81	-0.16	-0.70	10.7	-0.74	*Ethane/Ethylene*	Requires subtraction
41+ (32+)	-0.13		2.02	**481**	0.08	-0.74	-0.42	-0.44	0.14	7.99	1.81	*Propylene*	Unique, negligible contribution from other components
47+ (32+)	**55.8**	16.32	34.29	-0.19	-0.02	-0.08	0.03	0.31	7.17	0.37	-0.08	*Methane*	Requires subtraction
75+ (32+)	0.20		0.58	0.22	0.24	**73.7**	0.34	-0.59	-0.16	5.00	0.15	*Formaldehyde*	Requires propionaldehyde Subtraction

Response Factors Greater than 1 *Green* = Unique Product Ion *Orange* = Product Ion Requiring Deconvolution

responding for each analyte. Fairly high concentrations of each analyte were used in this analysis to ensure that all possible product ions responded regardless of reaction rate. Table 5.5 shows the results of this investigation. Highlighted cells represent those masses which have contributions from more than one analyte.

When compared to Table 5.2, it is observed that many more masses are responding for each analyte than the literature predicted. However, this investigation also shows that it should still be possible to deconvolute and quantify all of these chemicals. The masses with the largest response factors for each analyte were analyzed and a new framework was hypothesized. In Table 5.5, the masses which should provide the most sensitive unique detection of their corresponding analyte are highlighted in green. Highlighted in orange are the masses which can also be used to detect certain analytes but require deconvolution due to the contribution of multiple chemicals to that mass. It can be seen that there is at least one mass that can be used to detect every hydrocarbon, aldehyde, and alcohol. Experiments were run to see if formic acid could be detected; however, it was found that no mass responded. This reinforces the earlier hypothesis that formic acid and acetic acid vapor cannot be detected because they are fully deprotonated at typical CO2R electrolyte pHs.

Using the highlighted masses as the new detection framework, the response factors of all the analytes were compared (Table 5.6). In doing this, it can be seen which masses may have conflicts which need to be deconvoluted and which masses are truly unique. The response factor (RF) was calculated as,

$$RF = (PIC - BC) / BC \tag{5.9}$$

Where the product ion counts (PIC) are the number of counts per second obtained at a given *m/z* that responds to the analyte and the background counts (BC) are the counts per second obtained at the same *m/z* when pure CO_2 is injected into the SIFT-MS. Highlighted in purple are the masses for each analyte which gave a response factor greater than 1. For each *m/z*, the highest response factor is highlighted in green or in some cases orange. These highest response factors correspond to the masses for each analyte identified in Table 5.5 which are to be used to quantify the analyte. In some situations it is clear that for a given mass, more than one analyte has a comparable RF, and in these situations deconvolution will need to be applied. For example with mass 59(30+) (*m/z* 59+ in the NO^+ channel), there are comparable contributions of both propionaldehyde and 1-propanol. However, using the unique mass 57(30+) to quantify propionaldehyde, propionaldehyde's contribution to 59(30+) can be subtracted away, leaving just the contribution of 1-propanol.

5.4.3. Testing the New SIFT-MS Analytical Framework

With this new framework in place test cases were run to confirm that individual components could be identified in multiple component systems (Table 5.7). It should be noted here that only the *m/z*'s listed in Table 5.6 as well as the reagent ion masses were monitored for these experiments. With this streamlined SIMS experimental method, the relevant masses could

Table 5.7 Cross Sensitivity Response Factor Analysis of CO2R Products in SIFT-MS: Several case studies were taken to see if the RFs for a mixture would be the same as the sum of the two individual components of that mixture. It can be seen that in both systems that require deconvolution (formaldehyde + propionaldehyde & 1-propanol + propionaldehyde) and those that don't (ethane + propionaldehyde & propylene + propionaldehyde), the RF's for the mixture represent close to the sum of the individual components.

Mass Assignment	*M/Z*	Ethane	Propion-aldehyde	Ethane + Propionaldehyde	Propylene	Propion-aldehyde	Propylene + Propionaldehyde	Form-aldehyde	Propion-aldehyde	Formaldehyde + Propionaldehyde	1-Propanol	Propion-aldehyde	1-Propanol + Propionaldehyde
	NA	1000 ppm	1 mM	1000 ppm + 1 mM	100 ppm	1 mM	100 ppm + 1 mM	1 mM	1 mM	1 mM + 1 mM	1 mM	1 mM	1 mM + 1 mM
1-Propanol	*79+ (19+)*	-0.47	0.95	1.14	0.36	1.01	1.44	-0.22	1.01	0.88	18.4	1.01	17.2
Propionaldeyde	*57+ (30+)*	-0.83	262	271	-0.40	230	212	-0.66	230	232	-0.82	230	268
1-Propanol	*59+ (30+)*	-0.77	25.03	25.66	-0.54	20.7	17.1	-0.56	20.7	23.8	110	20.7	137
Ethane	*21+ (32+)*	12.06	0.54	11.4	-0.10	-0.20	-0.04	-0.38	-0.20	-0.02	-0.19	-0.20	-0.02
Propylene	*41+ (32+)*	0.60	1.17	2.92	366	15.3	358	-0.73	15.33	0.77	1.90	15.3	3.35
Formaldehyde	*75+ (32+)*	3.22	9.80	18.08	0.05	6.49	6.57	113	6.49	125	0.76	6.49	14.5

be measured every ~5 seconds instead of every ~90 seconds, which was required when doing the full mass range scan used for library development. Thus the time resolution of the experiments is within a nice range. This time resolution could be further improved if needed by focusing the method on only two compounds instead of the full set.

In the first two test cases, unique systems were combined. First ethane at 1000 ppm and 1 mM propionaldehyde were tested. The response factors of the individual components and then the response factors of their mixture are shown in Table 5.7. It can be seen that neither component was expected to contribute significantly to the other and the mixture showed that as well. Both 57(30+) (propionaldehyde) and 21(+32) (ethane) deviated less than 10% from the value obtained for the individual component. The second test was combining 100 ppm propylene and 1 mM propionaldehyde. Like the first test, neither component contributed significantly to the other. Furthermore, the test of the mixture gave response factors very similar to that of the individual components.

In the second two cases, mixtures that required subtraction were combined. The first was a combination of 1 mM formaldehyde and 1 mM propionaldehyde. From the individual component data, the propionaldehyde *m/z* (57(30+)) is expected to be unique while the formaldehyde *m/z* (75(32+)) has a small contribution from propionaldehyde. Appropriately, the mixture of the two at the 75(32+) mass has a higher RF than the individual components and the sum of the two individual component's RFs come within 10% of the mixture. The second combination tested was 1 mM 1-propanol and 1 mM propionaldehyde. Here two masses for 1-propanol are shown, 79(19+) which is not very sensitive but is mostly unique for 1-propanol, and 59(30+) which is more sensitive but convoluted with propionaldehyde. This experiment shows that either mass could be used for 1-propanol. 59(30+) is a combination of the two individual RFs within 10% and 79(19+) is within 10% of the individual component response of 1-propanol.

To further test this new analytical framework, a CO2R experiment was run using copper foil as a catalyst. In this simple experiment, the full electrochemical cell was set up as described in chapter 4, except using the cell made of PEEK. 0.1M $KHCO_3$ was used as the electrolyte and -1.0V vs. RHE was applied to the Cu. The unique masses 45(19+), 57(30+), and 79(19+) were measured to investigate the time evolution of acetaldehyde, propionaldehyde, and 1-propanol respectively. Figure 5.3a shows the raw counts produced by the SIFT-MS for each *m/z* being watched. Before time 0, there is a very low baseline of counts at each of these masses. Then at time 0, the potential is applied to the electrode and it can be observed that the masses start to rise immediately. This data can be further analyzed and converted into response factors, like was done above (Fig. 5.3b). The final step to analyze this data is to convert the response factors into concentrations (Fig. 5.3c). As an example, this was done here with the single concentration calibration point taken above, creating a 1-point calibration curve and assuming the response is linear as concentration increases. This is not a completely rigorous approach but it is instructive to show that different products have different response factors. Looking at the raw data alone can be misleading as it can be seen from the Figure 5.3c that 1-propanol and acetaldehyde are being

produced at close to the same rates, a point that is not obvious from examining the response factors or raw counts. The conclusion from this experiment is that all three of these liquids onset together and are produced at a fairly constant rate throughout the experiment. This kind of real-time information about the production rate of liquids from CO2R has not been readily available thus far and it is a strong motivation for further development of this SIFT-MS analytical technology.

5.5. Outlook

The preliminary analysis of SIFT-MS to detect the products of CO2R has shown some promise and a partial library of the product ions produced by the SIFT reagent ion reactions in a humid environment has been assembled. Based off the levels of analytical detail introduced earlier, it is worth revisiting SIFT-MS in comparison to the other real-time CO2R product detection systems. The results of the investigation here show that SIFT-MS is clearly capable of at least level 2 detection and with additional study, is likely capable of level 3 detection, for many if not all of the compounds studied here. This puts SIFT-MS on par with the system developed by Koper, but capable of detecting far more products. With additional study on the calibration of the *m/z* response factors, it should be possible to match the level 3 detection developed by Bell with the ability to detect additional products as well. This comparison has been summarized in Table 5.8.

In the future, the product ion library developed here will need to be completed with the remaining CO2R products which were not reviewed: glyoxal, glycolaldehyde, acetic acid, ethylene glycol, hydroxyacetone, acetone, and

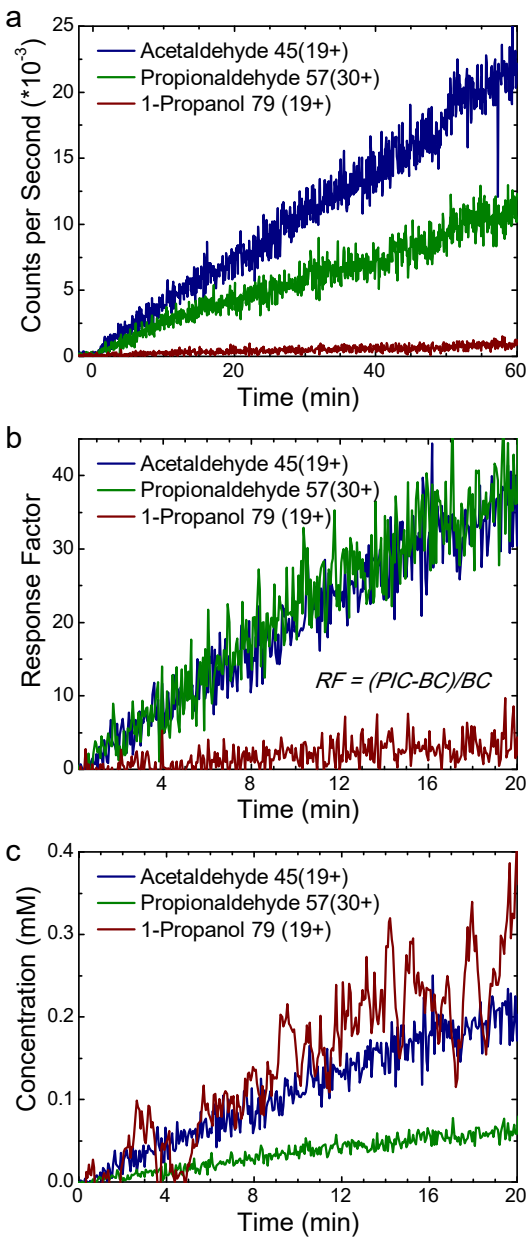

Figure 5.3 SIFT-MS Analysis of Cu for CO2R: Cu foil was used as a CO2R catalyst at ~1.0V vs. RHE in 0.1M $KHCO_3$. SIFT-MS was used to analyze the production of acetaldehyde, using mass 45(19+), propionaldehyde, using mass 57(30+), and 1-propanol, using mass 79(19+). (a) The raw counts over the 60 minute run are shown and it can be seen the counts steadily rise, corresponding to the expected rise in liquid product concentration in the electrolyte over time. (b) The raw counts are converted to a response factor, focusing on the first 20 minutes of the run. (c) The raw counts are converted to concentration using a rough 1-point calibration curve.

Table 5.8 Comparison of Real-Time CO2R Analytical Tools: A comparison of the SIFT-MS to the state of the art real-time CO2R product detection systems of Bell[85] and Koper[191] is given. The compounds that each system can detect are checked and highlighted in green. The analytical level is given of 1, 2, or 3 with 3 being the highest fully quantifiable detection level.

	H_2	CO	CH_4	C_2H_4	C_2H_6	C_3H_6	HCOOH	CH_2O	CH_3OH	CH_3CHO	C_2H_5OH	C_2H_5CHO	C_3H_7OH	Analytical Level	Comments
Koper	✓		✓	✓	✓				✓	✓	✓			Level 2	Can't be quantitative
Bell	✓		✓	✓	✓						✓		✓	Level 3	
SIFT-MS			✓	✓	✓	✓		✓	✓	✓	✓	✓	✓	Level 2 – Level 3 with additional study	Additional compounds may be detectable with further study

allyl alcohol. In light of this completed library, the analytical framework to select which *m/z* values can be used to identify each product will need to be reevaluated. This library will also need to be extended to include the testing of these chemicals at multiple concentration levels to ensure the product ion fingerprint doesn't change. This data can then be used to generate calibration curves to make this analytical technique quantitative.

Some promising initial tests performed here confirms that the chemicals, which were mostly detected as individual components, can still be detected in a mixture as a sum of the mixtures parts. Table 5.7 summarized a few experiments supporting this conclusion; however, additional tests are needed in this area, utilizing increasingly complex mixtures. The end goal would be to establish a reference table for 16 individual components RF's and then identifying a mixture of all 16 components showing the resulting RFs are a summation of the individual components. This is the capstone experiment that shows that all the products from a potentially new CO2R catalyst can be correctly identified with SIFT-MS (level 3 analytical system). Once the SIFT-MS analytical capabilities have been completely understood, the dynamics of liquid product generation on CO2R catalysts, in particular Cu and Cu based catalysts, should be studied in depth.

5.6. Conclusion

In this chapter, the application of SIFT-MS to the detection of the products of CO2R was explored. Hypothetically, there are many advantages to using SIFT-MS as an analytical tool over other real-time analysis tools like electron ionization MS. In particular, examination of the literature suggested that the soft chemical ionization utilized in SIFT-MS would allow for the simultaneous detection of most of the CO2R products. When the SIFT-MS was tested in a real experimental setting, it was found that the presence of water vapor in the sample stream dramatically changed the reaction chemistry and thus what product ions to expect for an injected

analyte. Nevertheless, thorough investigation of a subset of the CO2R products showed that these chemicals could all still be uniquely identified using SIFT-MS. Several sample product combination experiments confirmed the capability of the SIFT to successfully detect, in real-time, the individual components of a mixture qualitatively. Additionally there is a strong indication that this can be converted in the future to a quantitative analysis. Finally a preliminary examination of the production of acetaldehyde, propionaldehyde, and 1-propanol on Cu was performed. It was found that all three of these chemicals appear to onset at the same time and are produced at a constant rate throughout the reaction.

Further scrutiny still remains to fully confirm the capability of SIFT-MS to be used as a quantitative, real-time, analytical technique for detecting the products of CO2R; however, the promising results reported here provide a compelling proof of concept.

5.7. Acknowledgments

Work on this project was supported by the Singapore-Berkeley Research Initiative in Sustainable Energy (SinBeRISE). I acknowledge Dr. Lily Mandel and Dr. Mallikarjuna Rao Motapothula for their helpful discussions and especially Lily for her assistance in performing some of the experiments shown here. I acknowledge Prof. Jens Martina and Prof. Thiru Venky for their useful conversations related to the SIFT-MS. I acknowledge Prof. Joel Ager for his knowledgeable conversations about ion chemistry. I acknowledge Prof. David Smith for his deep knowledge of SIFT-MS and the invaluable conversations about the fundamental operation of the tool.

6. Activity of Hierarchal Templated Nanowires for CO2R

6.1. Introduction

Electrochemical CO_2 reduction (CO2R) has seen a large increase in interest over the past several years.[111,112,221–224] This has led to the discovery of a number of new catalysts where both selectivity and activity have been improved.[106,107,118,156,176,199,225–227] However, a coherent picture of how to tune a catalyst to affect a specific change in product distribution has not emerged experimentally, although some guidance has been provided by theory.[228–230] As an example, there has been a great deal of attention given to oxide-derived materials.[112] In particular, in the seminal work performed by Hori *et. al*[231] and expanded on by Li *et. al*,[118] oxide-derived copper was shown to greatly reduce the overpotential required to produce carbon monoxide (CO) and formic acid. However, this catalyst was made in such a way that there was a significant enhancement in surface area as well as a change in surface facet. Several other oxide-derived copper materials have also been investigated and suffer from the same convolution of a large change in surface area as well as surface facet.[108,118,226,232–235] In the previous chapters, I have outlined the methods by which a CO2R catalyst can be rigorously characterized, including the appropriate type of electrochemical cell to use in combination with reliable gaseous and liquid product detection systems. It is the goal of this study to investigate a well-defined catalyst where only surface area is changed and the surface facet exposed to the electrolyte is left largely unchanged. In this way the change in activity of a CO2R catalyst due to surface area enhancement alone can be elucidated.

It is desirable to separate out the effects of surface area and surface facet change because both could be affecting the catalyst activity. It has been shown previously that different facets of copper (Cu) show different activities to CO2R and it has been proposed and observed that highly disordered surfaces favor the production of C_2 products (ethylene, ethanol, 1-propanol etc).[236–239] On the other hand, it has also been proposed that an increase in the electrolyte pH near the electrode surface is responsible for increasing the selectivity of Cu to C_2 products.[104,109,158,240] It is expected that the pH at the electrode surface will rise during CO2R, sometimes many pH units higher than the bulk electrolyte pH.[104,117,158] This local surface pH rise is a widespread phenomenon in electrochemistry[241] and the magnitude of this change is linked directly to the production or consumption rates of hydroxide or hydronium respectively, or in other words, to the magnitude of the current. The importance of local pH has been quantified through experimental measurements for HER[242,243] and the electrodeposition of Ni, where the surface pH plays an important role in the quality of the deposit.[244,245] In the near neutral electrolyte conditions typical of CO2R, the pH change is expected to be more drastic. High surface area contributes to a larger rise in surface pH due to the larger geometric current densities. Thus the high surface area oxide-derived catalysts are a convolution of both of these effects and both have been used by various authors to explain the change in activity of their catalysts.

Many of the oxide-derived copper catalysts are nanowire-like in structure, thus, in order to study the effect of surface area only in a similar system a technique to fabricate a copper nanowire

structure was identified. Anodized aluminum oxide templated electrochemical growth was chosen as it has been utilized to grow a wide array of nanowire structures[246] and it should allow rigorous control over the growth process. The template sets the diameters of the nanowires, allowing access to wire diameters on the order of those seen in oxide-derived catalysts (d ~ 20 nm) as well as much larger diameter wires (d ~ 150 nm). The length of the nanowires is directly controlled by the electrodeposition parameters used. Thus the surface area of the catalyst is highly controllable.

There have been previous efforts to investigate nanowire and micro-porous copper catalysts, although none have specifically targeted understanding the effect of surface area enhancement. There have only been a few studies where the copper nanostructure fabrication did not use an intermediate oxide.[122,247] Details from these studies along with relevant Faradaic efficiencies (FEs) are reported in Table 6.1 along with reference data for planar Cu.[121] These studies show a large production rate of hydrogen and the main CO2R product is formic acid, with little hydrocarbon or alcohol production. This is despite relatively low current densities at applied potentials of greater than -0.9V vs RHE. It should be noted that neither study used iR compensation in their electrochemical measurements, so it is likely that the reported voltage is an overestimate of the electrode surface potential.

Many other nanowire and micro-porous copper catalysts have been prepared through an oxide intermediate, such as copper hydroxide nanowires,[232,233] thermally-grown copper oxide nanowires,[118,234] or air-oxidized copper foam.[226] Some of the data from this literature is summarized in Table 6.1 as well.[4,5] These oxide-derived catalysts tend to show a high selectivity to ethylene over methane. In some cases these catalysts show high current densities, due to an over 100x increase in surface area (Raciti *et al.*: 321x, Li *et al.*: 475x), which is accompanied by a fairly high hydrogen FE (Raciti *et al.*: 67% versus Kuhl *et al.*: 25%). The high HER activity is possibly due to mass transfer limiting the availability of CO_2 at the electrode surface and thus hindering CO2R. The concentration of CO_2 in the electrolyte is governed by Henry's law and the solubility limit is only 33 mM in water. This results in a mass transfer limited flux of ~46 nmol cm^{-2} s^{-1} of CO_2 to the electrode surface for a typical 100 μm boundary layer when solving a diffusion model similar to that developed by Gupta *et al*.[158] If a catalyst produced 100% CO, then a current density of only ~9 mA cm^{-2} would reach this mass transfer limited flux. This high HER activity isn't observed when the catalyst surface area enhancement is limited, as shown by Dutta *et al.* where the surface area enhancement was limited to 4.4x.

Combined, these studies show there has been a limited investigation of high surface area

---

[4] The work by Ming *et al.* is not included as their measured reference data for planar Cu does not conform to the accepted activity for planar Cu as measured in our lab and others,[28,121] thus their data is deemed unreliable.

[5] It should be noted that Li and Kanan conclude that the change in selectivity for their catalyst is not due to the nanowire morphology, as similar enhancements were observed on oxide derived catalysts that didn't show nanowire morphology

Table 6.1 Literature Review of Nanowire and Microporous Cu Catalysts: Data from recently published work is summarized here. Highlighted in green are the catalysts that were synthesized directly from Cu. Highlighted in red are catalysts that were synthesized through an oxide intermediate. * = H_2 is calculated through subtraction because data not given

Sen *et al*. 2014	Cu foam synthesized electrochemically - 15 sec Cu deposition data shown												
Electrolyte	**iR Comp**	**Voltage (vs. RHE)**	**J_{geo} (mA cm^{-2})**	**H_2**	**CO**	**CH_4**	**C_2H_4**	**C_2H_6**	**HCOOH**	**EtOH**	**C_3H_6**	**FE to CO2R**	**FE to > 2e- Products**
0.1 M $KHCO_3$	No	-1.1	8	60	7.2	0.2	1.2	1.4	25.2	<1%	0.1	35.3	2.9
		-0.9	4.1	55	7.4	0.2	1.3	1.1	36.6	<1%	0.2	46.8	2.8
Chung *et al*. 2016	Cu nanowires grown in AAO - Cu-5h data shown												
Electrolyte	**iR Comp**	**Voltage (vs. RHE)**	**J_{geo} (mA cm^{-2})**	**H_2**	**CO**	**CH_4**	**C_2H_4**	**C_2H_6**	**HCOOH**	**EtOH**		**FE to CO2R**	**FE to > 2e- Products**
0.1 M $KHCO_3$	No	-0.9	4.5	76	3	NM	NM	NM	17.4	NM		20.4	0
		-0.8	3.3	73	2.1	NM	NM	NM	21.6	NM		23.7	0
Raciti *et al.* 2015	Electrochemically reduced CuO nanowires on gauze - ECR Cu data shown												
Electrolyte	**iR Comp**	**Voltage (vs. RHE)**	**J_{geo} (mA cm^{-2})**	**H_2**	**CO**	**CH_4**	**C_2H_4**	**C_2H_6**	**HCOOH**	**EtOH**		**FE to CO2R**	**FE to > 2e- Products**
0.1 M $KHCO_3$	Yes	-0.995	119	67	0.6	0.5	6.5	0.9	0.9	8.9		18.2	16.7
		-0.895	64	59	0.9	0	8.2	3.5	3.6	11.3		27.5	23
Dutta *et al*. 2016	Electrochemically reduced CuO foam synthesized electrochemically - 20 sec Cu deposition data shown												
Electrolyte	**iR Comp**	**Voltage (vs. RHE)**	**J_{geo} (mA cm^{-2})**	**H_2**	**CO**	**CH_4**	**C_2H_4**	**C_2H_6**	**HCOOH**	**EtOH**		**FE to CO2R**	**FE to > 2e- Products**
0.5 M $NaHCO_3$	Yes	-1	23.7	36	4.8	ND	18.8	22.8	4	NM		50.4	41.6
		-0.9	16.5	28	9.2	ND	18.4	29.9	6	NM		63.5	48.3
		-0.8	12.7	15	15	ND	19.6	33.9	6	NM		74.6	53.5
Li *et al*. 2012	Electrochemically reduced thermally grown CuO nanowires												
Electrolyte	**iR Comp**	**Voltage (vs. RHE)**	**J_{geo} (mA cm^{-2})**	**H_2***	**CO**	**CH_4**	**C_2H_4**	**C_2H_6**	**HCOOH**	**EtOH**	**PrOH**	**FE to CO2R**	**FE to > 2e- Products**
0.5 M $NaHCO_3$	No	-1	31	98	2.3	ND	ND	ND	ND	NM	NM	2.3	0
		-0.9	19	83	5.1	ND	4.4	7.6	ND	NM	NM	17.1	12
		-0.8	12.2	50	7.8	ND	3.3	5.8	22.1	3.7	7.1	49.8	19.9
		-0.6	3.2	32	28	ND	1.2	2.2	32.5	4.6	ND	68.5	8
Kuhl *et al*. 2012	Planar Cu Reference Data												
Electrolyte	**iR Comp**	**Voltage (vs. RHE)**	**J_{geo} (mA cm^{-2})**	**H_2**	**CO**	**CH_4**	**C_2H_4**	**C_2H_6**	**HCOOH**	**EtOH**	**PrOH**	**FE to CO2R**	**FE to > 2e- Products**
0.1 M $KHCO_3$	Yes	-1.09	9.2	22	0.6	29.6	20.9	ND	1.4	9.2	2.1	63.9	61.8
		-1.01	3.6	25	4	17.4	17.9	ND	10.7	5.6	4	59.8	45
		-0.89	1.2	38	8.7	0.7	3.6	ND	24.6	0	0	37.7	4.4
		-0.82	0.9	44	7.6	0.1	1.8	ND	22.7	0	0	32.3	2

copper catalysts and a consensus has yet to emerge on what the activity of such a catalyst should be. Furthermore, the use of an oxide intermediate growth pathway in some of the studies prevents the evaluation of the change in activity solely based on surface area enhancement. Finally, the high hydrogen production rates exhibited by most of these catalysts are indicative of CO_2 mass transport limitations which may be inhibiting the observation of intrinsic catalyst activity. This literature review confirms that there is a need for a rigorous study of the activity of controlled surface area catalysts.

In this study, the activity of copper nanowires grown by template-assisted electrodeposition is investigated. In order to be able to investigate the effect of surface area on the production of hydrocarbons, it will likely be necessary to be able to drive the catalyst in excess of -0.9V vs. RHE. At this high potential, it is expected that a high surface area catalyst will draw a proportionally higher current density. This is a concern due to the known mass transport limitations that exist in CO2R when attempting to access high current density regimes. Thus the length of the nanowire (NW) array, and accordingly the surface area enhancement, will need to be controlled in a regime where mass transport doesn't dominate the overall activity of the catalyst. This will enable a systematic study of the effect of surface area on the production of hydrocarbons and alcohols on a Cu surface that has not undergone surface facet modification.

6.2. Experimental

6.2.1. Growth of Copper Nanowires

Copper nanowires were grown using anodized aluminum oxide template-assisted electrodeposition, a common practice used to grow a wide variety of metal and semiconducting materials.[248] The procedure used here to grow metal nanowires was adapted from Banholzer *et. al*.[249] To start, anodized aluminum oxide (AAO) membranes (Hefei Pu-Yuan Nanotechnology Limited Company) with various pore sizes were used as the templates. These AAO templates are approximately 60 um thick, 25 mm in diameter, and both sides of the pores have been completely opened. This resulted in a membrane with periodically spaced columns that can be filled with different materials. The AAO templates were not removed from their aluminum surround material, from which the templates were grown (the template is shown schematically in Fig.6.1 and pictured in Fig. 6.2). For the following experiments, only the AAO templates with 110-150 nm diameter pores were used.

An overview of the nanowire growth process is given schematically in Figure 6.1. The nanowires are grown in the AAO pores by electrodeposition; however, in order to deposit the copper an electrical contact first needed to be applied to one side of the membrane. Two μm of high purity Cu deposited by electron-beam evaporation served as this contact. This thickness of copper was found to be necessary to completely close the AAO pores, which was important during the electrodeposition procedure to prevent electrolyte solution from leaking through the membrane. Once the Cu contact was put down, the sample was mounted into a custom Teflon

electrochemical deposition cell. The cell consisted of a 1.77 cm^2 cylinder drilled through the rectangular Teflon block. A fluorinated ethylene propylene (FEP)-coated Viton O-ring (McMaster Carr), the AAO membrane with the evaporated Cu facing away from the cylinder, a piece of aluminum foil (which served as a contact to the Cu), and a Teflon back plate were compressed onto one side of the column. On the other end, a coil of platinum wire served as the counter electrode. An Ag/AgCl reference electrode (CH Instruments) was inserted perpendicularly to the cylinder through the side of the Teflon cell and sealed with an O-ring compression fitting (Fig. 6.2). The column was then filled with the Cu electrodeposition electrolyte, which consisted of 500 mM copper sulfate (99.999%, Alfa Aesar) adjusted to pH 1 with sulfuric acid (99.99% Sigma Aldrich).

Electrodeposition was performed at constant current via a two-step sequence with a Bio-Logic SP-300 potentiostat. First a high current pulse (40 mA) was applied for a short time (3 seconds) to encourage uniform nucleation of the wires in the pores. Then a low current pulse (2 mA) was applied to grow the nanowires. The time of the low current pulse controlled the amount of copper deposited which controlled the height of the resulting nanowires. At the end of the deposition the AAO template was washed thoroughly with DI water and gently blown dry with N_2. To confirm the height of the deposited NWs, a small section of the AAO template was cracked off and examined by cross-sectional scanning electron microscopy (SEM, FEI Quanta 200 FEG).

The remaining piece of the AAO template needed to be mounted to a substrate in order to continue with the etching procedure to remove the aluminum oxide and release the free standing NWs. The 2 μm Cu film did not have the structural integrity to remain flat once the 60 um of aluminum oxide was etched away. To overcome this, the filled template was mounted on a glass

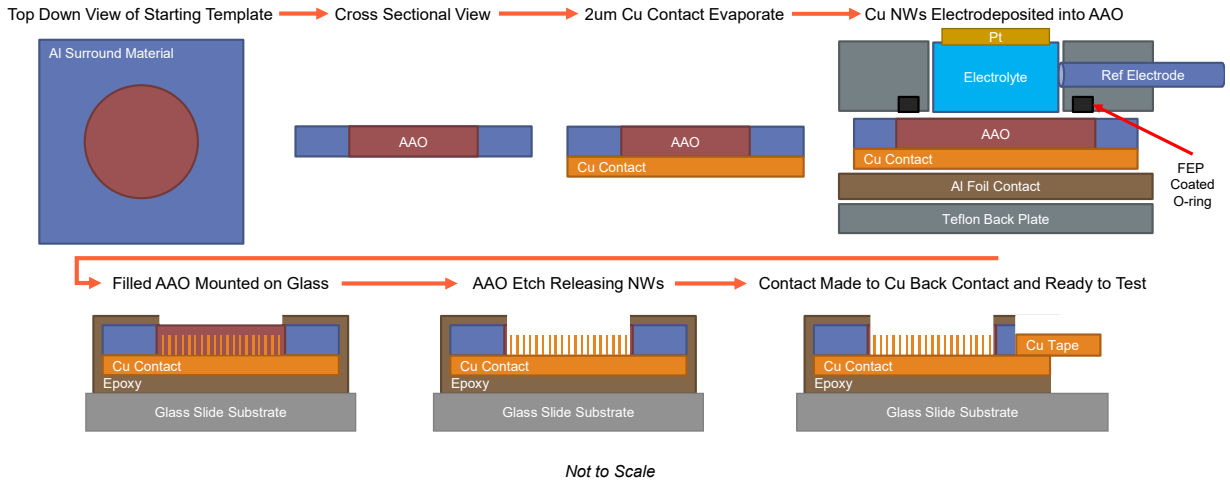

Figure 6.1 Schematic of Cu NW Deposition Process: In the top left an as-received AAO template is shown schematically. First a 2 um Cu film is evaporated onto the back of the template. Then the template is mounted into the electrodeposition cell and Cu is electrodeposited into the AAO pores. The AAO, with Cu NWs now inside it, is mounted with epoxy onto a glass slide and the Al metal surround is covered with epoxy. Then the AAO is etched away to release the free standing Cu NWs. Finally, part of the Al surround and epoxy is cut away to gain access to the Cu back contact to which adhesive Cu tape is attached to make electrical contact to the NW array for CO2R testing.

slide using DP-105 epoxy (3M). Many different epoxies were tested, including silver based paints, and this epoxy was found to be the only one that was both strong enough to secure the film and capable of surviving the 1M sodium hydroxide (NaOH) etch used to remove the aluminum oxide. The Al metal surround to the template also needed to be covered so that it would not etch and contaminate the sample during the etching treatment. To accomplish this a simple doctor blading technique was used with the epoxy to insure a flat and even coating of epoxy over the Al. It was important that the epoxy coating be flat so that the sample could be directly mounted into the CO2R electrochemical cell for testing. The epoxied stack was cured at 70°C for 3.5 hours.

To remove the AAO template and leave behind the Cu NWs, a 1M NaOH etching procedure was used. The NaOH is expected to rapidly etch the AAO while not attacking the Cu.[250] The stack was etched in 1M NaOH (ACS grade, Sigma-Aldrich) for 30 minutes and then rinsed with water. Then a second etch in 1M NaOH was performed for 15 minutes after which the sample was again rinsed with water. Finally a third etch in high purity 1M NaOH (99.99%, Sigma Aldrich) was performed for 15 minutes to ensure the complete removal of any Al impurities from the Cu surface. This is important as Al is known to produce hydrogen under CO2R conditions.[174] The sample was then rinsed thoroughly with water and gently blown dry with N_2. The removal of all Al was confirmed by energy dispersive x-ray spectroscopy (EDX) analysis of the sample. Further inductively coupled plasma mass spectrometry analysis of the samples should be done in the future to confirm the complete absence of impurity metals. Top down SEM of the released Cu NW samples confirmed the removal of the AAO and showed freestanding NWs.

Finally electrical contact was made to the released NW array by cutting away a small section of the epoxy covered Al surround. It was found that the Al could easily be pulled apart from the evaporated Cu back contact. Thus peeling and cutting away the epoxy covered Al

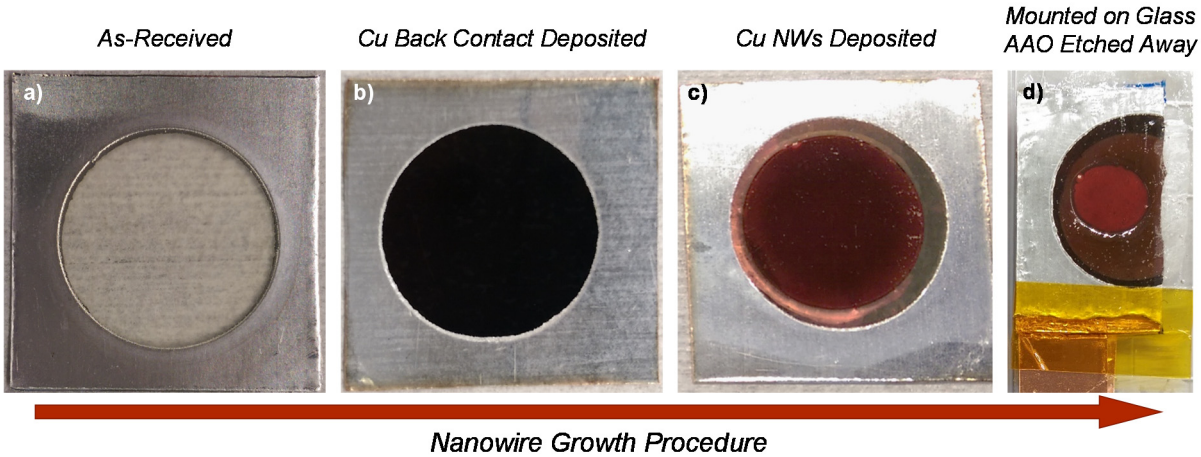

Figure 6.2 Example of Cu NW Deposition Process: (a) An as-received AAO template is shown. The metallic surface is the remaining aluminum coupon which was not converted into AAO in the growth process. (b) The top of the AAO template is shown after the 2 um of Cu has been evaporated on the back. The darkened center is due to evaporated metal. (c) The AAO template after electrochemical deposition is shown. It can be seen that the deposit appears quite uniform. (d) A sample is shown which has been mounted on glass and undergone the etching procedure to release freestanding NWs. The exposed red area in the center is what is tested electrochemically.

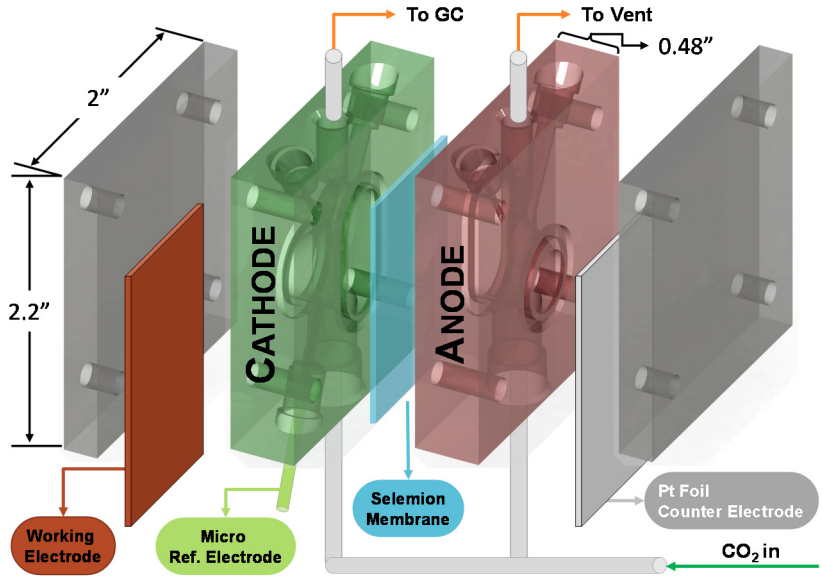

Figure 6.3 CO2R Electrochemical Cell: The design of the cell used for the experiments here is largely similar to that presented in Ch 4. Although the cell is now made of PEEK, the O-rings being used are FEP coated Viton, and a glass sheath has been placed around the micro reference electrode.

exposed a section of the evaporated Cu which was still firmly adhered to the glass slide and electrically connected to the NW array. Adhesive Cu tape (Ted Pella) was used to contact this metal and served as the connection to NW array for electrochemical testing. An example of a sample that has gone through this complete process is shown in Figure 6.2.

6.2.2. CO2R Electrochemical Cell Design

The same electrochemical cell used in chapter 4 was used for these experiments, with some minor modifications (Fig. 6.3). Like the cell used in chapter 4, this cell is composed of an anode and cathode chamber, separated by an anion-conducting membrane, Selemion AMV (AGC Engineering Co.). A 1 mm OD Ag/AgCl reference electrode (Innovative Instruments) was inserted into the cathode chamber to monitor the working electrode potential. This reference electrode was calibrated against an ideal reversible hydrogen electrode.

The cell used in these experiments differed in that it was machined out of polyether ether ketone (PEEK) instead of polycarbonate. PEEK is a more chemically-resistant material, in comparison with polycarbonate, which allowed for the use of strong acids in the cleaning procedures. However, PEEK is not transparent. Nevertheless, the improvements in reproducible experimental results (due to the improved cleaning procedure, see below for more detail) outweighed the loss of visibility into the reaction chamber. In addition, a small glass sheath was added to the reference electrode port, which prevented the accumulation of bubbles on the electrode and produced more stable chronoamperometry data.

The cell was sealed by compressing the stack of counter electrode, anode chamber, membrane, membrane, cathode chamber, and working electrode between two outer plates secured with bolts. The seals were made with FEP-coated Viton O-rings (McMaster Carr), as these O-rings are more chemically resistant than the Buna-N ones used previously. During measurements, both sides of the cell were sparged with CO_2 at 1 atmosphere and the gas exiting the cathode compartment was directed to the GC for gaseous product analysis.

6.2.3. Electrochemical Cell Operation and Product Detection

The testing apparatus used to evaluate the Cu NWs activity to CO2R has already been outlined in detail in chapter 4. In brief, on-line gas chromatography (GC) was used to measure the gaseous products periodically throughout the experiment, and high performance liquid chromatography (HPLC) was used to measure the liquid products generated once at the end of each experiment.

99.995% base metal pure cesium carbonate (Cs_2CO_3) (Sigma-Aldrich) was used as the precursor salt for making the 0.1 M cesium bicarbonate ($CsHCO_3$) electrolyte used in this study. Cs electrolyte was used in these experiments as it has been shown to favor the production of CO2R products over hydrogen evolution, specifically, the selective production of ethylene over methane.[251] The conversion of carbonate to bicarbonate electrolyte is achieved by sparging the carbonate electrolyte with 1 atmosphere of CO_2. The complete conversion of the electrolyte was confirmed by measuring the pH of the solution to be less than 6.82.

The cell was assembled with a new Cu NW sample as the working electrode, a platinum foil counter electrode, and a piece of Selemion membrane. Before each experiment 2 ml of electrolyte was injected into each compartment of the cell and CO_2 was bubbled through the cell. A Biologic VSP-300 potentiostat with electrochemical impedance package was used to measure the electrochemical impedance of the cell in order to enable *in-situ* iR compensation. 85% compensation was used to correct for the cell resistance (the uncompensated resistance was ~60 ohms). The remaining 15% of the uncompensated resistance was corrected for ex-situ. A constant voltage was applied versus the Ag/AgCl reference electrode for 70 minutes and the product distribution measured by the GC and HPLC was converted back into Faradaic efficiencies for each product.

6.2.4. Electrochemical Cell Cleaning Procedure

Contamination has been a long standing issue in the CO2R literature[115] and small amounts of impurity metals are known to dominate the activity of CO2R catalysts.[136] Thus rigorous cleaning of the electrochemical cell is critical to getting reproducible results. I developed a procedure to confirm that any PEEK cell I used was clean. To start the cell was designed to be composed exclusively of PEEK, Teflon, and glass parts, which are compatible with strong acid cleaning. The Teflon and glass parts were all cleaned with aqua regia (3:1 Hydrochloric Acid:Nitric Acid) for 3 hours and then sonicated multiple times in deionized water (DI, Millipore with water resistivity of 18.2 MΩ cm). The PEEK cell was degreased in iso-propyl alcohol and then sonicated in 20 wt% nitric acid for 2 hours followed by multiple sonications in fresh DI water. After this initial cleaning the cell could be assembled and tested for cleanliness.

To test the cleanliness of the cell electrochemical CO2R tests were run with silver foil (99.99%, Alfa Aesar) as the working electrode. The selectivity of Ag to producing CO at -1.0V

vs. RHE should be very high (FE ≥ 90%).[175] However, the presence of any hydrocarbon production would indicate that the cell is contaminated with copper impurities. The presence of hydrogen selectivity greater than 10% indicates the contamination of other transition metals. Thus the selectivity to CO was used as a metric to judge the cleanliness of the cell.

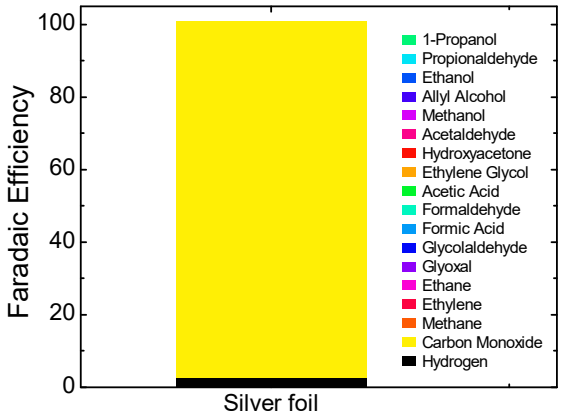

Figure 6.4 Selectivity of Ag Foil: Silver foil was used to test the cleanliness of the electrochemical cell. Running silver in 0.1M $CsHCO_3$ at -1.0 V vs. RHE, it is expected to have a FE to CO of over 90%. A FE to CO of 98% is observed here confirming the cell is clean and ready for experiments.

The silver foil was prepared by degreasing in acetone and iso-propyl alcohol (30 minute sonication each), followed by sanding with increasing grades of sandpaper from 400 to 1200 grit. Finally, the Ag foil was sonicated in DI water to remove any debris left behind by the sanding procedure. With the cell properly cleaned, CO FEs above 95% were regularly observed at -1.0V vs. RHE in 0.1M $CsHCO_3$ (Fig. 6.4). However, it was possible that sometime after the initial cleaning the cell becomes contaminated. Data typical of a contaminated cell is show in Figure 6.5. It can be observed that the CO FE drops with time while the hydrogen FE increases with time. There was also the trace production of methane and ethylene which rose with time. This is indicative of an impurity plating onto the surface of the Ag over time. The average FE to CO over the 70 minute run was 73%, well below the expected 90%.

When data such as this was obtained, the cell was re-cleaned and Ag foil was tested again until an acceptable FE to CO was obtained. It is possible to do a less rigorous cleaning procedure

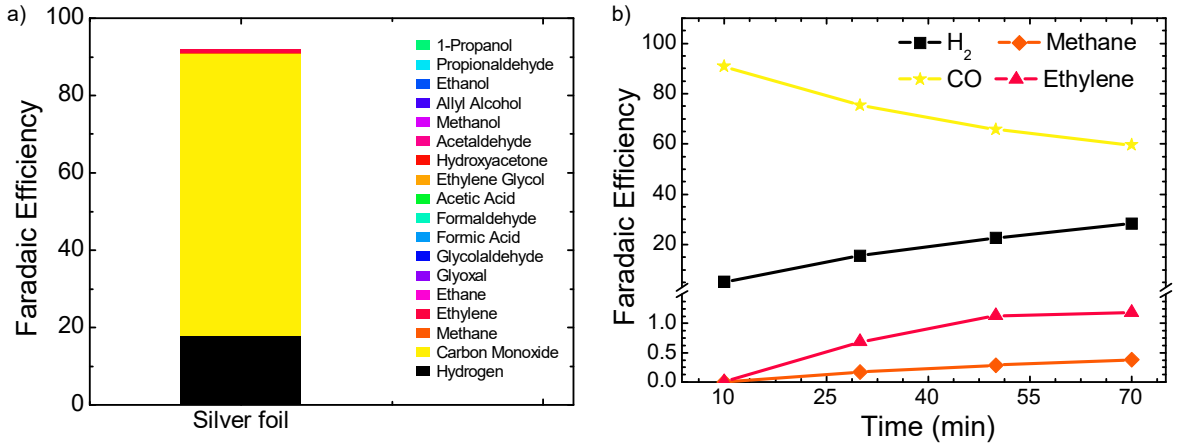

Figure 6.5 Selectivity of Ag Foil in Dirty Cell: Silver foil was used to test the cleanliness of the electrochemical cell. The overall FE to CO is only 73% (a) and the FE to all products is changing with time (b). The increase in hydrogen, methane, and ethylene selectivity with time is indicative of an impurity metal in the cell plating onto the Ag surface. When data like this is obtained, the electrochemical cell must be re-cleaned.

than the one outlined above to handle mild cell contamination. For this procedure the assembled cell could be sonicated in 20 wt% nitric acid for 2 hours followed by multiple sonications in fresh DI water. This cleaning was repeated as necessary to obtain stable Ag foil data (as shown in Fig. 6.4). If the less rigorous procedure could not achieve acceptable results, the full cleaning procedure outlined earlier on the disassembled cell was used.

6.2.5. Electrochemically Active Surface Area Measurements (ECSA)

ECSA measurements were done following the typical double layer capacitance measurement by cyclic voltammetry (CV).[107,252] Here the electrochemical cell was assembled as usual with a Pt counter electrode, Selemion membrane, and the working electrode to be measured. 2 ml of 0.05 M K_2HCO_3 was used as the electrolyte in each chamber. Argon was bubbled through both the anode and cathode chamber at 5 sccm for 15 minutes prior to running the experiment to remove any dissolved oxygen in the solution. The Ar was bubbled continuously throughout the experiment as well.

In order to properly run the CV scans, a potential window where no faradaic processes occur needed to be identified first. In this region the current is assumed to be due to double layer charging only.[252] To accomplish this, a linear sweep voltammetry scan from -1.5 V to -0.3 V vs. Ag/AgCl was run. A potential window of ~100 mV was identified where only a small amount of current was passing but before the catalyst went to an oxidizing potential. This window was typically between -0.35 and -0.55 V vs. Ag/AgCl. Then CV cycles were run within this 100 mV window at 6 different scan rates (100, 80, 60, 40, 20, 10 mV/sec). As the scan rate is decreased, the difference between the cathodic and anodic current decreases. It is known that this charging current is proportional to the scan rate, scaled by the double layer capacitance. The current is

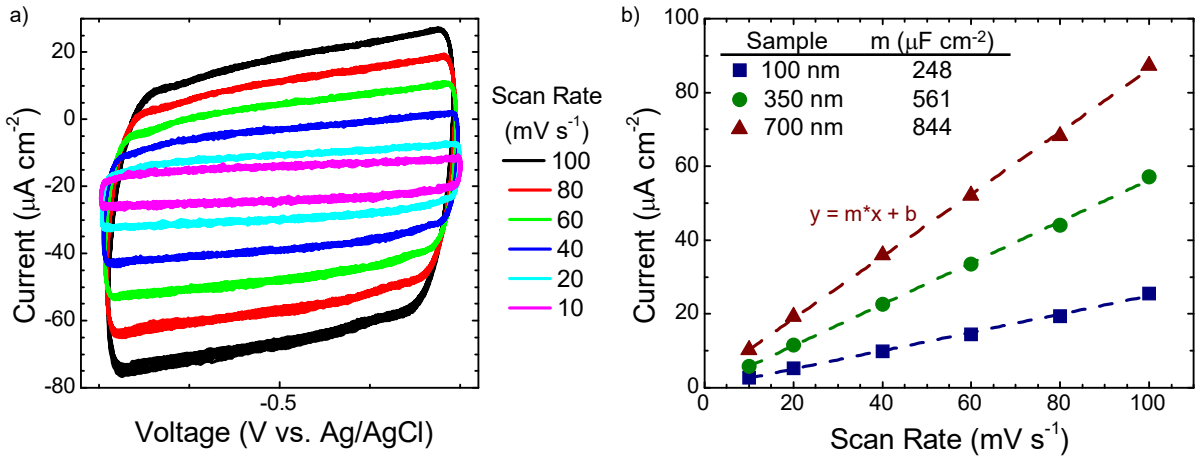

Figure 6.6 ECSA Analysis: (a) CV scans preformed at different scan rates on the 700 nm Cu NW sample. As expected the splitting between the anodic and cathodic scan decreases with decreasing scan rate. (b) The average difference between the current in the anodic and cathodic scan directions are plotted versus scan rate for the 3 different length nanowires. It can be seen that the capacitance goes down as the nanowire height decreases, as expected. For a flat reference, an evaporated copper sample on glass was used (not pictured here). Its capacitance was 213 μF cm^{-2}.

plotted versus scan rate and the slope of this linear regression is the double layer capacitance of the sample. The magnitude of this capacitance can be compared to a reference sample to estimate a surface area enhancement. An example of the CV cycles and corresponding linear regression is given in Figure 6.6 for the Cu NW samples.

6.3. Results and Discussion

Figure 6.7 (a-c) shows the results of cross-sectional SEM imaging of the electrodeposited Cu NWs in the AAO template. The growth time for these wires were 1, 4, and 8 minutes at 2 mA. It can be seen that the length of the nanowires corresponded well with the change in electrodeposition time: ~100 nm for 1 minute, ~350 nm for 4 minutes, and ~700 nm for 8 minutes. Figure 6.7 also shows top-down SEM images of the NWs after the etching procedure. The imaging shows that the aluminum oxide template has been fully removed and that free standing nanowires can be

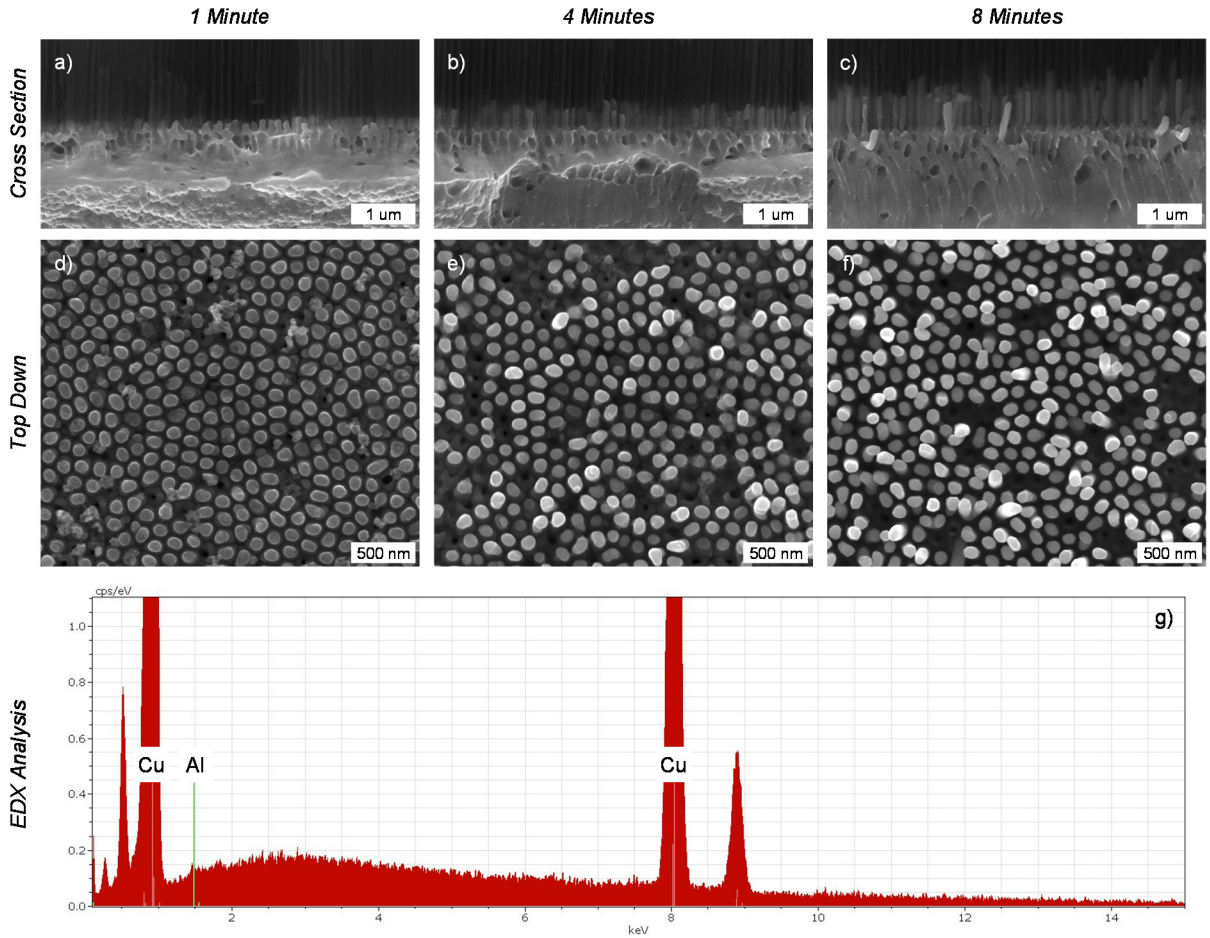

Figure 6.7 Imaging Electrodeposited Cu Nanowires: (a-c) Cross sectional SEM images show the change in nanowire height for different deposition times (~100nm (a), ~350nm (b), ~700nm(c)). (d-f) Top down SEM images of the released Cu NWs after the etching procedure removed the AAO template. (g) EDX analysis of the released NW film shows no signal for any element other than Cu.

obtained in this height regime. Finally, EDX analysis of the samples shows that only Cu can be detected at the sensitivity of this technique.

The CO2R activity of these samples was then tested at -1.0 ± 0.05 V vs. RHE. This potential was chosen because on planer Cu, it provides close to the maximum production rate of C_2+ products.[121] For comparison purposes, 3 reference samples were fabricated and tested: 1) 2 μm evaporated Cu on glass (Evap Cu) 2) an electrodeposited Cu film on the planar evaporated Cu substrate (E-Dep Cu) 3) an AAO membrane with 2 μm evaporated Cu that went through the full NW sample processing but had no NWs deposited in it leaving only the planar Cu behind (FP Cu). The electrodeposited film was deposited using the same sequence as that used for the nanowires with an 8 minute deposition time at 2 mA. The activity of these samples is summarized in Figure 6.8 along with the current density for each sample. The morphology of the NWs was examined after CO2R as well to confirm that it had not changed substantially (Fig. 6.9).

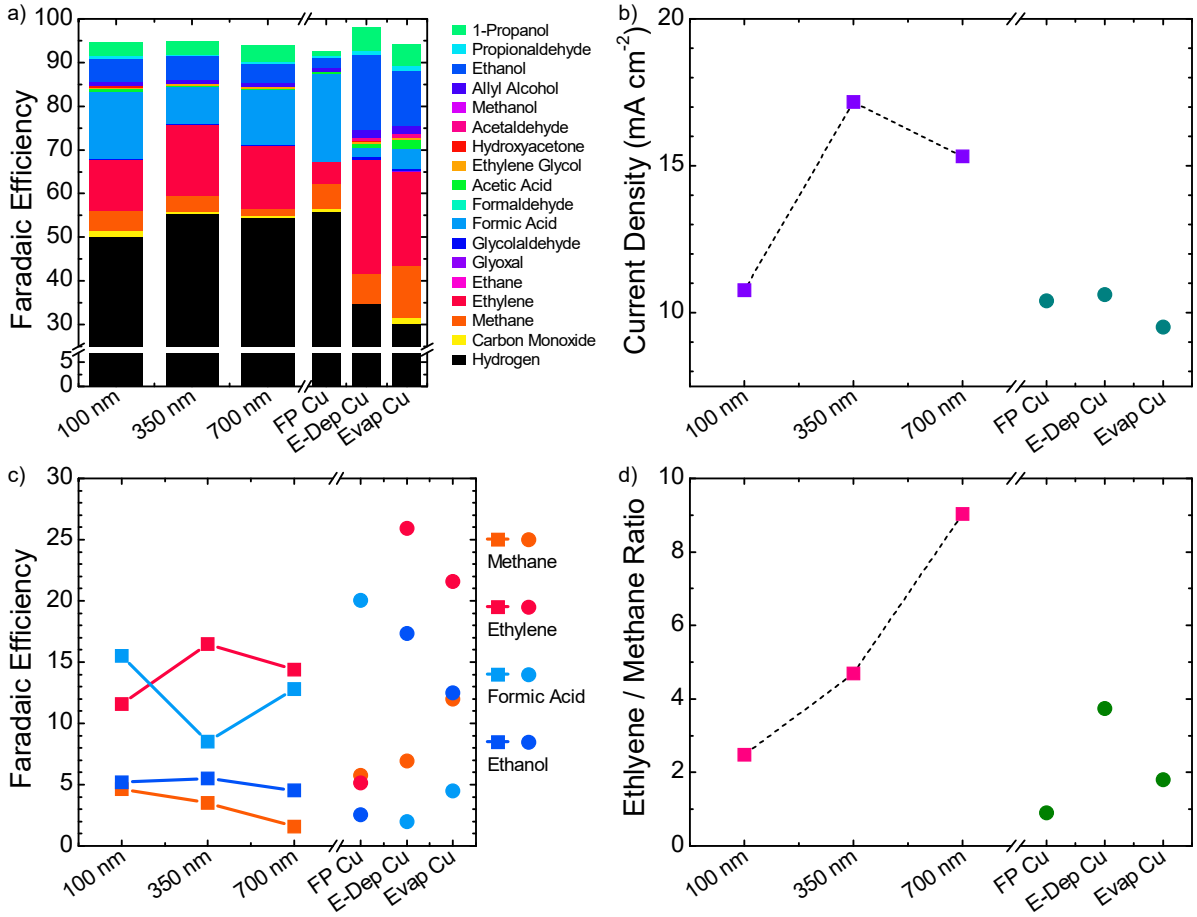

Figure 6.8 CO2R Activity of Cu Nanowires: (a) The overall Faradaic efficiency of the 3 different length Cu NW samples are shown, as well as for the fully processed Cu back contact (FP Cu), the electrodeposited copper (E-Dep Cu), and the evaporated copper (Evap Cu) reference samples. The current density (b), the FE to a select number of major products (c), and the ethylene to methane ratio (d) of the samples are shown. It can be observed that while the FE to ethylene and formic acid go through a maximum and minimum respectively for the intermediate length NWs, the C_2/C_1 ratio increases monotonically as the NW length increases.

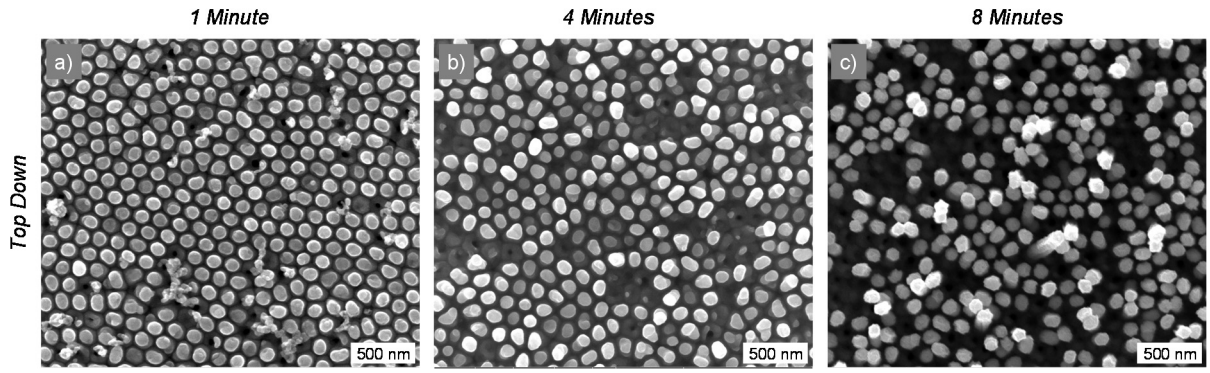

Figure 6.9 Imaging of Cu NWs after CO2R Electrolysis: SEM images of the 100 nm (a), 350 nm (b), and 700 nm (c) Cu NW samples taken after 70 minutes of CO2R at -1.0V vs. RHE. They all show that the morphology of the NWs has been largely unaffected by the reduction experiment.

First it can be observed from this data that the purity of the evaporated and electrodeposited Cu is sufficient for the purposes of CO2R (Fig. 6.8a). A high hydrogen FE is indicative of low purity copper that may be contaminated with other types of transition metal.[115] Here however, substantial amounts of hydrocarbons and alcohols are produced and, most importantly, the hydrogen FE is below 40% for each sample. Thus impure starting materials are not a concern here and the catalytic activity of the NWs can be investigated. It should be noted that the inability to produce data like this for planar Cu is the reason some previous literature studies were discounted in the introduction.

Examining the data in Figure 6.8 more closely, several different trends can be observed. First, the current density of the NW samples are all higher than that of the reference planar samples, although the 100 nm NWs show only a slight increase. SEM imaging (not shown here) indicated that the electrodeposited Cu surface was roughened in comparison to the evaporated Cu, which may explain this observation. To further explore this issue electrochemically active surface area (ECSA) measurements were performed on the samples and the results are tabulated in Table 6.2. It can be seen that the 100 nm NWs have only a slightly higher surface area in comparison to the evaporated Cu sample and have a similar surface area enhancement to the electrodeposited Cu. Thus explaining the similar current densities. What is unclear at this point is why the 700 nm NWs show a higher ECSA yet a lower current density than the 350 nm NWs. It is possible that under driving conditions gas bubbles are trapped along the longer NWs, effectively blocking the active surface area and reducing the catalyst's overall activity. Further study is needed to understand this unexpected result.

Table 6.2 ECSA Results on Cu NWs: The surface area of the different samples was measured and the enhancement in area is shown in comparison to the flat evaporated Cu sample.

Sample	Surface Area Enhancement
100 nm	1.16
350 nm	2.62
700 nm	4.16
Evap Cu	1.00
E-Dep Cu	1.28
FP Cu	1.00

Examining only the major CO2R products produced here (Fig. 6.8c), it can be seen that several of

these products show some trend with NW length. Most interestingly, it appears that the FE to ethylene goes through a maximum, while the FE to formic acid goes through a minimum at intermediate NW length. The fact that these two products trend competitively suggests that the nanowire length is affecting a branching ratio earlier in the mechanistic pathway.

In addition it can be seen that all the NWs produce ~50% FE to hydrogen, which is substantially more than the 30-35% FE produced by the electrodeposited and evaporated Cu samples. On first inspection, it is reasonable to think that the high surface area of the NW catalysts is causing this increased FE to hydrogen because CO_2 is being depleted down the length of the NWs. However, as the ECSA shows, the NW surface area is not dramatically higher than that of the planar samples. The FP Cu sample provides some insight as it is planar Cu but has gone through the entire 1M NaOH etching procedure like the NW samples. This sample also shows elevated FE to hydrogen (~55%). This suggests that there is some damage or contamination caused during the etch process which causes the higher hydrogen formation. This is important as it shows that a high FE to hydrogen may not be an intrinsic issue with high surface area catalysts, but with how these catalysts are made. Certainly beyond a certain enhancement factor, hydrogen FE will increase as CO_2 is heavily depleted at the surface; however, this shows there is some range of factors which can be explored where this CO_2 depletion is not the dominating affect.

Examining the FP Cu data further, it can be observed that it also shows a high FE to formic acid (~20%), substantially higher than the other planer Cu references (~2-5%), and even higher than the NW samples (~8-15%). Examining the NW samples alone would suggest that the NW morphology supports the formation of formic acid and depresses the formation of ethanol in comparison to E-Dep Cu and Evap Cu. However, again, it seems that the high formic acid production on the NW samples may be due to the etching process as the FP Cu shows the same trend. The one previous study using this type of growth technique also showed this high FE to formic acid on Cu NWs.[247] My work suggests that what they saw may have been due mainly to the etching process and not the NWs themselves.

Furthermore, it can be observed that the length of the NWs causes the ratio of ethylene to methane being produced to monotonically increase (Fig. 6.8d). It has been hypothesized that there is a high pH pathway which favors C-C bonding over hydrogenation. This in turn leads to an increased selectivity to ethylene over methane.[253] Due to the structure of the NW catalyst, it is likely that the base of the NWs experience a more basic environment than the tips. This is because CO_2 is depleted and OH^- is generated by the CO2R reaction and thus the local chemical environment will likely change down the wire. The further down the wire (i.e. the further away from the bulk electrolyte) the more reaction will have occurred and the more basic the environment will be. As the NWs grow in length, a larger section of the surface area will experience this high pH, which could explain the preference to produce ethylene over methane observed here.

6.4. Growth of Bi-Metallic Nanowires for Sequential Catalysis

The templated electrodeposition approach to catalyst synthesis that has been outlined so far can be easily tuned to investigate bi-metallic systems. By changing the electrodeposition solution, many combinations of substrate and wire metals are possible, as long as they are chemically compatible with the 1M NaOH etching procedure. There is interest in bi- or multi-metallic catalysts because of their potential to break the scaling relationships that have been proposed to limit a single metal surface in CO2R.[254,255] By providing two different metal centers, different binding can be obtained to the carbon bound and oxygen bound intermediates on the catalyst surface. Multiple approaches to bi-metallic catalysts can be found in the literature, including alloys[28,120,256–258] and *in-situ* deposited metals.[28,259,260] These endeavors have shown limited success in improving the activity or selectivity of CO2R to greater than 2 electron products. Here a different approach is investigated, that of sequential catalysis. In this case, the two metals are not combined to change their material properties, or otherwise attempt to break the scaling relationships like alloying. Instead, the metals are segregated and chosen in such a way that each one preferentially and efficiently performs one step of a multistep reaction. This approach can allow for the creation of a local reaction environment different than that which would otherwise be achievable and in this way influence the selectivity and activity of the catalyst. In the CO2R literature, this approach has gone largely unexplored up to this point.

Cu is currently the only known metal which is able to produce hydrocarbons and alcohols at appreciable rates in CO2R.[28] However, Cu does not produce any of these chemicals selectively and it still produces significant amounts of less desirable 2 electron transfer products (carbon monoxide and formic acid).[28,121] Of these 2 electron products, formic acid is less desirable as it is not known to be upgradable to any further reduced products.[230] On the other hand, CO is a known intermediate in the production of hydrocarbons and alcohols on Cu.[104,261–263] Thus for hydrocarbon or alcohol production to be maximized, the production of formic acid should be eliminated as a pathway on a Cu surface.

Conversely, there are many catalysts which are known to be highly selective to the production of CO under CO2R conditions,[264] including gold,[265] silver,[175] molybdenum carbide,[266] and indium-copper alloys.[267] Thus, one way to improve the overall CO2R activity of Cu would be to combine it in series with a CO producing catalyst. In this way, the Cu will only see CO, which it can further reduce to hydrocarbons and alcohols. This will effectively eliminate formic acid as a product of the combined system and this kind of control is the primary goal in designing a sequential catalysis system.

Using CO as a direct feedstock for reduction on Cu has been investigated previously[261,262] and it can be thought of as a simple version of a sequential catalysis system, where a second completely separate catalyst is used to produce pure CO from CO_2. However, when attempting to perform CO reduction in the same way as CO_2 reduction, it becomes clear there are some issues with this approach. The primary problem being the much lower solubility of CO in water as compared to CO_2 (1 mM vs 33 mM at 25ºC and 1 atm). This lower reactant concentration leads

to more sever mass transport limitations that those seen in CO2R, which inhibits driving the system at comparable voltages on Cu without also getting high FEs to H_2.[261,262]

To overcome the low solubility of CO, and the intrinsic mass transport limitations this imposes, a sequential catalysis platform needs to be designed to allow for the close production of CO to the Cu surface. This requires the intimate co-location of the CO producing catalyst and the CO consuming catalyst. This will reduce the mass transfer constraints for the CO and provide a higher local CO concentration on the co-catalyst than could be accessed in a traditional system. The nanowire platform that has been investigated so far is one such platform that could provide such a sequential catalysis system. As a proof of concept, the growth of Ag nanowires on top of a Cu substrate is investigated here.

6.4.1. Experimental

The AAO template preparation used here was identical to that described above. The only difference was that the electrodeposition was performed using a silver deposition bath consisting of 10 mM silver nitrate (99.999%, Alfa Aeser) and 323 mM boric acid (99.9%, Sigma Aldrich). The bath was adjusted to pH 2.5 using nitric acid (99.99%, Sigma Aldrich). A 0.5 mA constant current deposition was used to grow the NWs. It is important to note that due to differences in standard reduction potentials, Ag will galvanically replace Cu. In order to be able to electrodeposit Ag on Cu, a dilute Ag electrolyte was needed to slow the galvanic replacement reaction. For this reason it was also important to limit the amount of time between introducing the electrolyte to the electrodeposition cell and beginning the deposition.

For the experiments shown here, Ag NWs were grown in AAO templates with 40-70 nm pores and 110-150 nm pores. In the 40-70 nm template, a deposition time of 30 minutes was used, which is resulted in nanowires 4 – 5 μm in length (referred to as 4.5 μm Ag). In the 110-150 nm template, two deposition times were investigated, 8 minutes and 4 minutes, which produced 1 – 1.5 μm wires (referred to as 1.25 μm Ag) and 600 – 800 nm wires (referred to as 700 nm Ag) respectively.

6.4.2. Results and Discussion

Figure 6.10a shows a cross-sectional image of the Ag NWs grown in the 40-70 nm pore AAO template on top of the evaporated Cu back contact. It can be seen that NW height is fairly uniform across the imaged area. EDX mapping of this cross-section confirms that the wires are composed of Ag and the substrate is still Cu, despite any galvanic displacement reaction which may have occurred during the electrodeposition (Fig. 6.10b). Figure 6.10 also shows a top-down SEM image of the released NWs after the etching procedure and EDX mapping of this confirms that the nanowires are Ag and the exposed substrate is Cu. From the SEM it is clear that the NWs are not freestanding but instead clumped together. This is most likely due to the long length of these NWs. It was believed that by reducing the aspect ratio of the NWs, by making them shorter in height and larger in diameter, they would be able to be freestanding, like those produced in Figure 6.6. However, this clumping was also observed in the released shorter Ag NWs grown in the 110-150

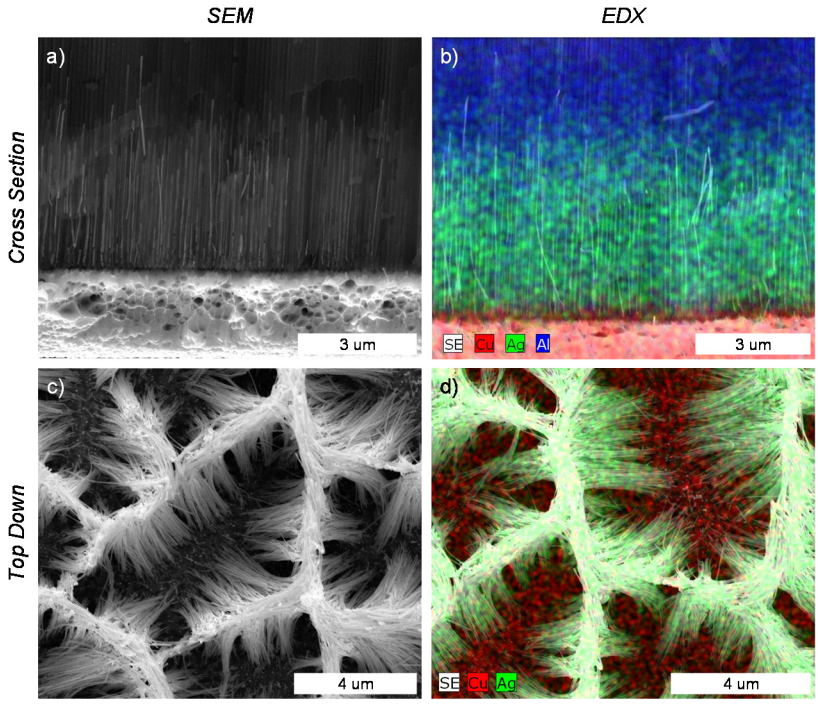

Figure 6.10 Imaging Electrodeposited Ag Nanowires on Cu: (a) Cross sectional SEM shows the Ag NWs grown in the AAO template (4.5 μm Ag) (b) EDX mapping shows that the wires are Ag (green) in the AAO template (blue) on top of the Cu substrate (red). (c) Top down SEM of the released Ag NWs after the etching procedure removed the AAO template (4.5 μm Ag). Due to their long length the NWs clump together. (d) EDX mappings shows the wires are Ag (green) and the exposed areas underneath are Cu (red). EDX also confirmed no aluminum was present.

nm AAO template. Further optimization of the Ag electrodeposition is necessary to better control the NW height and adhesion to the Cu substrate to enable the production of freestanding NWs.

The CO2R activity of the bi-metallic NW structures were tested at -1.0 ± 0.05 V vs. RHE in 0.1M $CsHCO_3$. The same conditions as those used to test the Cu NWs, to facilitate comparison. It is expected that the Ag will largely consume the CO_2 present near the electrode surface to produce CO. Thus the substrate Cu will see very little CO_2 and instead should see a high concentration of CO. At the potential chosen here, this CO can be further converted into hydrocarbons.[261] Due to the lack of CO_2 as a reactant for Cu, it is expected that formic acid selectivity will be highly suppressed on this bi-metallic catalyst. Examining the results of these experiments in Figure 6.11, it can be observed that the Ag NWs on Cu greatly suppress the activity to formic acid in comparison to the Cu NWs. This suggests that Cu is only seeing a CO environment, thus confirming the primary principle used in designing this sequential catalysis platform. While the selectivity to formic acid on the bimetallic catalysts is suppressed, the ethylene FE is approximately the same as the Cu NWs (~15%) and ethanol FE is enhanced (~10% vs 5%). Furthermore, the hydrogen FE of the bi-metallic catalysts is similar to that of the Cu samples (~50-55%), which again suggests that this high FE to hydrogen is coming from the AAO etching process as all samples which went through this process show approximately the same FE to hydrogen.

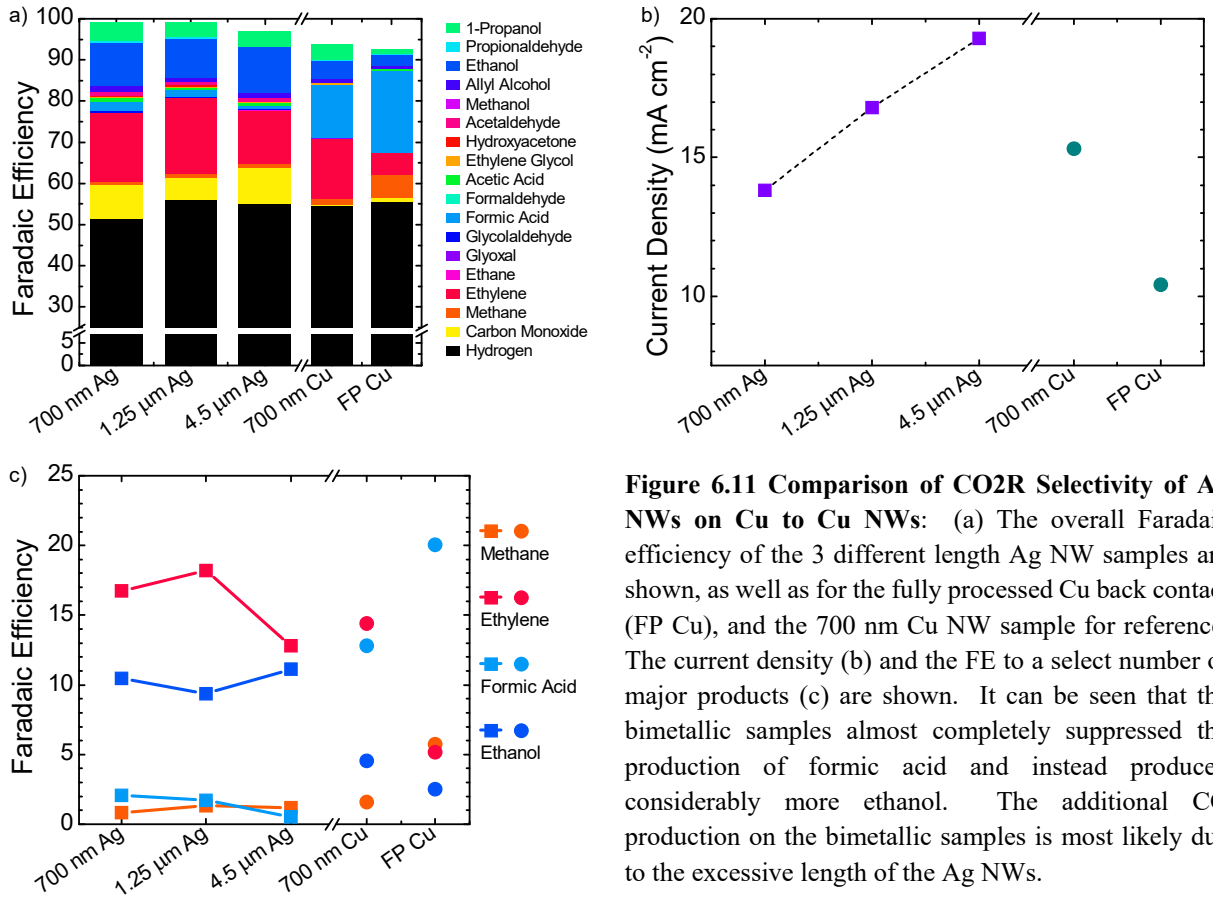

Figure 6.11 Comparison of CO2R Selectivity of Ag NWs on Cu to Cu NWs: (a) The overall Faradaic efficiency of the 3 different length Ag NW samples are shown, as well as for the fully processed Cu back contact (FP Cu), and the 700 nm Cu NW sample for reference. The current density (b) and the FE to a select number of major products (c) are shown. It can be seen that the bimetallic samples almost completely suppressed the production of formic acid and instead produced considerably more ethanol. The additional CO production on the bimetallic samples is most likely due to the excessive length of the Ag NWs.

Further examination of the experimental results reveals some surprising observations. The first is that despite the large amount of Ag that is on top of the Cu surface, only a modest amount of CO escapes to the solution to be detected as a product. This is especially surprising given that mono-layers of contaminant metals on Cu are known to dominate its activity. Clearly most of the CO being produced on the Ag wires is diffusing to the Cu surface to get further reduced. The second is that despite the range of Ag NWs grown on top of the Cu surface, there is little difference in the selectivity of the catalysts other than a monotonic increase in activity with the length of the nanowire (Fig. 6.11b). It is possible that the range of NW lengths explored here were not substantially different enough, explaining the lack of a trend with length; however, further investigation is needed.

6.5. Outlook

A framework has been presented here to controllably investigate the effects of high surface area the activity and selectivity of CO2R as well as to explore sequential catalysis utilizing a combination of close proximity metals. Preliminary investigations have been performed at this point and these results have shown promising indications of control over the product selectivity.

With the Cu NWs, there is an indication that ethylene is favored over methane, which suggests that at least part of the reason oxide-derived catalysts are so selective to C_2+ products is because of the accompanied surface area enhancement. However, the experiments presented here need to be reproduced to confirm this trend as well as some of the other unexpected trends. By exploring a wider range of nanowire lengths, it will be possible to see if the C_2/C_1 ratio ever plateaus or continues to increase. These experiments can be coupled with a mass transfer model, similar to that developed by Singh *et al*.[117] to get an estimate of how pH is changing down the length of the NWs. This could in turn provide insight into how pH influences the selectivity of ethylene over methane. By using AAO as a template, it is also possible to explore different diameters and densities of NW arrays. In this view, there are a wide array of combinations that will enable the probing of NW size and length to see which plays a more critical role, if any, at the same effective surface area.

The Ag NWs grown on Cu is only one of many potential sequential catalysis systems which can be envisioned with this platform. The templated growth allows for precise loading of a co-catalyst like Ag on top of Cu. In this way, the environment in which Cu reduces CO can be tuned. The different array of AAO templates available will allow further optimization as to which density of Ag NWs is best to allow transfer of CO down to the Cu as well as allow the escape of fully reduced products. This system would be best optimized if it were possible to flow the CO_2 reactant down the length of bimetallic nanowire. Such a system may be possible if the wires can be released from the AAO and then ripped off of the substrate, immobilized in a conducting membrane material.

6.6. Conclusion

In this chapter, the growth and catalytic activity of Cu NWs and Ag NWs on Cu for CO2R were explored. The main goal of the Cu NW study was to elucidate the effect of increasing surface area on CO2R activity. Many of the novel Cu catalysts presented in the literature show improved catalytic activity, but it is not possible to identify the source of this improvement as both the dominant surface facet and the surface area are substantially changed. The high surface area catalysts that are made directly from Cu, and don't go through an oxide intermediate, show little to no activity towards producing hydrocarbons and alcohols.[122,247] However, it is shown here that it is possible for a high surface area catalyst made directly from Cu to produce hydrocarbons and alcohols. In addition, the preliminary results shown here indicate that the surface area enhancement of Cu alone could lead to an improvement in selectivity of ethylene over methane, an improvement commonly shown in the aforementioned high surface area oxide derived Cu catalysts. This study was enabled by producing samples with controlled increases in surface area that were not so large as to cause mass transport to completely dominate the activity of the catalyst.

Additionally, the templated AAO NW growth developed here was shown to be a promising platform to explore sequential catalysis. An illustrative catalyst was synthesized here depositing

Ag NWs on top of a Cu substrate, in order to tune the selectivity of the catalyst and suppress the production of formic acid. It was shown that the selectivity of the bimetallic catalyst to formic acid could be almost entirely suppressed and instead the more reduced alcohol ethanol was made. In traditional systems where CO is fed directly to Cu, mass transfer limitations would cause the dominant reaction product to by hydrogen. Hydrogen production with this bimetallic catalyst was modest in comparison and highlights one of the key advantages to sequential catalysis with co-located catalysts. This catalyst also showed that it is possible for Cu to still produce hydrocarbons and alcohols even with large amounts of Ag deposited on top of this. This is surprising given that the activity to hydrocarbons and alcohols of Cu is typically easily suppressed in the presence of contaminant metals. This work suggests a framework which could be used to improve the control over selectivity of the CO_2 reduction reaction.

6.7. Acknowledgements

Work on this project was supported by the Singapore-Berkeley Research Initiative in Sustainable Energy (SinBeRISE). Some catalytic activity testing was performed in collaboration with the Joint Center for Artificial Photosynthesis, a DOE Energy Innovation Hub, supported through the Office of Science of the U.S. Department of Energy under Award Number DE-SC0004993. I acknowledge Ezra Clark, Dr. Meenesh Singh, and Prof. Alex Bell for their in depth discussions about mass transport limitations. I acknowledge Prof. Joel Ager for his thoughtful insight into how to design the overall catalyst system. I acknowledge Jeff Beeman for his assistance in finding the proper epoxy to use to mount the AAO template to glass. I acknowledge Prof. Xiaodong Chen and Dr. Xiaotian Wang for their assistance in developing the AAO electrodeposition procedure.

7. Bibliography

(1) Stocker, T. F.; Qin, D.; Plattner, G.-K.; Tignor, M.; Allen, S. K.; Boschung, J.; Nauels, A.; Xia, Y.; Bex, V.; Midgley, P. M. *IPCC, 2013: Summary for Policymakers. In: Climate Change 2013: The Physical Science Basis. Contribution of Working Group I to the Fifth Assessment Report of the Intergovernmental Panel on Climate Change*; Cambridge University Press, Cambridge, United Kingdom and New York, NY, USA, 2013.

(2) Field, C. B.; Barros, V. R.; Dokken, D. J.; Mach, K. J.; Mastrandrea, M. D.; Bilir, T. E.; Chatterjee, M.; Ebi, K. L.; Estrada, Y. O.; Genova, R. C.; et al. *IPCC, 2014: Summary for Policymakers. In: Climate Change 2014: Impacts, Adaptation, and Vulnerability. Part A: Global and Sectoral Aspects. Contribution of Working Group II to the Fifth Assessment Report of the Intergovernmental Panel on Climate Change*; Cambridge University Press, Cambridge, United Kingdom and New York, NY, USA, 2014.

(3) *State of the Climate: Global Analysis for Annual 2015*; 2016.

(4) *State of the Climate: Global Analysis for June 2016*; 2016.

(5) Tsao, J.; Lewis, N.; Crabtree, G. *Solar FAQs*; 2006.

(6) Company, B. P. *BP Statistical Review of World Energy 2016*; 2016.

(7) Energy Information Administration. *Levelized Cost and Levelized Avoided Cost of New Generation Resources in the Annual Energy Outlook*; 2016.

(8) Taylor, M.; Daniel, K.; Ilas, A.; So, E. Y. *Renewable Power Generation Costs in 2014*; 2014.

(9) Whiteman, A.; Rinke, T.; Esparrago, J.; Elsayed, S. *Renewable Capacity Statistics 2016*; 2016.

(10) Chung, D.; Davidson, C.; Fu, R.; Ardani, K.; Margolis, R. *U.S. Photovoltaic Prices and Cost Breakdowns : Q1 2015 Benchmarks for Residential , Commercial , and Utility-Scale Systems*; 2015.

(11) Green, M. A.; Emery, K.; Hishikawa, Y.; Warta, W.; Dunlop, E. D. Solar Cell Efficiency Tables (Version 48). *Prog. Photovoltaics Res. Appl.* **2016**, *24* (7), 905–913.

(12) Keavney, C. J.; Haven, V. E.; Vernon, S. M. Emitter Structures in MOCVD InP Solar Cells. *IEEE Conf. Photovolt. Spec.* **1990**, 141–144.

(13) Moss, R. H.; Evans, J. S. A New Approach to MOCVD of Indium Phosphide and Gallium-Indium Arsenide. *J. Cryst. Growth* **1981**, *55*, 129–134.

(14) Zheng, M.; Yu, Z.; Joon Seok, T.; Chen, Y.-Z.; Kapadia, R.; Takei, K.; Aloni, S.; Ager, J. W.; Wu, M.; Chueh, Y.-L.; et al. High Optical Quality Polycrystalline Indium Phosphide Grown on Metal Substrates by Metalorganic Chemical Vapor Deposition. *J. Appl. Phys.* **2012**, *111* (12), 123112.

(15) Cheng, K. Molecular Beam Epitaxy Technology of III-V Compound Semiconductors for Optoelectronic Applications. *Proc. IEEE* **1997**, *85* (11).

(16) Cho, A.; Arthur, J. Molecular Beam Epitaxy. *Prog. Solid State Chem.* **1975**, *10*, 157–191.

(17) Bosi, M.; Pelosi, C. The Potential of III-V Semiconductors as Terrestrial Photovoltaic Devices. *Prog. Photovoltaics Res. Appl.* **2007**, *15* (1), 51–68.

(18) Kapadia, R.; Yu, Z.; Wang, H.-H. H.; Zheng, M.; Battaglia, C.; Hettick, M.; Kiriya, D.; Takei, K.; Lobaccaro, P.; Beeman, J. W.; et al. A Direct Thin-Film Path towards Low-Cost Large-Area III-V Photovoltaics. *Sci. Rep.* **2013**, *3*, 2275.

(19) Zheng, M.; Horowitz, K.; Woodhouse, M.; Battaglia, C.; Kapadia, R.; Javey, A. III-Vs at Scale: A PV Manufacturing Cost Analysis of the Thin Film Vapor-Liquid-Solid Growth Mode. *Prog. Photovoltaics Res. Appl.* **2016**, *24* (6), 871–878.

(20) Kempener, R.; Komor, P.; Hoke, A. *Smart Grids and Renewables - A Guide for Effective Deployment*; 2013.

(21) IEA-ETSAP; IRENA. *Renewable Energy Integration in Power Grids: Technology Brief*; 2015.

(22) Vittal, V. The Impact of Renewable Resources on the Performance and Reliability of the Electricity Grid. *The Bridge: Linking Engineering and Society*. 2010, pp 5–12.

(23) Energy Density https://en.wikipedia.org/wiki/Energy_density.

(24) Crabtree, G. W.; Dresselhaus, M. S.; Buchanan, M. V. The Hydrogen Economy. *Phys. Today* **2004**, *57* (12), 39–44.

(25) Zeng, M.; Li, Y. Recent Advances in Heterogeneous Electrocatalysts for the Hydrogen Evolution Reaction. *J. Mater. Chem. A* **2015**, *3* (29), 14942–14962.

(26) *The Role of the Chemical Sciences in Finding Alternatives to Critical Resources: A Workshop Summary.*; Washington DC, 2012.

(27) Benck, J. D.; Hellstern, T. R.; Kibsgaard, J.; Chakthranont, P.; Jaramillo, T. F. Catalyzing the Hydrogen Evolution Reaction (HER) with Molybdenum Sulfide Nanomaterials. *ACS Catal.* **2014**, *4* (11), 3957–3971.

(28) Hori, Y. Electrochemical CO_2 Reduction on Metal Electrodes. In *Modern Aspects of Electrochemistry*; Springer New York: New York, NY, 2008; Vol. 29, pp 89–189.

(29) Hutt, D.; Stevens, B. Electrodeposition of Indium for Bump Bonding. *2008 58th Electron. Components Technol. Conf.* **2008**, 2096–2100.

(30) Tian, Y.; Liu, C.; Hutt, D.; Stevens, B.; Flynn, D.; Desmulliez, M. P. Y. High Density Indium Bumping Using Electrodeposition Enhanced by Megasonic Agitation. *2009 11th Electron. Packag. Technol. Conf.* **2009**, 31–35.

(31) Walsh, F. C.; Gabe, D. R. The Electrodeposition of Indium. *Surf. Technol.* **1979**, *8*, 87–99.

(32) Piercy, R.; Hampson, N. A. The Electrochemistry of Indium. *J. Appl. Electrochem.* **1975**, *5* (1), 1–15.

(33) Kiriya, D.; Zheng, M.; Kapadia, R.; Zhang, J.; Hettick, M.; Yu, Z.; Takei, K.; Hank Wang, H.-H.; Lobaccaro, P.; Javey, A. Morphological and Spatial Control of InP Growth Using Closed-Space Sublimation. *J. Appl. Phys.* **2012**, *112* (12), 123102.

(34) Gayen, R. N. N.; Hussain, S.; Ghosh, D.; Bhar, R.; Pal, A. K. K. Two-Source Coevaporation Technique for Synthesis of Indium Phosphide Films with Controlled Composition. *J. Alloys*

Compd. **2012**, *531*, 34–40.

(35) Hibberd, C. J.; Chassaing, E.; Liu, W.; Mitzi, D. B.; Lincot, D.; Tiwari, A. N. Non-Vacuum Methods for Formation of Cu(In, Ga)(Se, S)$_2$ Thin Film Photovoltaic Absorbers. *Prog. Photovoltaics Res. Appl.* **2010**, *18* (6), 434–452.

(36) Bhattacharya, R. N. CIGS-Based Solar Cells Prepared from Electrodeposited Stacked Cu/In/Ga Layers. *Sol. Energy Mater. Sol. Cells* **2013**, *113*, 96–99.

(37) Bhattacharya, R. N.; Oh, M.-K.; Kim, Y. CIGS-Based Solar Cells Prepared from Electrodeposited Precursor Films. *Sol. Energy Mater. Sol. Cells* **2012**, *98*, 198–202.

(38) Raffaelle, R. P.; Forsell, H.; Potdevin, T.; Friedfeld, R.; Mantovani, J. G.; Bailey, S. G.; Hubbard, S. M.; Gordon, E. M.; Hepp, A. F. Electrodeposited CdS on CIS Pn Junctions. *Sol. Energy Mater. Sol. Cells* **1999**, *57* (2), 167–178.

(39) Wade, T.; Flowers, B.; Vaidyanathan, R.; Mathe, K.; Maddox, C. B.; Stickney, J. L. Electrochemical Atomic-Layer Epitaxy: Electrodeposition of III-V and II-VI Compound Semiconductors. *Mater. Res. Soc. Symp. Proc.* **2000**, *581*, 145–150.

(40) Wade, T. L.; Ward, L. C.; Maddox, C. B.; Happek, U.; Stickney, J. L. Electrodeposition of InAs. *Electrochem. Solid-State Lett.* **1999**, *2* (12), 616–618.

(41) Wade, T. L.; Vaidyanathan, R.; Happek, U.; Stickney, J. L. Electrochemical Formation of a III–V Compound Semiconductor Superlattice: InAs/InSb. *J. Electroanal. Chem.* **2001**, *500* (1–2), 322–332.

(42) Sahu, S. N. Aqueous Electrodeposition of InP Semiconductor Films. *J. Mater. Sci. Lett.* **1989**, *8* (5), 533–534.

(43) Sahu, S. N. Structural, Optical, and Electrical Properties of First Aqueous Electrodeposited InP Semiconductor Films. *Sol. Energy Mater.* **1990**, *20*, 349–358.

(44) Sahu, S. N. Some Properties of the First Non-Aqueous Electro-Codeposited InP, In and P Thin Films. *J. Mater. Sci. Mater. Electron.* **1992**, *3*, 102–106.

(45) Dharmadasa, I. M.; Haigh, J. Strengths and Advantages of Electrodeposition as a Semiconductor Growth Technique for Applications in Macroelectronic Devices. *J. Electrochem. Soc.* **2006**, *153* (1), G47.

(46) Woodhouse, M.; Goodrich, A.; Margolis, R.; James, T. L.; Lokanc, M.; Eggert, R. Supply-Chain Dynamics of Tellurium, Indium, and Gallium Within the Context of PV Manufacturing Costs. *IEEE J. Photovoltaics* **2013**, *3* (2), 833–837.

(47) Green, M. A.; Emery, K.; Hishikawa, Y.; Warta, W.; Dunlop, E. D. Solar Cell Efficiency Tables (Version 42). *Prog. Photovoltaics Res. Appl.* **2013**, *21*, 827–837.

(48) Cattarin, S.; Musiani, M.; Casellato, U.; Rassetto, G.; Razzini, G.; Decker, F.; Scrosati, B. Preparation of N- and P-lnP Films by PH_3 Treatment of Electrodeposited In Layers. *J. Electrochem. Soc.* **1995**, *142* (4), 1267–1272.

(49) Petukhov, I. V. Of the Mechanism Governing the Growth of Electrolessly Deposited Nickel-Phosphorus Coatings. *Russ. J. Electrochem.* **2007**, *43* (1), 34–41.

(50) Mimani, T.; Mayanna, S. M. Study of the Role of Sodium Hypophosphite in Electroless

Nickel Bath Solution. *J. Chem. Sci.* **1997**, *109* (3), 203–209.

(51) Ortega, J. Seminconductor Preparation by Electroplating. *An. Quim.* **1991**, *87*, 641–644.

(52) Kapadia, R.; Yu, Z.; Hettick, M.; Xu, J.; Zheng, M.; Chen, C.-Y.; Balan, A. D.; Chrzan, D. C.; Javey, A. Deterministic Nucleation of InP on Metal Foils with the Thin-Film Vapor-Liquid-Solid Growth Mode. *Chem. Mater.* **2014**.

(53) Huang, Q.; Reuter, K.; Amhed, S.; Deligianni, L.; Romankiw, L. T.; Jaime, S.; Grand, P.-P.; Charrier, V. Electrodeposition of Indium on Copper for CIS and CIGS Solar Cell Applications. *J. Electrochem. Soc.* **2011**, *158* (2), D57.

(54) Valderrama, R. C.; Miranda-Hernández, M.; Sebastian, P. J.; Ocampo, A. L. Electrodeposition of Indium onto Mo/Cu for the Deposition of Cu(In,Ga)Se_2 Thin Films. *Electrochim. Acta* **2008**, *53* (10), 3714–3721.

(55) Lee, S. M.; Ikeda, S.; Otsuka, Y.; Septina, W.; Harada, T.; Matsumura, M. Homogeneous Electrochemical Deposition of in on a Cu-Covered Mo Substrate for Fabrication of Efficient Solar Cells with a $CuInS_2$ Photoabsorber. *Electrochim. Acta* **2012**, *79*, 189–196.

(56) Venables, J. A.; Spiller, G. D. T.; Hanbucken, M. Nucleation and Growth of Thin Films. *Rep. Prog. Phys* **1984**, *47*, 399–469.

(57) Pettit, C. M.; Garland, J. E.; Etukudo, N. R.; Assiongbon, K. A.; Emery, S. B.; Roy, D. Electrodeposition of Indium on Molybdenum Studied with Optical Second Harmonic Generation and Electrochemical Impedance Spectroscopy. *Appl. Surf. Sci.* **2002**, *202* (1–2), 33–46.

(58) Chandrasekar, M. S.; Pushpavanam, M. Pulse and Pulse Reverse plating—Conceptual, Advantages and Applications. *Electrochim. Acta* **2008**, *53* (8), 3313–3322.

(59) Monroe, C.; Newman, J. Dendrite Growth in Lithium/Polymer Systems. *J. Electrochem. Soc.* **2003**, *150* (10), A1377.

(60) Bales, G.; Chrzan, D. Dynamics of Irreversible Island Growth during Submonolayer Epitaxy. *Phys. Rev. B* **1994**, *50* (9).

(61) Villain, J.; Pimpinelli, A.; Tang, L.; Wolf, D. Terrace Sizes in Molecular Beam Epitaxy. *J. Phys. I* **1992**, *2* (11), 2107–2121.

(62) Ho, J.; Yerushalmi, R.; Smith, G.; Majhi, P.; Bennett, J.; Halim, J.; Faifer, V. N.; Javey, A. Wafer-Scale, Sub-5 nm Junction Formation by Monolayer Doping and Conventional Spike Annealing. *Nano Lett.* **2009**, *9* (2), 725–730.

(63) Chu, S.; Majumdar, A. Opportunities and Challenges for a Sustainable Energy Future. *Nature* **2012**, *488* (7411), 294–303.

(64) Gray, H. B. Powering the Planet with Solar Fuel. *Nat. Chem.* **2009**, *1* (1), 7–7.

(65) Lewis, N. S.; Nocera, D. G. Powering the Planet: Chemical Challenges in Solar Energy Utilization. *Proc. Natl. Acad. Sci.* **2006**, *103* (43), 15729–15735.

(66) Walter, M. G.; Warren, E. L.; McKone, J. R.; Boettcher, S. W.; Mi, Q.; Santori, E. A.; Lewis, N. S. Solar Water Splitting Cells. *Chem. Rev.* **2010**, *110* (11), 6446–6473.

(67) Cook, T. R.; Dogutan, D. K.; Reece, S. Y.; Surendranath, Y.; Teets, T. S.; Nocera, D. G.

Solar Energy Supply and Storage for the Legacy and Nonlegacy Worlds. *Chem. Rev.* **2010**, *110* (11), 6474–6502.

(68) Turner, J. A. Sustainable Hydrogen Production. *Science (80-.).* **2004**, *305* (5686), 972–974.

(69) Ng, J. W. D.; Hellstern, T. R.; Kibsgaard, J.; Hinckley, A. C.; Benck, J. D.; Jaramillo, T. F. Polymer Electrolyte Membrane Electrolyzers Utilizing Non-Precious Mo-Based Hydrogen Evolution Catalysts. *ChemSusChem* **2015**, *8* (20), 3512–3519.

(70) Lu, Q.; Yu, Y.; Ma, Q.; Chen, B.; Zhang, H. 2D Transition-Metal-Dichalcogenide-Nanosheet-Based Composites for Photocatalytic and Electrocatalytic Hydrogen Evolution Reactions. *Adv. Mater.* **2016**, *28* (10), 1917–1933.

(71) Hinnemann, B.; Moses, P. G.; Bonde, J.; Jørgensen, K. P.; Nielsen, J. H.; Horch, S.; Chorkendorff, I.; Nørskov, J. K. Biomimetic Hydrogen Evolution: MoS_2 Nanoparticles as Catalyst for Hydrogen Evolution. *J. Am. Chem. Soc.* **2005**, *127* (15), 5308–5309.

(72) Karunadasa, H. I.; Montalvo, E.; Sun, Y.; Majda, M.; Long, J. R.; Chang, C. J. A Molecular MoS_2 Edge Site Mimic for Catalytic Hydrogen Generation. *Science (80-.).* **2012**, *335* (6069), 698–702.

(73) Xie, J.; Zhang, H.; Li, S.; Wang, R.; Sun, X.; Zhou, M.; Zhou, J.; Lou, X. W. D.; Xie, Y. Defect-Rich MoS_2 Ultrathin Nanosheets with Additional Active Edge Sites for Enhanced Electrocatalytic Hydrogen Evolution. *Adv. Mater.* **2013**, *25* (40), 5807–5813.

(74) Jaramillo, T. F.; Jorgensen, K. P.; Bonde, J.; Nielsen, J. H.; Horch, S.; Chorkendorff, I. Identification of Active Edge Sites for Electrochemical H_2 Evolution from MoS_2 Nanocatalysts. *Science (80-.).* **2007**, *317* (5834), 100–102.

(75) Li, Y.; Wang, H.; Xie, L.; Liang, Y.; Hong, G.; Dai, H. MoS_2 Nanoparticles Grown on Graphene: An Advanced Catalyst for the Hydrogen Evolution Reaction. *J. Am. Chem. Soc.* **2011**, *133* (19), 7296–7299.

(76) Liao, L.; Zhu, J.; Bian, X.; Zhu, L.; Scanlon, M. D.; Girault, H. H.; Liu, B. MoS_2 Formed on Mesoporous Graphene as a Highly Active Catalyst for Hydrogen Evolution. *Adv. Funct. Mater.* **2013**, *23* (42), 5326–5333.

(77) Kibsgaard, J.; Chen, Z.; Reinecke, B. N.; Jaramillo, T. F. Engineering the Surface Structure of MoS_2 to Preferentially Expose Active Edge Sites for Electrocatalysis. *Nat. Mater.* **2012**, *11* (11), 963–969.

(78) Zhang, Y.; Zuo, L.; Huang, Y.; Zhang, L.; Lai, F.; Fan, W.; Liu, T. In-Situ Growth of Few-Layered MoS_2 Nanosheets on Highly Porous Carbon Aerogel as Advanced Electrocatalysts for Hydrogen Evolution Reaction. *ACS Sustain. Chem. Eng.* **2015**, *3* (12), 3140–3148.

(79) Wang, H.; Lu, Z.; Xu, S.; Kong, D.; Cha, J. J.; Zheng, G.; Hsu, P.-C.; Yan, K.; Bradshaw, D.; Prinz, F. B.; et al. Electrochemical Tuning of Vertically Aligned MoS_2 Nanofilms and Its Application in Improving Hydrogen Evolution Reaction. *Proc. Natl. Acad. Sci.* **2013**, *110* (49), 19701–19706.

(80) Lu, Z.; Zhu, W.; Yu, X.; Zhang, H.; Li, Y.; Sun, X.; Wang, X.; Wang, H.; Wang, J.; Luo, J.; et al. Ultrahigh Hydrogen Evolution Performance of Under-Water "Superaerophobic" MoS_2 Nanostructured Electrodes. *Adv. Mater.* **2014**, *26* (17), 2683–2687.

(81) Yang, Y.; Fei, H.; Ruan, G.; Li, Y.; Tour, J. M. Vertically Aligned WS_2 Nanosheets for Water Splitting. *Adv. Funct. Mater.* **2015**, *25* (39), 6199–6204.

(82) Voiry, D.; Salehi, M.; Silva, R.; Fujita, T.; Chen, M.; Asefa, T.; Shenoy, V. B.; Eda, G.; Chhowalla, M. Conducting MoS_2 Nanosheets as Catalysts for Hydrogen Evolution Reaction. *Nano Lett.* **2013**, *13* (12), 6222–6227.

(83) Lukowski, M. A.; Daniel, A. S.; Meng, F.; Forticaux, A.; Li, L.; Jin, S. Enhanced Hydrogen Evolution Catalysis from Chemically Exfoliated Metallic MoS_2 Nanosheets. *J. Am. Chem. Soc.* **2013**, *135* (28), 10274–10277.

(84) Ambrosi, A.; Sofer, Z.; Pumera, M. 2H → 1T Phase Transition and Hydrogen Evolution Activity of MoS_2 , $MoSe_2$, WS_2 and WSe_2 Strongly Depends on the MX_2 Composition. *Chem. Commun.* **2015**, *51* (40), 8450–8453.

(85) Clark, E. L.; Singh, M. R.; Kwon, Y.; Bell, A. T. Differential Electrochemical Mass Spectrometer Cell Design for Online Quantification of Products Produced during Electrochemical Reduction of CO_2. *Anal. Chem.* **2015**, *87* (15), 8013–8020.

(86) Newman, J.; Thomas-Alyea, K. E. *Electrochemical Systems*; John Wiley & Sons, Inc.: Hoboken, NJ, USA, 2004.

(87) Liu, D.; Chen, X.; Li, D.; Wang, F.; Luo, X.; Yang, B. Simulation of MoS_2 Crystal Structure and the Experimental Study of Thermal Decomposition. *J. Mol. Struct.* **2010**, *980* (1–3), 66–71.

(88) Zheng, Y.; Jiao, Y.; Jaroniec, M.; Qiao, S. Z. Advancing the Electrochemistry of the Hydrogen-Evolution Reaction through Combining Experiment and Theory. *Angew. Chemie Int. Ed.* **2015**, *54* (1), 52–65.

(89) Conway, B. E.; Tilak, B. V. Interfacial Processes Involving Electrocatalytic Evolution and Oxidation of H_2, and the Role of Chemisorbed H. *Electrochim. Acta* **2002**, *47* (22–23), 3571–3594.

(90) Cheng, L.; Huang, W.; Gong, Q.; Liu, C.; Liu, Z.; Li, Y.; Dai, H. Ultrathin WS_2 Nanoflakes as a High-Performance Electrocatalyst for the Hydrogen Evolution Reaction. *Angew. Chemie Int. Ed.* **2014**, *53* (30), 7860–7863.

(91) Lukowski, M. A.; Daniel, A. S.; English, C. R.; Meng, F.; Forticaux, A.; Hamers, R. J.; Jin, S. Highly Active Hydrogen Evolution Catalysis from Metallic WS_2 Nanosheets. *Energy Environ. Sci.* **2014**, *7* (8), 2608–2613.

(92) Hashimoto, K.; Habazaki, H.; Yamasaki, M.; Meguro, S.; Sasaki, T.; Katagiri, H.; Matsui, T.; Fujimura, K.; Izumiya, K.; Kumagai, N.; et al. Advanced Materials for Global Carbon Dioxide Recycling. *Mater. Sci. Eng.* **2001**, *A304-306* (0), 88–96.

(93) Graves, C.; Ebbesen, S. D.; Mogensen, M.; Lackner, K. S. Sustainable Hydrocarbon Fuels by Recycling CO_2 and H_2O with Renewable or Nuclear Energy. *Renew. Sustain. Energy Rev.* **2011**, *15* (1), 1–23.

(94) Centi, G.; Perathoner, S. Perspectives and State of the Art in Producing Solar Fuels and Chemicals from CO_2. In *Green Carbon Dioxide*; John Wiley & Sons, Inc.: Hoboken, NJ, USA, NJ, USA, 2014; pp 1–24.

(95) Centi, G.; Perathoner, S.; Wine, G.; Gangeri, M. Electrocatalytic Conversion of CO_2 to Long Carbon-Chain Hydrocarbons. *Green Chem.* **2007**, *9* (6), 671–678.

(96) Gattrell, M.; Gupta, N.; Co, A. Electrochemical Reduction of CO_2 to Hydrocarbons to Store Renewable Electrical Energy and Upgrade Biogas. *Energy Convers. Manag.* **2007**, *48* (4), 1255–1265.

(97) Newman, J.; Hoertz, P. G.; Bonino, C. A.; Trainham, J. A. Review: An Economic Perspective on Liquid Solar Fuels. *J. Electrochem. Soc.* **2012**, *159* (10), A1722–A1729.

(98) Goeppert, A.; Czaun, M.; Jones, J.-P.; Surya Prakash, G. K.; Olah, G. A. Recycling of Carbon Dioxide to Methanol and Derived Products – Closing the Loop. *Chem. Soc. Rev.* **2014**, *43* (23), 7995–8048.

(99) Teeter, T. E.; Rysselberghe, P. Van. Reduction of Carbon Dioxide on Mercury Cathodes. *J. Chem. Phys.* **1954**, *22* (4), 759–760.

(100) Hori, Y.; Kikuchi, K.; Suzuki, S. Production of CO and CH_4 in Electrochemical Reduction of CO_2 at Metal Electrodes in Aqueous Hydrogencarbonate Solution. *Chem. Lett.* **1985**, No. 11, 1695–1698.

(101) Hori, Y.; Kikuchi, K.; Murata, A.; Suzuki, S. Production of Methane and Ethylene in Electrochemical Reduction of Carbon Dioxide at Copper Electrode in Aqueous Hydrogencarbonate Solution. *Chem. Lett.* **1986**, No. 6, 897–898.

(102) Hori, Y.; Murata, A.; Takahashi, R.; Suzuki, S. Electrochemical Reduction of Carbon Monoxide to Hydrocarbons at Various Metal Electrodes in Aqueous Solution. *Chem. Lett.* **1987**, *16* (8), 1665–1668.

(103) Hori, Y.; Murata, A.; Takahashi, R.; Suzuki, S. Electroreduction of Carbon Monoxide to Methane and Ethylene at a Copper Electrode in Aqueous Solutions at Ambient Temperature and Pressure. *J. Am. Chem. Soc.* **1987**, *109* (16), 5022–5023.

(104) Hori, Y.; Murata, A.; Takahashi, R. Formation of Hydrocarbons in the Electrochemical Reduction of Carbon Dioxide at a Copper Electrode in Aqueous Solution. *J. Chem. Soc. Faraday Trans. 1* **1989**, *85* (8), 2309–2326.

(105) Lu, Q.; Rosen, J.; Zhou, Y.; Hutchings, G. S.; Kimmel, Y. C.; Chen, J. G.; Jiao, F. A Selective and Efficient Electrocatalyst for Carbon Dioxide Reduction. *Nat. Commun.* **2014**, *5*, 3242.

(106) Fan, M.; Bai, Z.; Zhang, Q.; Ma, C.; Zhou, X.-D.; Qiao, J. Aqueous CO_2 Reduction on Morphology Controlled Cu_xO Nanocatalysts at Low Overpotential. *RSC Adv.* **2014**, *4* (84), 44583–44591.

(107) Roberts, F. S.; Kuhl, K. P.; Nilsson, A. High Selectivity for Ethylene from Carbon Dioxide Reduction over Copper Nanocube Electrocatalysts. *Angew. Chemie Int. Ed.* **2015**, *54* (17), 5179–5182.

(108) Li, C. W.; Ciston, J.; Kanan, M. W. Electroreduction of Carbon Monoxide to Liquid Fuel on Oxide-Derived Nanocrystalline Copper. *Nature* **2014**, *508* (7497), 504–507.

(109) Gattrell, M.; Gupta, N.; Co, A. A Review of the Aqueous Electrochemical Reduction of CO_2 to Hydrocarbons at Copper. *J. Electroanal. Chem.* **2006**, *594* (1), 1–19.

(110) Kumar, B.; Llorente, M.; Froehlich, J.; Dang, T.; Sathrum, A.; Kubiak, C. P. Photochemical and Photoelectrochemical Reduction of CO_2. *Annu. Rev. Phys. Chem.* **2012**, *63* (1), 541–569.

(111) Qiao, J.; Liu, Y.; Hong, F.; Zhang, J. A Review of Catalysts for the Electroreduction of Carbon Dioxide to Produce Low-Carbon Fuels. *Chem. Soc. Rev.* **2014**, *43*, 631–675.

(112) Lu, Q.; Rosen, J.; Jiao, F. Nanostructured Metallic Electrocatalysts for Carbon Dioxide Reduction. *ChemCatChem* **2015**, *7* (1), 38–47.

(113) Albo, J.; Alvarez-Guerra, M.; Castaño, P.; Irabien, A. Towards the Electrochemical Conversion of Carbon Dioxide into Methanol. *Green Chem.* **2015**, *17* (4), 2304–2324.

(114) Chen, Z.; Jaramillo, T. F.; Deutsch, T. G.; Kleiman-Shwarsctein, A.; Forman, A. J.; Gaillard, N.; Garland, R.; Takanabe, K.; Heske, C.; Sunkara, M.; et al. Accelerating Materials Development for Photoelectrochemical Hydrogen Production: Standards for Methods, Definitions, and Reporting Protocols. *J. Mater. Res.* **2010**, *25* (1), 3–16.

(115) Hori, Y.; Konishi, H.; Futamura, T.; Murata, A.; Koga, O.; Sakurai, H.; Oguma, K. "Deactivation of Copper Electrode" in Electrochemical Reduction of CO_2. *Electrochim. Acta* **2005**, *50* (27), 5354–5369.

(116) Hori, Y.; Murata, A.; Takahashi, R.; Suzuki, S. Enhanced Formation of Ethylene and Alcohols at Ambient Temperature and Pressure in Electrochemical Reduction of Carbon Dioxide at a Copper Electrode. *J. Chem. Soc. Chem. Commun.* **1988**, *109* (1), 17–19.

(117) Singh, M. R.; Clark, E. L.; Bell, A. T. Effects of Electrolyte, Catalyst, and Membrane Composition and Operating Conditions on the Performance of Solar-Driven Electrochemical Reduction of Carbon Dioxide. *Phys. Chem. Chem. Phys.* **2015**, *17* (29), 18924–18936.

(118) Li, C. W.; Kanan, M. W. CO_2 Reduction at Low Overpotential on Cu Electrodes Resulting from the Reduction of Thick Cu_2O Films. *J. Am. Chem. Soc.* **2012**, *134* (17), 7231–7234.

(119) Manthiram, K.; Beberwyck, B. J.; Alivisatos, A. P. Enhanced Electrochemical Methanation of Carbon Dioxide with a Dispersible Nanoscale Copper Catalyst. *J. Am. Chem. Soc.* **2014**, *136* (38), 13319–13325.

(120) Kim, D.; Resasco, J.; Yu, Y.; Asiri, A. M.; Yang, P. Synergistic Geometric and Electronic Effects for Electrochemical Reduction of Carbon Dioxide Using Gold-Copper Bimetallic Nanoparticles. *Nat. Commun.* **2014**, *5* (May), 4948.

(121) Kuhl, K. P.; Cave, E. R.; Abram, D. N.; Jaramillo, T. F. New Insights into the Electrochemical Reduction of Carbon Dioxide on Metallic Copper Surfaces. *Energy Environ. Sci.* **2012**, *5* (5), 7050–7059.

(122) Sen, S.; Liu, D.; Palmore, G. T. R. Electrochemical Reduction of CO_2 at Copper Nanofoams. *ACS Catal.* **2014**, *4* (9), 3091–3095.

(123) Kas, R.; Kortlever, R.; Yılmaz, H.; Koper, M. T. M.; Mul, G. Manipulating the Hydrocarbon Selectivity of Copper Nanoparticles in CO_2 Electroreduction by Process Conditions. *ChemElectroChem* **2015**, *2* (3), 354–358.

(124) Kortlever, R.; Peters, I.; Koper, S.; Koper, M. T. M. Electrochemical CO2 Reduction to

Formic Acid at Low Overpotential and with High Faradaic Efficiency on Carbon-Supported Bimetallic Pd-Pt Nanoparticles. *ACS Catal.* **2015**, *5* (7), 3916–3923.

(125) Rosen, B. a; Salehi-Khojin, A.; Thorson, M. R.; Zhu, W.; Whipple, D. T.; Kenis, P. J. a; Masel, R. I. Ionic Liquid-Mediated Selective Conversion of CO_2 to CO at Low Overpotentials. *Science (80-.).* **2011**, *334* (6056), 643–644.

(126) Li, H.; Oloman, C. The Electro-Reduction of Carbon Dioxide in a Continuous Reactor. *J. Appl. Electrochem.* **2005**, *35* (10), 955–965.

(127) Hashiba, H.; Yotsuhashi, S.; Deguchi, M.; Yamada, Y. Systematic Analysis of Electrochemical CO_2 Reduction with Various Reaction Parameters Using Combinatorial Reactors. *ACS Comb. Sci.* **2016**, *18* (4), 203–208.

(128) Houghton, R. W.; Kuhn, A. T. Mass-Transport Problems and Some Design Concepts of Electrochemical Reactors. *J. Appl. Electrochem.* **1974**, *4* (3), 173–190.

(129) Jansson, R. E. W. Electrochemical Reaction Engineering. *Chem. Eng. Sci.* **1980**, *35* (9), 1979–2004.

(130) Gabe, D. R.; Walsh, F. C. The Rotating Cylinder Electrode: A Review of Development. *J. Appl. Electrochem.* **1983**, *13* (1), 3–21.

(131) Sigrist, L.; Dossenbach, O.; Ibl, N. Mass Transport in Electrolytic Cells with Gas Sparging. *Int. J. Heat Mass Transf.* **1979**, *22* (10), 1393–1399.

(132) Economou, D. J. Two-Phase Mass Transfer in Channel Electrolyzers with Gas-Liquid Flow. *J. Electrochem. Soc.* **1985**, *132* (3), 601.

(133) Cavatorta, O. N.; Bohm, U. Mass Transfer in Electrolytic Cells with Gas Stirring. *J. Appl. Electrochem.* **1987**, *17* (2), 340–346.

(134) Reisener, J.; Reuter, M. A.; Krüger, J. Modelling of the Mass Transfer in Gas-Sparged Electrolysers with Neural Nets. *Chem. Eng. Sci.* **1993**, *48* (6), 1089–1101.

(135) Zhong, H.; Fujii, K.; Nakano, Y.; Jin, F. Effect of CO 2 Bubbling into Aqueous Solutions Used for Electrochemical Reduction of CO 2 for Energy Conversion and Storage. *J. Phys. Chem. C* **2015**, *119* (1), 55–61.

(136) Lum, Y.; Kwon, Y.; Lobaccaro, P.; Chen, L.; Clark, E. L.; Bell, A. T.; Ager, J. W. Trace Levels of Copper in Carbon Materials Show Significant Electrochemical CO_2 Reduction Activity. *ACS Catal.* **2016**, *6* (1), 202–209.

(137) Hong, J.; Zhang, W.; Ren, J.; Xu, R. Photocatalytic Reduction of CO_2: A Brief Review on Product Analysis and Systematic Methods. *Anal. Methods* **2013**, *5* (5), 1086–1097.

(138) Zhong, H.; Fujii, K.; Nakano, Y.; Jin, F. Effect of CO_2 Bubbling into Aqueous Solutions Used for Electrochemical Reduction of CO_2 for Energy Conversion and Storage. *J. Phys. Chem. C* **2015**, *119* (1), 55–61.

(139) Harned, H. S.; Scholes, S. R. The Ionization Constant of HCO_3 from 0 to 50°. *J. Am. Chem. Soc.* **1941**, *63* (6), 1706–1709.

(140) Harned, H. S.; Davis, R. The Ionization Constant of Carbonic Acid in Water and the Solubility of Carbon Dioxide in Water and Aqueous Salt Solutions from 0 to 50°. *J. Am.*

Chem. Soc. **1943**, *65* (10), 2030–2037.

(141) Carroll, J. J.; Slupsky, J. D.; Mather, A. E. The Solubility of Carbon Dioxide in Water at Low Pressure. *J. Phys. Chem. Ref. Data* **1991**, *20* (6), 1201–1209.

(142) Bandura, A. V.; Lvov, S. N. The Ionization Constant of Water over Wide Ranges of Temperature and Density. *J. Phys. Chem. Ref. Data* **2006**, *35* (1), 15–30.

(143) Markham, A. E.; Kobe, K. A. The Solubility of Carbon Dioxide and Nitrous Oxide in Aqueous Salt Solutions. *J. Am. Chem. Soc.* **1941**, *63* (2), 449–454.

(144) Weiss, R. F. Carbon Dioxide in Water and Seawater: The Solubility of a Non-Ideal Gas. *Mar. Chem.* **1974**, *2* (3), 203–215.

(145) Dickson, A. .; Riley, J. . The Estimation of Acid Dissociation Constants in Seawater Media from Potentionmetric Titrations with Strong Base. I. The Ionic Product of Water — Kw. *Mar. Chem.* **1979**, *7* (2), 89–99.

(146) Millero, F. J.; Pierrot, D.; Lee, K.; Wanninkhof, R.; Feely, R. A.; Sabine, C. L.; Key, R. M.; Takahashi, T. Dissociation Constants for Carbonic Acid Determined from Field Measurements. *Deep. Res. Part I Oceanogr. Res. Pap.* **2002**, *49* (10), 1705–1723.

(147) Millero, F. J. The Marine Inorganic Carbon Cycle. *Chem. Rev.* **2007**, *107* (2), 308–341.

(148) Riebesell, U.; Fabry, V. J.; Hansson, L.; Gattuso, J.-P. *Guide to Best Practices for Ocean Acidification Research and Data Reporting*; Publications Office of the European Union Luxembourg, 2010.

(149) Elhajj, J.; Al-Hindi, M.; Azizi, F. A Review of the Absorption and Desorption Processes of Carbon Dioxide in Water Systems. *Ind. Eng. Chem. Res.* **2014**, *53* (1), 2–22.

(150) Schumpe, A. The Estimation of Gas Solubilities in Salt Solutions. *Chem. Eng. Sci.* **1993**, *48* (1), 153–158.

(151) Weisenberger, S.; Schumpe, A. Estimation of Gas Solubilities in Salt Solutions at Temperatures from 273 K to 363 K. *AIChE J.* **1996**, *42* (1), 298–300.

(152) Plummer, L. N.; Busenberg, E. The Solubilities of Calcite, Aragonite and Vaterite in CO_2-H_2 O Solutions between 0 and 90°C, and an Evaluation of the Aqueous Model for the System $CaCO_3$-CO_2-H_2O. *Geochim. Cosmochim. Acta* **1982**, *46* (6), 1011–1040.

(153) Hikita, H.; Konishi, Y. Desorption of Carbon Dioxide from Supersaturated Water in an Agitated Vessel. *AIChE J.* **1984**, *30* (6), 945–951.

(154) Kraemer, J. T.; Bagley, D. M. Supersaturation of Dissolved H_2 and CO_2 During Fermentative Hydrogen Production with N_2 Sparging. *Biotechnol. Lett.* **2006**, *28* (18), 1485–1491.

(155) Kyriacou, G.; Anagnostopoulos, A. Electroreduction of CO_2 on Differently Prepared Copper Electrodes: The Influence of Electrode Treatment on the Current Efficiences. *J. Electroanal. Chem.* **1992**, *322* (1–2), 233–246.

(156) Kas, R.; Kortlever, R.; Milbrat, A.; Koper, M. T. M.; Mul, G.; Baltrusaitis, J. Electrochemical CO_2 Reduction on Cu_2O-Derived Copper Nanoparticles: Controlling the Catalytic Selectivity of Hydrocarbons. *Phys. Chem. Chem. Phys.* **2014**, *16* (24), 12194.

(157) Varela, A. S.; Kroschel, M.; Reier, T.; Strasser, P. Controlling the Selectivity of CO_2 Electroreduction on Copper: The Effect of the Electrolyte Concentration and the Importance of the Local pH. *Catal. Today* **2016**, *260*, 8–13.

(158) Gupta, N.; Gattrell, M.; MacDougall, B. Calculation for the Cathode Surface Concentrations in the Electrochemical Reduction of CO_2 in $KHCO_3$ Solutions. *J. Appl. Electrochem.* **2006**, *36* (2), 161–172.

(159) Calderbank, P. H.; Moo-Young, M. B. The Continuous Phase Heat and Mass-Transfer Properties of Dispersions. *Chem. Eng. Sci.* **1961**, *16* (1–2), 39–54.

(160) Akita, K.; Yoshida, F. Gas Holdup and Volumetric Mass Transfer Coefficient in Bubble Columns. Effects of Liquid Properties. *Ind. Eng. Chem. Process Des. Dev.* **1973**, *12* (1), 76–80.

(161) Akita, K.; Yoshida, F. Bubble Size, Interfacial Area, and Liquid-Phase Mass Transfer Coefficient in Bubble Columns. *Ind. Eng. Chem. Process Des. Dev.* **1974**, *13* (1), 84–91.

(162) Shah, Y. T.; Kelkar, B. G.; Godbole, S. P.; Deckwer, W.-D. Design Parameters Estimations for Bubble Column Reactors. *AIChE J.* **1982**, *28* (3), 353–379.

(163) Kawase, Y.; Moo-Young, M. Correlations for Liquid-Phase Mass Transfer Coefficients in Bubble Column Reactors with Newtonian and Non-Newtonian Fluids. *Can. J. Chem. Eng.* **1992**, *70* (1), 48–54.

(164) Deckwer, W.-D.; Schumpe, A. Improved Tools for Bubble Column Reactor Design and Scale-Up. *Chem. Eng. Sci.* **1993**, *48* (5), 889–911.

(165) Shimizu, K.; Takada, S.; Minekawa, K.; Kawase, Y. Phenomenological Model for Bubble Column Reactors: Prediction of Gas Hold-Ups and Volumetric Mass Transfer Coefficients. *Chem. Eng. J.* **2000**, *78* (1), 21–28.

(166) Dhaouadi, H.; Poncin, S.; Hornut, J. M.; Midoux, N. Gas–liquid Mass Transfer in Bubble Column Reactor: Analytical Solution and Experimental Confirmation. *Chem. Eng. Process. Process Intensif.* **2008**, *47* (4), 548–556.

(167) Ramezani, M.; Mostoufi, N.; Mehrnia, M. R. Improved Modeling of Bubble Column Reactors by Considering the Bubble Size Distribution. *Ind. Eng. Chem. Res.* **2012**, *51* (16), 5705–5714.

(168) Gruber, M. C.; Radl, S.; Khinast, J. G. Rigorous Modeling of CO_2 Absorption and Chemisorption: The Influence of Bubble Coalescence and Breakage. *Chem. Eng. Sci.* **2015**, *137*, 188–204.

(169) Yoshida, F.; Akita, K. Performance of Gas Bubble Columns: Volumetric Liquid-Phase Mass Transfer Coefficient and Gas Holdup. *AIChE J.* **1965**, *11* (1), 9–13.

(170) Lau, R.; Lee, P. H. V.; Chen, T. Mass Transfer Studies in Shallow Bubble Column Reactors. *Chem. Eng. Process. Process Intensif.* **2012**, *62*, 18–25.

(171) Clift, R.; Grace, J. R.; Weber, M. E. *Bubbles, Drop, and Particles*; 1978.

(172) Sechenov, I. M. On the Properties of Salt Solutions on the Basis of Their Interaction with Carbon Dioxide. *Z. Phys. Chem* **1889**, *4*, 117.

(173) Kim, Y.-G.; Baricuatro, J. H.; Javier, A.; Gregoire, J. M.; Soriaga, M. P. The Evolution of the Polycrystalline Copper Surface, First to Cu(111) and Then to Cu(100), at a Fixed CO2RR Potential: A Study by Operando EC-STM. *Langmuir* **2014**, *30* (50), 15053–15056.

(174) Azuma, M.; Hashimoto, K.; Hiramoto, M.; Watanabe, M.; Sakata, T. Electrochemical Reduction of Carbon Dioxide on Various Metal Electrodes in Low-Temperature Aqueous KHCO3 Media. *J. Electrochem. Soc.* **1990**, *137* (6), 1772–1778.

(175) Hatsukade, T.; Kuhl, K. P.; Cave, E. R.; Abram, D. N.; Jaramillo, T. F. Insights into the Electrocatalytic Reduction of CO_2 on Metallic Silver Surfaces. *Phys. Chem. Chem. Phys.* **2014**, *16* (27), 13814–13819.

(176) Loiudice, A.; Lobaccaro, P.; Kamali, E. A.; Thao, T.; Huang, B. H.; Ager, J. W.; Buonsanti, R. Tailoring Copper Nanocrystals towards C_2 Products in Electrochemical CO_2 Reduction. *Angew. Chemie Int. Ed.* **2016**, *55*, 1–5.

(177) Kwon, Y.; Koper, M. T. M. Combining Voltammetry with HPLC: Application to Electro-Oxidation of Glycerol. *Anal. Chem.* **2010**, *82* (13), 5420–5424.

(178) Bertheussen, E.; Verdaguer-Casadevall, A.; Ravasio, D.; Montoya, J. H.; Trimarco, D. B.; Roy, C.; Meier, S.; Wendland, J.; Nørskov, J. K.; Stephens, I. E. L.; et al. Acetaldehyde as an Intermediate in the Electroreduction of Carbon Monoxide to Ethanol on Oxide-Derived Copper. *Angew. Chemie Int. Ed.* **2016**, *55* (4), 1450–1454.

(179) Potyrailo, R.; Rajan, K.; Stoewe, K.; Takeuchi, I.; Chisholm, B.; Lam, H. Combinatorial and High-Throughput Screening of Materials Libraries: Review of State of the Art. *ACS Comb. Sci.* **2011**, *13* (6), 579–633.

(180) Haber, J. A.; Cai, Y.; Jung, S.; Xiang, C.; Mitrovic, S.; Jin, J.; Bell, A. T.; Gregoire, J. M. Discovering Ce-Rich Oxygen Evolution Catalysts, from High Throughput Screening to Water Electrolysis. *Energy Environ. Sci.* **2014**, *7* (2), 682.

(181) Seley, D.; Ayers, K.; Parkinson, B. A. Combinatorial Search for Improved Metal Oxide Oxygen Evolution Electrocatalysts in Acidic Electrolytes. *ACS Comb. Sci.* **2013**, *15* (2), 82–89.

(182) Gerken, J. B.; Chen, J. Y. C.; Massé, R. C.; Powell, A. B.; Stahl, S. S. Development of an O_2 -Sensitive Fluorescence-Quenching Assay for the Combinatorial Discovery of Electrocatalysts for Water Oxidation. *Angew. Chemie Int. Ed.* **2012**, *51* (27), 6676–6680.

(183) Minguzzi, A.; Alpuche-Aviles, M. A.; López, J. R.; Rondinini, S.; Bard, A. J. Screening of Oxygen Evolution Electrocatalysts by Scanning Electrochemical Microscopy Using a Shielded Tip Approach. *Anal. Chem.* **2008**, *80* (11), 4055–4064.

(184) Xiang, C.; Suram, S. K.; Haber, J. A.; Guevarra, D. W.; Soedarmadji, E.; Jin, J.; Gregoire, J. M. High-Throughput Bubble Screening Method for Combinatorial Discovery of Electrocatalysts for Water Splitting. *ACS Comb. Sci.* **2014**, *16* (2), 47–52.

(185) Goldsmith, J. I.; Hudson, W. R.; Lowry, M. S.; Anderson, T. H.; Bernhard, S. Discovery and High-Throughput Screening of Heteroleptic Iridium Complexes for Photoinduced Hydrogen Production. *J. Am. Chem. Soc.* **2005**, *127* (20), 7502–7510.

(186) Jaramillo, T. F.; Ivanovskaya, A.; McFarland, E. W. High-Throughput Screening System for Catalytic Hydrogen-Producing Materials. *J. Comb. Chem.* **2002**, *4* (1), 17–22.

(187) Grote, J. P.; Zeradjanin, A. R.; Cherevko, S.; Savan, A.; Breitbach, B.; Ludwig, A.; Mayrhofer, K. J. J. Screening of Material Libraries for Electrochemical CO_2 Reduction Catalysts - Improving Selectivity of Cu by Mixing with Co. *J. Catal.* **2015**.

(188) Grote, J.-P.; Zeradjanin, A. R.; Cherevko, S.; Mayrhofer, K. J. J. Coupling of a Scanning Flow Cell with Online Electrochemical Mass Spectrometry for Screening of Reaction Selectivity. *Rev. Sci. Instrum.* **2014**, *85* (10), 104101.

(189) Baltruschat, H. Differential Electrochemical Mass Spectrometry. *J. Am. Soc. Mass Spectrom.* **2004**, *15* (12), 1693–1706.

(190) Wolter, O.; Heitbaum, J. Differential Electrochemical Mass Spectroscopy (DEMS) - a New Method for the Study of Electrode Processes. *Berichte der Bunsengesellschaft für Phys. Chemie* **1984**, *88* (1), 2–6.

(191) Wonders, A. H.; Housmans, T. H. M.; Rosca, V.; Koper, M. T. M. On-Line Mass Spectrometry System for Measurements at Single-Crystal Electrodes in Hanging Meniscus Configuration. *J. Appl. Electrochem.* **2006**, *36* (11), 1215–1221.

(192) Javier, A.; Chmielowiec, B.; Sanabria-Chinchilla, J.; Kim, Y. G.; Baricuatro, J. H.; Soriaga, M. P. A DEMS Study of the Reduction of CO_2, CO, and HCHO Pre-Adsorbed on Cu Electrodes: Empirical Inferences on the CO2RR Mechanism. *Electrocatalysis* **2015**, *6* (2), 127–131.

(193) Watson, J. T.; Sparkman, O. D. Electron Ionization. In *Introduction to Mass Spectrometry: Instrumentation, Applications, and Strategies for Data Interpretation*; John Wiley & Sons, Inc.: Chichester, UK, 2007; pp 317–447.

(194) Gross, J. H. Principles of Ionization and Ion Dissociation. In *Mass Spectrometry*; Springer Berlin Heidelberg: Berlin, Heidelberg, 2011; pp 21–66.

(195) Ghadimkhani, G.; de Tacconi, N. R.; Chanmanee, W.; Janaky, C.; Rajeshwar, K. Efficient Solar Photoelectrosynthesis of Methanol from Carbon Dioxide Using Hybrid CuO-Cu_2O Semiconductor Nanorod Arrays. *Chem. Commun.* **2013**, *49* (13), 1297–1299.

(196) Won, D. H.; Choi, C. H.; Chung, J.; Woo, S. I. Photoelectrochemical Production of Formic Acid and Methanol from Carbon Dioxide on Metal-Decorated CuO/Cu_2O-Layered Thin Films under Visible Light Irradiation. *Appl. Catal. B Environ.* **2014**, *158–159*, 217–223.

(197) Kuhl, K. P.; Hatsukade, T.; Cave, E. R.; Abram, D. N.; Kibsgaard, J.; Jaramillo, T. F. Electrocatalytic Conversion of Carbon Dioxide to Methane and Methanol on Transition Metal Surfaces. *J. Am. Chem. Soc.* **2014**, *136* (40), 14107–14113.

(198) Rajeshwar, K.; de Tacconi, N. R.; Ghadimkhani, G.; Chanmanee, W.; Janaky, C. Tailoring Copper Oxide Semiconductor Nanorod Arrays for Photoelectrochemical Reduction of Carbon Dioxide to Methanol. *ChemPhysChem* **2013**, *14* (10), 2251–2259.

(199) Chen, C. S.; Wan, J. H.; Yeo, B. S. Electrochemical Reduction of Carbon Dioxide to Ethane Using Nanostructured Cu_2O-Derived Copper Catalyst and Palladium(II) Chloride. *J. Phys. Chem. C* **2015**, *119* (48), 26875–26882.

(200) Lee, S.; Kim, D.; Lee, J. Electrocatalytic Production of C_3-C_4 Compounds by Conversion of CO_2 on a Chloride-Induced Bi-Phasic Cu_2O-Cu Catalyst. *Angew. Chemie Int. Ed.* **2015**, *54* (49), 14701–14705.

(201) Barton, E. E.; Rampulla, D. M.; Bocarsly, A. B. Selective Solar-Driven Reduction of CO_2 to Methanol Using a Catalyzed P-GaP Based Photoelectrochemical Cell. *J. Am. Chem. Soc.* **2008**, *130* (20), 6342–6344.

(202) NIST Mass Spec Data Center, S.E. Stein, D. Mass Spectra. In *NIST Chemistry WebBook, NIST Standard Reference Database Number 69*; Linstrom, P. J., Mallard, W. G., Eds.; National Institute of Standards and Technology, Gaithersburg, MD, 2016.

(203) Adams, N. G.; Smith, D. The Selected Ion Flow Tube (SIFT); A Technique for Studying Ion-Neutral Reactions. *Int. J. Mass Spectrom. Ion Phys.* **1976**, *21* (3–4), 349–359.

(204) Ferguson, E. E. Ion-Molecule Reactions. *Annu. Rev. Phys. Chem.* **1975**, *26* (1), 17–38.

(205) *Kinetics of Ion-Molecule Reactions*; Ausloos, P., Ed.; Springer US: Boston, MA, 1979.

(206) Spaněl, P.; Smith, D. Selected Ion Flow Tube: A Technique for Quantitative Trace Gas Analysis of Air and Breath. *Med. Biol. Eng. Comput.* **1996**, *34* (6), 409–419.

(207) Španěl, P.; Smith, D. Progress in SIFT-MS: Breath Analysis and Other Applications. *Mass Spectrom. Rev.* **2011**, *30* (2), 236–267.

(208) Smith, D.; Španěl, P. Selected Ion Flow Tube Mass Spectrometry (SIFT-MS) for on-Line Trace Gas Analysis. *Mass Spectrom. Rev.* **2005**, *24* (5), 661–700.

(209) Smith, D.; Španěl, P. Ambient Analysis of Trace Compounds in Gaseous Media by SIFT-MS. *Analyst* **2011**, *136* (10), 2009.

(210) Smith, D.; Španěl, P.; Herbig, J.; Beauchamp, J. Mass Spectrometry for Real-Time Quantitative Breath Analysis. *J. Breath Res.* **2014**, *8* (2), 27101.

(211) Milligan, D. B.; Francis, G. J.; Prince, B. J.; McEwan, M. J. Demonstration of Selected Ion Flow Tube MS Detection in the Parts per Trillion Range. *Anal. Chem.* **2007**, *79* (6), 2537–2540.

(212) Španěl, P.; Smith, D. SIFT Studies of the Reactions of H_3O^+, NO^+ and O_2^+ with Several Ethers. *Int. J. Mass Spectrom. Ion Process.* **1998**, *172* (3), 239–247.

(213) Spanel, P.; Smith, D. SIFT Studies of the Reactions of H3O+, NO+ and O2+ with a Series of Alcohols. *Int. J. Mass Spectrom. Ion Process.* **1997**, *167–168*, 375–388.

(214) Ŝpaněl, P.; Smith, D. SIFT Studies of the Reactions of H_3O^+, NO^+ and O_2^+ with a Series of Volatile Carboxylic Acids and Esters. *Int. J. Mass Spectrom. Ion Process.* **1998**, *172* (1–2), 137–147.

(215) Španěl, P.; Ji, Y.; Smith, D. SIFT Studies of the Reactions of H_3O^+, NO^+ and O_2^+ with a Series of Aldehydes and Ketones. *Int. J. Mass Spectrom. Ion Process.* **1997**, *165–166*, 25–37.

(216) Wilson, P. F.; Freeman, C. G.; McEwan, M. J. Reactions of Small Hydrocarbons with H_3O^+, O_2^+, and NO^+ Ions. *Int. J. Mass Spectrom.* **2003**, *229* (3), 143–149.

(217) Smith, D.; Cheng, P.; Spanel, P. Analysis of Petrol and Diesel Vapour and Vehicle Engine Exhaust Gases Using Selected Ion Flow Tube Mass Spectrometry. *Rapid Commun. Mass Spectrom.* **2002**, *16* (11), 1124–1134.

(218) Francis, G. J.; Langford, V. S.; Milligan, D. B.; McEwan, M. J. Real-Time Monitoring of

Hazardous Air Pollutants. *Anal. Chem.* **2009**, *81* (4), 1595–1599.

(219) Lias, S. G. Ionization Energy Evaluation. In *NIST Chemistry WebBook, NIST Standard Reference Database Number 692*; Linstrom, P. J., Mallard, W. G., Eds.; National Institute of Standards and Technology, Gaithersburg MD, 2016.

(220) Lias, E. P. H. and S. G. Proton Affinity Evaluation. In *NIST Chemistry WebBook, NIST Standard Reference Database Number 69*; Linstrom, P. J., Mallard, W. G., Eds.; National Institute of Standards and Technology, Gaithersburg MD, 2016.

(221) Jones, J.-P.; Prakash, G. K. S.; Olah, G. a. Electrochemical CO_2 Reduction: Recent Advances and Current Trends. *Isr. J. Chem.* **2014**, *54* (10), 1451–1466.

(222) Zhu, S.; Shao, M. Surface Structure and Composition Effects on Electrochemical Reduction of Carbon Dioxide. *J. Solid State Electrochem.* **2016**, *20* (4), 861–873.

(223) Jhong, H.-R. "Molly"; Ma, S.; Kenis, P. J. Electrochemical Conversion of CO_2 to Useful Chemicals: Current Status, Remaining Challenges, and Future Opportunities. *Curr. Opin. Chem. Eng.* **2013**, *2* (2), 191–199.

(224) Wang, Z.; Li, C.; Yamauchi, Y. Nanostructured Nonprecious Metal Catalysts for Electrochemical Reduction of Carbon Dioxide. *Nano Today* **2016**, *11* (3), 373–391.

(225) Ren, D.; Deng, Y.; Handoko, A. D.; Chen, C. S.; Malkhandi, S.; Yeo, B. S. Selective Electrochemical Reduction of Carbon Dioxide to Ethylene and Ethanol on Copper(I) Oxide Catalysts. *ACS Catal.* **2015**, *5* (5), 2814–2821.

(226) Dutta, A.; Rahaman, M.; Luedi, N. C.; Mohos, M.; Broekmann, P. Morphology Matters: Tuning the Product Distribution of CO_2 Electroreduction on Oxide-Derived Cu Foam Catalysts. *ACS Catal.* **2016**, *6* (6), 3804–3814.

(227) Ren, D.; Wong, N. T.; Handoko, A. D.; Huang, Y.; Yeo, B. S. Mechanistic Insights into the Enhanced Activity and Stability of Agglomerated Cu Nanocrystals for the Electrochemical Reduction of Carbon Dioxide to N -Propanol. *J. Phys. Chem. Lett.* **2016**, *7* (1), 20–24.

(228) Li, Y.; Su, H.; Chan, S. H.; Sun, Q. CO_2 Electroreduction Performance of Transition Metal Dimers Supported on Graphene: A Theoretical Study. *ACS Catal.* **2015**, *5* (11), 6658–6664.

(229) Nie, X.; Luo, W.; Janik, M. J.; Asthagiri, A. Reaction Mechanisms of CO_2 Electrochemical Reduction on Cu(111) Determined with Density Functional Theory. *J. Catal.* **2014**, *312*, 108–122.

(230) Kortlever, R.; Shen, J.; Schouten, K. J. P.; Calle-Vallejo, F.; Koper, M. T. M. Catalysts and Reaction Pathways for the Electrochemical Reduction of Carbon Dioxide. *J. Phys. Chem. Lett.* **2015**, *6* (20), 4073–4082.

(231) Koga, O.; Nakama, K.; Murata, A.; Hori, Y. Effects of Surface State of Copper Electrode on the Selectivity of Electrochemical Reduction of Carbon Dioxide. *Denki Kagaku* **1989**, *57* (12), 1137–1140.

(232) Ma, M.; Djanashvili, K.; Smith, W. A. Controllable Hydrocarbon Formation from the Electrochemical Reduction of CO_2 over Cu Nanowire Arrays. *Angew. Chemie Int. Ed.* **2016**, *55* (23), 6680–6684.

(233) Ma, M.; Djanashvili, K.; Smith, W. A. Selective Electrochemical Reduction of CO_2 to CO

on CuO-Derived Cu Nanowires. *Phys. Chem. Chem. Phys.* **2015**, *17* (32), 20861–20867.

(234) Raciti, D.; Livi, K. J.; Wang, C. Highly Dense Cu Nanowires for Low-Overpotential CO_2 Reduction. *Nano Lett.* **2015**, *15* (10), 6829–6835.

(235) Xie, J.; Huang, Y.; Yu, H. Tuning the Catalytic Selectivity in Electrochemical CO_2 Reduction on Copper Oxide-Derived Nanomaterials. *Front. Environ. Sci. Eng.* **2015**, *9* (5), 861–866.

(236) Hori, Y.; Takahashi, I.; Koga, O.; Hoshi, N. Selective Formation of C_2 Compounds from Electrochemical Reduction of CO_2 at a Series of Copper Single Crystal Electrodes. *J. Phys. Chem. B* **2002**, *106* (1), 15–17.

(237) Takahashi, I.; Koga, O.; Hoshi, N.; Hori, Y. Electrochemical Reduction of CO_2 at Copper Single Crystal Cu(S)-[n(111)×(111)] and Cu(S)-[n(110)×(100)] Electrodes. *J. Electroanal. Chem.* **2002**, *533* (1–2), 135–143.

(238) Hori, Y.; Takahashi, I.; Koga, O.; Hoshi, N. Electrochemical Reduction of Carbon Dioxide at Various Series of Copper Single Crystal Electrodes. *J. Mol. Catal. A Chem.* **2003**, *199* (1–2), 39–47.

(239) Schouten, K. J. P.; Qin, Z.; Gallent, E. P.; Koper, M. T. M. Two Pathways for the Formation of Ethylene in CO Reduction on Single-Crystal Copper Electrodes. *J. Am. Chem. Soc.* **2012**, *134* (24), 9864–9867.

(240) Schouten, K. J. P.; Pérez Gallent, E.; Koper, M. T. M. The Influence of pH on the Reduction of CO and to Hydrocarbons on Copper Electrodes. *J. Electroanal. Chem.* **2014**, *716*, 53–57.

(241) Kuhn, A. T.; Chan, C. Y. pH Changes at near-Electrode Surfaces. *J. Appl. Electrochem.* **1983**, *13* (2), 189–207.

(242) Auinger, M.; Katsounaros, I.; Meier, J. C.; Klemm, S. O.; Biedermann, P. U.; Topalov, A. a; Rohwerder, M.; Mayrhofer, K. J. J. Near-Surface Ion Distribution and Buffer Effects during Electrochemical Reactions. *Phys. Chem. Chem. Phys.* **2011**, *13* (36), 16384.

(243) Katsounaros, I.; Meier, J. C.; Klemm, S. O.; Topalov, A. A.; Biedermann, P. U.; Auinger, M.; Mayrhofer, K. J. J. The Effective Surface pH during Reactions at the Solid–liquid Interface. *Electrochem. commun.* **2011**, *13* (6), 634–637.

(244) Deligianni, H.; Romankiw, L. T. In Situ Surface pH Measurement during Electrolysis Using a Rotating pH Electrode. *IBM J. Res. Dev.* **1993**, *37* (2), 85–95.

(245) Harris, L. B. Change in pH near the Cathode During the Electrodeposition of a Bivalent Metal. Analysis. *J. Electrochem. Soc.* **1973**, *120* (8), 1034.

(246) Lee, W.; Park, S.-J. Porous Anodic Aluminum Oxide: Anodization and Templated Synthesis of Functional Nanostructures. *Chem. Rev.* **2014**, *114* (15), 7487–7556.

(247) Chung, J. H.; Won, D. H.; Koh, J.; Kim, E.-H.; Woo, S. I. Hierarchical Cu Pillar Electrode for Electrochemical CO_2 Reduction to Formic Acid with Low Overpotential. *Phys. Chem. Chem. Phys.* **2016**, *18*, 6252–6258.

(248) Stępniowski, W. J.; Salerno, M. Fabrication of Nanowires and Nanotubes by Anodic Alumina Template-Assisted Electrodeposition. In *Manufacturing nanostructures*; Ahmed,

P. W., Ali, P. N., Eds.; One Central Press, 2014; pp 321–357.

(249) Banholzer, M. J.; Qin, L.; Millstone, J. E.; Osberg, K. D.; Mirkin, C. A. On-Wire Lithography: Synthesis, Encoding and Biological Applications. *Nat. Protoc.* **2009**, *4* (6), 838–848.

(250) Williams, K. R.; Member, S.; Gupta, K.; Member, S.; Wasilik, M. Etch Rates for Micromachining Processing — Part II. **2003**, *12* (6), 761–778.

(251) Murata, A.; Hori, Y. Product Selectivity Affected by Cationic Species in Electrochemical Reduction of CO_2 and CO at a Cu Electrode. *Bull. Chem. Soc. Jpn.* **1991**, *64* (1), 123–127.

(252) McCrory, C. C. L.; Jung, S.; Ferrer, I. M.; Chatman, S. M.; Peters, J. C.; Jaramillo, T. F. Benchmarking Hydrogen Evolving Reaction and Oxygen Evolving Reaction Electrocatalysts for Solar Water Splitting Devices. *J. Am. Chem. Soc.* **2015**, *137* (13), 4347–4357.

(253) Xiao, H.; Cheng, T.; Goddard, W. A.; Sundararaman, R. Mechanistic Explanation of the pH Dependence and Onset Potentials for Hydrocarbon Products from Electrochemical Reduction of CO on Cu (111). *J. Am. Chem. Soc.* **2016**, *138* (2), 483–486.

(254) Greeley, J. Theoretical Heterogeneous Catalysis: Scaling Relationships and Computational Catalyst Design. *Annu. Rev. Chem. Biomol. Eng.* **2016**, *7* (1), 605–635.

(255) Peterson, A. A.; Nørskov, J. K. Activity Descriptors for CO_2 Electroreduction to Methane on Transition-Metal Catalysts. *J. Phys. Chem. Lett.* **2012**, *3* (2), 251–258.

(256) Christophe, J.; Doneux, T.; Buess-Herman, C. Electroreduction of Carbon Dioxide on Copper-Based Electrodes: Activity of Copper Single Crystals and Copper–Gold Alloys. *Electrocatalysis* **2012**, *3* (2), 139–146.

(257) Watanabe, M.; Shibata, M.; Katoh, A.; Sakata, T.; Azuma, M. Design of Alloy Electrocatalysts for Reduction: Improved Energy Efficiency , Selectivity , and Reaction Rate for the CO_2 Electroreduction on Cu Alloy Electrodes. *J. Electroanal. Chem. Interfacial Electrochem.* **1991**, *305*, 319–328.

(258) Watanabe, M.; Shibata, M.; Kato, A.; Azuma, M.; Sakata, T. Design of Alloy Electrocatalysts for CO_2 Reduction 3. The Selective and Reversible Reduction of CO_2 on Cu Alloy Electrodes. *J. Electrochem. Soc.* **1991**, *138* (11), 3382.

(259) Hori, Y.; Murata, A.; Ito, S.; Yoshinami, Y.; Koga, O. Nickel and Iron Modified Copper Electrode for Electroreduction of CO2 by in-Situ Electrodeposition. *Chem. Lett.* **1989**, No. 9, 1567–1570.

(260) Hori, Y.; Murata, A.; Ito, S. Enhanced Evolution of CO and Suppressed Formation of Hydrocarbons in Electroreduction of CO2 at a Copper Electrode Modified with Cadmium. *Chem. Lett.* **1990**, No. 7, 1231–1234.

(261) Hori, Y.; Murata, A.; Takahashi, R.; Suzuki, S. Electroreduction of CO to CH_4 and C_2H_4 at a Copper Electrode in Aqueous Solutions at Ambient Temperature and Pressure. *J. Am. Chem. Soc.* **1987**, *109* (16), 5022–5023.

(262) Hori, Y.; Takahashi, R.; Yoshinami, Y.; Murata, A. Electrochemical Reduction of CO at a Copper Electrode. *J. Phys. Chem. B* **1997**, *101* (36), 7075–7081.

(263) Peterson, A. A.; Abild-Pedersen, F.; Studt, F.; Rossmeisl, J.; Nørskov, J. K. How Copper Catalyzes the Electroreduction of Carbon Dioxide into Hydrocarbon Fuels. *Energy Environ. Sci.* **2010**, *3* (9), 1311.

(264) Hori, Y.; Wakebe, H.; Tsukamoto, T.; Koga, O. Electrocatalytic Process of CO Selectivity in Electrochemical Reduction of CO_2 at Metal Electrodes in Aqueous Media. *Electrochim. Acta* **1994**, *39* (11–12), 1833–1839.

(265) Hori, Y.; Murata, A.; Kikuchi, K.; Suzuki, S. Electrochemical Reduction of Carbon Dioxides to Carbon Monoxide at a Gold Electrode in Aqueous Potassium Hydrogen Carbonate. *J. Chem. Soc. Chem. Commun.* **1987**, No. 10, 728–729.

(266) Porosoff, M. D.; Yang, X.; Boscoboinik, J. A.; Chen, J. G. Molybdenum Carbide as Alternative Catalysts to Precious Metals for Highly Selective Reduction of CO_2 to CO. *Angew. Chemie - Int. Ed.* **2014**, *53* (26), 6705–6709.

(267) Rasul, S.; Anjum, D. H.; Jedidi, A.; Minenkov, Y.; Cavallo, L.; Takanabe, K. A Highly Selective Copper-Indium Bimetallic Electrocatalyst for the Electrochemical Reduction of Aqueous CO_2 to CO. *Angew. Chemie - Int. Ed.* **2015**, *54* (7), 2146–2150.

(268) Köleli, F.; Atilan, T.; Palamut, N.; Gizir, A.; Aydin, R.; Hamann, C. H. Electrochemical Reduction of CO_2 at Pb- and Sn-Electrodes in a Fixed-Bed Reactor in Aqueous K_2CO_3 and $KHCO_3$ Media. *J. Appl. Electrochem.* **2003**, *33* (5), 447–450.